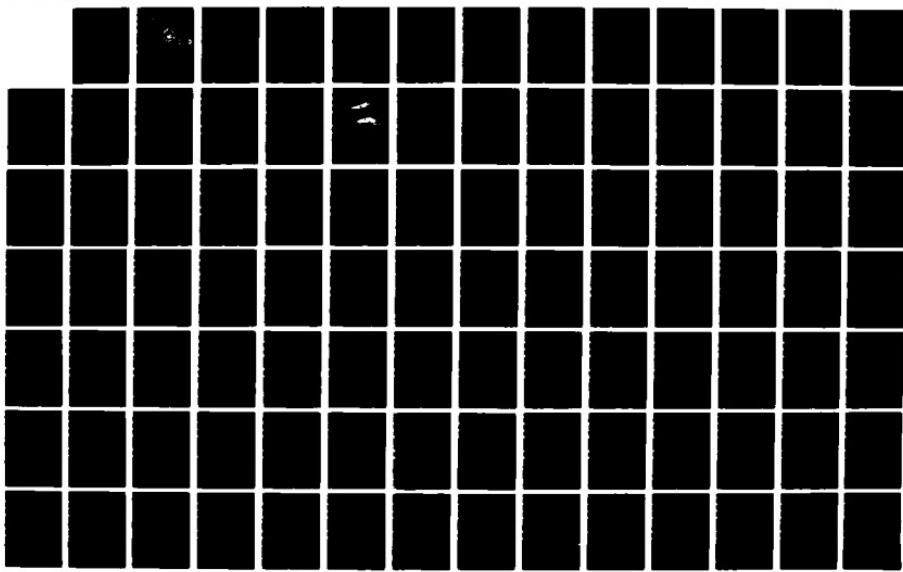


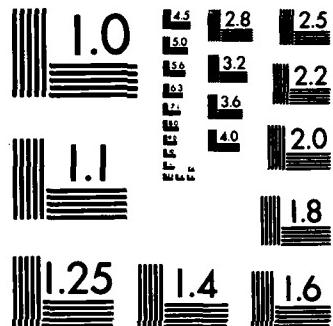
AD-A189 588 APPLICATION OF A FLUX VECTOR SPLITTING METHODOLOGY
TOWARDS THE SOLUTION O (U) NAVAL POSTGRADUATE SCHOOL
MONTEREY CA T H FRANSSON JUL 87 NPS67-87-006 1/3

UNCLASSIFIED

F/G 28/4

NL





MICROCOPY RESOLUTION TEST CHART
NATIONAL BUREAU OF STANDARDS-1963-A

DTIC FILE COPY

NAVAL POSTGRADUATE SCHOOL
Monterey, California



2
DTIC
SELECTED
MAR 01 1988
S D
SH

AD-A189 500

APPLICATION OF A FLUX VECTOR SPLITTING METHODOLOGY
TOWARDS THE SOLUTION OF UNSTEADY TRANSONIC FLOWS,
WITH FUTURE EMPHASIS ON THE BLADE FLUTTER PROBLEM

TORSTEN H. FRANSSON

JULY 1987

Approved for public release; distribution unlimited.
Prepared for: National Research Council
Washington, D.C. 20418

88 2 29 063

NAVAL POSTGRADUATE SCHOOL
MONTEREY, CALIFORNIA

Rear Admiral R. C. Austin
Superintendent

K. T. Marshall
Acting Provost

The work reported herein was performed at the Department of Aeronautics and Astronautics, Naval Postgraduate School, while the author was a National Research Council Associate from August 1986 through August 1987. The NRC technical advisor was Dr. M. F. Platzer of the Department of Aeronautics and Astronautics.

Publication of this report does not constitute approval of the sponsor for the findings or conclusions. It is published for information and for the exchange and stimulation of ideas.

This report was prepared by:

Torsten Fransson

T. H. FRANSSON
NRC Associate

M. F. Platzer

M. F. PLATZER
Professor
Department of Aeronautics and
Astronautics

Reviewed by:

Released by:

M. F. Platzer

M. F. PLATZER, Chairman
Department of Aeronautics and
Astronautics

Gordon E. Schacher

GORDON E. SCHACHER
Dean of Science and Engineering

AD-A1895-00

REPORT DOCUMENTATION PAGE

1a. REPORT SECURITY CLASSIFICATION UNCLASSIFIED		1b. RESTRICTIVE MARKINGS	
2a. SECURITY CLASSIFICATION AUTHORITY		3. DISTRIBUTION/AVAILABILITY OF REPORT Approved for public release; distribution is unlimited.	
2b. DECLASSIFICATION/DOWNGRADING SCHEDULE			
4. PERFORMING ORGANIZATION REPORT NUMBER(S) NPS67-87-006		5. MONITORING ORGANIZATION REPORT NUMBER(S)	
6a. NAME OF PERFORMING ORGANIZATION Naval Postgraduate School	6b. OFFICE SYMBOL (If applicable) Code 67	7a. NAME OF MONITORING ORGANIZATION	
6c. ADDRESS (City, State, and ZIP Code) Monterey, CA 93943		7b. ADDRESS (City, State, and ZIP Code)	
8a. NAME OF FUNDING/SPONSORING ORGANIZATION Chief of Naval Research	8b. OFFICE SYMBOL (If applicable)	9. PROCUREMENT INSTRUMENT IDENTIFICATION NUMBER N0001487WR4E011	
8c. ADDRESS (City, State, and ZIP Code) Arlington, VA 22217		10. SOURCE OF FUNDING NUMBERS	
		PROGRAM ELEMENT NO. 61153N	PROJECT NO. RR014-01
		TASK NO. 10P-011	WORK UNIT ACCESSION NO.
11. TITLE (Include Security Classification) Application of a Flux Vector Splitting Methodology Towards the Solution of Unsteady Trans Flows, With Future Emphasis on the Blade Flutter Problem			
12. PERSONAL AUTHOR(S) Torsten H. Fransson			
13a. TYPE OF REPORT Final	13b. TIME COVERED FROM 8/86 TO 8/87	14. DATE OF REPORT (Year, Month, Day) July 1987	15. PAGE COUNT 260
16. SUPPLEMENTARY NOTATION			
17. COSATI CODES		18. SUBJECT TERMS (Continue on reverse if necessary and identify by block number) Inviscid Compressible Flows Nozzle Flows Unsteady Transonic Flows Computational Fluid Dynamics	
FIELD	GROUP	SUB-GROUP	
19. ABSTRACT (Continue on reverse if necessary and identify by block number) The study presents a method based on the flux vector splitting approach, to the problem of unsteady two dimensional inviscid transonic flows, with emphasis on the numerical determination of the shock position, through nozzles with varying back pressure. The methodology, governed by the Euler equations, is first explained for one and two dimensional steady state applications, and the accuracy of the results is validated by comparison with exact (one dimension) and numerical (two dimensions) solutions.			
20. DISTRIBUTION/AVAILABILITY OF ABSTRACT <input checked="" type="checkbox"/> UNCLASSIFIED/UNLIMITED <input type="checkbox"/> SAME AS RPT <input type="checkbox"/> DTIC USERS		21. ABSTRACT SECURITY CLASSIFICATION UNCLASSIFIED UNLIMITED	
22a. NAME OF RESPONSIBLE INDIVIDUAL M. F. Platzer		22b. TELEPHONE (Include Area Code) 408/646-2311	22c. OFFICE SYMBOL 67

Application of a Flux Vector Splitting Methodology Towards the Solution of Unsteady Transonic Flows, With Future Emphasis on the Blade Flutter Problem.

Torsten H. Fransson
July 20, 1987.

The present study was conducted when the author held a National Research Council Associateship, with Dr. R. W. Kinney as program manager, at the Naval Postgraduate School
Department of Aeronautics
Monterey
California 93943

I. Abstract

The study presents a method, based on the flux vector splitting approach, to the problem of unsteady two dimensional inviscid transonic flows, with emphasis on the numerical determination of the shock position, through nozzles with varying back pressure. The methodology, governed by the Euler equations, is first explained for one and two dimensional steady state applications, and the accuracy of the results is validated by comparison with exact (one dimension) and numerical (two dimensions) solutions.

The model is then applied to the problem of fluctuating back pressure in quasi one dimensional and two dimensional flows. The one dimensional results are validated by comparison with a small perturbation analytical unsteady solution, whereafter sample cases are performed with the objective to understand fundamental aspects of unsteady flows.

It is concluded that both the amplitude and frequency of the imposed fluctuating exit pressure are important parameters for the location of the unsteady shock. It is also shown that the average unsteady shock position is not identical with the steady state position, and that the unsteady shock may, under certain circumstances, propagate upstream into the subsonic flow domain. The pressure jump over the shock, as well as the unsteady post-shock pressure, is different for identical shock-positions during the cycle of fluctuation, which implies that an unsteady shock movement, imposed by oscillating back pressure, may introduce a significant unsteady lift and moment. This may be of importance for flutter predictions.

It is also noted that, although the sonic velocity is obtained in the throat of steady state quasi one dimensional flow, this is not necessarily true for the unsteady solution. During part of the period with fluctuating back pressure, the flow velocity may be subsonic at the throat, and still reach a supersonic value later in the nozzle. This phenomena depends on the frequency and amplitude of the imposed pressure fluctuation, as well as on the nozzle geometry.



NTIS GRA&I	<input checked="" type="checkbox"/>
DTIC TAB	<input type="checkbox"/>
Unannounced	<input type="checkbox"/>
Justification	<input type="checkbox"/>
By	<input type="checkbox"/>
Distribution	<input type="checkbox"/>
Availability Codes	<input type="checkbox"/>
Dist	Aveil and/or Special
A-1	

II. Brief Information to the Reader.

The present report consists of four main parts, each of which can quickly be scanned in dependence of the reader's interest. The following gives a brief overview of the different parts.

A general introduction to blade flutter in axial flow turbomachines is given in section 1.1, followed by an introduction to existing numerical methods for attacking this problem. It is not necessary to go into this section in order to judge the results presented in the later sections. It may however be of interest if the reader would like to judge the implications of the results in the broader context of blade flutter.

The numerically method employed in the present study is briefly presented in sections 3.1 to 3.4 and 4.1 to 4.5. Again, the results can be judged essentially without reading these sections.

The validation of the method and a few sample cases are presented in sections 3.5 (quasi one dimensional steady state), 4.6 (two dimensional steady state), 5.1 to 5.2 (quasi one dimensional unsteady) and 5.3 (two dimensional unsteady). These sections are obviously the most important ones.

A few details about the method are given in the appendices, together with indications of how to run the program on the IBM main frame at the Naval Postgraduate School, Monterey.

It should also be stated that the report treats "Work in progress" and is largely meant to be a reference also for the author. Thus, several details that would normally not be found in a final report may be present here. On the other hand, certain aspects of a final report in the usual sense may also be missing.

List of Contents.

- I. **Abstract**
- II. **Brief Information to the Reader**

List of Contents

1. **Introduction**
 - 1.1. General Introduction to the Blade Flutter Problem.
 - 1.2. Introduction to the Present Numerical Methodology.
2. **Nomenclature**

Part I: Development, Implementation and Testing of the Methodology for Steady-State Flow.

3. One-Dimensional Inviscid Steady-State Flow

3.1 Flux Vector Splitting

3.1.1 *Steger/Warming Splitting*

3.1.2 *van Leer Splitting*

3.2 Spatial Differencing

3.3 Boundary Conditions at Inlet and Outlet

3.3.1 *First Method*

3.3.1.a *Extrapolation*

3.3.1.b *Inlet Boundary*

3.3.1.c *Outlet Boundary*

3.3.2 *Second Method*

3.3.2.a *Outlet Boundary*

3.3.2.b *Inlet Boundary*

3.4 Solution Algorithm for Quasi One Dimensional Flow

3.5 Test Problems and Computational Results

3.5.1 *First Test Problem*

3.5.2 *Second Test Problem*

3.5.3 *Third Test Problem*

3.5.4 *Test of "Non-Reflective" Boundary Condition at Inlet*

4. Two Dimensional Inviscid Steady-State Flow

4.1. Governing Equations in Generalized Coordinates

4.2. Grid Construction

4.2.1 *Grid Lines Situated At the Walls*

4.2.2 *Grid Lines Situated 1/2 Mesh Away From the Walls*

4.3. Flux Vector Splitting of the Governing Equations

4.3.1. Cartesian coordinates

4.3.1.a. Steger/Warming Splitting

4.3.1.b. Van Leer Splitting

4.3.2 Generalized coordinates

4.4. Boundary Conditions

4.4.1 Boundary Conditions At the Blade Walls.

4.4.1.a. Grid Points Situated On the Walls.

4.4.1.b. Grid Points Situated 1/2 Mesh From Walls.

4.4.2 Inlet Boundary.

4.4.3 Outlet Boundary.

4.5. Numerical Algorithm in Two Dimensions

4.6. Two Dimensional Test Problems and Computational Results.

4.6.1. First Test Problem

4.6.2. Second Test Problem

Part II: Testing of the Methodology for Unsteady Flows in Non-Moving Grids.

5. One Dimensional Unsteady Test Problems and Computational Results.

5.1. Shock Tube.

5.2. Shock Oscillations Induced by Time Varying Back Pressure.

6. Two Dimensional Unsteady Results.

7. Mapping from Physical to Computational Plane of Reference
8. Determination of the Matrix Terms
9. Recommendations for Improvements
10. Acknowledgements
11. References

Appendix (Only in Original):

A1: Derivation of basic equations in dimensionless form.

A2: Development of governing equations in strong conservative form for generalized coordinates.

A3: Relationship between flow variables in dimensionless form.

A4: Development of the Riemann Invariants.

A4.1 Compatibility Equations and Riemann Invariants.

A4.2 Postcorrection Technique

A5: Second Order Two Step Explicit Method.

A6: Development of Steger/Warming Flux Vector Splitting in Two Dimensions.

A7: Development of Modified Steger/Warming Flux Vector Splitting in Two Dimensions.

A8. Determination of Computational Time Step and Its Physical Value.

A9. Expression for Jacobian Determinant.

A10. Flux Vector Splitting by van Leer.

A11. Users Manual.

A11.1. General Information

A11.2. Example of Quasi One Dimensional Continuation Run.

A11.3. Example of Two Dimensional Run.

A11.4. Example of Plot Program Run.

- A11.5. Listing of Flow Calculation Program.
- A11.6. Listing of Joukowski Profile Generation Program.
- A11.7. Listing of Joukowski Profile Generation Output.
- A11.8. Listing of Plot Program.
- A11.9. Results From a One-Dimensional Sample Run.
- A11.10. Results From a Two-Dimensional Sample Run.

1. Introduction.

1.1. General Introduction to the Blade Flutter Problem.

One of the many serious problems encountered during the development of modern jet engines and industrial turbomachines is the prediction of flow induced vibrations which may lead to an eventual machine failure. Due to the interaction of several complicated phenomena in turbomachines, this problem is still today far from being resolved even though a significant amount of work has been performed in the domain of aeroelasticity, which concerns the vibration of a deformable structure in a fluid, during the two last decennia.

Among all the complicated phenomena, the ones concerning the aeroelastic stability of the turbomachine blades are part of the most vital. Such stability investigations will be even more significant in the future as blade vibration predictions become increasingly important as part of a trend towards higher unit powers, often without increase in the number of stages in the machine. This trend implies, as examples:

- longer and more slender blades
- higher blade loadings
- higher flow velocities
- higher inlet flow temperatures in turbines
- higher mass flow rates.

The excitation of blade vibrations may be either forced or selfsustained.

In the first group (forced vibrations), such phenomena as:

- multiples of rotor frequencies
- inlet distortions in temperature, velocity and flow direction
- stator-rotor interactions

may be classified.

The second group (self-excited blade vibrations or blade flutter) considers instead the interaction between a blade movement and the therefrom induced time dependent aerodynamic forces.

In a turbomachine, flow phenomena from both these groups interfere with each other and create complicated unsteady flow pattern through the bladings. This pattern can however not be predicted with present theoretical methods, wherefore several idealizations of the time dependent flow are normally made.

In the field of self-excited blade vibrations, different flutter domains, dependent upon the flow conditions in the machine, have been identified throughout the years, both in compressors and in turbines. Due to the high pretensions on modern jet engines, most of the flutter problems reported have occurred in fan stages of these machines. Flutter phenomena have recently also become of practical interest in transonic steam and gas turbines, especially at high back pressures. In these operating conditions, the flow in the blade passage is presumably transonic and eventually partially or fully stalled.

Some of the possible types of blade flutter are represented schematically in Figure 1.1, where a typical modern compressor chart is shown. Depending upon the flow conditions, the different flutter types in the Figure 1.1 may be characterized as (see for example /25/-/27/):

1. Subsonic/transonic positive incidence stall flutter where the compressor operates near the surge line at either part speed or near the design speed. Although the term "stalled" is generally used, it is not settled that the flow in this flutter region is always separated over the whole blade, or if instead the flutter is associated with high loading.

2. Negative incidence transonic choke flutter, at part speed. This type of flutter may appear when the flow in a compressor accelerates through sonic transition. This flutter region is probably associated with local blade separations and unsteady shock waves. An important question here is under which circumstances large shock oscillations occur.

3. Supersonic positive incidence stall flutter. The flow is supersonic at the outer portion of the blade and the stage operates near the surge limit. It is expected that the flow has strong in-passage shocks.

4. Unstalled supersonic flutter, at full speed and with attached flow. It can occur at design point and at higher or lower pressure ratios and may limit high speed operations.

5. Supersonic flutter (type "A100"). This type of blade flutter has been found to appear suddenly above a certain pressure ratio, below which no flutter is encountered. Increased loading may shift this critical pressure ratio.

All of the above mentioned flutter limits are of large practical interest, and several investigations, both experimentally and theoretically, have been conducted in each region. It should also be pointed out that most of

the regions in Fig. 1.1 seem to have some relation with the transonic flow region, i.e. they are liable to be associated with strong unsteady shock waves. If this unsteady shocks have an influence on the stability of a certain blading is still a very open question (the presented study should be viewed in this context as far as its shortterm goal is concerned). An unsteady shock moving around an a blade might eventually introduce some phase lag between the blade movement and the resulting pressure response, as well as an important change in the amplitude of the lift distribution on the blade.

Presently, fully theoretical models exist for the prediction of unstalled self-excited blade vibrations (domains 6, 7 and 8 in Fig. 1.1), but most prediction methods for partially or fully stalled flow are heavily coupled with extensive experimental data sets to yield semi-empirical models. These flutter predictions are thus normally of proprietary nature.

Many of the existing theoretical prediction models for unstalled flow look promising for the computation of aeroelastic forces acting upon vibrating blades. However, as the main interest from the industry is to compute the unsteady blade forces as fast and cheap as possible in order to avoid blade failures, only a very limited number of methods consider also the fully unsteady flow between the blades although the apprehension of how disturbances propagate from one blade to another is essential to the fundamental understanding of aeroelastic phenomena in blade rows.

1.2. Introduction to the Present Numerical Methodology.

It is the purpose of the present work to apply and test a fully unsteady numerical method for, in the future, predicting both the aeroelastic blade forces and the unsteady flow through vibrating cascades, and thus to contribute towards the comprehension of unsteady physical flow phenomena in turbomachines.

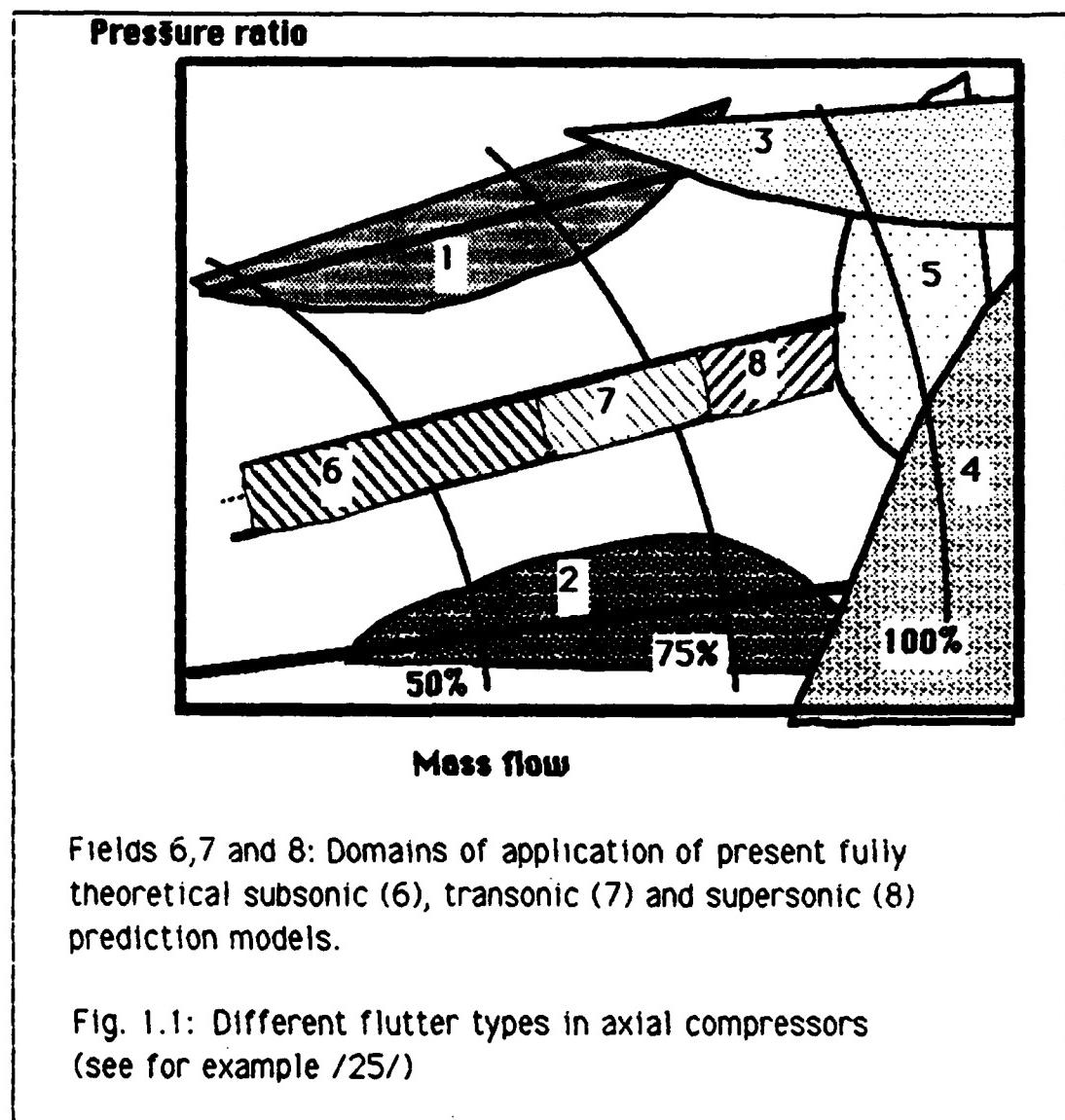
Recently a few studies, based upon the fully unsteady Euler equations, have been developed for predicting both the aeroelastic blade forces and the unsteady, unstalled flow through vibrating two dimensional cascades /7,15-17/. The study in /7/ showed the feasibility of the approach for two dimensional subsonic flow through a cascade of compressor blades with thin leading edges. However, the largest interest of aeroelasticity lies in the transonic flow region wherefore it is considered, as an extention of the work in /7/, to develop a method with the capability to

capture normal unsteady shock waves (and later to treat rounded leading edges) while maintaining the Euler equations and taking into consideration the significant development of new numerical techniques during the past years. These techniques have mainly been directed towards the consideration of the wave like (or hyperbolic) nature of the Euler equations, and performs the spatial differencing of the fluxes in an "upwind" (in regards to the wave propagation) manner (see for a few examples /11-14,18-23/). As pointed out in /23/ these methods, sometimes denoted "flux vector splitting" (ref. /11-14/) and "flux difference splitting" (ref. /18-23/), can all be regarded as similar in some respects although the way the fluxes are split are based on somewhat more physical reasoning in /18-23/ and more mathematical in /11-14/.

While this modern numerical methods seem to be robust and reliable (at least for steady-state flows), a drawback which should not be forgotten is their large computational cost because of the increased number of arithmetic operations that are needed to be solved per iteration step. The methods are, and should remain, only one aspect of a continuous ongoing effort to understand the flow in turbomachines.

The present study is based on a "flux vector splitting" method, with the application towards the unsteady flow through an oscillating cascade. Here, the method is briefly presented whereafter comparisons with existing numerical and exact (in one dimension) steady state solutions for one and two dimensional channel flows are made. Test cases (in one dimension) and numerical examples for unsteady transonic flows with oscillating back pressure are thereafter given, as regards to the methods capability to accurately capture unsteady normal shock waves in a non-moving reference plane (i.e. pressure oscillations are introduced from upstream or downstream and the nozzle walls and the blades do not move). A small attempt to evaluate how well the numerical method represents the expected physical phenomena and the implications of the results towards the blade flutter problem is given.

Figures for section 1.



2. Nomenclature

Latin:

-	A:	area	[m ² , -]
-	a:	speed of sound	[m/s, -]
-	c _p :	specific heat at constant pressure	[m ² /(Ks ²)]
-	c _v :	specific heat at constant volume	[m ² /(Ks ²)]
-	e:	internal energy/unit mass	[m ² /s ² , -]
-	e _c :	total energy/unit mass=	
		=e+q ² /2=p/[(γ-1)ρ]+q ² /2:	[m ² /s ² , -]
-	e _r =h _r :	reference value for energy and entalphy=q _r ²	[m ² /s ²]
-	e _x , e _y :	unity vectors	[-]
-	f:	frequency	[Hz]
-	F:	flux vector in ξ direction	[-]
-	G:	flux vector in η direction	[-]
-	h=e+p/ρ:	entalphy/unit mass	[m ² /s ² , -]
-	h _c :	total entalphy/unit mass=	
		=h+q ² /2=e _c +p/ρ=[γp]/[(γ-1)ρ]+q ² /2	[m ² /s ² , -]
-	k:	reduced frequency, based on half chord k={ωl _r }/{2q _r }	[-]
		(Note that we here will use q=q _r , i.e. the velocity used for computing the reduced frequency is not the inlet, nor the outlet velocity.)	
-	k:	time step indicator	[-]
-	l _r :	reference value for length, l _r =x _r =y _r =c(=chord)	[m]
-	P:	pressure	[N/m ² , -]
-	P _{amp} :	amplitude of sinusoidal pressure fluctuation	[N/m ² , -]
-	P _r :	reference value for pressure	[N/m ²]
-	q:	velocity vector=u _x +v _y	[m/s, -]
-	q _r :	reference value for velocity=(RT _r) ^{0.5} (Note that q _r =speed of sound/√γ.)	[m/s]
-	R:	gas constant (≈286.7 for air)	[m ² /s ² /K]

-	R^+ :	Riemann invariant in positive coordinate direction	[-]
-	R^- :	Riemann invariant in negative coordinate direction	[-]
-	s :	dimensionless entropy = $(s-s_r)/c_v$	[-]
-	t :	time	[s, -]
-	t_{cycle} :	time for a period of oscillation	[s, -]
-	t_0 :	time when oscillation starts	[s, -]
-	t_0 :	old time before next iteration step	[s, -]
-	t_r :	reference value for time = t_r/q_r	[s]
-	t_{sh} :	time for pressure disturbances to travel from the exit to the shock	[s, -]
-	T :	temperature	[K, -]
-	T_r :	reference value for temperature	
-	u :	velocity component in x direction	[m/s, -]
-	u_s :	shock velocity in x direction	[m/s, -]
-	v :	velocity component in y direction	[m/s, -]
-	x :	Cartesian coordinate direction	[m, -]
-	x_s :	shock position	[m, -]
-	y :	Cartesian coordinate direction	[m, -]

Greek:

-	Δt :	time increment for one time step	[s, -]
-	ρ :	density	[kg/m ³ , -]
-	ρ_r :	reference value for density = $\rho_r/(RT_r)$	[kg/m ³]
-	γ :	ratio of specific heats (= 1.4 for air)	[-]
-	ω :	circular frequency	[rad/s]
-	ξ :	curvilinear coordinate direction	[-]
-	η :	curvilinear coordinate direction	[-]

Subscripts:

-	amp :	amplitude of sinusoidal oscillations in time
-	c :	stagnation value in the absolute frame of reference
-	e :	values at downstream (=exit)

- $r:$ reference values
- $s:$ shock
- $(\cdot)_t, (\cdot)_x, (\cdot)_y$ partial derivative in t, x and y resp.
- $-\infty:$ infinity upstream
- $+\infty:$ infinity downstream

Superscripts:

- $^*:$ critical values
- $^{**}:$ intermediate values in two step integration method
- $^-:$ dimensionless values (only used in ambiguous context)
- $^{\xi\eta}:$ variables in (ξ, η) plane

Special Notations:

- **Bold symbols:** Matrices

**Part I: Development, Implementation and
Testing of the Methodology for Steady-State
Flow.**

3. One Dimensional Inviscid Steady-State Flow.

Before going into the general application of two dimensional flow, some basic one dimensional investigations are necessary to assess the flux vector splitting method in conjunction with the proposed explicit numerical time integration scheme.

The one dimensional inviscid gasdynamic equations of motion can be expressed in conservation law form as:

$$\mathbf{W}_t + \mathbf{F}_x = 0 \quad (3.0-1)$$

where \mathbf{W} and \mathbf{F} are vectors expressing the dependent variables and the fluxes:

$$\mathbf{W} = \begin{bmatrix} \rho \\ \rho u \\ \rho e_c \end{bmatrix}; \quad \mathbf{F} = \begin{bmatrix} \rho u \\ \rho u^2 + p \\ u(\rho e_c + p) \end{bmatrix} \quad (3.0-2)$$

Furthermore, the equation of state for a perfect gas is given by:

$$e_c = p / ((\gamma - 1)\rho) + u^2 / 2 \quad (3.0-3)$$

For the present application, the mass, momentum and energy components of the flux vector \mathbf{F} are split into upwind parts, expressing (in some splittings) the "positive" and "negative" eigenvalues of \mathbf{F} . Several methods of performing such "flux vector splittings" can be found in the literature. Out of these, two have been adopted and tested for the present application. These are the splittings according to Steger/Warming (/13/,/29/,/11/) and van Leer (/28/,/11/). The basic idea behind any of these is that if \mathbf{F} can be split into $\mathbf{F} = \mathbf{F}^+ + \mathbf{F}^-$, where

$\mathbf{W}_t + \mathbf{F}^+_x = 0$ is stable for backward differencing

$\mathbf{W}_t + \mathbf{F}^-_x = 0$ is stable for forward differencing

the same differencing can be used for the full equation

$$W_t + F^+ x + F^- x = 0,$$

with similar (although not identical) stability characteristics /38/.

3.1. Flux Vector Splitting.

3.1.1. *Steger/Warming Splitting.*

In the Steger/Warming approach the fluxes are split according to the sign of the local eigenvalues of the flux vector F . The mathematical development of the eigenvalues and the splittings are given in ref. /13,11/ and, in a shorter version, in Appendix A6. For brevity, only the final results are given here.

Three eigenvalues, λ_1 , λ_2 and λ_3 , of the flux vector F exist in one dimensional flow. These are normally expressed as:

$$\begin{cases} \lambda_1 = u \\ \lambda_2 = u + a \\ \lambda_3 = u - a \end{cases} \quad (3.1.1-1)$$

These eigenvalues can be, depending on the magnitude of the velocity u ($u \leq 0$, $0 < u \leq a$, $u > a$), separated into positive and negative parts:

$$\lambda_n = \lambda_n^+ + \lambda_n^- \quad (3.1.1-2)$$

where, in the original study by Steger/Warming /13/, the λ_n^+ , λ_n^- are defined as:

$$\begin{aligned} \lambda_n^+ &= (\lambda_n + |\lambda_n|)/2 \\ \lambda_n^- &= (\lambda_n - |\lambda_n|)/2 \end{aligned} \quad (3.1.1-3)$$

These definitions were later slightly modified by Steger, due to some problems of accurately capturing the rarefaction through the sonic point, to /29/:

$$\begin{aligned} \lambda_n^+ &= (\lambda_n + [\lambda_n^2 + \epsilon]^{0.5})/2 \\ \lambda_n^- &= (\lambda_n - [\lambda_n^2 + \epsilon]^{0.5})/2 \end{aligned} \quad (3.1.1-4)$$

where ϵ is a small number in the order of $\epsilon = 0.04$ /29/. However, it should be pointed out that this is a numerical trick (it introduces a numerical

dissipation different from the one created with the use of the relation (3.1.1-3)) only to eliminate a small glitch around the sonic point, with no other apparent physical reason than creating continuous λ^+, λ^- through this point /29,11/.

In whichever of the above ways the λ^+ and λ^- are created, the flux vector F can be split into two terms F^+ and F^- /13/, with:

$$F = F^+ + F^- \quad (3.1.1-5)$$

where each of the splitted flux vectors F^+ and F^- can be expressed as /13,11/:

$$F^\pm = \rho/[2\gamma] \left[\begin{array}{l} 2[\gamma-1]\lambda_1^\pm + \lambda_2^\pm + \lambda_3^\pm \\ 2[\gamma-1]\lambda_1^\pm u + \lambda_2^\pm [u+a] + \lambda_3^\pm [u-a] \\ [\gamma-1]\lambda_1^\pm u^2 + \lambda_2^\pm [u+a]^2/2 + \lambda_3^\pm [u-a]^2/2 + w \end{array} \right]$$

where

$$w = \{[3-\gamma][\lambda_2^\pm + \lambda_3^\pm]a^2\}/\{2[\gamma-1]\} \quad (3.1.1-6)$$

With the definition (3.1.1-3) of λ^\pm , it is seen that

$$F^+ = F; F^- = 0 \text{ if } M = u/a \geq 1 \quad (3.1.1-7)$$

$$F^+ = 0; F^- = F \text{ if } M = u/a \leq -1$$

However, the relation (3.1.1-7) is not any more valid if the forward and backward eigenvalues λ^\pm are defined according to (3.1.1-4).

3.1.2. van Leer Splitting.

A somewhat different approach of splitting the flux vector F was taken by van Leer /28,11/. Here, the flux vector is split into forward and backward parts in function of the local Mach number g instead of in function of the eigenvalues g , which gives:

For supersonic flow (i.e. $|M| = |u/a| \geq 1$), the relation (3.1.1-7) still holds:

$$\begin{aligned} F^+ &= F; F^- = 0 \quad \text{if } M = u/a \geq 1 \\ F^+ &= 0; F^- = F \quad \text{if } M = u/a \leq -1 \end{aligned} \quad (3.1.1-7)$$

and for subsonic flow, the vectors F^+ and F^- are expressed as:

$$F^\pm = \begin{bmatrix} f_1^\pm \\ f_2^\pm \\ f_3^\pm \end{bmatrix} \quad (3.1.1-8)$$

where $f_1^\pm = \pm \rho a ([M \pm 1]/2)^2$
 $f_2^\pm = f_1^\pm \cdot \{[\gamma - 1]u \pm 2a\}/\gamma$
 $f_3^\pm = f_1^\pm \cdot \{[(\gamma - 1)u \pm 2a]^2\}/\{2[\gamma^2 - 1]\}$

It has been shown in /11/ that this splitting gives continuously differentiable split fluxes at sonic and stagnation points. This is contrary to the Steger/Warming splitting (see /11/ for detailed comparison of the splitted fluxes).

A recent review article by van Leer, Thomas, Roe and Newsome /46/ indicates that, out of the two splittings above, the van Leer splitting has the smoothest properties and should capture a shock with slightly less numerical grid points than the Steger/Warming splitting.

3.2 Spatial Differencing

In the flux vector splitting formulation the governing equations can be expressed, both for the Steger/Warming and van Leer splittings, as:

$$W_t + F^+_{x+} + F^-_{x-} = 0 \quad (3.2-1)$$

In the original work by Steger/Warming /13/ the spatial derivatives were approximated with differences taken "upwind" for both F^+ and F^- , i.e. backward (in the negative x direction) for the F^+ and forward (in the positive x direction) for the F^- . In the case of generalized coordinates this approach does however not preserve "free stream" values, i.e. it introduces a dependency of the transformation metrics on the result (see for example /30/). van Leer proposed instead (see for ex. /11/) to use an approach, called the "Monotone Upwind Schemes for Conservation Laws" or "MUSCL" approach, in which the data is first prepared and eventually limited before the numerical differences are performed. The spatial derivatives are here approximated as centered differences, with values at half points:

$$F^\pm_x \approx \Delta F^\pm_i / \Delta x = (F^\pm_{i+1/2} - F^\pm_{i-1/2}) / \Delta x \quad (3.2-2)$$

Furthermore, the $F^\pm_{i+1/2}$ and $F^\pm_{i-1/2}$ are evaluated with two point "upwind" (i.e. backward for F^+ and forward for F^-) extrapolation /11/:

$$\begin{cases} F^+_{i+1/2} = F^+(W^-_{i+1/2}) \\ F^-_{i+1/2} = F^-(W^+_{i+1/2}) \end{cases} \quad (3.2-3)$$

$$\begin{cases} W^-_{i+1/2} = W_i + \Phi^-_i \cdot (W_i - W_{i-1}) / 2 \\ W^+_{i+1/2} = W_{i+1} + \Phi^+_i \cdot (W_{i+1} - W_{i+2}) / 2 \end{cases} \quad (3.2-4)$$

In these expressions, the scalar function Φ is denoted the flux limiter. It has the function to switch from first order spatial accuracy to second order at appropriate points. The value $\Phi=1$ gives second order spatial accuracy while $\Phi=0$ reduces the accuracy to first order.

It has been demonstrated in ref. /11/ (which is an implicit computational code) that, due to the fact that both the ΔF^+ and ΔF^- are evaluated at the same computational locations in the MUSCL approach¹, a method with this approach (independent of whether the Steger/Warming or the van Leer version is used to split the fluxes) gives smoother results around a sonic rarefaction point than the original Steger/Warming spatial differencing. It also reduces, at least in ref. /11/, the overshoots just upstream of the shock region for one dimensional transonic flows.

¹ Contrary to the original Steger/Warming approach where ΔF^+ and ΔF^- are evaluated as

$$\Delta F^+ = \Delta b F^+ = [\Delta \text{backward} F^+] = (F^+_{i+1} - F^+_{i-1})$$

$$\Delta F^- = \Delta f F^- = [\Delta \text{forward} F^-] = (F^-_{i+1} - F^-_i)$$

3.3. Boundary Conditions at Inlet and Outlet

In the present application two different options for treating the boundary conditions-at inlet and outlet were implemented. In the first they are treated in essentially the same way as in /7/ where they are implemented with the "postcorrection method" after Moretti/deNeff /6/. In this technique the numerical treatment of computational points located on the boundaries is conceived in two steps. First the computation is done using, for the approximation of derivatives at the boundaries, values from interior points (and eventually extrapolated therefrom) only. In this preliminary computation the boundary condition has not yet been imposed. Therefore the flow variables so calculated are not correct. However, considering the hyperbolic or wave-like nature of the Euler equations, the Riemann variables (a specific one dimensional combination of speed of sound and velocity, see Appendix A4) carried on characteristics impinging on the boundary are expected to be correct. The values of the primitive variables (velocity and speed of sound) computed so far have thus to be changed by imposing the required boundary condition, while preserving the value of the Riemann variable just computed /7/.

This updating is performed as the final logic at every time step.

In section 3.3.1 this postcorrection technique is discussed for the inlet and outlet boundaries for a one dimensional flow.

In section 3.3.2 a second method, employed in most calculations presented later, is given.

3.3.1. *First Method*

The first method for implementing the boundary condition is based upon the method used for a solution with the MacCormack predictor-corrector solver in /24/, and requires an extrapolation of the flow variables at the boundaries.

3.3.1.a. *Extrapolation of values at the boundary.*

For completeness, it is here noted that the points outside of the computational domain are extrapolated with a three point parabola from the inner of the flowfield according to the formula

$$f = ax^2 + bx + c$$

where a , b and c are constants. This gives thus, with constant spacing in x direction:

- If the point $(i+1/2)$ lies outside the computational domain:

$$a\Delta x^2 = 0.5 \cdot \{f_{i-2} - 2f_{i-1} + f_i\}$$

$$b\Delta x = 0.5 \cdot \{f_{i-2} - 4f_{i-1} + 3f_i\}$$

$$c = f_i$$

and thus

$$f_{i+1} = f_{i-2} - 3f_{i-1} + 3f_i \quad (3.3.1.a-1a)$$

$$f_{i+2} = 3f_{i-2} - 8f_{i-1} + 6f_i \quad (3.3.1.a-1b)$$

whereafter the formula (3.2-4b) gives:

$$f^{+}_{i+1/2} = f_{i+1} + \Phi^{+}_{i+1} \cdot \{f_{i+1} - f_{i+2}\}/2 \quad (3.3.1.a-1c)$$

- If the point $(i-1/2)$ lies outside the computational domain:

$$a\Delta x^2 = 0.5 \cdot \{f_{i+2} - 2f_{i+1} + f_i\}$$

$$b\Delta x = -0.5 \cdot \{f_{i+2} - 4f_{i+1} + 3f_i\}$$

$$c = f_i$$

and thus

$$f_{i-1} = f_{i+2} - 3f_{i+1} + 3f_i \quad (3.3.1.a-2a)$$

$$f_{i-2} = 3f_{i+2} - 8f_{i+1} + 6f_i \quad (3.3.1.a-2b)$$

whereafter the formula (3.4-2a) gives:

$$f^{-}_{i-1/2} = f_{i-1} + \Phi^{-}_{i-1} \cdot \{f_{i-1} - f_{i-2}\}/2 \quad (3.3.1.a-2c)$$

3.3.1.b. Inlet Boundary.

At the permeable inlet surface (AB in Fig.3.3-1), the space derivatives in x direction are defined with an extrapolation according to the spatial differencing in section 3.3.1.a. After the computation of the whole flow field (including the boundary points) the boundary condition is imposed according to the post correction technique. Presently, two methods are implemented, corresponding to the "radiative" and "capacity" conditions respectively /7/.

In the first ("capacity") technique, the flow is considered to be discharged, from an infinitely large capacity, through a set of small nozzles. In this capacity the stagnation temperature and stagnation pressure are constant. This leads to the following two relationships for the entropy and enthalphy:

$$\begin{aligned} s &= \ln\{\rho_{c1}/\rho_{c1}\gamma\} = \ln\{\rho_{c1}(1-\gamma)\cdot T_{c1}\gamma\} \\ &\quad (=0 \text{ if } T_{c1}=\rho_{c1}=1) \\ h_{c1} &= T_{c1}/(\gamma-1) = a_{1,\text{new}}^2/(\gamma-1) + q_{1,\text{new}}^2/2 \end{aligned} \quad (3.3.1.b-1)$$

where subscript "new" indicates that the values include the correction for the boundary conditions.

In addition, a compatibility equation carries the information on the left-running¹ characteristic from inside the flow field onto the boundary. This can be expressed as:

$$R^{-1,\text{old}} = f(\text{inner of flow field}) = \text{known} = 2a_{1,\text{old}}/(\gamma-1) - q_{1,\text{old}} \quad (3.3.1.b-2)$$

where subscript "old" indicates that the values do not include the correction for the boundary conditions.

As the value of R^- is assumed to be correct, we have

$$R^{-1,\text{old}} = R^{-1,\text{new}} = R^{-1} \quad (3.3.1.b-3)$$

¹ Left-running characteristic indicates in the present study a characteristic in the negative coordinate directions. Similarly, the right-running characteristic is in the positive coordinate directions.

where

$$R^{-1,\text{new}} = 2a_{1,\text{new}}/(\gamma-1) - q_{1,\text{new}} \quad (3.3.1.b-4)$$

From the enthalpy and compatibility equations, $a_{1,\text{new}}$ and $q_{1,\text{new}}$ can be calculated as:

$$a_{1,\text{new}} = \left\{ R^{-1} \pm [R^{-1}^2(1-\gamma)/2 + h_{c1}(\gamma+1)]^{0.5} \right\} (\gamma-1)/(\gamma+1)$$

$$q_{1,\text{new}} = 2a_{1,\text{new}}/(\gamma-1) - R^{-1} \quad (3.3.1.b-5)$$

whereafter the pressure, density and energy can be determined from the entropy equation above.

The second ("non-reflective" or "radiative") technique to treat the boundary is an attempt to decrease the reflections at the inlet.

The basic idea behind this boundary condition is that in a cascade, in contrast to an isolated airfoil where disturbances propagated away from the airfoil diminish in strength with the radial distance from the profile, the flow is bounded. The disturbances in an inviscid flow will thus not always decrease in strength (for vibrating blades, see discussions on sub- and superresonant blade vibrations /8-10/). However, if the flow upstream of the cascade is undisturbed from the left, the left-running disturbances will be simple wave fronts. If, after a certain distance, these wave fronts become straight, it is expected that the reflections from an upstream computational boundary may be reduced. This way of treating the boundary can be visualized as an infinitely long duct with undisturbed flow upstream of the cascade, and it is implemented in the present study in the following way:

As in the first technique, the compatibility equation on the left running characteristic is considered to carry the information from inside the flow field onto the boundary:

$$R^{-1,\text{old}} = f(\text{inner of flow field}) = \text{known} = 2a_{1,\text{old}}/(\gamma-1) - q_{1,\text{old}} \quad (3.3.1.b-6)$$

Contrary to the first technique, however, the boundary conditions are now not imposed at the inlet. It is instead considered that a right running

characteristic (coming from infinity upstream) carries information in an isentropic way from infinity upstream to the inlet and into the flow field. This compatibility equation can be written as:

$$R^+_{1,new} = f(\text{upstream infinity}) = \text{imposed} = 2a_{-\infty,new}/(\gamma-1) + q_{-\infty,new}$$

(3.3.1.b-7)

As the value of R^- is assumed to be correct, we have as before

$$R^-_{1,old} = R^-_{1,new} = 2a_{1,new}/(\gamma-1) - q_{1,new}$$

(3.3.1.b-8)

The boundary conditions imposed are thus $s_{-\infty}$ and $a_{-\infty}$, which gives

$$\begin{aligned} a_{1,new} &= (R^+_{1,new} + R^-_{1,new})/2 \\ q_{1,new} &= (R^+_{1,new} - R^-_{1,new})/4 \end{aligned}$$

(3.3.1.b-9)

It should be pointed out that, as the stagnation values of temperature and pressure are not explicitly imposed at the inlet, the "radiative" boundary condition can not always keep these two variables at their initial values /7/.

3.3.1.c. *Outlet Boundary.*

In subsonic flow, only one boundary condition may be specified at the outlet. This is usually taken to be the static pressure.

In the present study, the static pressure is held constant (for steady state flows, sinusoidal variation for unsteady flows) at the outlet, and this boundary condition is implemented much in the same way as at the inlet.

First it is noted that the Riemann invariant coming from the interior of the flow domain is calculated as above

$$R^+_{2,old} = 2a_{2,old}/(\gamma-1) + q_{2,old}$$

(3.3.1.c-1)

Thereafter this value is considered to be correct also including the boundary conditions, wherefore

$$R^+_{2,new} = 2a_{2,new}/(\gamma - 1) + q_{2,new} = R^+_{2,old} \quad (3.3.1.c-2)$$

Furthermore, if the entropy calculated without considering the boundary conditions is also considered to be correct (i.e. $s_{2,new} = s_{2,old}$), it is possible to determine, from the specified value $p_{2,new}$, the speed of sound $a_{2,new}$. The velocity $q_{2,new}$ is then immediately determined as

$$q_{2,new} = R^+_{2,new} - 2a_{2,new}/(\gamma - 1) \quad (3.3.1.c-3)$$

3.3.2 Second Method

The above method of extrapolating the flow variables to half a grid point outside the computational domain may eventually lead to some problems and/or eventually introduce some unwanted reflections at the boundaries. Another method for treating the inlet and outlet boundary conditions was for these reasons also developed. This second method considers only information from the inside of the flow field and combines the boundary conditions as in the first method (i.e. Riemann invariant from the left or constant stagnation pressure and temperature at the inlet; given static pressure at the outlet) with the information carried along the other family of characteristics (i.e. left-running Riemann invariant at the inlet; right-running Riemann invariant at the outlet).

However, also in this method some special treatment is necessary, for the 2nd order spatial accuracy, in the point next to the boundary. In the present application this is performed by reducing the accuracy of F^+ at point $i=2$ and F^- at point $i=ic-1$ to first order spatial accuracy. This introduces some numerical inaccuracies at the boundaries, but if the flow gradients are not large (as at the inlet and outlet) or if the mesh size is reduced close to the boundaries (as close to a leading edge of a blade), the overall result will still be good.

3.3.2.a. Outlet Boundary.

To the 0th order, the following procedure can be used, with reference to Fig. 3.3-2. The characteristic leaving point "4" at time $t=t_0$ and which impinges in point "3" at time $t=t_0+\Delta t$ is replaced, as in the first method above, by the boundary condition that the static pressure is given, i.e.

$p=p_e$. Thereafter the entropy is invariant along the characteristic between points "2" and "3". Furthermore, the right-running Riemann invariant R^+ is constant along the characteristic between points "1" and "3". The following information is thus obtained:

$$\begin{aligned}\rho_3 &= \rho_e \\ R^+_3 &= R^+_1 \\ s_3 &= s_2\end{aligned}$$

wherefore

$$\begin{aligned}a_3 &= \gamma \cdot \rho_3 \{(\gamma-1)/\gamma\} \cdot e^{(s_3/\gamma)} \\ u_3 &= R^+_1 - 2a_3/(\gamma-1)\end{aligned}$$

The problem which then remains to be solved is to find the location of the points "1" and "2". To the 0th order the entropy can be obtained by a simple extrapolation from the last point inside the boundary, i.e.

$$s_3 = s_{ic-1}$$

The point "1" can, also to the 0th order, be found by considering linear interpolation

$$\begin{aligned}(u_i + a_i) \cdot \Delta t &= (x_{ic} - x_i) \\ ((u_i + a_i) - (u_{i-1} + a_{i-1})) &= ((u_i + a_i) - (u_{i-1} + a_{i-1})) \cdot (x_i - x_{i-1}) / (x_i - x_{i-1})\end{aligned}$$

where the interval $[i-1, i]$ is found by considering when

$$(x_{ic} - x_i) / (u_i + a_i) - \Delta t$$

changes sign. From the above relationships, the value of x_i can be determined as:

$$x_i = -((u_{i-1} + a_{i-1}) \Delta t - x_{ic} - ((u_i + a_i) - (u_{i-1} + a_{i-1})) x_{i-1} \Delta t) / (1 + ((u_i + a_i) - (u_{i-1} + a_{i-1})) / (x_i - x_{i-1}))$$

wherafter the values of u and a can be found in point 1 with linear interpolation as:

$$\begin{aligned} u_1 &= \frac{(u_i - u_{i-1}) \cdot (x_1 - x_{i-1})}{(x_i - x_{i-1})} + u_{i-1} \\ a_1 &= \frac{(a_i - a_{i-1}) \cdot (x_1 - x_{i-1})}{(x_i - x_{i-1})} + a_{i-1} \end{aligned}$$

Obviously, here a more sophisticated interpolation in order to consider the curvature of the characteristics, perhaps along the lines as presented in ref. /47/, would improve the time accuracy of the results.

3.3.2.b Inlet Boundary.

At the inlet boundary, the boundary conditions should instead replace the Riemann invariants along the lines ("1"→"3") and ("2"→"3") (see Fig. 3.3-2), exactly as in the first method in section 3.3.1.a. Thereafter, the point "4" and the values of the flow variables in this point can be found according to the treatment in section 3.3.2.a above. Thus

$$x_4 = \frac{(a_{i-1} - u_{i-1}) \Delta t - [(u_i - a_i) - (u_{i-1} - a_{i-1})] \cdot x_{i-1} \cdot \Delta t / [x_i - x_{i-1}] + x_i}{1 + [(u_i - a_i) - (u_{i-1} - a_{i-1})] \cdot \Delta t / [x_i - x_{i-1}]}$$

whererafter

$$\begin{aligned} 2a_4 / (\gamma - 1) - u_4 &= R^-_4 = R^-_3 \\ 2a_1 / (\gamma - 1) + u_1 &= R^+_1 = R^+_3 \end{aligned}$$

and

$$\begin{aligned} u_3 &= 0.5 \cdot (R^+_1 - R^-_4) \\ a_3 &= 0.5 \cdot (R^+_1 + R^-_4) \cdot \{(\gamma - 1) / 2\} \end{aligned}$$

As at the outlet, a more sophisticated interpolation would not be amiss.

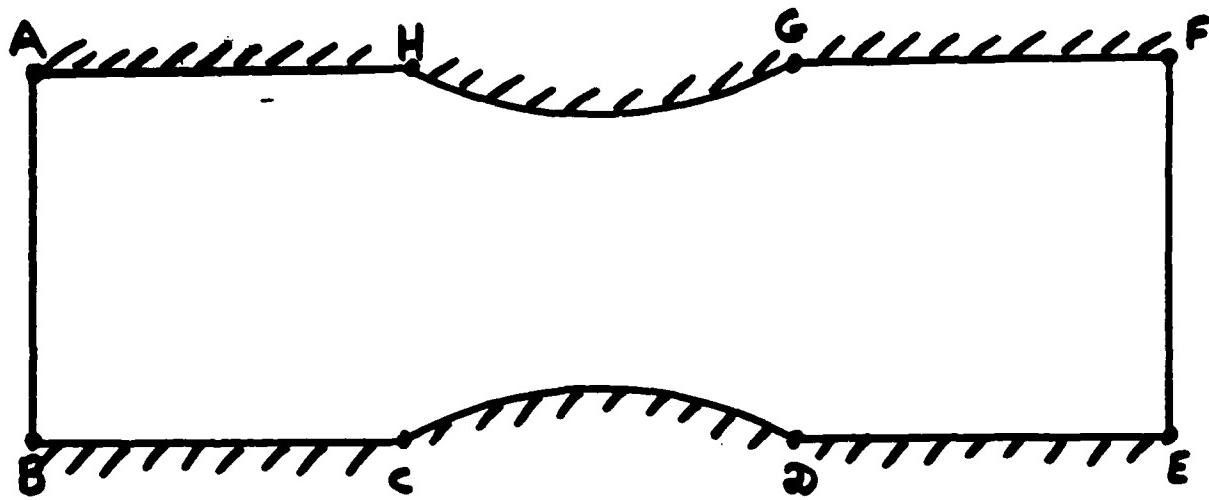


Fig. 3.3-1. Computational domain of interest.

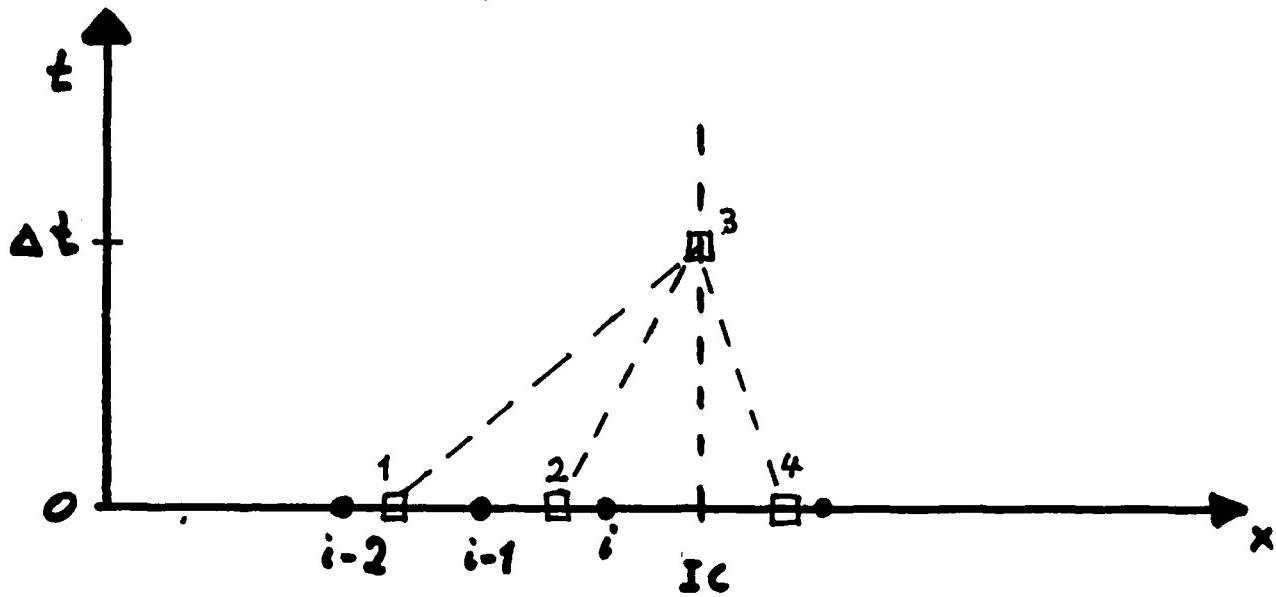


Fig. 3.3-2. Illustration of characteristic lines at the outlet for second treatment of boundary conditions.

3.4. Solution Algorithm for Quasi One Dimensional Flow.

The quasi one dimensional Euler equations can be expressed in flux vector splitting form as /11/

$$W_t + (F^+ + F^-)_x = -H$$

where the H-vector takes into account the variation of the area A and can be expressed as

$$H = (F - P)A_x/A \quad , \text{ with } P = \begin{bmatrix} 0 \\ p \\ 0 \end{bmatrix}$$

The numerical solution to this equation is obtained with an explicit method, considering the area change as a source term with A_x evaluated as a centered difference.

With the above mentioned "MUSCL" approach /11/, an explicit second order numerical scheme can be conceived as a two step method for the left hand side of the above equation (see Appendix A5 as well as ref. /12/). This method is modified from the original Steger-Warming explicit two step method for flux splitting /13/ and can be expressed as /12/:

$$\text{First step: } W_{i+1/2}^{*} = W_i^k - \Delta t \cdot \{\Delta(F_i^+)^k + \Delta(F_i^-)^k\} / \Delta x$$

$$\text{Second step: } W_i^{k+1} = 0.5 \cdot (W_{i+1/2}^{*} + W_i^k - \Delta t \cdot [\Delta(F_{i+1/2}^*)^k + \Delta(F_{i-1/2}^*)^k]) / \Delta x$$

where superscript "*" indicates values at an intermediate time level and the spatial differences $[\Delta(F_i^+), \Delta(F_i^-)]$ are expressed as centered between points $(i+1/2)$ and $(i-1/2)$:

$$\Delta(F_i^+) = \{F^+(W_{i+1/2}^-) - F^+(W_{i-1/2}^-)\}$$

$$\Delta(F_i^-) = \{F^-(W_{i+1/2}^+) - F^-(W_{i-1/2}^+)\}$$

with the values of the vector \mathbf{W} extrapolated as follows /11-12/:

$$\mathbf{W}_{i+1/2}^* = \mathbf{W}_{i+1} + \Phi_{i+1}^* \cdot (\mathbf{W}_{i+1} - \mathbf{W}_{i+2})/2$$

$$\mathbf{W}_{i+1/2}^- = \mathbf{W}_i + \Phi_i^- \cdot (\mathbf{W}_i - \mathbf{W}_{i-1})/2$$

Here the scalar function Φ is the flux limiter /11/ used to switch from first order spatial accuracy ($\Phi=0$) to second order ($\Phi=1$).

3.5. Test Problems and Computational Results.

3.5.1. First Test Problem

The first test problem is the one of a step shock in a duct of constant cross section. Unless the exact solution is initially specified, such a case could not be computed as stable. However, by initially specifying the shock in a certain position it is possible to determine the important information of how much the shock is smeared out through the numerical dissipation inherent in the flux vector splitting method and whether the method can keep the shock in the correct position, in cases with no influence of an area change. Such a computation is represented in Fig. 3.5.1-1 for an upstream Mach number of 1.2909, and for a case where the shock is located exactly at a grid point (Steger-Warming splitting, with 61 grid points). It is seen that 3 grid points lies in the shock region and that a slight undershoot is present downstream of the shock (corresponding to 0.7% of the upstream Mach number).

It should be pointed out that, in the presented calculation, the flux limiter function (Φ) was 1, corresponding to a second order spatial accuracy, in all grid points, except for the calculation of the $\Delta F^+_{\text{shock}+3/2}$, where first order was used ($\Phi^-_{\text{shock}+1}=0$) in order not to extrapolate the $\Delta F^+_{\text{shock}+3/2}$ over the shock surface. The reason for this special treatment is that F^+ and F^- are discontinuous across a shock, although their sum (total flux=F) is continuous (see definition of $F^+_{i+1/2}$).

Averaging the flux over the shock by, in point $(\text{shock}+1/2)$, defining $F_{\text{shock}+1/2} = \{F_{\text{shock}} + F_{\text{shock}+1}\}/2$ obviously eliminates the numerical dissipation of the flux splitting method and reproduces the exact solution.

3.5.2. Second Test Problem

The second test case is the quasi one dimensional test case used by Steger /14/ and Anderson, Thomas, van Leer /11/ in connection with their implicit flux vector splitting methods, implemented with finite volume approaches. The area of the duct is given by, in the present formulation,

$$A(x) = 1 - 0.2 \cdot (x+0.5) \cdot (1.5-x), \quad \text{with } -0.5 \leq x \leq 1.5.$$

(or, in the notation of ref. /11/

$$A(x) = 1 - 0.8x_A(1-x_A) \quad \text{with } 0 \leq x_A \leq 1.$$

The inlet and outlet boundary conditions are such that the shock is positioned at 75% of the nozzle length /11/, with the following characteristics of the flow:

$$\begin{aligned} M_{\text{inlet}} &= 0.5533 \\ M_{\text{upstream of shock}} &= 1.2909 \\ M_{\text{outlet}} &= 0.5701 \\ S_{\text{downstream of shock}} &= 0.0077 \end{aligned}$$

The steady state results presented below were obtained after a large number of iterations, with a total CFL (one dimensional) in the order of $\text{CFL}_{\text{total}} = 2000-3000$ ¹,².

Fig. 3.5.2-1 presents the Mach number and entropy for the case of second order spatial accuracy throughout the flow field (Steger-Warming splitting, with 61 grid points). The shock is covered by two grid points (note that the shock is exactly at a grid point for the exact solution), and a slight undershoot (corresponding to $\{M_{\text{max}} - M_{\text{undershoot}} - M_{\text{exact}}\}/M_{\text{upstream.of.shock}} = -2\%$) is noted downstream.

The same results are presented in Fig. 3.5.2-2 for the case when flux limiting is used for ΔF^+ in one point downstream of the shock. The shock is again represented by two grid points, and the undershoot downstream of it is somewhat smaller (corresponding to $\{M_{\text{max}} - M_{\text{undershoot}} - M_{\text{exact}}\}/M_{\text{upstream.of.shock}} = -1\%$). Similarly, the over- and undershoots in entropy are reduced.

¹ This value should be compared to the indication given in /11/ that several hundred iterations, with a CFL for the there used implicit finite volume method between 10 and 20, was needed to obtain the stationary solution. The total CFL time ($= \text{CFL}_{\text{total}}$) for obtaining the steady state solution is thus comparable for both methods.

² All the one dimensional steady state test cases where run with a $\text{CFL} = 0.4$ per iteration step, i.e. a stability factor according to eq. (A8-6= of STAB=0.4).

If the numerical dissipation over the shock (introduced by the splitting of the flux vector into the two parts F^+ and F^-) is eliminated by averaging the flux vector in point (shock+1/2) as $F_{\text{shock}+1/2} = \{F_{\text{shock}} + F_{\text{shock}+1}\}$, the shock is steeper (covered by one grid point only), as is seen in Fig. 3.5.2-3. However, as expected, the undershoot in both Mach number and entropy is much larger than in the previous two cases (corresponding to $\{M_{\text{max-undershoot}} - M_{\text{exact}}\}/M_{\text{upstream.of.shock}} = -5\%$).

It is also interesting to note that the glitch in the rarefaction through the sonic point as originally pointed out by Steger /14/ (see for example Fig. 3.5.2-5, which is copied from Fig. 10 in ref. /14/) does not appear in the present method /11,14/. This is due to the "MUSCL" extrapolation of the flux splitted values to halfway between gridpoints /11/, instead of creating the flux differences in an upwind and downwind manner as originally proposed by Steger/Warming /13/.

In general, results from the present explicit method correspond well with implicit results as presented in ref. 11.

This can for example be seen by comparing Fig. 3.5.2-6 (copied from Fig. 5, ref. /11/) and Figs. 3.5.2-1a,2a. The undershoots in the shock region seems to be somewhat smaller in the present study than in the results presented in ref. /11/, Fig. 5.

Results presented so far have been obtained by, as in /11/, overspecifying the boundary conditions as the exact values at the outlet. By instead treating the outlet boundary as proposed in the section "Boundary Conditions, Method 1" above (while still overspecifying the inlet boundary conditions), the results are similar (compare Figs. 3.5.2-2 and 3.5.2-4). The only noticeable difference is that the Mach number in the last point upstream of the shock has now decreased slightly from the exact solution ($\approx 0.5\%$). Outside of the shock region, no difference is noticeable (Fig. 3.5.2-4).

It is thus concluded that the present method captures the shock in the correct position in a quasi one dimensional steady state flow, and that the smearing of the shock is in general limited to two grid elements (=3.3% of the nozzle length with 61 grid points). Furthermore, the under- and overshoots in the flow variables are so small as to be of negligible importance for the application under consideration.

3.5.3. Third Test Problem.

The third test problem is considered here because of its later application in two dimensional flow. The quasi one dimensional nozzle has an area change given by:

$$A(x)=0.1\{5-x\} \quad \text{with } -0.5 \leq x \leq 1.5 \quad (3.5.3-1)$$

and the flow conditions, subsonic along the whole nozzle, are governed by an outlet Mach number of 0.8864 (see Fig. 3.5.3-1).

The quasi one dimensional calculation as presented above reproduces the exact solution if 61 grid points are used (Fig. 3.5.3-1a). A three times coarser grid (21 grid points) gives a slight displacement of the isomach lines (Fig. 3.5.3-1b, 3.5.3-2). As previous, it is concluded that the calculation with 61 grid points reproduces the exact solution within the required accuracy, whereas the numerical dissipation introduced with the splitting tends to shift the solution from the exact values if only 21 grid points are used. In this latter case, a non negligible entropy is generated (Fig. 3.5.3-3) and the results from the other flow variables are also shifted.

3.5.4. Test of "Radiative" Boundary Condition At Inlet.

To find out how large the reflection of disturbances from the inner of the flow field can be expected to be at the inlet boundary a one dimensional test was run with the "radiative" boundary treatment according to section 3.3.2.b. The initial distribution corresponds to a step function (Fig. 3.5.4-1) and the calculation was run until steady state. The development of pressure in the nozzle is shown in Fig. 3.5.4-1 and lines of constant pressure in the (x,t) plane is represented in Fig. 3.5.4-2. It is seen that a certain reflection is present at the inlet (notice the slight turn of the lines of constant pressure in time as the disturbance wave approaches the inlet), but that the irregularities are not, in this test case at least, transported more than a few points into the flow field. This is seen by comparing Fig. 3.5.4-2a with Fig. 3.5.4-2b where the same computation is performed with the inlet boundary moved 10 grid points further upstream. The isobars in both figures show a similar behavior. For most practical purposes, this reflection is judged to be of a small nature. More tests of a

similar nature should be performed also in two dimensions, especially with application of the unsteady flow.

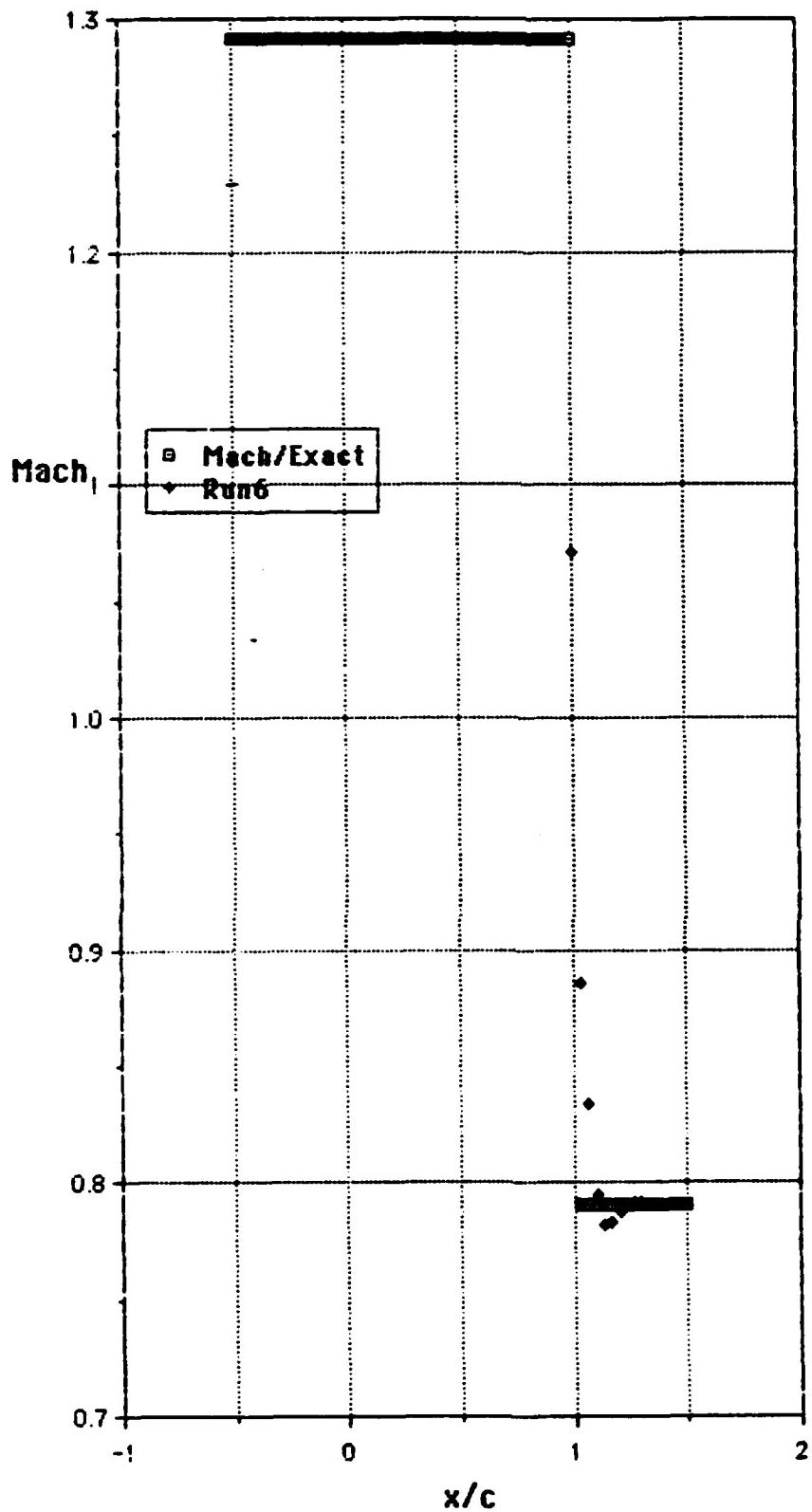


Fig. 3.5.1-1.

Stepshock calculation. First quasi one dimensional sample case. Mach number distribution along the nozzle. Boundary conditions overspecified at inlet and outlet.

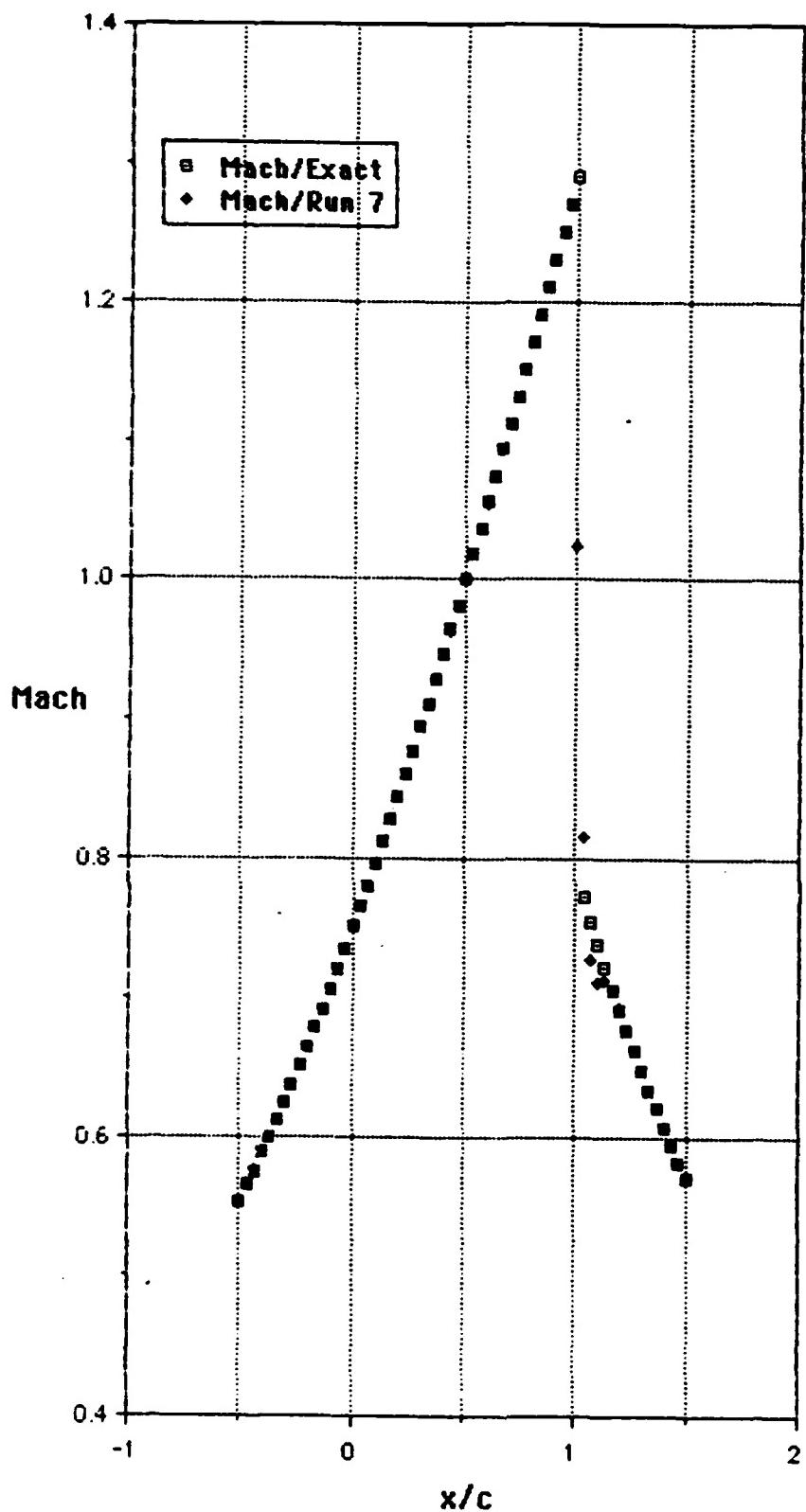


Fig. 3.5.2-1a.

Mach number distribution for the second quasi one dimensional sample case. Steger/Warming splitting, 61 grid points. Second order spatial accuracy throughout the flow field. Boundary conditions overspecified at inlet and outlet.

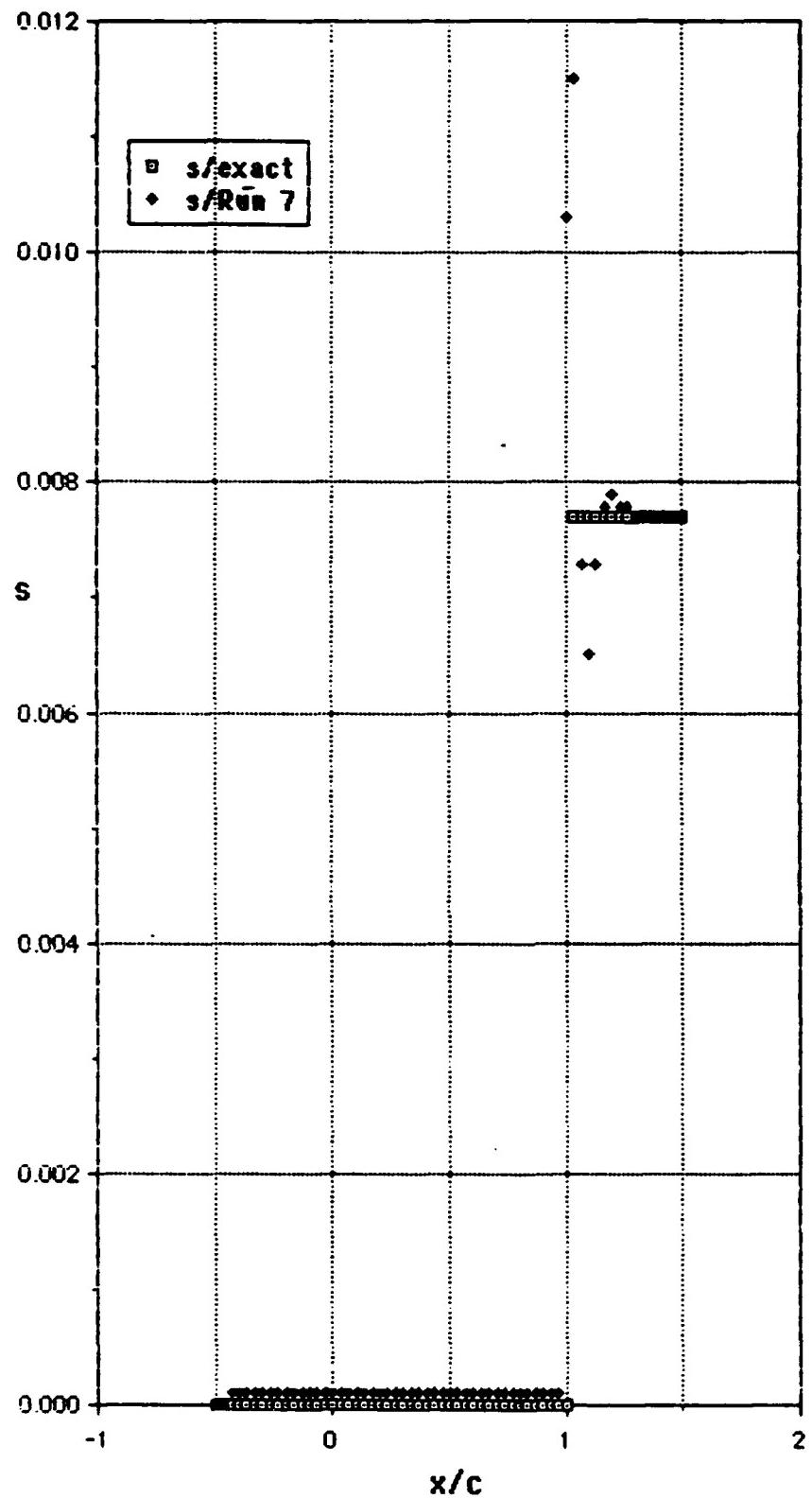


Fig. 3.5.2-1b.

Entropy distribution for the second quasi one dimensional sample case. Steger/Warming splitting, 61 grid points. Second order spatial accuracy throughout the flow field. Boundary conditions overspecified at inlet and outlet.

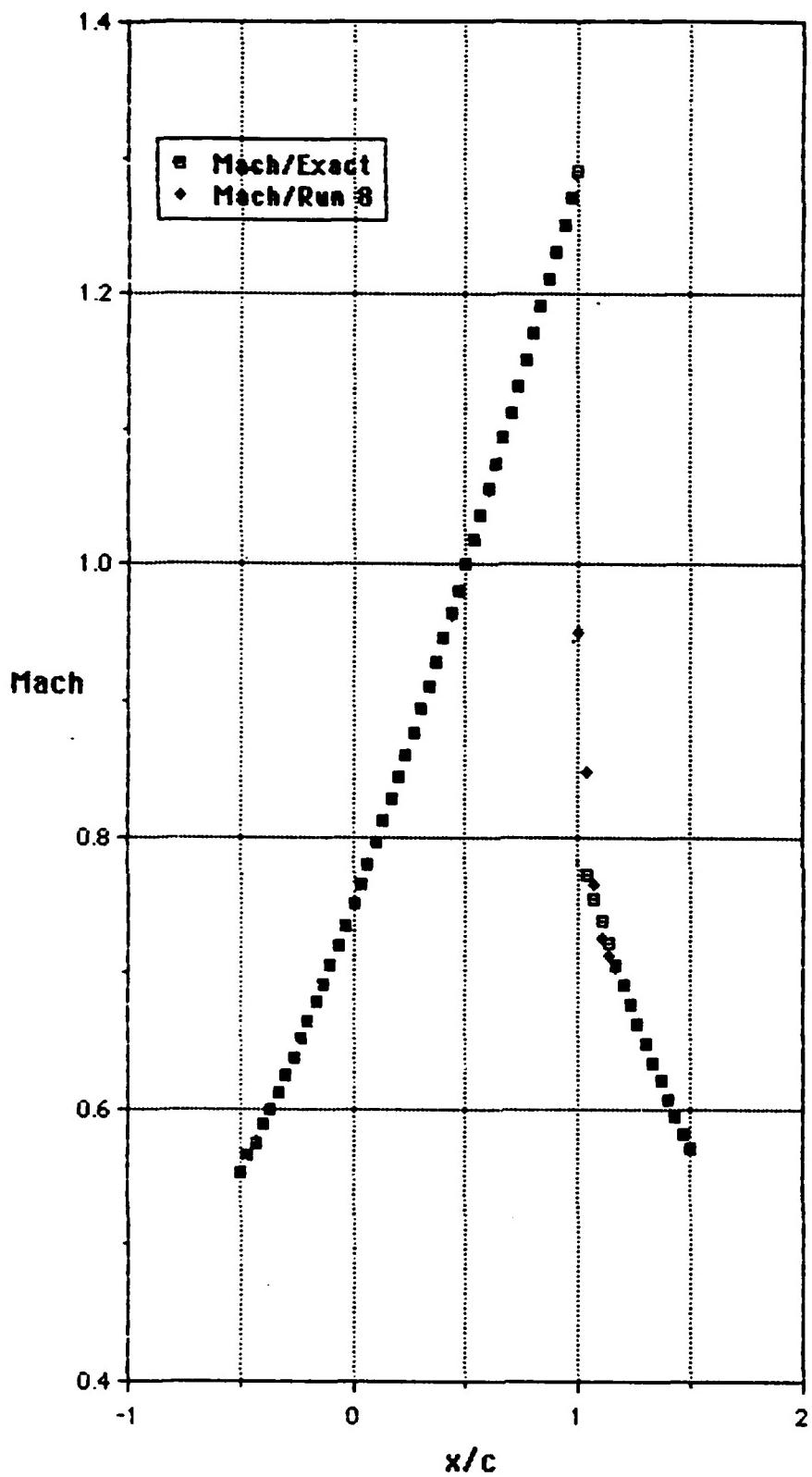


Fig. 3.5.2-2a.

Mach number distribution for the second quasi one dimensional sample case. Steger/Warming splitting, 61 grid points. Second order spatial accuracy, flux limiter to first order spatial accuracy in first point downstream of shock. Boundary conditions overspecified at inlet and outlet.

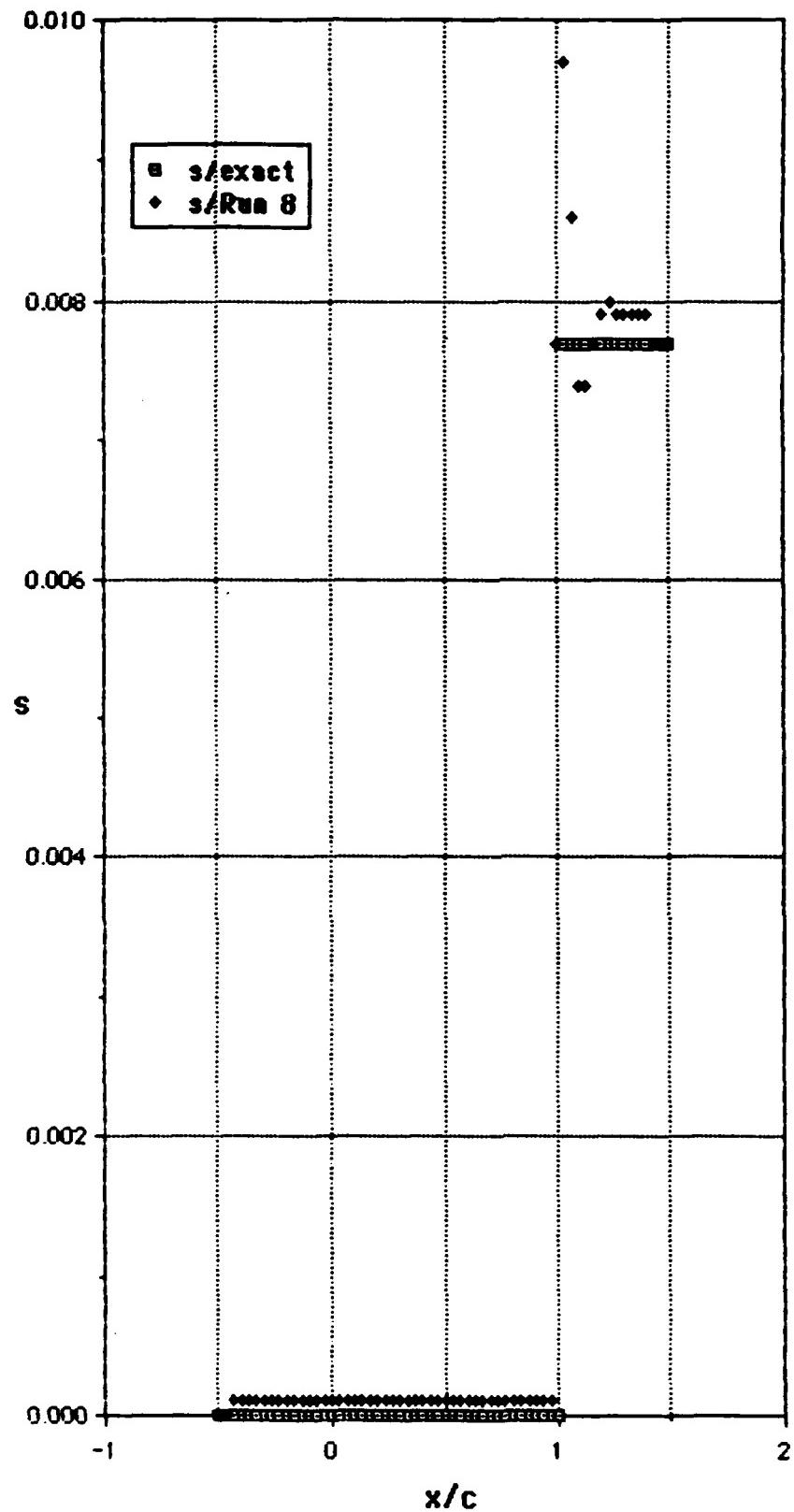


Fig. 3.5.2-2b.

Entropy distribution for the second quasi one dimensional sample case. Steger/Warming splitting, 61 grid points. Second order spatial accuracy, flux limiter to first order spatial accuracy in first point downstream of shock. Boundary conditions overspecified at inlet and outlet.

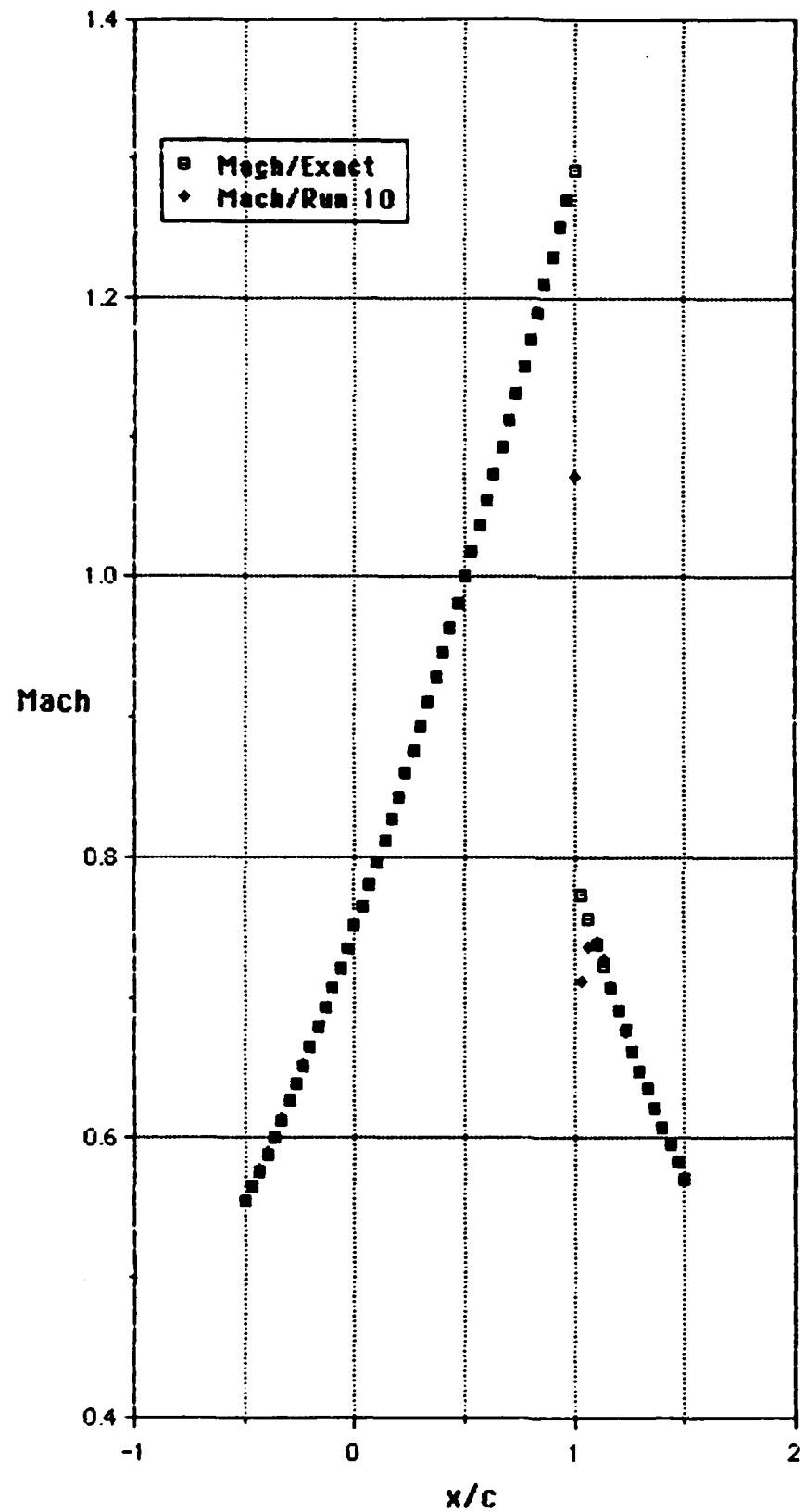


Fig. 3.5.2-3a.

Mach number distribution for the second quasi one dimensional sample case. Steger/Warming splitting, 61 grid points. Second order spatial accuracy, averaging of flux vector in point (shock+1/2). Boundary conditions overspecified at inlet and outlet.

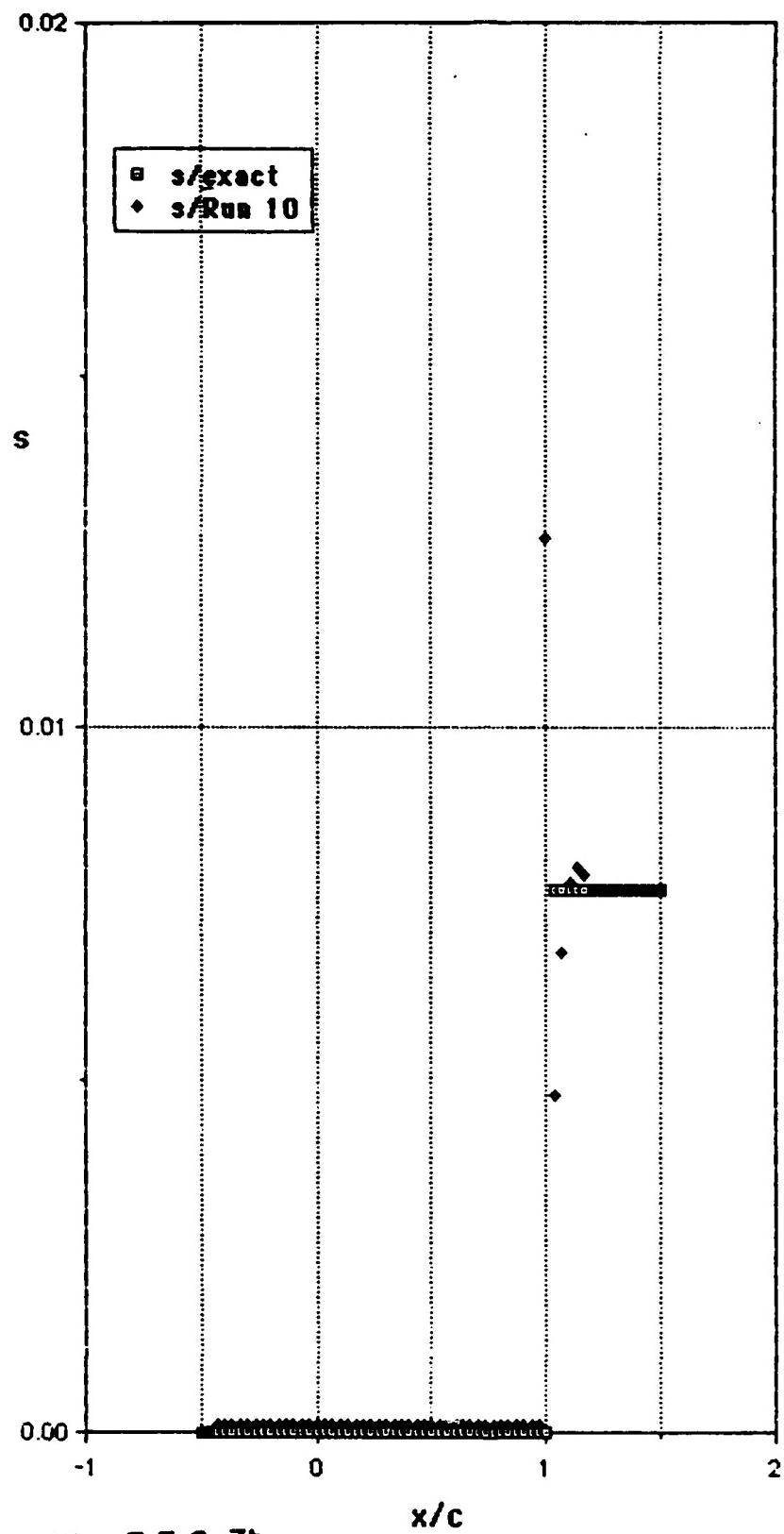


Fig. 3.5.2-3b.

Entropy distribution for the second quasi one dimensional sample case. Steger/Warming splitting, 61 grid points. Second order spatial accuracy, averaging of flux vector in point (shock+1/2). Boundary conditions overspecified at inlet and outlet.

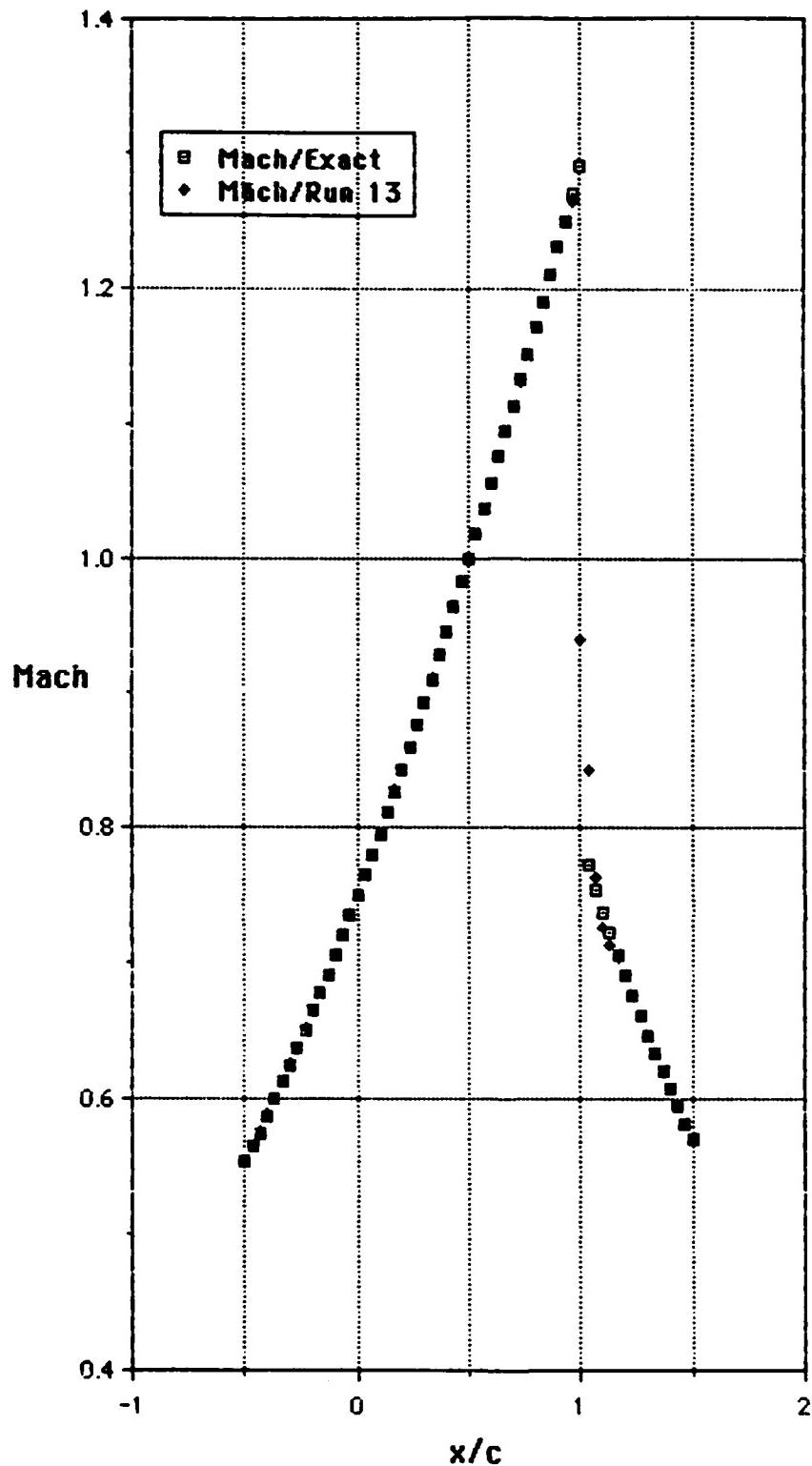


Fig. 3.5.2-4a.

Mach number distribution for the second quasi one dimensional sample case. Steger/Warming splitting, 61 grid points. Second order spatial accuracy, first order in first point downstream of shock. Boundary condition overspecified at inlet, constant pressure at outlet.

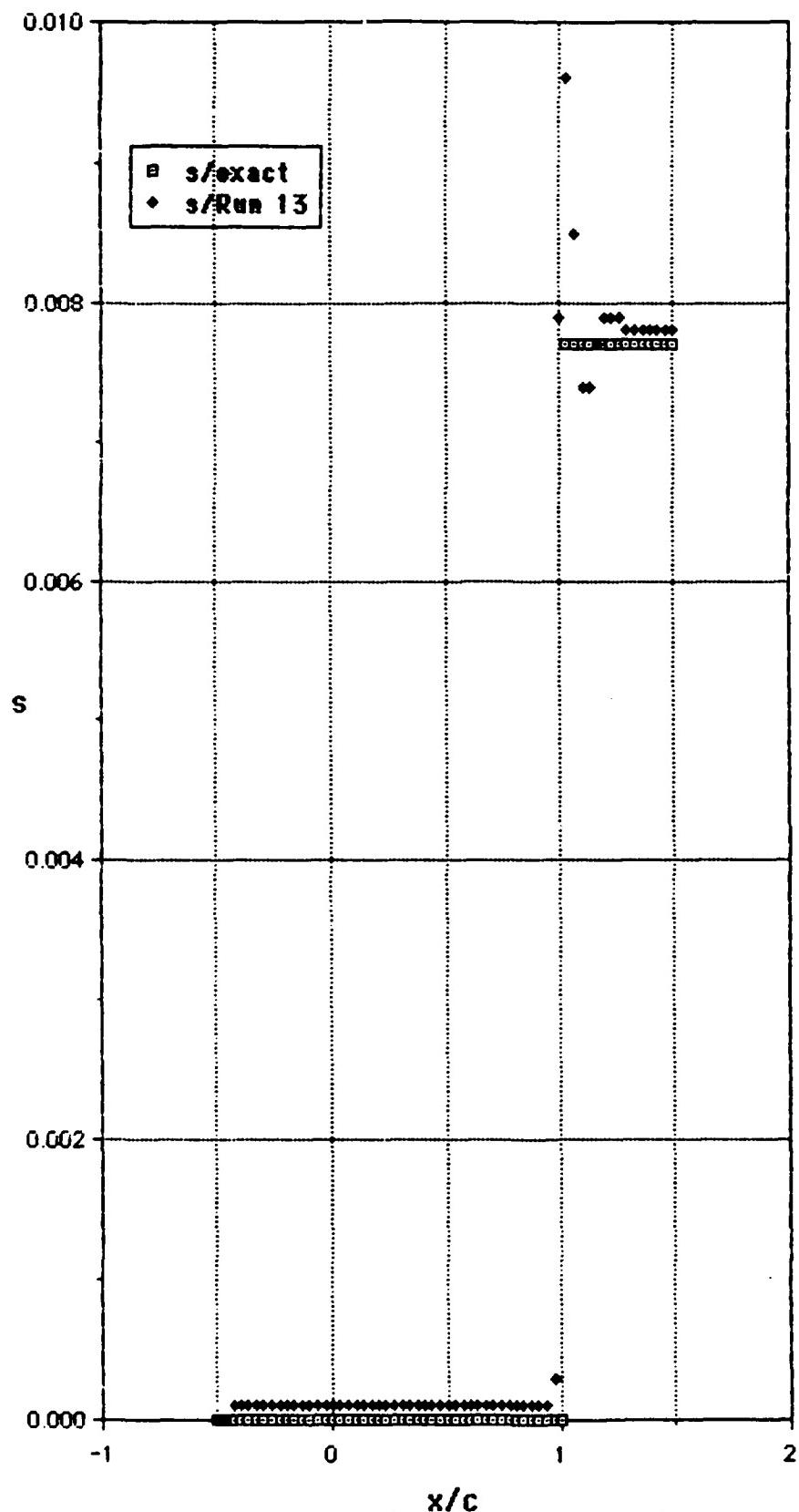


Fig. 3.5.2-4b.

Entropy distribution for the second quasi one dimensional sample case.
 Steger/Warming splitting, 61 grid points. Second order spatial accuracy,
 first order in first point downstream of shock. Boundary condition
 overspecified at inlet, constant pressure at outlet.

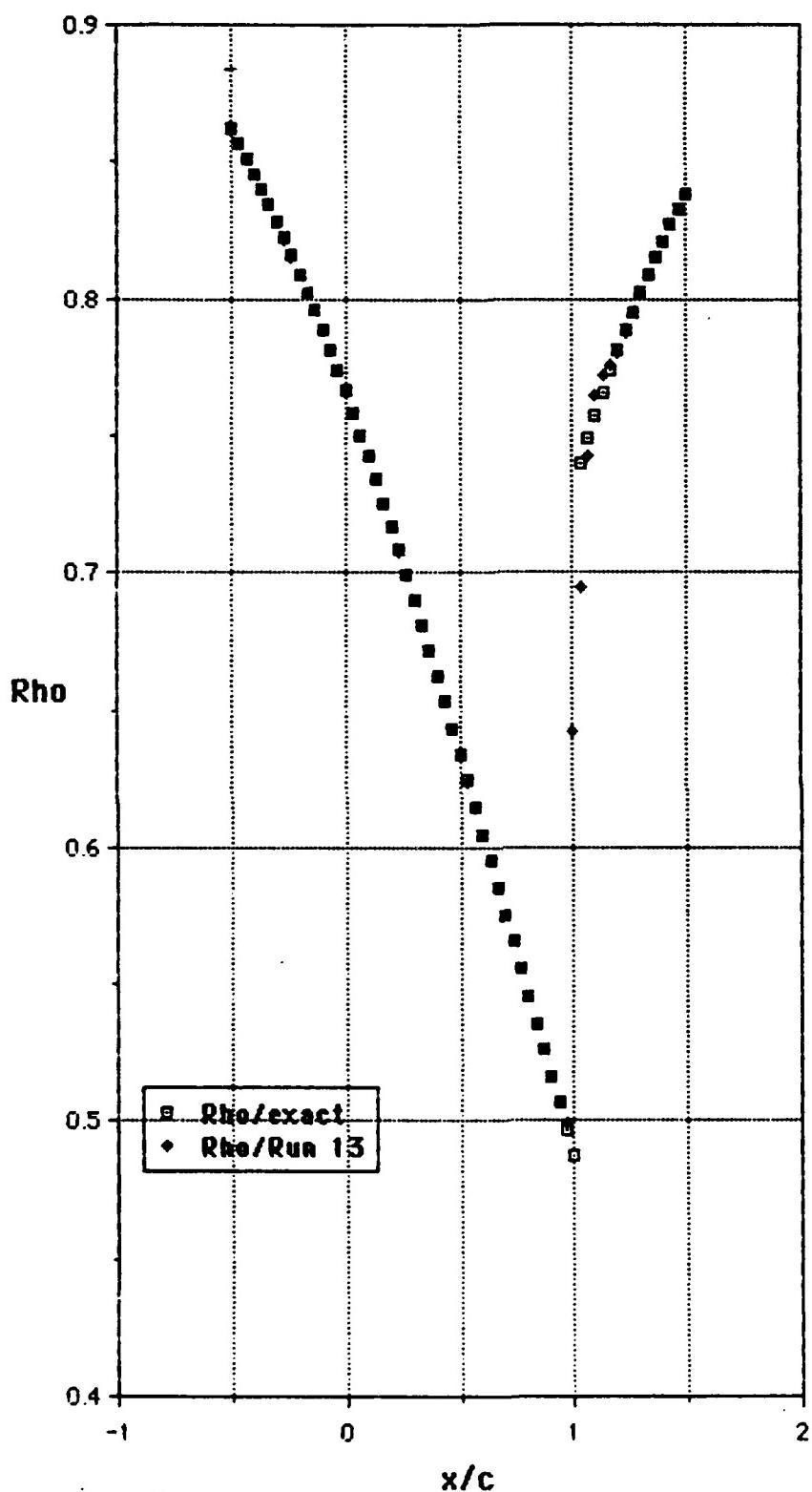


Fig. 3.5.2-4c.

Density distribution for the second quasi one dimensional sample case. Steger/Warming splitting, 61 grid points. Second order spatial accuracy, first order in first point downstream of shock. Boundary condition overspecified at inlet, constant pressure at outlet.

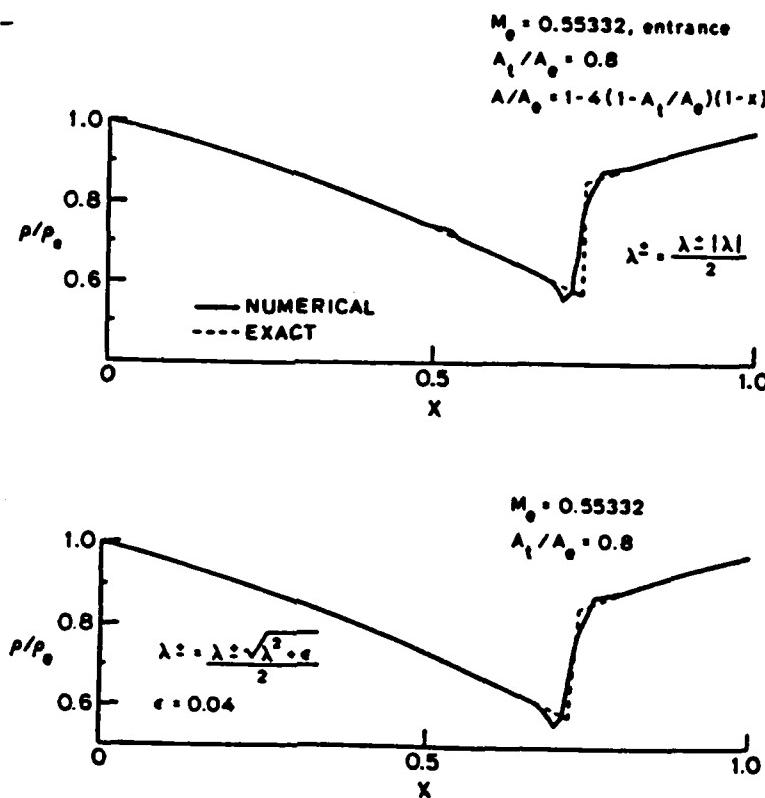
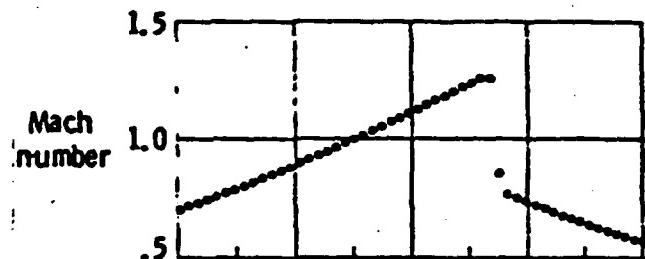
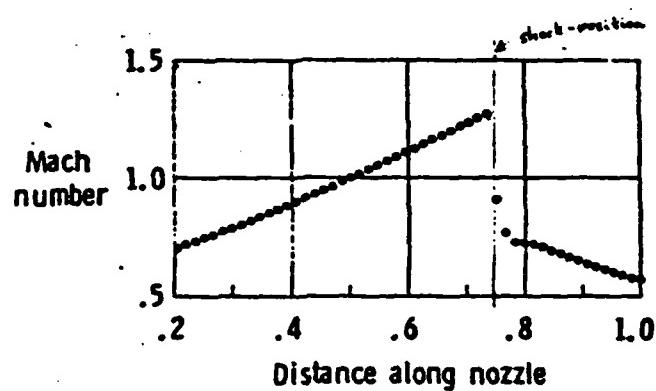


Fig. 10. Computational comparison of λ^+ formulations.

Fig. 3.5.2-5 (=Fig. 10 in ref. /14/).
 Illustration of "glitch" at sonic rarefaction for quasi one dimensional flow.



(a) Van Leer splitting



(b) Steger-Warming splitting ($\epsilon = 0$)

Figure 5. - Mach number distribution along transonic nozzle using MUSCL-type differencing.

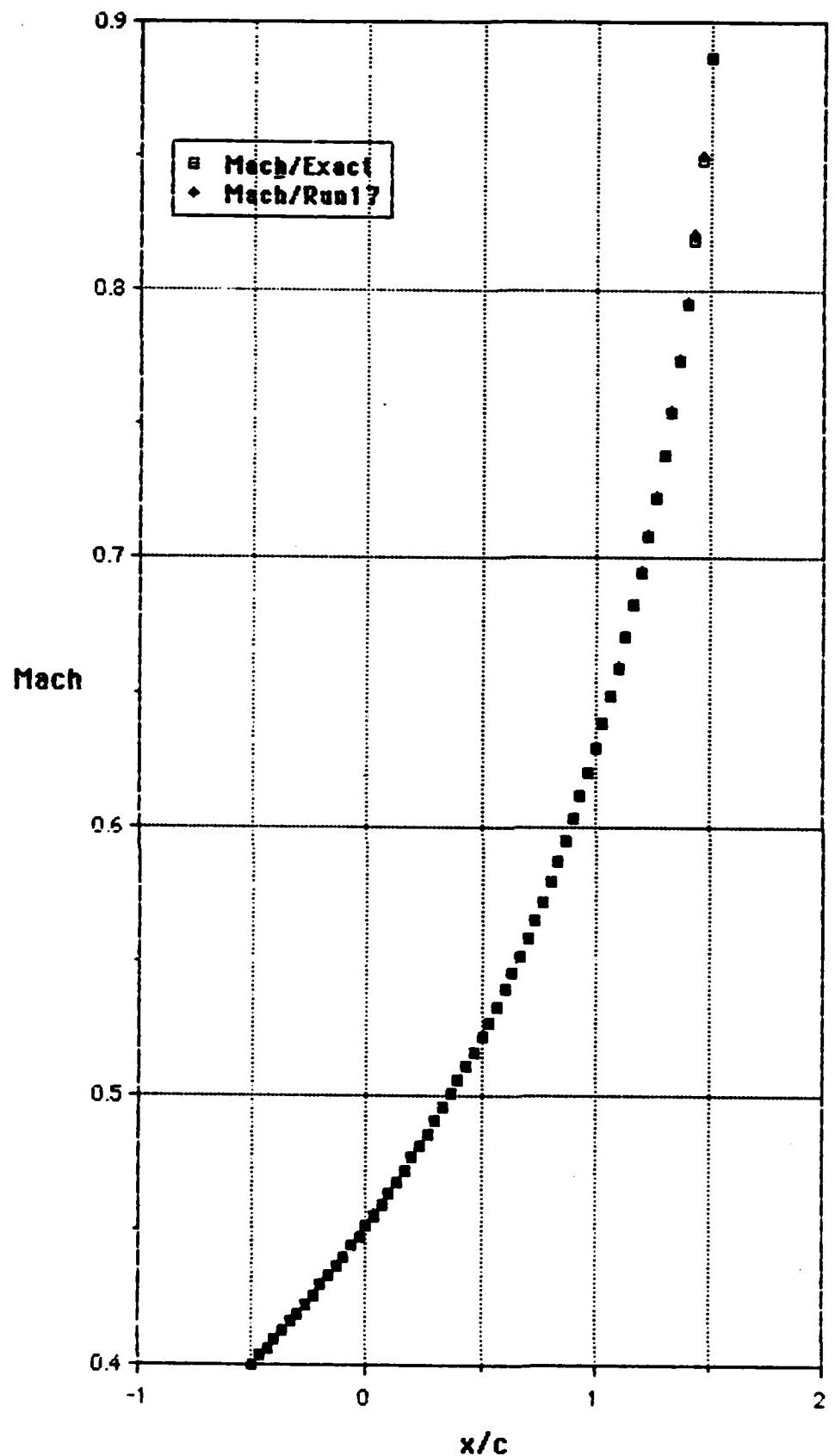
Fig. 3.5.2-6 (=Fig. 5 in ref. /11/).

Mach number distribution from ref. /11/.

Please note the different definitions of nozzle length.

Ref. /11/: $0 \leq x \leq 1$; $x_s = 0.75$

Present study: $-0.5 \leq x \leq 1.5$ $x_s = 1.00$



Run 17
61 grid points

Fig. 3.5.3-1a.

Mach number distribution for the third quasi one dimensional sample case.
Steger/Warming splitting, 61 grid points. Second order spatial accuracy,
first order in first point downstream of shock.

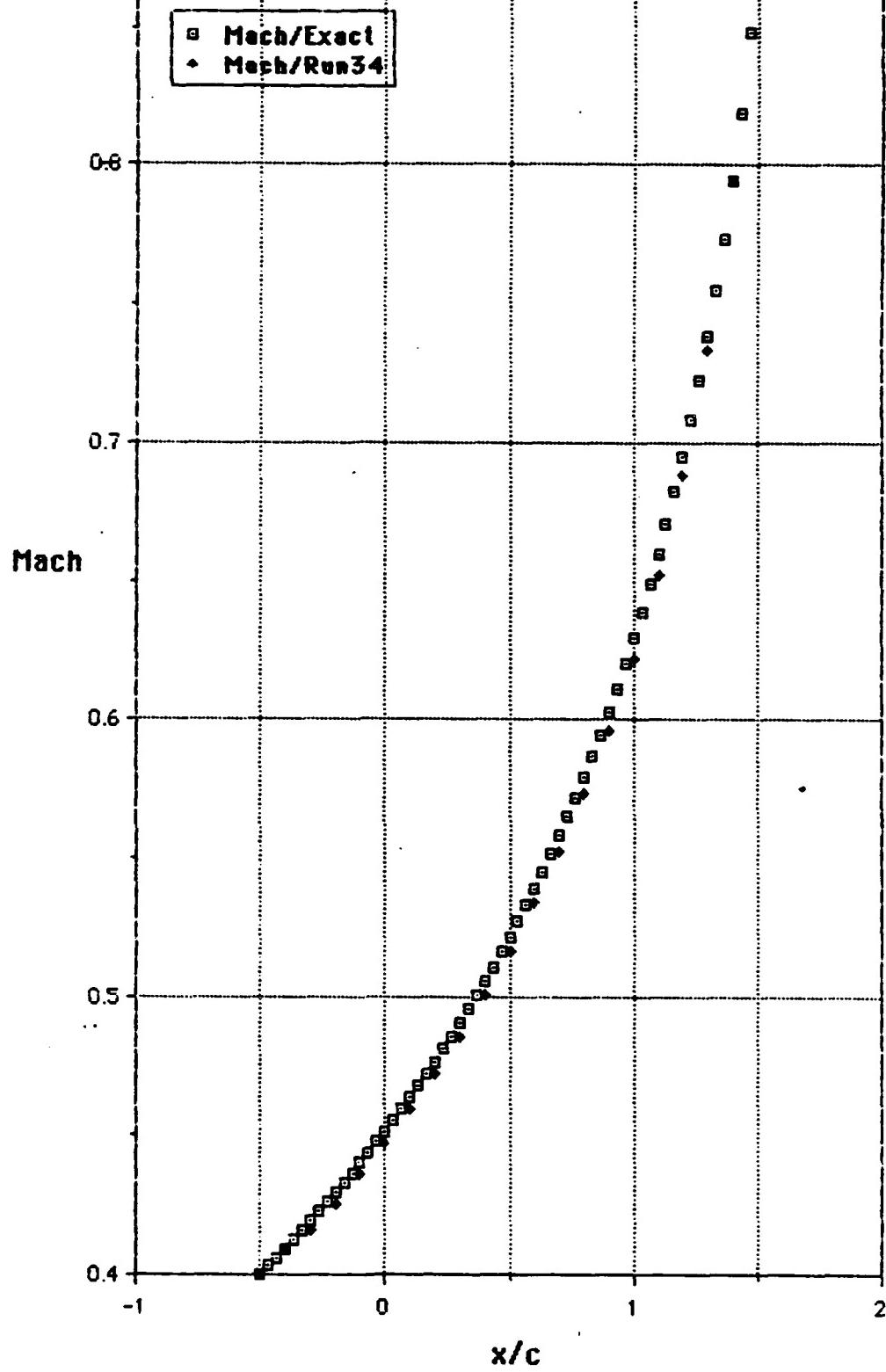


Fig. 3.5.3-1b.

Mach number distribution for the third quasi one dimensional sample case.
Steger/Warming splitting, 21 grid points. Second order spatial accuracy,
first order in first point downstream of shock.

$$A(x) = 0.1 \{ 5 - x^2 \}$$

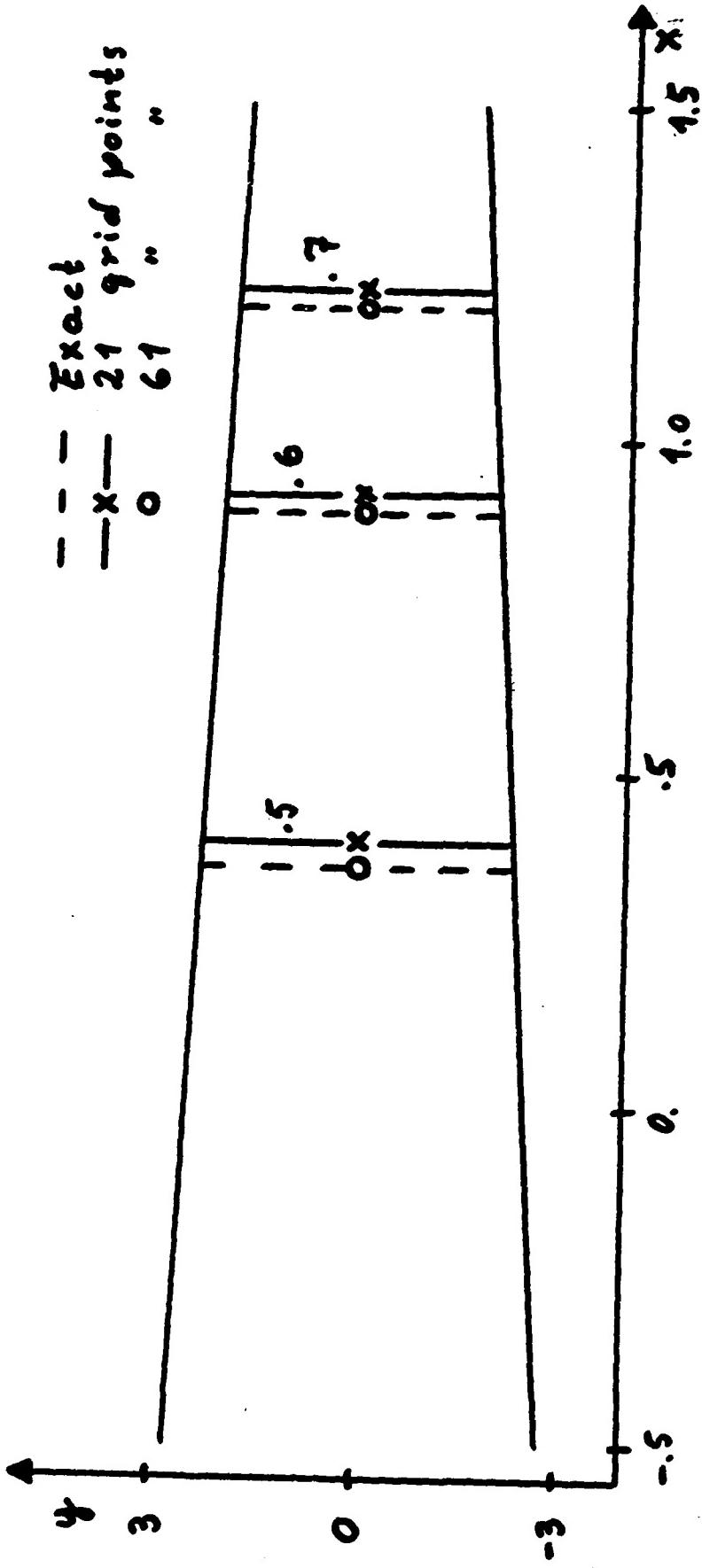
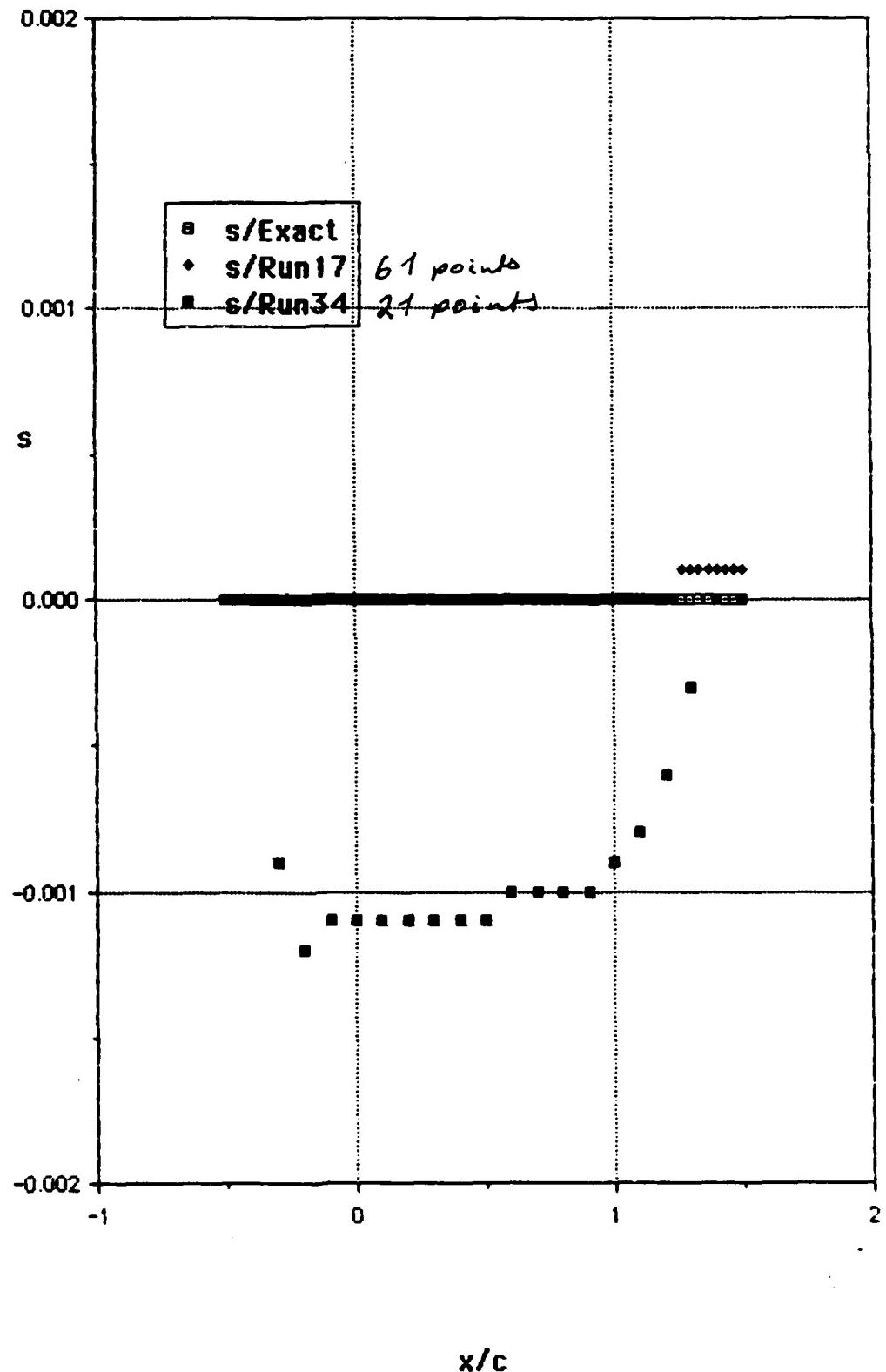


Fig. 3.5.3-2.
Iso Mach lines for the third quasi one dimensional test case.
Influence of the number of grid points on the result.

Fig. 3.5.3-3.

Entropy distribution for the third quasi one dimensional sample case.
Steger/Warming splitting, 21 and 61 grid points. Second order spatial
accuracy, first order in first point downstream of shock.



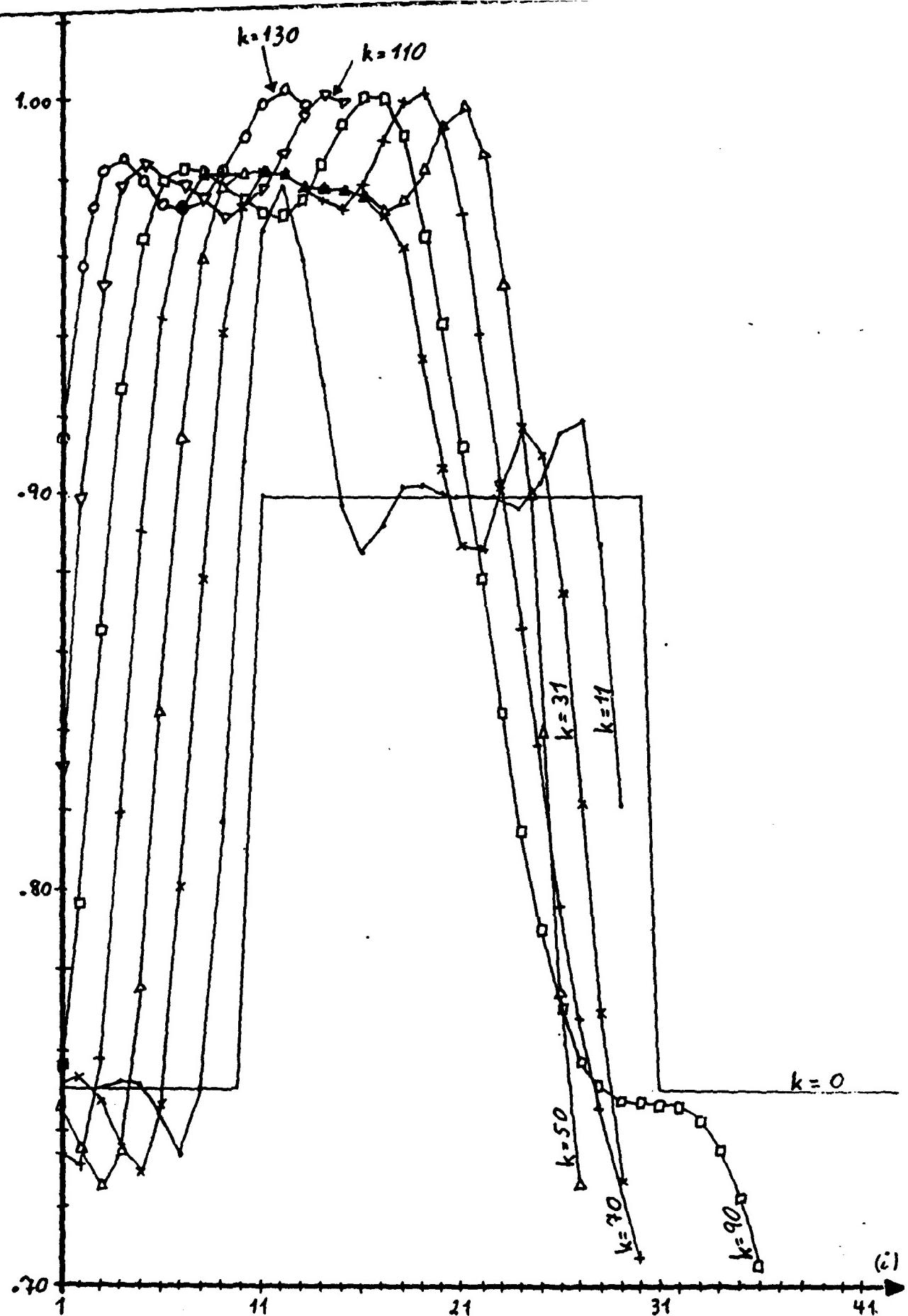


Fig. 3.5.4-1 .

Pressure along the nozzle at different time steps. Fourth quasi one dimensional test case, "non-reflecting" inlet boundary condition according to method 1 (section 3.3.1.b).

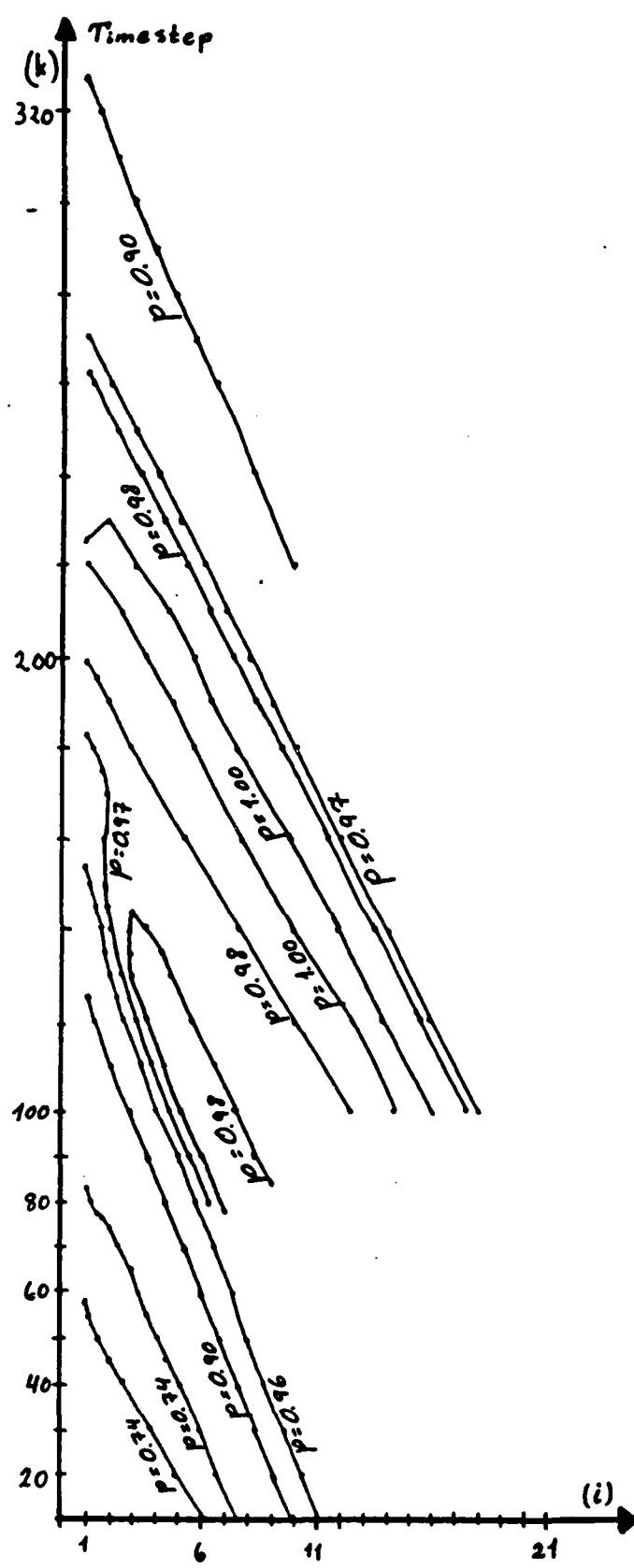


Fig. 3.5.4-2a.

Isobars in the (x, t) plane for the fourth quasi one dimensional test case. Initial pressure distribution according to Fig. 3.5.4-1. "Non-reflective" inlet boundary condition according to method 1 (section 3.3.1.b).

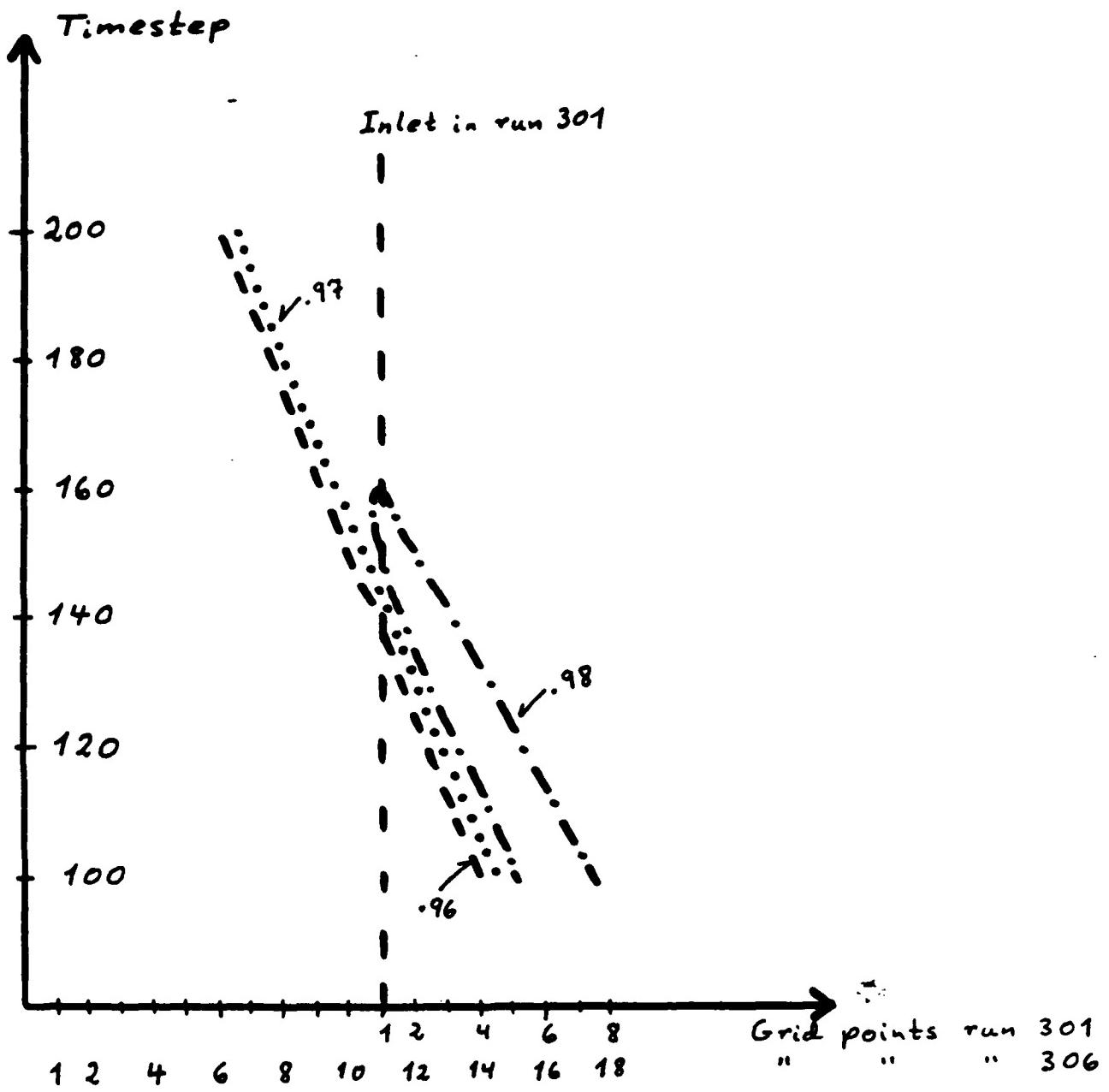


Fig. 3.5.4-2b.

Isobars in the (x, t) plane for the fourth quasi one dimensional test case. Initial pressure distribution according to Fig. 3.5.4-1. "Non-reflective" inlet boundary condition according to method 1 (section 3.3.1.b). Same calculation as in Fig. 3.5.4-2b but computational inlet moved 10 grid points upstream.

4. Two Dimensional Steady State Inviscid Flow.

The rotational inviscid, unsteady, two dimensional flow (without mass forces, heat transfer and exchange of energy), considering a perfect gas, can be described in differential, conservative, form by the continuity, momentum and energy equations (see for example /3/):

$$\text{Continuity: } \rho_t + (\rho u)_x + (\rho v)_y = 0 \quad (4.0-1)$$

$$\text{Momentum in } x: (\rho u)_t + (\rho u^2 + p)_x + (\rho uv)_y = 0 \quad (4.0-2)$$

$$\text{in } y: (\rho v)_t + (\rho uv)_x + (\rho v^2 + p)_y = 0 \quad (4.0-3)$$

$$\text{Energy: } (\rho [e + q^2/2])_t + (\rho u [e + p/\rho + q^2/2])_x + (\rho v [e + p/\rho + q^2/2])_y = 0 \quad (4.0-4)$$

as well as the equation of state:

$$\text{Perfect gas: } p/\rho = RT \quad (4.0-5)$$

The energy equation can also be written in the form:

$$\text{Energy: } (\rho e_c)_t + (\rho h_c u)_x + (\rho h_c v)_y = 0 \quad (4.0-6)$$

where e_c and h_c are the total energy and enthalpy per unit mass respectively, with

$$e_c = p/\{\rho[\gamma-1]\} + q^2/2$$

$$h_c = e_c + p/\rho = \gamma p/\{\rho[\gamma-1]\} + q^2/2$$

These equations are identical in dimensionless form if the following reference values are used (see Appendix A1 for validation):

- ρ_r, x_r, T_r
- $\rho_r = \rho_r/(RT_r)$
- $x_r = y_r = c (= \text{chord})$
- $q_r = (RT_r)^{0.5}$ (Note that $q_r = \text{speed of sound}/\sqrt{\gamma}$)
- $t_r = c/q_r$
- $e_r = h_r = q_r^2$
- $s = (s - s_r)/c_v$

From here on, all values are thus expressed in dimensionless form unless stated otherwise.

With these reference values, the relationship between the flow variables ρ , q , p , e_c and a (=speed of sound), M (=Mach number), T (=temperature) is given in Appendix A3.

The equations (4.0-1 to 4.0-4) above can be expressed in vectorform as

$$\mathbf{W}_t + \mathbf{F}_x + \mathbf{G}_y = 0 \quad (4.0-7)$$

with

$$\mathbf{W} = \begin{bmatrix} \rho \\ \rho u \\ \rho v \\ \rho e_c \end{bmatrix}; \quad \mathbf{F} = \begin{bmatrix} \rho u \\ \rho u^2 + p \\ \rho uv \\ \rho u(e_c + p/\rho) \end{bmatrix}; \quad \mathbf{G} = \begin{bmatrix} \rho v \\ \rho uv \\ \rho v^2 + p \\ \rho v(e_c + p/\rho) \end{bmatrix} \quad (4.0-8)$$

4.1. Governing Equations in Generalized Coordinates.

The equation system (4.0-8) can be mapped from the physical plane of reference (x,y,t) into a computational plane of reference (ξ,η,τ) with a general transformation:

$$\begin{aligned}\xi &= \xi(x, y, t) \\ \eta &= \eta(x, y, t) \\ \tau &= t\end{aligned}\quad (4.1-1)$$

Viviand /4/ has shown that eq. (4.0-8) can stay in strong conservative form with a transformation of the above type. The eq. (4.0-8) is then transformed into (see Appendix A2):

$$W'_{\tau} + F'_{\xi} + G'_{\eta} = 0 \quad (4.1-2)$$

with

$$\begin{aligned}W' &= D^{-1}W \\ F' &= D^{-1}\{\xi_t W + \xi_x F + \xi_y G\} \\ G' &= D^{-1}\{\eta_t W + \eta_x F + \eta_y G\} \\ D &= \xi_x \eta_y - \xi_y \eta_x = 1/\{x_\xi y_\eta - x_\eta y_\xi\}\end{aligned}\quad (4.1-3)$$

where D is the Jacobian determinant of the transformation (4.1-1) and the metric terms are related to the derivatives of x , y and t by (see for ex. /31, eq. (4)/):

$$\left\{ \begin{array}{lcl} \xi_x & = & y_\eta D \\ \xi_y & = & -x_\eta D \\ \xi_t & = & -x_\tau \xi_x - y_\tau \xi_y \end{array} \right. \quad (4.1-4a)$$

$$\left\{ \begin{array}{lcl} \eta_x & = & -y_\xi D \\ \eta_y & = & x_\xi D \\ \eta_t & = & -x_\tau \eta_x - y_\tau \eta_y \end{array} \right. \quad (4.1-4b)$$

The Jacobian determinant, in the center of an element, corresponds physically to the inverse of the cell area (Fig. 4.1-1).

In component form, eq. (4.1-3) can be written as:

$$\mathbf{W}' = D^{-1} \begin{bmatrix} p \\ \rho u \\ \rho v \\ \rho e_c \end{bmatrix} \quad (4.1-5a)$$

$$\mathbf{F}' = D^{-1} \begin{bmatrix} \xi_t p + \xi_x \rho u + \xi_y \rho v \\ \xi_t \rho u + \xi_x \{\rho u^2 + p\} + \xi_y \rho u v \\ \xi_t \rho v + \xi_x \rho u v + \xi_y \{\rho v^2 + p\} \\ \xi_t \rho e_c + \xi_x \rho u \{e_c + p/\rho\} + \xi_y \rho v \{e_c + p/\rho\} \end{bmatrix} \quad (4.1-5b)$$

$$\mathbf{G}' = D^{-1} \begin{bmatrix} \eta_t p + \eta_x \rho u + \eta_y \rho v \\ \eta_t \rho u + \eta_x \{\rho u^2 + p\} + \eta_y \rho u v \\ \eta_t \rho v + \eta_x \rho u v + \eta_y \{\rho v^2 + p\} \\ \eta_t \rho e_c + \eta_x \rho u \{e_c + p/\rho\} + \eta_y \rho v \{e_c + p/\rho\} \end{bmatrix} \quad (4.1-5c)$$

In the first part of the present study we treat only non-moving grids, wherefore the terms ξ_t and η_t are zero. The expressions (4.1-5) are then reduced to (see for example ref. /11/, eq. (35)):

$$\mathbf{W}' = D^{-1} \begin{bmatrix} p \\ \rho u \\ \rho v \\ \rho e_c \end{bmatrix} \quad (4.1-6a)$$

$$\mathbf{F}' = D^{-1} \begin{bmatrix} \xi_x \rho u + \xi_y \rho v \\ \xi_x \{\rho u^2 + p\} + \xi_y \rho u v \\ \xi_x \rho u v + \xi_y \{\rho v^2 + p\} \end{bmatrix} \quad (4.1-6b')$$

$$\left[\xi_x \rho u \{e_c + p/\rho\} + \xi_y \rho v \{e_c + p/\rho\} \right]$$

or

$$F' = \left[\begin{array}{l} y_\eta \rho u - x_\eta \rho v \\ y_\eta \{\rho u^2 + p\} - x_\eta \rho uv \\ y_\eta \rho uv - x_\eta \{\rho v^2 + p\} \\ y_\eta \rho u \{e_c + p/\rho\} - x_\eta \rho v \{e_c + p/\rho\} \end{array} \right] \quad (4.1-6b'')$$

or

$$F' = \left[\begin{array}{l} f'_1 \\ f'_1 u + y_\eta p \\ f'_1 v - x_\eta p \\ f'_1 \{e_c + p/\rho\} \end{array} \right] \quad (4.1-6b''')$$

as well as

$$G' = D^{-1} \left[\begin{array}{l} \eta_x \rho u + \eta_y \rho v \\ \eta_x \{\rho u^2 + p\} + \eta_y \rho uv \\ \eta_x \rho uv + \eta_y \{\rho v^2 + p\} \\ \eta_x \rho u \{e_c + p/\rho\} + \eta_y \rho v \{e_c + p/\rho\} \end{array} \right] \quad (4.1-6c')$$

$$G' = \left[\begin{array}{l} -y_\xi \rho u + x_\xi \rho v \\ -y_\xi \{\rho u^2 + p\} + x_\xi \rho uv \\ -y_\xi \rho uv + x_\xi \{\rho v^2 + p\} \\ -y_\xi \rho u \{e_c + p/\rho\} + x_\xi \rho v \{e_c + p/\rho\} \end{array} \right] \quad (4.1-6c'')$$

$$G' = \left[\begin{array}{l} g'_1 \\ g'_1 u - y_\xi p \\ g'_1 v + x_\xi p \\ g'_1 \{e_c + p/\rho\} \end{array} \right] \quad (4.1-6c''')$$

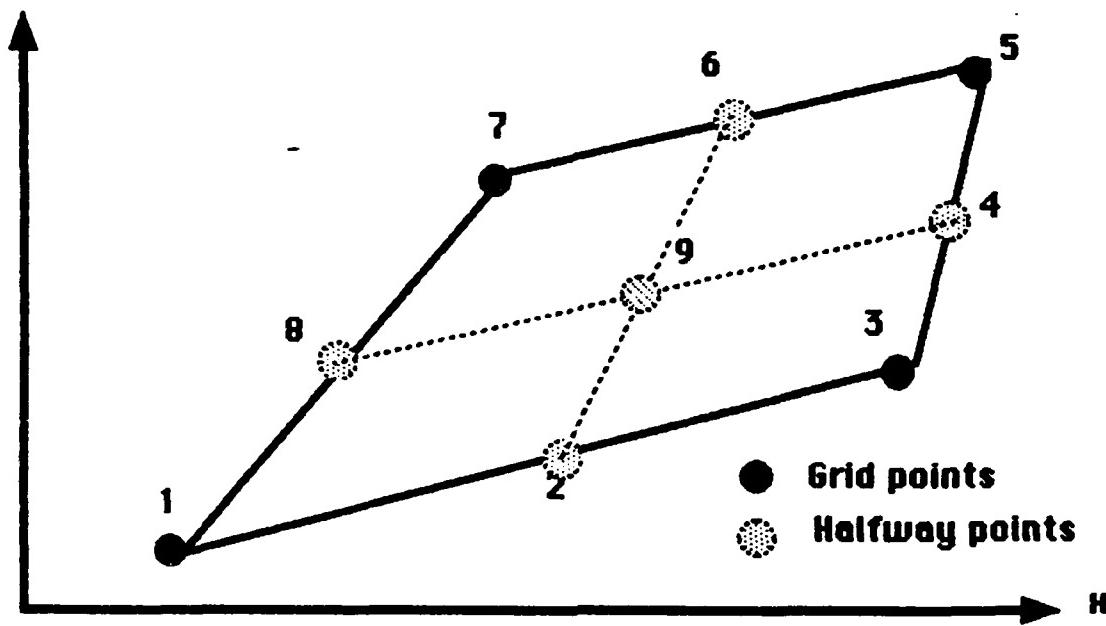


Fig. 4.1-1a: Computational cell with grid points and half grid points.

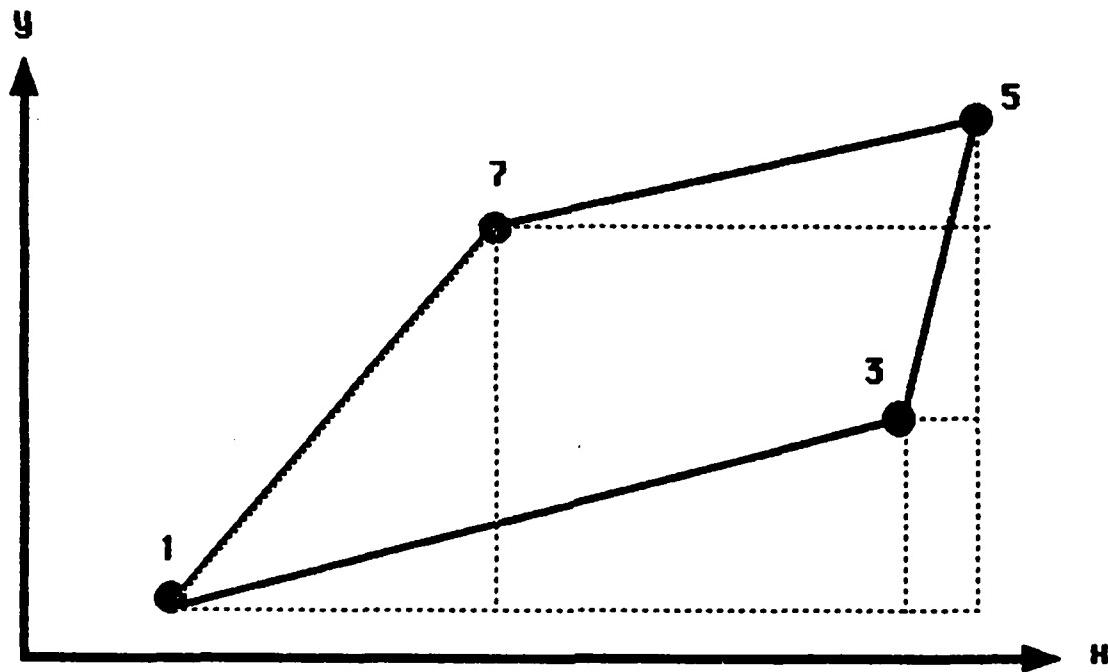


Fig. 4.1-1b: Construction of cell area

$$\begin{aligned}
 D^{-1} &= \{x_\xi y_\eta - x_\eta y_\xi\} \\
 &= \{(x_4-x_8)(y_6-y_2) - (x_6-x_2)(y_4-y_8)\} / \{(\xi_4-\xi_8)(\eta_6-\eta_2)\} \\
 &= -0.25 \cdot \{[(x_5+x_3-x_7-x_1)(y_5+y_7-y_3-y_1) - (x_5+x_7-x_3-x_1)(y_5+y_3-y_7-y_1)] \\
 &\quad / \{(\xi_4-\xi_8)(\eta_6-\eta_2)\}\} \\
 &= 0.25 \cdot \{x_5y_5 + x_5y_7 - x_5y_3 - x_5y_1 + x_3y_5 + x_3y_7 - x_3y_3 - x_3y_1 - x_7y_5 - x_7y_7 \\
 &\quad + x_7y_3 + x_7y_1 - x_1y_5 - x_1y_7 + x_1y_3 + x_1y_1 \\
 &\quad - x_5y_5 - x_5y_3 + x_5y_7 + x_5y_1 - x_7y_5 - x_7y_3 + x_7y_7 + x_7y_1 + x_3y_5 + x_3y_3 \\
 &\quad - x_3y_7 - x_3y_1 + x_1y_5 + x_1y_3 - x_1y_7 - x_1y_1\} / \{(\xi_4-\xi_8)(\eta_6-\eta_2)\} \\
 &= 0.5 \cdot \{x_5[y_7-y_3] + x_3[y_5-y_1] + x_7[y_1-y_5] + x_1[y_3-y_7]\} / \{(\xi_4-\xi_8)(\eta_6-\eta_2)\} \\
 &= 0.5 \cdot \{[x_5-x_1][y_7-y_3] + [x_3-x_7][y_5-y_1]\} / \{(\xi_4-\xi_8)(\eta_6-\eta_2)\} \\
 &= 0.5 \cdot \{[x_5-x_1][y_7-y_3] + [x_3-x_7][y_5-y_1]\} \quad \text{if } \Delta\xi = \Delta\eta = 1
 \end{aligned}$$

$$\begin{aligned}
 \text{Area} &= [y_7-y_1][x_7-x_1]/2 + [y_5-y_7][x_5-x_7]/2 + [y_7-y_1][x_5-x_7] \\
 &\quad - [x_3-x_1][y_3-y_1]/2 - [x_5-x_3][y_5-y_3]/2 - [x_5-x_3][y_3-y_1] \\
 &= 0.5 \cdot \{y_7x_7 - y_7x_1 - y_1x_7 + y_1x_1 + y_5x_5 - y_5x_7 - y_7x_5 + y_7x_7 \\
 &\quad + 2y_7x_5 - 2y_7x_7 - 2y_1x_5 + 2y_1x_7 - x_3y_3 + x_3y_1 + x_1y_3 - x_1y_1 \\
 &\quad - 2x_5y_3 + 2x_5y_1 + 2x_3y_3 - 2x_3y_1 - x_5y_5 + x_5y_3 + x_3y_5 - x_3y_3\} \\
 &= 0.5 \cdot \{y_7x_5 - y_7x_1 + y_1x_7 - y_1x_3 + y_5x_3 - y_5x_7 + y_3x_1 - y_3x_5\} \\
 &= 0.5 \cdot \{y_7[x_5-x_1] - y_3[x_5-x_1] + y_5[x_3-x_7] - y_1[x_3-x_7]\} \\
 &= 0.5 \cdot \{[x_3-x_7][y_5-y_1] + [x_5-x_1][y_7-y_3]\}
 \end{aligned}$$

Fig. 4.1-1: Geometrical interpretation of the Jacobian determinant.

4.2 Grid Construction.

A grid for numerical calculations can be constructed in several different ways, for example in a finite difference or finite volume manner. The authors previous work has consisted of methods when the grid points are designed to coincide with the boundaries of the computational domain. In the present study, some problems appeared in the implementation of such a grid in connection with the imposed boundary conditions in the flux vector splitting formulation. To this end the numerical grid points were instead constructed as in a finite volume approach, i.e. the grid points are in the cell center and the cell interface coincide with the computational boundaries. As both approaches were used, both will briefly be explained.

4.2.1 Grid Lines Situated at the Walls.

The grid chosen first was one where the grid lines coincide with the boundaries of the computational domain, in agreement with the author's previous work /24/ (see Fig. 4.2.1-1). In this previous work, the unknown quantities (outside the computational domain) have been parabolically extrapolated (according to section 3.3.1.a). This gave good results in /24/, where numerical method by MacCormack /48/ was employed together with the postcorrection technique after Moretti /6/. However, with this grid construction, the present implementation of the flux vector splitting method showed large convergence problems for H-grids.

The reason therefore is believed to be found at the boundaries.

In a grid as in Fig. 4.2.1-1 the implementation of the boundary conditions is not straightforward in the "MUSCL"-approach of the flux vector splitting. This is immediately seen from Fig. 4.2.1-1, where it is noted that, for computation of the flow variables in point j , the flow variables in point " $j-1/2$ " are needed (as $[G_j]_y = (G_{j+1/2} - G_{j-1/2})/\Delta y$). This does not pose any problem for the flux $G^-_{j-1/2}$ which is constructed with information from points " j " and " $j+1$ ", i.e. from known values. However, $G^+_{j-1/2}$ should be constructed with information from points " $j-1$ " and " $j-2$ ", according to eq. (3.2-4). This implies an extrapolation of two points outside the boundary for all the flow variables.

4.2.2 Grid Lines Situated Half a Mesh Away from the Walls.

The second method to construct the grid is instead to put the computational points in the middle of a computational element (Fig. 4.2.2-1). In this case the computation of the flow variables on line "j" consists of, as before, $[G_j]_y = [G_{j+1/2} - G_{j-1/2}] / \Delta y$. However, "j-1/2" coincides now with the wall, wherefore the boundary condition of no mass flow through the wall gives

$$G_{j-1/2} = \begin{bmatrix} \rho v \\ \rho v u \\ \rho v^2 + p \\ \rho [e_c + p/\rho] \end{bmatrix} = \begin{bmatrix} 0 \\ 0 \\ p \\ 0 \end{bmatrix}$$

It is therefore not necessary to perform the flux vector splitting at the wall. It should however be noted here that this procedure introduces a different numerical dissipation at the wall than in all other points. The reason for this is obviously that the total flux in point "j-1/2" is without the numerical dissipation the flux vector splitting introduces in the general points. However, if the cells are small close to the blade surfaces, the numerical dissipation is small anyway, wherefore no problems are to be expected for a grid that clusters points close to the blade surface.

Thus, instead of extrapolating all flow variables to two points as in section 4.2.1, it is only necessary to determine the pressure 1/2 point away from the known value.

The value of the pressure in point "j" can be found by several methods, for example by extrapolation:

For the lower boundary

- 0th order extrapolation: $p_{j-1/2,i} = p_{j,i}$
- 1st " " : $p_{j-1/2,i} = 3p_{j,i}/2 - p_{j+1,i}/2$
- 2nd " " : $p_{j-1/2,i} = (5p_{j,i} + 18p_{j+1,i} + 21p_{j+2,i})/8$

For the upper boundary

- 0th order extrapolation: $p_{j+1/2,i} = p_{j,i}$
- 1st " " : $p_{j+1/2,i} = 3p_{j,i}/2 - p_{j-1,i}/2$
- 2nd " " : $p_{j+1/2,i} = (5p_{j,i} - 18p_{j-1,i} + 21p_{j-2,i})/8$

Better still, in the case of an orthogonal grid, is to solve the momentum equation normal to the wall and to obtain the pressure therefrom (see for example ref. /11/).

For the steady state sample cases in section 4.6, only the simple 0th order extrapolation was employed.

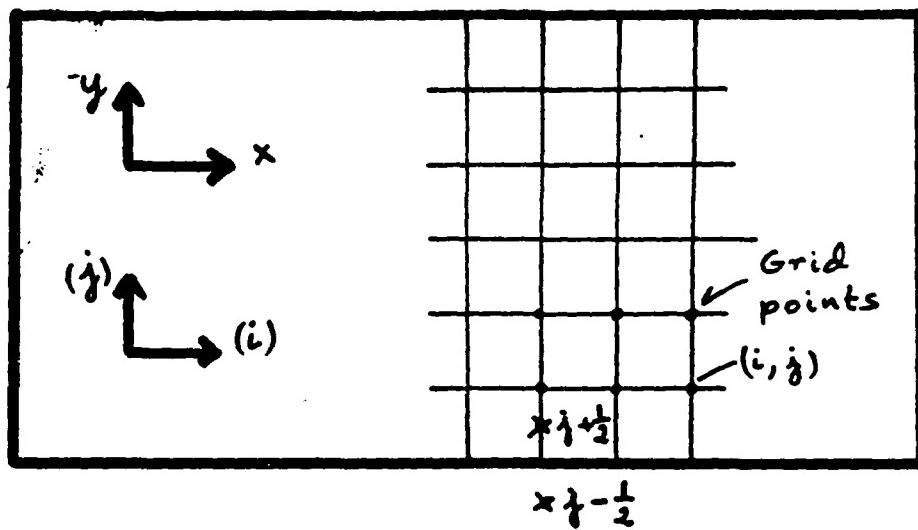


Fig. 4.2.1-1. Grid construction with mesh points located at the computational boundaries.

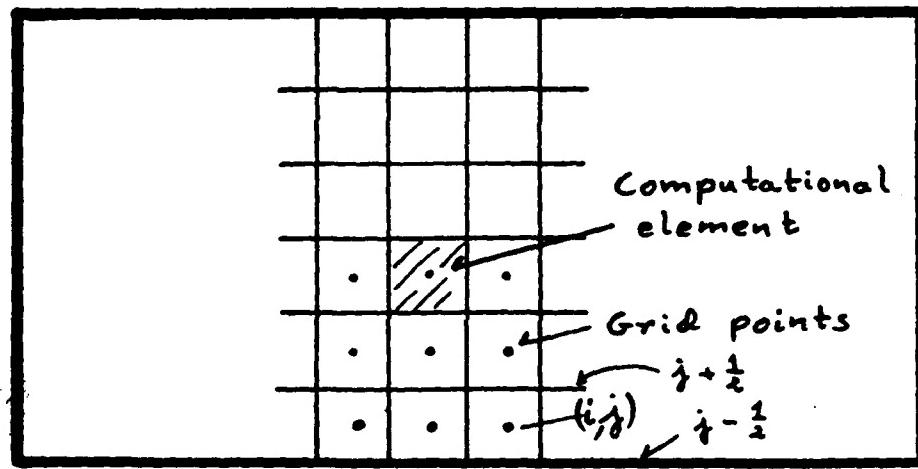


Fig. 4.2.2-1. Grid construction with cell interfaces located at the computational boundaries.

4.3. Flux Vector Splitting.

4.3.1 Cartesian Coordinates.

4.3.1.a. Steger/Warming Splitting.

As in one dimensional flow, the fluxes in the Steger/Warming approach are split according to the sign of the local eigenvalues of the flux vectors \mathbf{F} and \mathbf{G} .

The equation (4.0-8) has four eigenvalues, $\lambda_1^x, \lambda_2^x, \lambda_3^x$ and λ_4^x , of the flux vector \mathbf{F} in the x direction. Similarly, four eigenvalues of the the flux vector \mathbf{G} exist in the y direction ($\lambda_1^y, \lambda_2^y, \lambda_3^y$ and λ_4^y). The eigenvalues are normally expressed as:

$$\left\{ \begin{array}{l} \lambda_1^x = u \\ \lambda_2^x = u \\ \lambda_3^x = u+a \\ \lambda_4^x = u-a \end{array} \right. \quad (4.3.1.a-1a)$$

$$\left\{ \begin{array}{l} \lambda_1^y = v \\ \lambda_2^y = v \\ \lambda_3^y = v+a \\ \lambda_4^y = v-a \end{array} \right. \quad (4.3.1.a-1b)$$

These eigenvalues can be, depending on the magnitude of the velocities u and v ($u,v \leq 0, 0 < u,v \leq a, u,v > a$), separated into positive and negative parts as in one dimensional flow:

$$\lambda_n = \lambda_n^+ + \lambda_n^- \quad (4.3.1.a-2)$$

where, in the original study by Steger/Warming /13/, the λ_n^+, λ_n^- are defined as:

$$\begin{aligned} \lambda_n^+ &= (\lambda_n + |\lambda_n|)/2 \\ \lambda_n^- &= (\lambda_n - |\lambda_n|)/2 \end{aligned} \quad (4.3.1.a-3)$$

As in one dimensional flow, the flux vectors \mathbf{F} and \mathbf{G} can be split into two terms $\mathbf{F}^+, \mathbf{G}^+$ and $\mathbf{F}^-, \mathbf{G}^-$ /13/, with:

$$\begin{aligned}\mathbf{F} &= \mathbf{F}^+ + \mathbf{F}^- \\ \mathbf{G} &= \mathbf{G}^+ + \mathbf{G}^-\end{aligned}\quad (4.3.1.a-5)$$

where the splitted flux vectors \mathbf{F}^+ and \mathbf{F}^- can be expressed as (see Appendix A7 and, for example, ref./11/, eq. (28)):

$$\mathbf{F}^\pm = \frac{\rho}{2\gamma} \begin{vmatrix} 2(\gamma-1)\lambda_1^{x\pm} & +\lambda_3^{x\pm} & +\lambda_4^{x\pm} \\ | & | & | \\ 2(\gamma-1)\lambda_1^{x\pm}\lambda_1^{x\pm} & +\lambda_3^{x\pm}\lambda_3^{x\pm} & +\lambda_4^{x\pm}\lambda_4^{x\pm} \\ | & | & | \\ 2(\gamma-1)v\lambda_1^{x\pm} & +v\lambda_3^{x\pm} & +v\lambda_4^{x\pm} \\ | & | & | \\ (\gamma-1)q^2\lambda_1^{x\pm} + \left[\frac{\lambda_3^{x2}+v^2}{2}\right]\lambda_3^{x\pm} & + \left[\frac{\lambda_4^{x2}+v^2}{2}\right]\lambda_4^{x\pm} + w^{x\pm} & \end{vmatrix}$$

whith

$$w^{x\pm} = \frac{(3-\gamma)(\lambda_3^{x\pm}+\lambda_4^{x\pm})a^2}{2(\gamma-1)} \quad (4.3.1.a-6a)$$

and the splitted vectors \mathbf{G}^+ and \mathbf{G}^- as (Appendix A7):

$$\mathbf{G}^\pm = \frac{\rho}{2\gamma} \begin{vmatrix} 2(\gamma-1)\lambda_1^{y\pm} & +\lambda_3^{y\pm} & +\lambda_4^{y\pm} \\ | & | & | \\ 2(\gamma-1)u\lambda_1^{y\pm} & +u\lambda_3^{y\pm} & +u\lambda_4^{y\pm} \\ | & | & | \\ 2(\gamma-1)\lambda_1^{y\pm}\lambda_1^{y\pm} & +\lambda_3^{y\pm}\lambda_3^{y\pm} & +\lambda_4^{y\pm}\lambda_4^{y\pm} \\ | & | & | \\ (\gamma-1)q^2\lambda_1^{y\pm} + \left[\frac{u^2+\lambda_3^{y2}}{2}\right]\lambda_3^{y\pm} & + \left[\frac{u^2+\lambda_4^{y2}}{2}\right]\lambda_4^{y\pm} + w^{y\pm} & \end{vmatrix}$$

where

$$w^{y\pm} = \frac{(3-\gamma)(\lambda_3^{y\pm}+\lambda_4^{y\pm})a^2}{2(\gamma-1)} \quad (4.3.1.a-6b)$$

As for one dimensional flow, it is seen that

$$\mathbf{F}^+ = \mathbf{F}; \mathbf{F}^- = 0 \quad \text{if } Mx = u/a_s 1 \quad (4.3.1.a-7a)$$

$$\mathbf{F}^+ = 0; \mathbf{F}^- = \mathbf{F} \quad \text{if } Mx = u/a_s - 1$$

$$\mathbf{G}^+ = \mathbf{G}; \mathbf{G}^- = 0 \quad \text{if } My = v/a_s 1 \quad (4.3.1.a-7b)$$

$$\mathbf{G}^+ = \mathbf{0}; \quad \mathbf{G}^- = \mathbf{G} \quad \text{if } M\gamma = v/a_s - 1$$

However, as for one dimensional flow, the relations (4.3.1-7) are not any more valid if the forward and backward eigenvalues λ^\pm are defined according to (3.1.1-4).

4.3.1.b. van Leer Splitting.

As in one dimensional flow, van Leer proposes to split the flux vectors into forward and backward parts in function of the local, one dimensional, Mach number instead of in function of the eigenvalues, which gives:

For supersonic flow (i.e. $|Mx| \geq 1$ and/or $|My| \geq 1$) the relations (4.3.1.a-7) still hold:

$$\mathbf{F}^+ = \mathbf{F}; \quad \mathbf{F}^- = \mathbf{0} \quad \text{if } Mx = u/a \geq 1 \quad (4.3.1.a-7a)$$

$$\mathbf{F}^+ = \mathbf{0}; \quad \mathbf{F}^- = \mathbf{F} \quad \text{if } Mx = u/a_s - 1$$

$$\mathbf{G}^+ = \mathbf{G}; \quad \mathbf{G}^- = \mathbf{0} \quad \text{if } My = v/a \geq 1 \quad (4.3.1.a-7b)$$

$$\mathbf{G}^+ = \mathbf{0}; \quad \mathbf{G}^- = \mathbf{G} \quad \text{if } My = v/a_s - 1$$

and for subsonic flow, the vectors $\mathbf{F}^+, \mathbf{G}^+$ and $\mathbf{F}^-, \mathbf{G}^-$ are expressed as /11,28/:

$$\mathbf{F}^\pm = \begin{bmatrix} f_1^\pm \\ f_2^\pm \\ f_3^\pm \\ f_4^\pm \end{bmatrix} \quad (4.3.1.a-8a)$$

where $f_1^\pm = \pm p a \{ [Mx \pm 1]/2 \}^2$

$$f_2^\pm = f_1^\pm \cdot \{ (\gamma - 1) u \pm 2a \} / \gamma$$

$$f_3^\pm = f_1^\pm \cdot v$$

$$f_4^\pm = f_1^\pm \cdot \{ \{ (\gamma - 1) u \pm 2a \}^2 / \{ 2[\gamma^2 - 1] \} + v^2 / 2 \}$$

$$\mathbf{G}^{\pm} = \begin{bmatrix} g_1^{\pm} \\ g_2^{\pm} \\ -g_3^{\pm} \\ g_4^{\pm} \end{bmatrix} \quad (4.3.1.a-8b)$$

where $g_1^{\pm} = \pm \rho a \{ [M\gamma \pm 1]/2 \}^2$

$$g_2^{\pm} = g_1^{\pm} \cdot u$$

$$g_3^{\pm} = g_1^{\pm} \cdot \{ [\gamma - 1] v \pm 2a \} / \gamma$$

$$g_4^{\pm} = g_1^{\pm} \cdot \{ \{ [(\gamma - 1)v \pm 2a]^2 \} / \{ 2[\gamma^2 - 1] \} + u^2 / 2 \}$$

4.3.2 Generalized Coordinates.

The original flux vector splitting study by Steger/Warming /13/ contained a splitting in generalized coordinates which was different from the one in cartesian coordinates, and consisted of a mixture of ξ and η derivatives in both the \mathbf{F}' and \mathbf{G}' fluxes (see section 4.1 for definition of \mathbf{F}' and \mathbf{G}'). Anderson/Thomas/van Leer /11/ proposed instead to locally rotate the fluxes into a "body-fitted" coordinate system, first for the \mathbf{F}' flux, while treating the \mathbf{G}'_{η} as a source term, and thereafter the \mathbf{G}' flux, while treating the \mathbf{F}'_{ξ} as a source term. This procedure is explained in detail below (see ref. /11/).

The equation (4.1-2) can be multiplied, from the left, by a transformation matrix T^{ξ} :

$$(T^{\xi}W')_{\tau} + (T^{\xi}F')_{\xi} = -T^{\xi}G'_{\eta} + (T^{\xi})_{\tau}W' + (T^{\xi})_{\xi}F' \quad (4.3.2-1)$$

which by defining

$$\begin{aligned} W &= T^{\xi}W' \\ F &= T^{\xi}F' \end{aligned} \quad (4.3.2-2)$$

reduces to

$$(W')_{\tau} + (F')_{\xi} = -T^{\xi}G'_{\eta} + (T^{\xi})_{\tau}W' + (T^{\xi})_{\xi}F' \quad (4.3.2-3)$$

Splitting of $(\bar{W})_\xi$, yet undetermined, gives:

$$(\bar{W})_T + (\bar{F}^+ + \bar{F}^-)_\xi = -T^\xi G'_{\eta} + (T^\xi)_T W' + (T^\xi)_\xi F' \quad (4.3.2-4)$$

whereafter multiplication, from the left, with $T^{\xi-1}$ (=the inverse of T^ξ) gives:

$$T^{\xi-1}(\bar{W}_T - T^\xi_T W') + T^{\xi-1}(\bar{F}^+ + \bar{F}^-)_\xi = -T^{\xi-1}(T^\xi G'_{\eta}) + T^{\xi-1}(T^\xi)_\xi F' \quad (4.3.2-5)$$

$$\begin{aligned} &\Rightarrow \\ T^{\xi-1}(T^\xi W'_T) + (T^{\xi-1}F^+ + T^{\xi-1}F^-)_\xi - (T^{\xi-1})_\xi(F^+ + F^-) &= \\ &= -T^{\xi-1}(T^\xi G'_{\eta}) + T^{\xi-1}(T^\xi)_\xi F' \end{aligned} \quad (4.3.2-6)$$

$$\begin{aligned} &\Rightarrow \\ I W'_T + (T^{\xi-1}F^+ + T^{\xi-1}F^-)_\xi - (T^{\xi-1})_\xi(F^+ + F^-) &= \\ &= -IG'_{\eta} + T^{\xi-1}(T^\xi)_\xi F' \end{aligned} \quad (4.3.2-7)$$

where I = identity matrix =

$$\begin{bmatrix} 1 & 0 & 0 & 1 \\ 0 & 1 & 0 & 0 \\ 0 & 0 & 1 & 0 \\ 0 & 0 & 0 & 1 \end{bmatrix} \quad (4.3.2-8)$$

This implies furthermore that

$$\begin{aligned} I W'_T + (F'^+ + F'^-)_\xi + IG'_{\eta} &= \\ &= T^{\xi-1}(T^\xi)_\xi F' + (T^{\xi-1})_\xi(F^+ + F^-) \end{aligned} \quad (4.3.2-9)$$

where

$$F'^+ = (T^\xi)^{-1}F^+ \quad (4.3.2-10)$$

$$F'^- = (T^\xi)^{-1}F^-$$

Thereafter, the RHS of equation (4.3.2-9) becomes, as $F = T^\xi F'$.

$$\begin{aligned} T\xi^{-1}(T\xi)_{\xi}F^+ + (T\xi^{-1})_{\xi}(F^+ + F^-) &= T\xi^{-1}(T\xi)_{\xi}F^+ + (T\xi^{-1})_{\xi}(T\xi F^-) = \\ &= (T\xi^{-1}T\xi)_{\xi}F^+ = I_{\xi}F^+ = 0 \end{aligned} \quad (4.3.2-11)$$

Equation (4.3-9) becomes thus:

$$W^*_{\tau^+}(F^{++} + F^{+-})_{\xi} + G^*_{\eta} = 0 \quad (4.3.2-12)$$

which is identical with the original equation (4.1-2).

It is interesting to note that the term G^*_{η} has not been affected by the above manipulation. Thus, it is possible to perform a similar procedure also for this flux. This gives:

$$W^*_{\tau^+}(F^{++} + F^{+-})_{\xi} + (G^{++} + G^{+-})_{\eta} = 0 \quad (4.3.2-13)$$

with

$$\begin{aligned} G^{++} &= (T\Pi)^{-1}\bar{G}^+ \\ G^{+-} &= (T\Pi)^{-1}\bar{G}^- \end{aligned} \quad (4.3.2-14)$$

Note that no assumption has, up till now, been made concerning how the flux splitting should be performed.

If now the rotation matrices $T\xi$ and $T\Pi$ are chosen in a special way, the transformed fluxes \bar{F} and \bar{G} can be of the same form as the original equations, wherefore any of the splittings (4.3.1.a-6a) and (4.3.1.a-6b), as developed for the cartesian coordinates, can be applied directly.

To obtain such a form for \bar{F} and \bar{G} , define the rotation matrix $T\xi$, in the case of a non-moving grid, as:

$$T\xi = \left[\begin{array}{cccc} 1 & 0 & 0 & 0 \\ 0 & c\xi_1 & c\xi_2 & 0 \\ 0 & -c\xi_2 & c\xi_1 & 0 \\ 0 & 0 & 0 & 1 \end{array} \right] \quad (4.3.2-15)$$

with

$$c\xi_1 = \xi_x / (\xi_x^2 + \xi_y^2)^{0.5} = y_{\eta} / (y_{\eta}^2 + x_{\eta}^2)^{0.5} \quad (4.3.2-16)$$

$$\xi_2 = \xi_y / (\xi_x^2 + \xi_y^2)^{0.5} = -x_\eta / (y_\eta^2 + x_\eta^2)^{0.5}$$

This rotation gives then:

$$\bar{\mathbf{W}} = T\xi\mathbf{W}' = D^{-1} \begin{bmatrix} \rho \\ \rho\bar{u}\xi \\ \rho\bar{v}\xi \\ \rho e_c \end{bmatrix} \quad (4.3.2-17a)$$

$$\begin{aligned} \bar{\mathbf{F}} &= T\xi\mathbf{F}' = D^{-1} \cdot (\xi_x^2 + \xi_y^2)^{0.5} \begin{bmatrix} \rho\bar{u}\xi \\ \rho\bar{u}\xi \bar{u}\xi + p \\ \rho\bar{v}\xi \bar{u}\xi \\ \rho\bar{u}\xi [e_c + p/\rho] \end{bmatrix} \\ &= (\xi_x^2 + \xi_y^2)^{0.5} \begin{bmatrix} \rho\bar{u}\xi \\ \rho\bar{u}\xi \bar{u}\xi + p \\ \rho\bar{v}\xi \bar{u}\xi \\ \rho\bar{u}\xi [e_c + p/\rho] \end{bmatrix} \end{aligned} \quad (4.3.2-17b)$$

where

$$\bar{u}\xi = (\xi_x u + \xi_y v) / (\xi_x^2 + \xi_y^2)^{0.5} = (y_\eta u - x_\eta v) / (y_\eta^2 + x_\eta^2)^{0.5} \quad (4.3.2-17c)$$

$$\bar{v}\xi = (-\xi_y u + \xi_x v) / (\xi_x^2 + \xi_y^2)^{0.5} = (x_\eta u + y_\eta v) / (y_\eta^2 + x_\eta^2)^{0.5}$$

are the rotated velocity components. $\bar{u}\xi$ is the velocity normal to a line of constant ξ , representing the scaled contravariant velocity component //11/, and $\bar{v}\xi$ is normal to $\bar{u}\xi$ (Fig. 4.3.2-1a).

As the eqs. (4.3.2-17a,17b) are in the same form as the eqs. (4.1-6a,6b) for the cartesian coordinates, splittings identical to the ones in the cartesian system can be used for splitting of the flux vector \mathbf{F}' in generalized coordinates.

In a similar way, let us define for the rotation matrix $T\eta$ (non-moving grid):

$$T\eta = \begin{bmatrix} 1 & 0 & 0 & 0 \\ 0 & -c\eta_1 & c\eta_2 & 0 \\ 0 & c\eta_2 & c\eta_1 & 0 \\ 0 & 0 & 0 & 1 \end{bmatrix} \quad (4.3.2-18)$$

with

$$\begin{aligned} c\eta_1 &= \eta_y / (\eta_x^2 + \eta_y^2)^{0.5} = x_\xi / (x_\xi^2 + y_\xi^2)^{0.5} \\ c\eta_2 &= \eta_x / (\eta_x^2 + \eta_y^2)^{0.5} = -y_\xi / (x_\xi^2 + y_\xi^2)^{0.5} \end{aligned} \quad (4.3.2-19)$$

This rotation gives then:

$$\bar{W} = T\eta W^* = D^{-1} \begin{bmatrix} \rho \\ \rho \bar{u}\eta \\ \rho \bar{v}\eta \\ \rho e_c \end{bmatrix} \quad (4.3.2-20a)$$

$$\begin{aligned} \bar{G} &= T\eta G^* = D^{-1} \cdot (\eta_x^2 + \eta_y^2)^{0.5} \begin{bmatrix} \rho \bar{v}\eta \\ \rho \bar{u}\eta \bar{v}\eta \\ \rho \bar{v}\eta \bar{v}\eta + p \\ \rho \bar{v}\eta [e_c + p/\rho] \end{bmatrix} \\ - &= \{y_\xi^2 + x_\xi^2\}^{0.5} \begin{bmatrix} \rho \bar{v}\eta \\ \rho \bar{u}\eta \bar{v}\eta \\ \rho \bar{v}\eta \bar{v}\eta + p \\ \rho \bar{v}\eta [e_c + p/\rho] \end{bmatrix} \end{aligned} \quad (4.3.2-20b)$$

where

$$\begin{aligned} \bar{u}\eta &= (-\eta_y u + \eta_x v) / (\eta_x^2 + \eta_y^2)^{0.5} = -x_\xi u - y_\xi v / (x_\xi^2 + y_\xi^2)^{0.5} \\ \bar{v}\eta &= (\eta_x u + \eta_y v) / (\eta_x^2 + \eta_y^2)^{0.5} = -y_\xi u + x_\xi v / (x_\xi^2 + y_\xi^2)^{0.5} \end{aligned} \quad (4.3.2-20c)$$

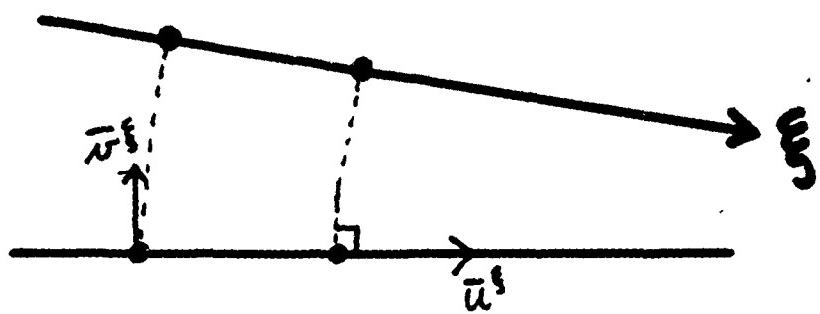
are the rotated velocity components. \bar{v}^η is the velocity normal to a line of constant η , representing the scaled contravariant velocity component, and \bar{u}^η is normal to \bar{v}^η (Fig. 4.3.2-1b).

As the eqs. (4.3.2-20a,20b) are in the same form as the eqs. (4.1-6a,6c) for the cartesian coordinates, splittings identical to the ones in the cartesian system can be used for splitting of the flux vector \mathbf{G}' in generalized coordinates.

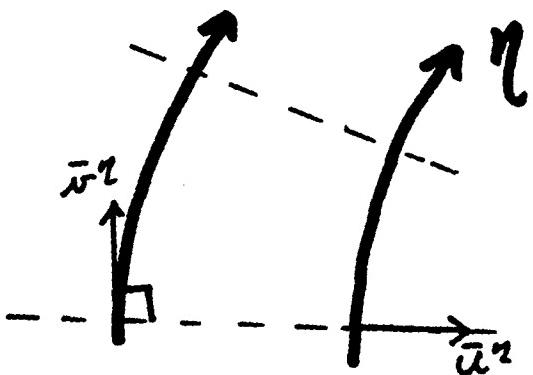
After performing the splittings of \mathbf{F} and \mathbf{G} , these fluxes have to be rotated back into the \mathbf{F}' and \mathbf{G}' fluxes with the inverse of the transformation matrices T^ξ and T^η (see eqs. (4.3.2-10,14)). These can be expressed as:

$$T^{\xi^{-1}} = \begin{bmatrix} 1 & 0 & 0 & 0 \\ 0 & c\xi_1 & -c\xi_2 & 0 \\ 0 & c\xi_2 & c\xi_1 & 0 \\ 0 & 0 & 0 & 1 \end{bmatrix} \quad (4.3.2-21)$$

$$T^{\eta^{-1}} = T^\eta = \begin{bmatrix} 1 & 0 & 0 & 0 \\ 0 & -c\eta_1 & c\eta_2 & 0 \\ 0 & c\eta_2 & c\eta_1 & 0 \\ 0 & 0 & 0 & 1 \end{bmatrix} \quad (4.3.2-22)$$



a. Definition of \bar{u}^e, \bar{v}^e



b. Definition of \bar{u}^n, \bar{v}^n

Fig. 4.3.2-1.

Definition of contravariant velocities.

4.4. Boundary Conditions

4.4.1. Boundary Conditions at the Blade Walls.

4.4.1.a. Grid Points Situated on the Walls.

In the O-grid, the treatment of the boundary conditions at the walls (no mass through the wall) are straightforward as a mirror image. This is the case as the grid can be continuously generated in one point inside the boundary (as the grid is then orthogonal to the boundary) and thus the fluxes can be split in the same way as in the interior points. Then, the consideration of a mirror image immediately gives that:

- at the lower wall:

$$\begin{aligned}
 \bar{u}\eta_{j-1/2,i} &= \bar{u}\eta_{j+1/2,i} \\
 p_{j-1/2,i} &= p_{j+1/2,i} \\
 \rho_{j-1/2,i} &= \rho_{j+1/2,i} \\
 \bar{v}\eta_{j-1/2,i} &= -\bar{v}\eta_{j+1/2,i} \\
 y_{j-1/2,i} &= -y_{j+1/2,i} \\
 \eta_{j-1/2,i} &= -\eta_{j+1/2,i}
 \end{aligned} \tag{4.4.1-1a}$$

wherefore

$$\begin{aligned}
 \bar{G}_{j-1/2,i}^+ &= \text{sign} \cdot \bar{G}_{j+1/2,i}^- \\
 \bar{G}_{j+1/2,i}^+ &= \text{sign} \cdot \bar{G}_{j-1/2,i}^-
 \end{aligned} \tag{4.4.1-2a}$$

- at the upper wall:

$$\begin{aligned}
 \bar{u}\eta_{j+1/2,i} &= u\eta_{j-1/2,i} \\
 p_{j+1/2,i} &= p_{j-1/2,i} \\
 \rho_{j+1/2,i} &= \rho_{j-1/2,i} \\
 \bar{v}\eta_{j+1/2,i} &= -\bar{v}\eta_{j-1/2,i}
 \end{aligned} \tag{4.4.1-1b}$$

wherefore

$$\bar{G}_{j+1/2,i}^+ = \text{sign} \cdot \bar{G}_{j-1/2,i}^- \quad (4.4.1-20)$$

$$\bar{G}_{j-1/2,i}^+ = \text{sign} \cdot \bar{G}_{j+1/2,i}^-$$

where $\text{sign} = \begin{cases} -1 & \text{for the mass, x-momentum and energy fluxes.} \\ +1 & \text{for the y-momentum flux.} \end{cases}$

In the case of the H-grid, on the other hand, the same simple implementation of a mirror image at the boundary is clearly not correct. This can for example be seen in Fig. 4.4.1-1, where a discontinuity in the grid is introduced at the boundary for the mirror image. It is seen by considering the elements created by the mid grid points throughout the computational domain that, at the boundary, the flow which should be calculated in point $(j,1)$ is instead calculated for a point, in the present example, at $(j,1+5)$.

For the H-grid, the boundary conditions are instead implemented in different ways for the option that the grid points are situated directly at the computational boundaries. The F' flux can be calculated as in the interior points, as no information from outside the computational domain is necessary for this flux at the blade walls (obviously, at the inlet and outlet F' would need information from outside the computational domain, whereas G' would not need any extra information). For determining the G' flux, different possibilities exist. One (Method 1) would be to extrapolate, linearly or parabolically, the $\bar{G}^{+/-}$ fluxes, from the splitted fluxes inside the computational domain, towards the first mid point outside the computational domain. This would be consistent with the way the fluxes are determined in the rest of the computational domain, and would introduce a numerical dissipation at the walls similar to the rest of the flow field. Another, slightly different approach (Method 2), consists instead of extrapolating the splitted fluxes $\bar{G}^{+/-}$ from the mid points, we instead compute the total fluxes in the gridpoints close to the walls and extrapolate G' , in the first mid grid point outside the computational domain, parabolically from these. This gives:

- For the upper wall:

$$G'_{j+1/2,i} = (3G'_{j-2,i} - 10G'_{j-1,i} + 15G'_{j,i})/8 \quad (4.4.1-3a)$$

- For the lower wall:

$$G'_{j-1/2,i} = (3G'_{j+2,i} - 10G'_{j+1,i} + 15G'_{j,i})/8 \quad (4.4.1-3b)$$

Furthermore, in this approach, we are also missing the information of $G'_{j+1/2,i}$ at the lower wall calculation and the $G'_{j-1/2,i}$ at the upper wall calculation. This is seen from the way the $G'_{j\pm 1/2,i}$ fluxes are calculated with the second order spatial accuracy (see section 3.2). Therefore, for calculation of the G'_{η} at the walls and the point next to the wall, the total flux in point $(j+1/2,i)$, for the lower wall, and point $(j-1/2,i)$, for the upper wall, is computed as:

$$\begin{aligned} \text{Lower wall: } G'_{j+1/2,i} &= (G'_{j,i} + G'_{j+1,i})/2 \\ \text{Upper wall: } G'_{j-1/2,i} &= (G'_{j,i} + G'_{j-1,i})/2 \end{aligned} \quad (4.4.1-4)$$

respectively¹.

Obviously, the so computed flow variables at the walls do not satisfy the boundary condition of no mass flow through the wall. Therefore, the Riemann invariant normal to the wall (R^+ at the upper wall, R^- at the lower wall, see for example Appendix A4) is calculated from the computed flow variables. The introduction of the boundary condition (zero normal velocity at the wall) is thereafter used together with the Riemann invariant to determine the relationship between normal velocity and pressure at the wall.

These methods of extrapolation for the boundary is known from the author's previous work (with a MacCormack predictor-corrector method without explicit numerical dissipation) /7/ to give good results as regards to the pressure and density. However, some error can be introduced (with the magnitude depending on the angle between the $\xi=\text{const}$ and $\eta=\text{const}$ lines) in the stagnation pressure. Therefore, the velocity tangential to the

¹ Such an averaging must be carefully checked as it eventually may introduce errors and/or instabilities in some cases.

blade surface can be updated, in steady state flow, by considering that the wall corresponds to a streamline, wherefore the enthalpy is known along it. This gives the following relationship, as $\bar{v}=0$ (velocity component normal to the wall):

$$\tilde{u}^2 = 2\{h_{c-\infty} - a^2/[\gamma - 1]\} \quad (4.4.1-5)$$

with \tilde{u} = velocity component tangential to the wall.

However, previous work of extrapolation at the boundaries has not included splitting of the fluxes, and thus not any special treatment for the points $(j+1/2,i)$ for the lower wall calculation and the point $(j-1/2,i)$ for the upper wall calculation. Simple averaging of the total fluxes as in eq. (4.4.1-4) may eventually lead to instability.

The experience with the present flux vector splitting method has shown that the Method 2 of implementing the boundary conditions gave good results for the first two dimensional test problem (section 4.6.1), both for the O-grid and the H-grid (at least as long as the boundary conditions at the inlet and outlet are overspecified), but that most of the cases for the second test problem (section 4.6.2) did not converge.

4.4.1.b. Grid Points Situated 1/2 Point from the Walls.

To eliminate these convergence problems, it was instead tried, with better results, to implement the flux vector splitting methodology in a finite volume direction, although the actual solution algorithm is still a finite difference approach.

The grid was then instead constructed such that the cell interface lies on the boundary of the computational domain (section 4.2.2).

The boundary conditions are then incorporated as already explained in section 4.2.2.

4.4.2. Boundary Conditions at the Inlet.

This is performed in exactly the same way as in one dimensions (section 3.3.2.b) with the additional constraint of the inlet flow direction.

4.4.3. Boundary Conditions at the Outlet.

As in one dimensional flow (section 3.3.2.a) with the additional condition that \tilde{v} is accepted from the calculation, or (as a second, non-physical, option) that $\tilde{v}=0$.

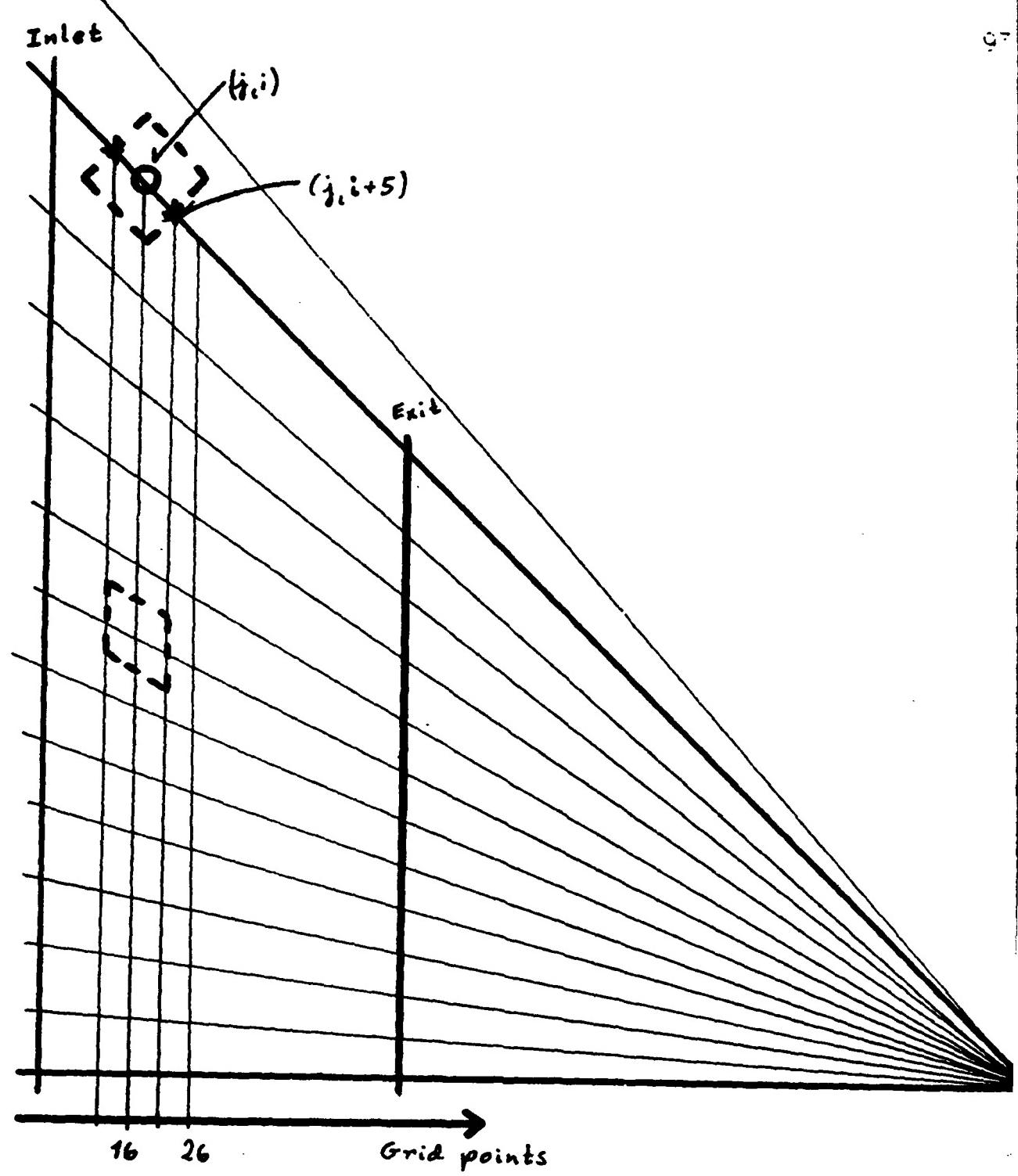


Fig. 4.4.1-1. Illustration of inaccuracy of mirror image treatment of the boundary for an H-grid.

4.5. Numerical Algorithm in Two Dimensions.

The solution algorithm is the same as in one-dimensional flow, with the second dimension added.

First step:

$$\mathbf{W}^*_{j,i} = \mathbf{W}_{j,i}^k - \Delta t \{ \Delta(F_{j,i}^+)^k + \Delta(F_{j,i}^-)^k \} / \Delta x \\ - \Delta t \{ \Delta(G_{j,i}^+)^k + \Delta(G_{j,i}^-)^k \} / \Delta y$$

Second step:

$$\mathbf{W}_{j,i}^{k+1} = 0.5 \cdot \{ \mathbf{W}^*_{j,i} + \mathbf{W}_{j,i}^k - \Delta t [\Delta(F^*_{j,i}^+)^k + \Delta(F^*_{j,i}^-)^k] / \Delta x \\ - \Delta t [\Delta(G^*_{j,i}^+)^k + \Delta(G^*_{j,i}^-)^k] / \Delta y \}$$

with the spatial differencing (in both dimensions, one at a time) as in section 3.4.

4.6.1. First Test Problem.

The first -two dimensional test problem is identical to the third one dimensional problem, i.e. a duct with radial subsonic flow (Fig. 4.6.1-1) with an outlet Mach number of, at the centerline, $M=0.8864$. For the purpose of a detailed investigation of the influence of the number of grid elements on the numerical solution, the opening of the duct was chosen to be fairly large (wedge angle=90°). Furthermore, two sets of grids were investigated. The first is a O-grid (Fig. 4.6.1-1a) and the second an H-grid (Fig. 4.6.1-1b). As the flow in the case under study is radial, it is obviously expected that the first grid will give the most accurate result for a predefined number of grid points.

The results from the two dimensional O-grid is illustrated in Fig. 4.6.1-2. Here, the lines of constant Mach number are compared to the exact results. (For the first test problem all computations shown are performed with overspecified boundary conditions at the inlet and outlet.) The comparison is done in the physical plane for a general view (Fig. 4.6.1-2a) and in the computational plane for more details (Fig. 4.6.1-2b). The symmetry of the solution is exact. However, as already concluded for the quasi one dimensional computations, 21 grid points in the streamwise direction is not enough to accurately reproduce the exact solution (due to the numerical dissipation inherent in the flux vector splitting). With 21 streamwise points (and 9 circumferential) the numerical solution is shifted approximately 1 element at Isomachline $M=0.5$ (a similar shift is present also in the density and pressure). Furthermore, as expected, 3 grid points (=2 elements) in the circumferential direction gives a very inaccurate solution (Fig. 4.6.1-2b), whereas 9 and 13 circumferential points give similar results.

For the H-grid, results are presented in Fig. 4.6.1-3 for the case with the boundary conditions at the walls implemented according to Method 2 in section 4.4.1.a (extrapolation of total fluxes to a midpoint outside the computational domain). For the computational grid consisting of 60x12 elements there is virtually no difference between the exact and computed solutions, if the tangential velocity component at the wall is corrected as part of the boundary condition implementation according to eq. (4.4.1-5). This is shown for the density (Fig. 4.6.1-3a), pressure (Fig. 4.6.1-3b) and Mach number (Fig. 4.6.1-3c). If the correction of \tilde{U} is not performed, a slight difference between the computed and exact results is found in the

upper left corner of the nozzle for the density and pressure (Fig. 4.6.1-3a,b). The Isomachlines show however in this case a larger deviation from the exact values (Fig. 4.6.1-3c). This is due to the fact that the stagnation pressure is overestimated at the wall. This is a local effect, and the turning of the Isomachlines is limited to the gridpoints at the wall. This is seen from Fig. 4.6.1-3c, where the values agree in all points inside the flow field.

A stability factor of STAB=0.4 (see eq. 6.0-4, 6.0-6) was used for all these calculations.

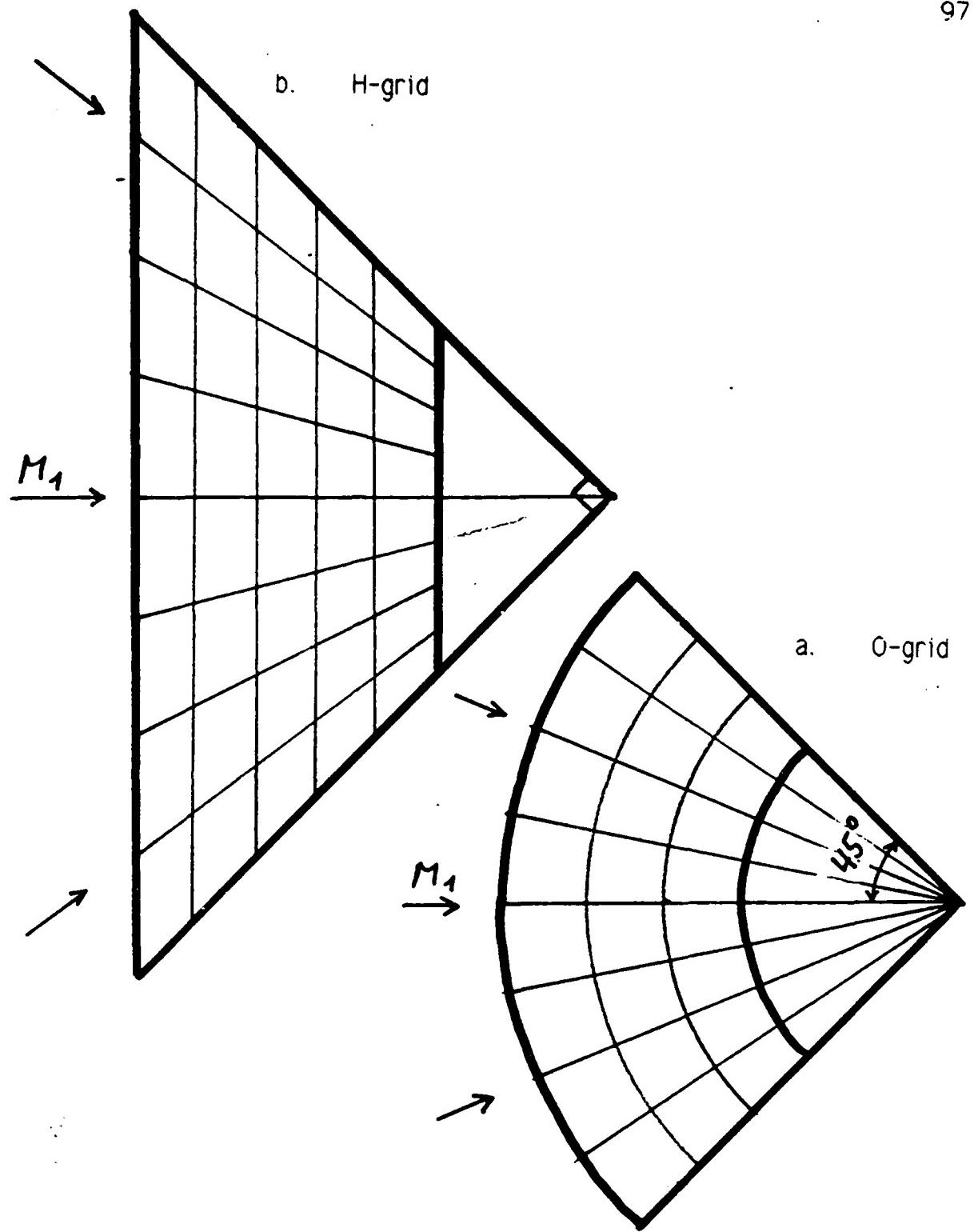


Fig. 4.6.1-1.

Grids for first two-dimensional test problem.

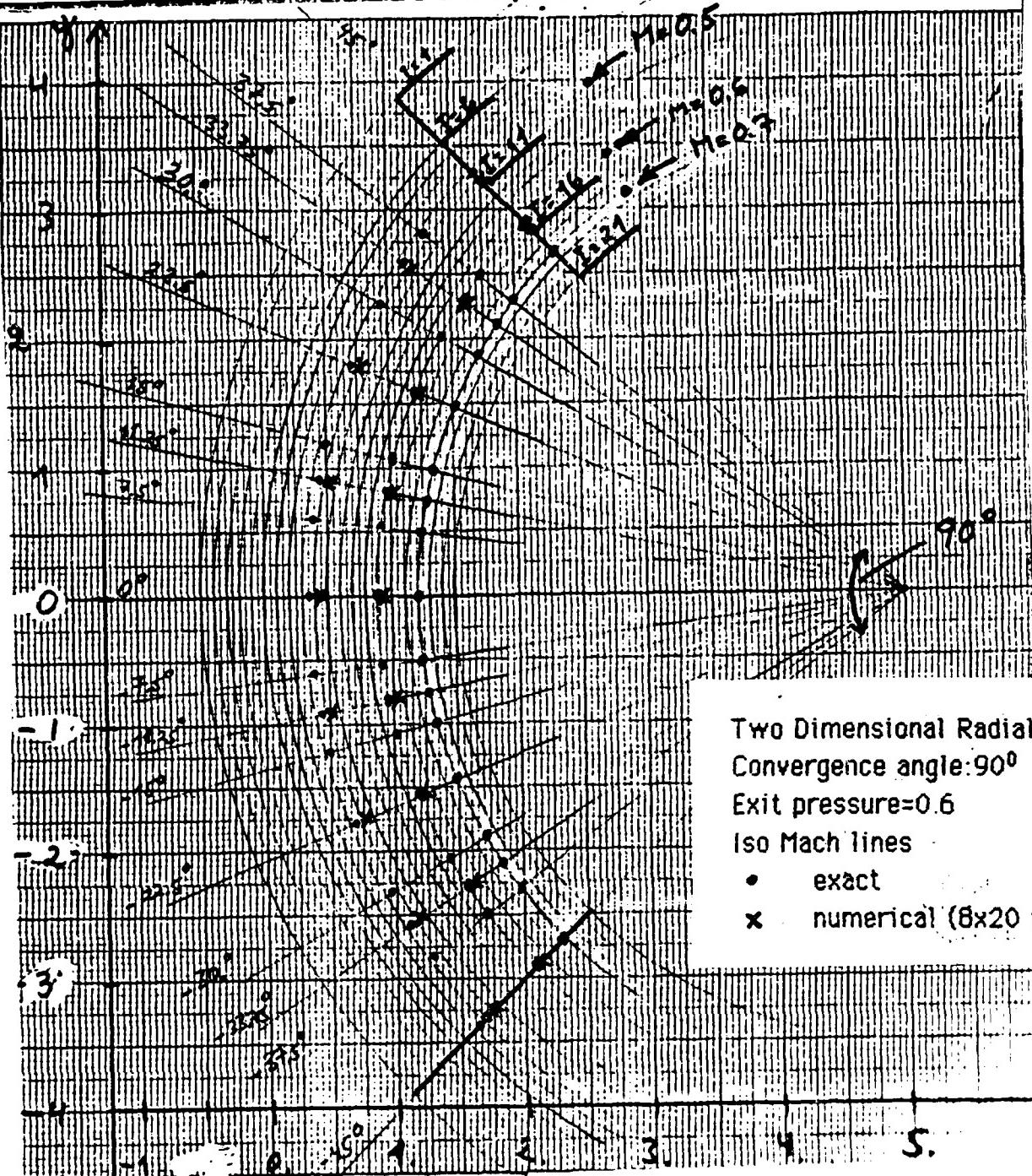


Fig. 4.6.1-2a. Iso Mach lines in the physical domain of a two dimensional test problem.

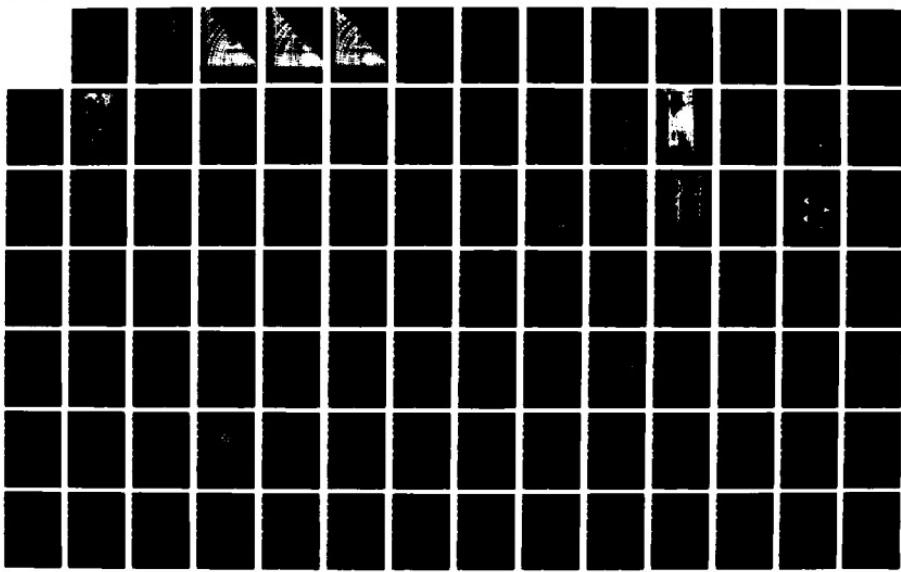
AD-A189 588 APPLICATION OF A FLUX VECTOR SPLITTING METHODOLOGY
TOWARDS THE SOLUTION O (U) NAVAL POSTGRADUATE SCHOOL
MONTEREY CA T H FRANSSON JUL 87 NPS67-87-006

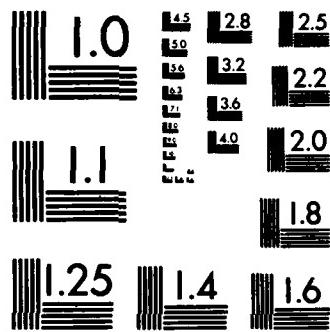
2/3

UNCLASSIFIED

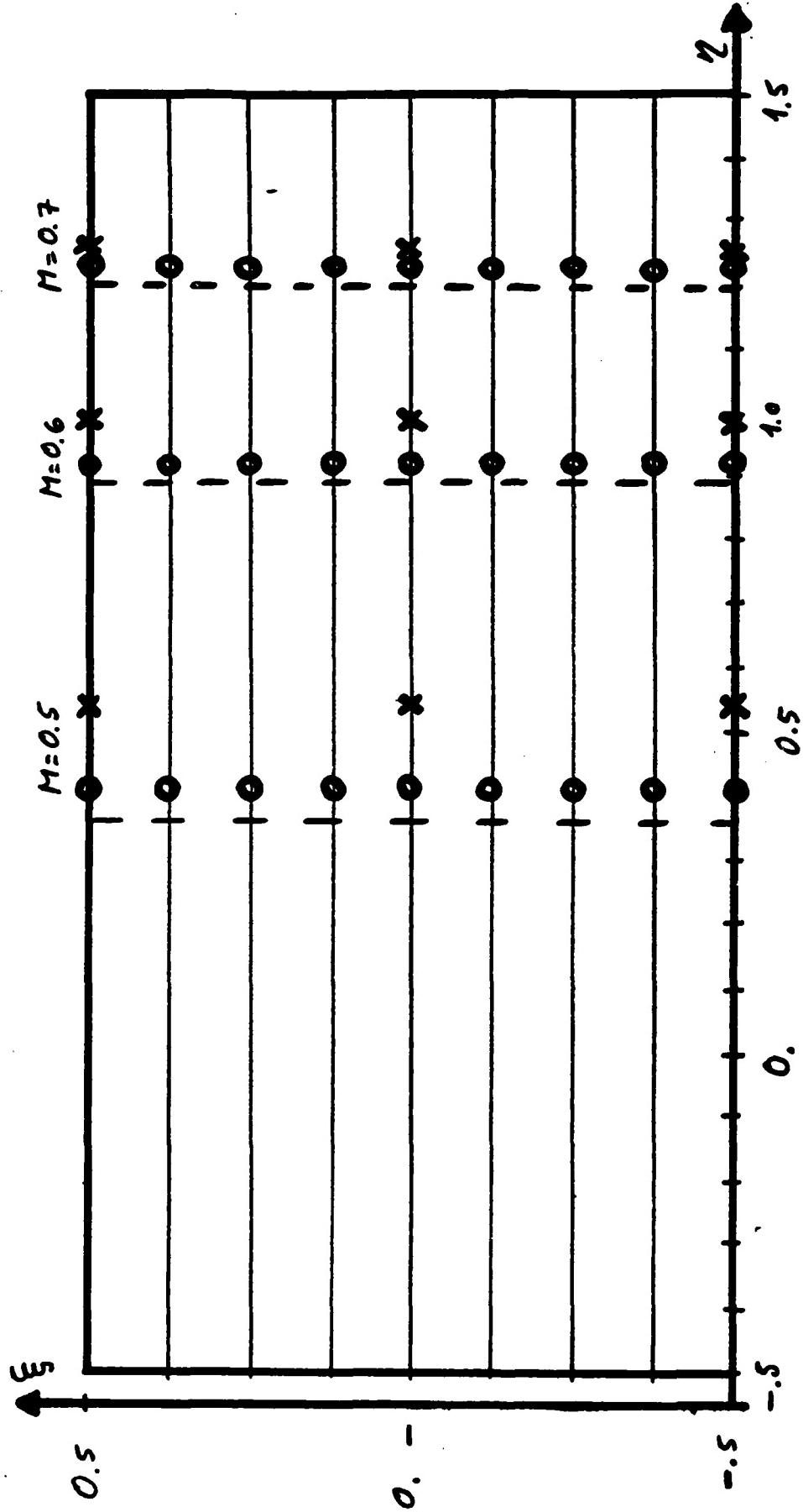
F/G 28/4

NL





MICROCOPY RESOLUTION TEST CHART
NATIONAL BUREAU OF STANDARDS-1963-A



Two Dimensional Radial Flow
 Convergence angle: 90°
 Exit pressure = 0.6

Fig. 4.6.1-2b. Iso Mach lines in the computational plane. First

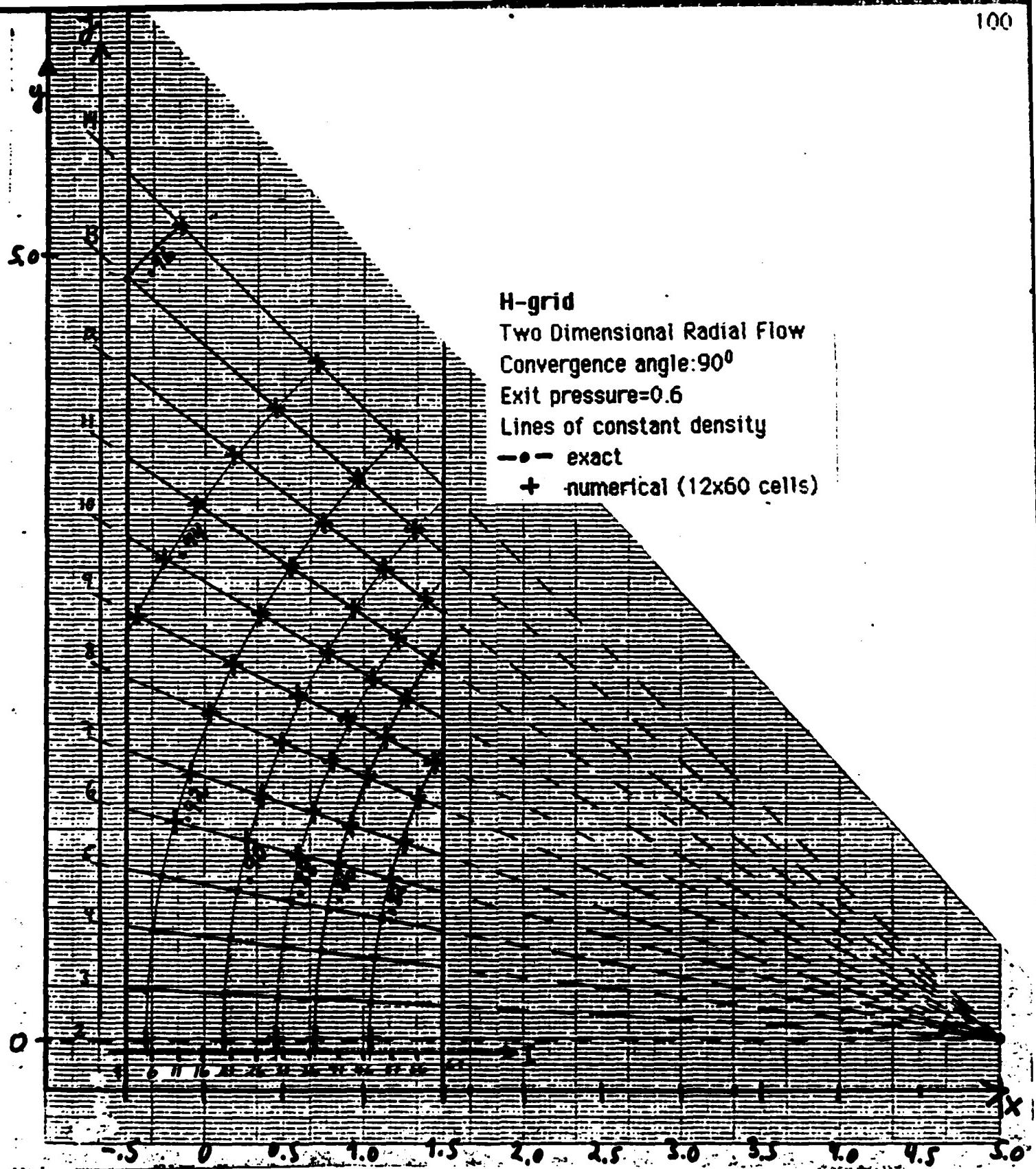
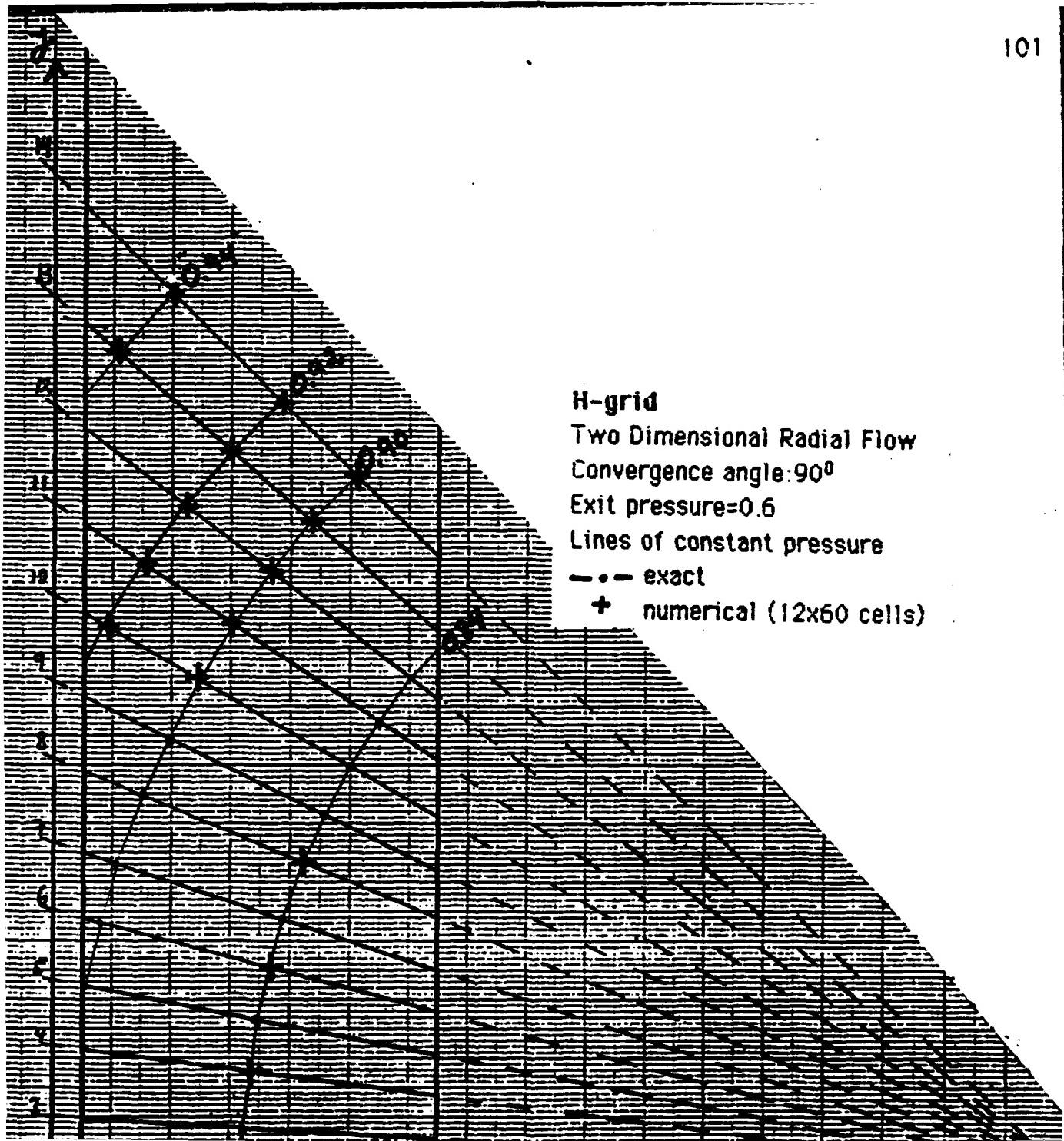


Fig. 4.6.1-3a. Lines of constant density in the physical plane.
First two-dimensional test problem.



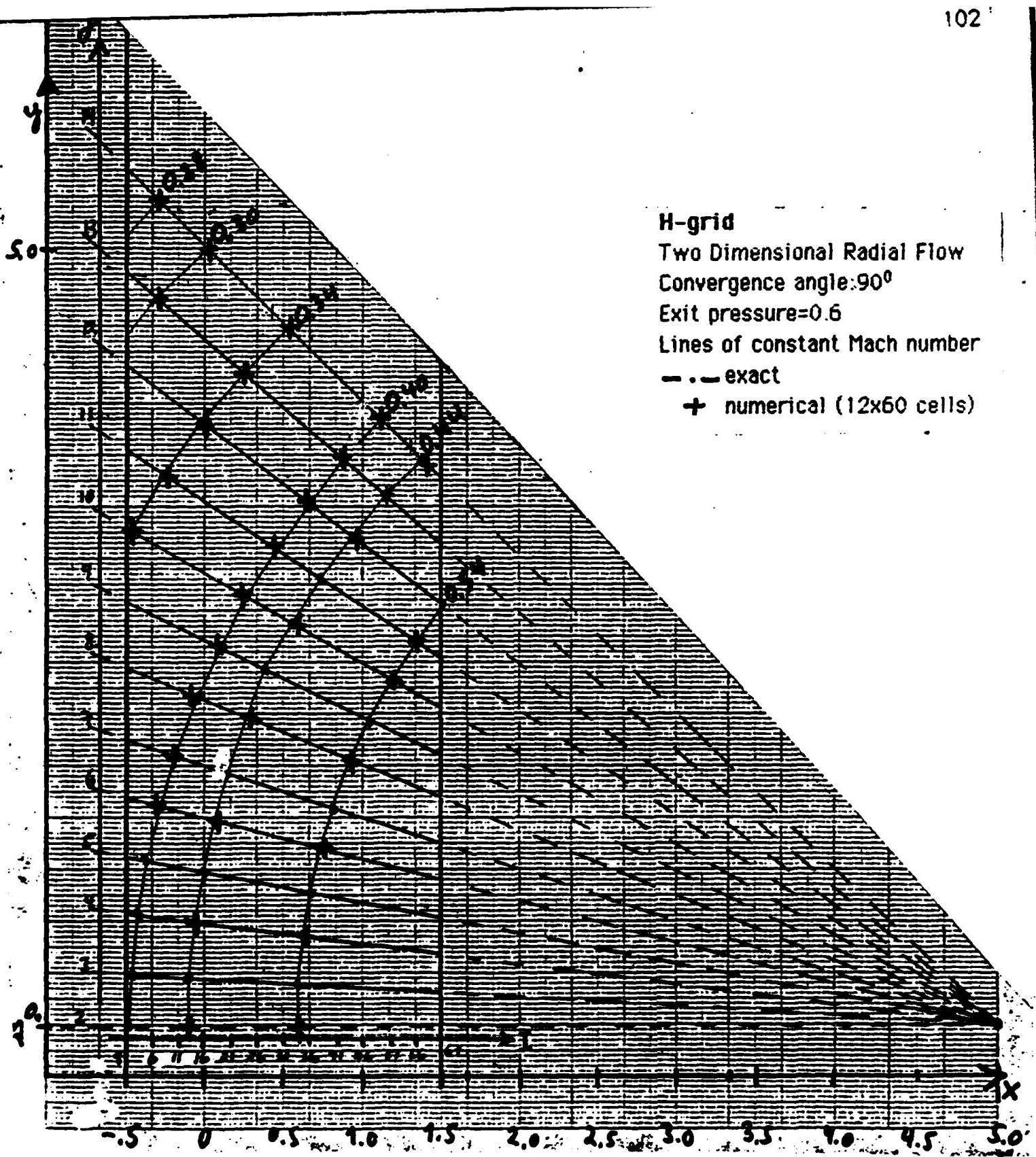


Fig. 4.6.1-3c. Iso Mach lines in the physical plane. First two-dimensional test problem.

4.6.2. Second Test Problem.

The second two dimensional test problem is the one, by now standard (/32-35/, /7/), consisting of a straight channel, with a 10% double circular arc bump on one of the walls (Fig. 4.6.2-1). Computed inviscid results with this geometry have been presented by several authors, for different inlet flow conditions, since its introduction by G. Moretti in 1981 /32/. No experimental data can be compared to results from the inviscid methods as the viscous flow separates at about 70% of the bump length for an inlet Mach number of $M_{\infty} \approx 0.5$ /36/.

Calculations with the present method were performed with an H-grid at inlet Mach numbers of $M_{\infty}=0.5$ (completely subsonic flow) and $M_{\infty}=0.675$ (transonic flow).

The first case ($M_{\infty}=0.5$) was computed using only 6x20 elements (7x21 grid points) and with

- grid lines *at* the walls (section 4.2.1)
- boundary treatment of η -fluxes according to method 2 in section 4.4.1.a.

This method gave results (for overspecified boundary conditions at inlet and outlet) in good agreement with the ones presented in /7,33/, but instabilities were found for other thicknesses of the bump, when the overspecification of the boundary conditions at the inlet and outlet was taken away.

The second case ($M_{\infty}=0.675$) was then instead computed with the grid generated so that the *wall is located 1/2 cell away from the grid points* (section 4.2.2), with corresponding boundary conditions at the walls (section 4.4.1.b).

The pressure on the wall with the bump is presented in Fig. 4.6.2-2a. For this computation the pressure at the walls was calculated according to the zeroth order extrapolation in section 4.4.1.b, i.e. $p_{j\pm 1/2,i} = p_{j,i}$ with $j \pm 1/2$ located on the upper and lower walls, respectively. The first calculation (Run 201) was performed with overspecified boundary conditions at inlet and outlet, and the second (Run 202) with radiative boundary condition at inlet and constant pressure at outlet (implemented with "Method 1" in section 3.3.1). Both computations are performed without special treatment at the first point downstream of the shock, i.e. second order spatial accuracy (flux limiter $\Phi=1$, see section 3.2) everywhere, and with the

entropy in the two points closest to the wall put equal to the entropy in the third point away from the wall in order to reduce numerical entropy errors at the wall (see for example /11,37/). There is virtually no difference between the solutions, apart from close to the inlet and outlet boundaries.

The highest Mach number is approximately $M_{\max} \approx 1.38$ and is reached at 70% of the bump length. This is in close agreement with results from /33/ ($M_{\max} \approx 1.38$, 72%) and /34/ ($M_{\max} \approx 1.32$, 72%), whereas there is some difference towards the results presented in /35/ ($M_{\max} \approx 1.5$, 70%).

In Fig. 4.6.2-2b the lines of constant isentropic Mach numbers are presented in the computational domain for the same calculations. The results are again in agreement with ref. /33,34/.

It should however be noted that the results introduce an increase of stagnation enthalpy at the wall with the bump in the case of the radiative boundary condition at the inlet (compare /24/ where this also occur). This increase corresponds to $\Delta h_c \approx 2\%$, with an increase also at the inlet. If h_c is instead specified at the inlet (for example as in the "capacity" boundary condition) the level of error in enthalpy stays approximatively the same, but there is no increase of h_c at the inlet.

If the stagnation enthalpy at inlet and outlet are not the same due to numerical errors, the Mach number as calculated will also have numerical errors (compare for example the previous discussion on this matter in section 3.3.1.b), even if the pressure is correct. More points, and clustered, close to the wall would improve this inaccuracy, as would a better extrapolation of the pressure at the wall (section 4.2.2).

Furthermore, a grid which is orthogonal to the walls would increase the accuracy.



Fig. 4.6.2-1. Second two dimensional test problem: Nozzle with 10% thick double circular arc bump.

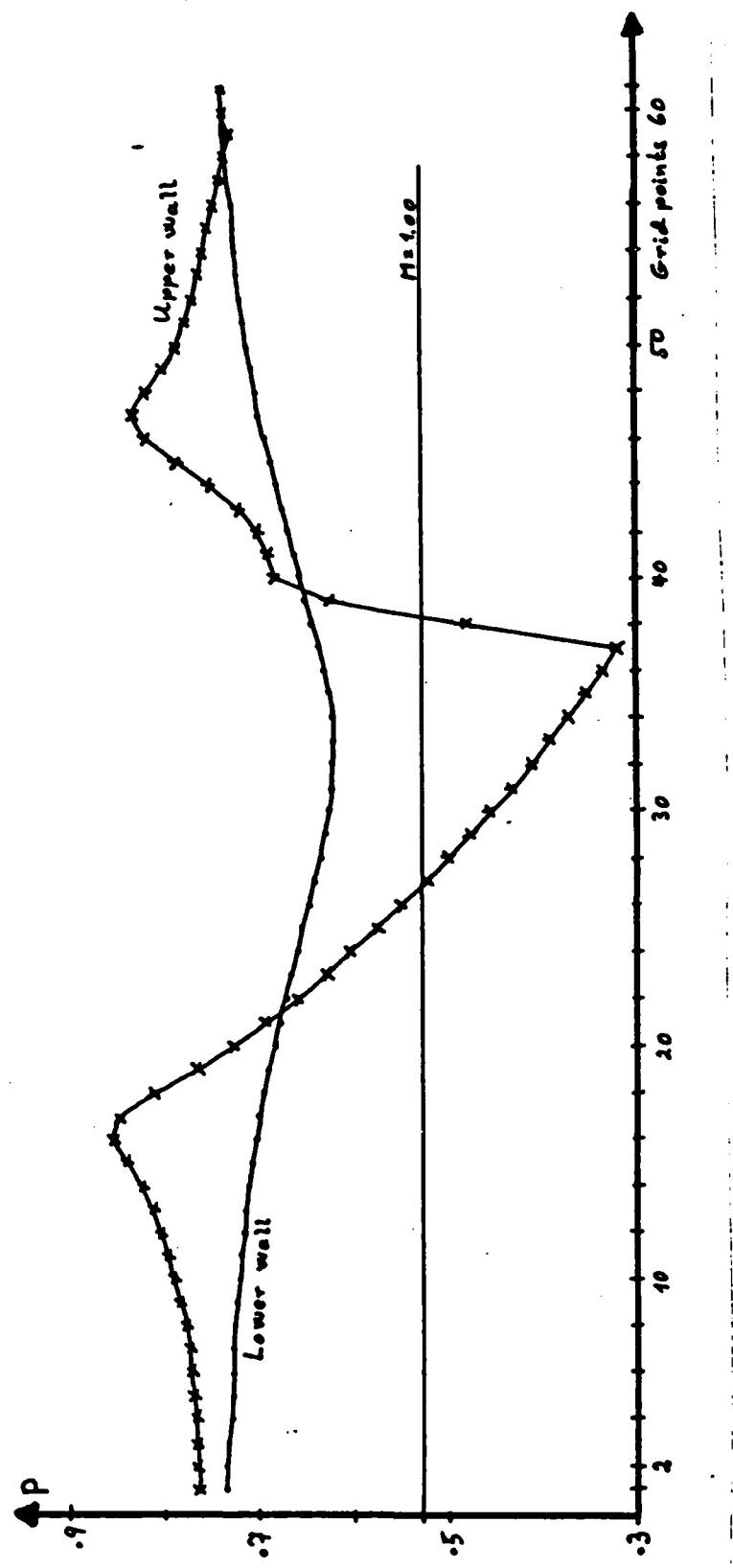


Fig. 4.6.2-2.a. Second two dimensional test problem: Pressure distribution $\frac{1}{2}$ cell from the wall (Grid 15x61).

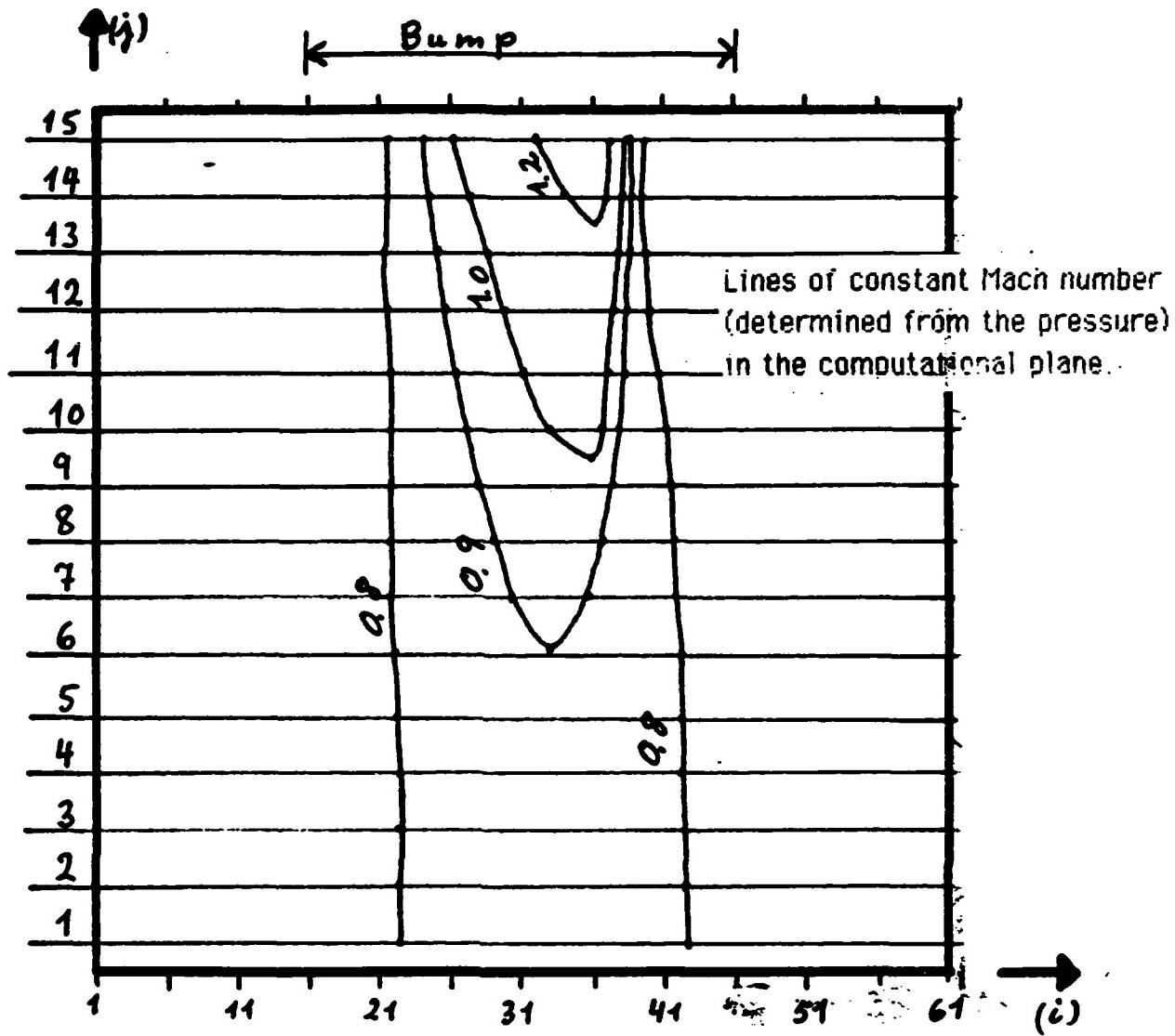
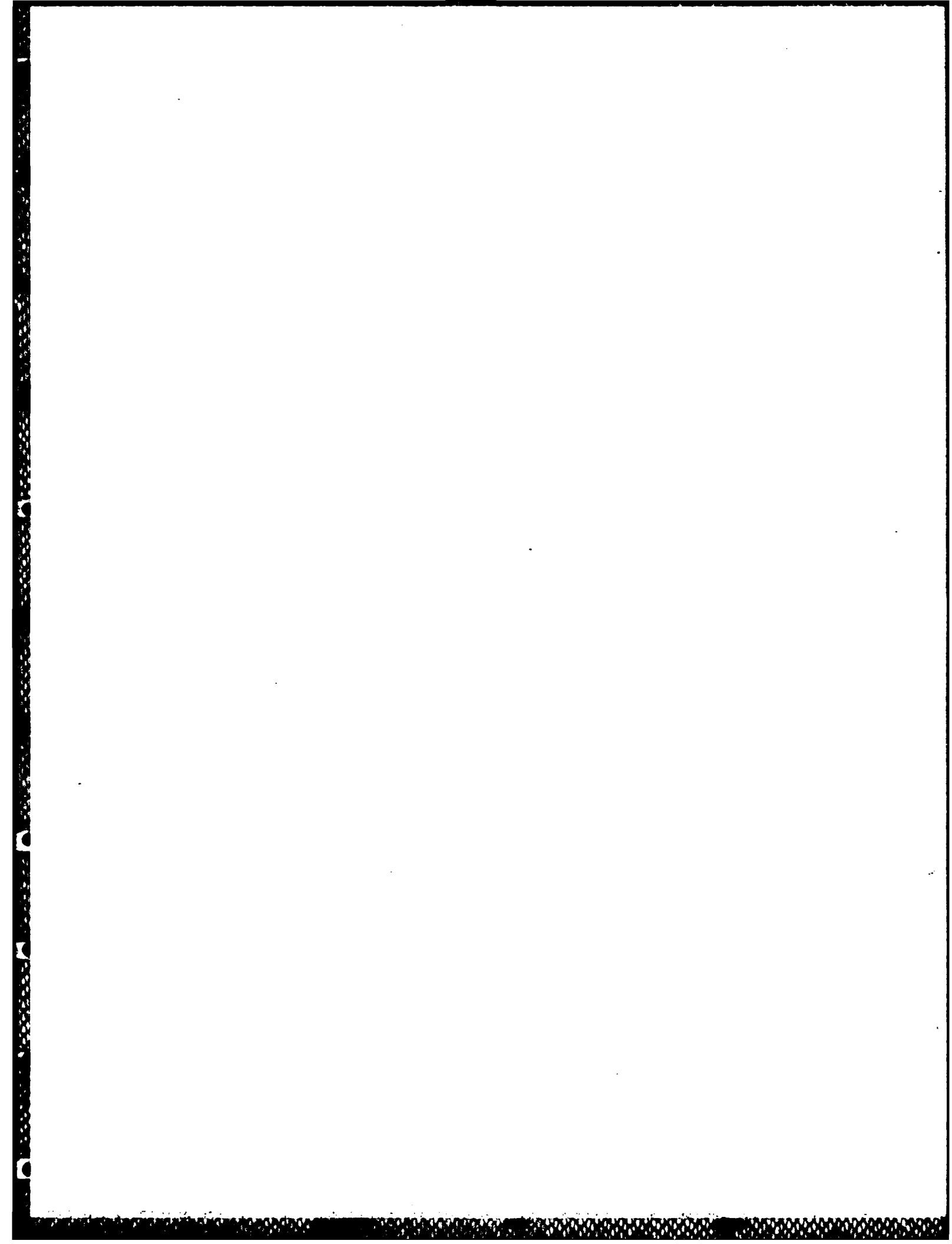


Fig. 4.6.2-2.b. Second two dimensional test problem: Lines of constant Mach number (Grid 15x61).



**Part II: Testing of the Methodology for
Unsteady Flows in Non-Moving Grids.**

5. One Dimensional Unsteady Test Problems and Computational Results.

Before going into the application of the unsteady flow in a moving cascade the algorithm should first be tested on unsteady flows in a fixed reference system. For these tests, two cases were chosen. The first (section 5.1) is the shock tube problem in order to determine if the shock speed as captured by the method corresponds to the exact solution, and how accurately the moving shock and expansion fans can be determined. The second (section 5.2), concerns the unsteady shock movement in a quasi one dimensional nozzle with oscillating back pressure.

It should be pointed out that all results presented in this section are based on the original flux vector splitting by Steger/Warming, with the spatial differencing performed according to the "MUSCL" approach (see sections 3 and 4 for details)

5.1. Shock Tube.

The shock tube chosen corresponds to the one employed in /13/. The ratio of the high pressure (left region in Fig. 5.1-1) and low pressure (right region) is 10. The diaphragm is situated at $x=0.95$ and bursted at time $t=0$. The solution of density at a time $t=1$ is given in Fig. 5.1-1. The following information can be drawn:

- The positions of the shock, contact discontinuity and expansion fan are accurately captured, which means that the speeds of these waves are correctly calculated.
- The expansion fan starts with an overshoot of approximately 4% and is smoothed out over approximately 15 points instead of 12 points for the exact solution.
- The contact discontinuity is completely smeared out and extends over 6 points.
- The shock is accurately captured with a slight undershoot before and after, and it extends over two elements only (one point in the shock region).
- The density in all four regions, separated by the different surfaces, is accurately predicted.

It can thus be concluded that the present methodology can predict the correct shock speed and density ratio in a shock tube problem.

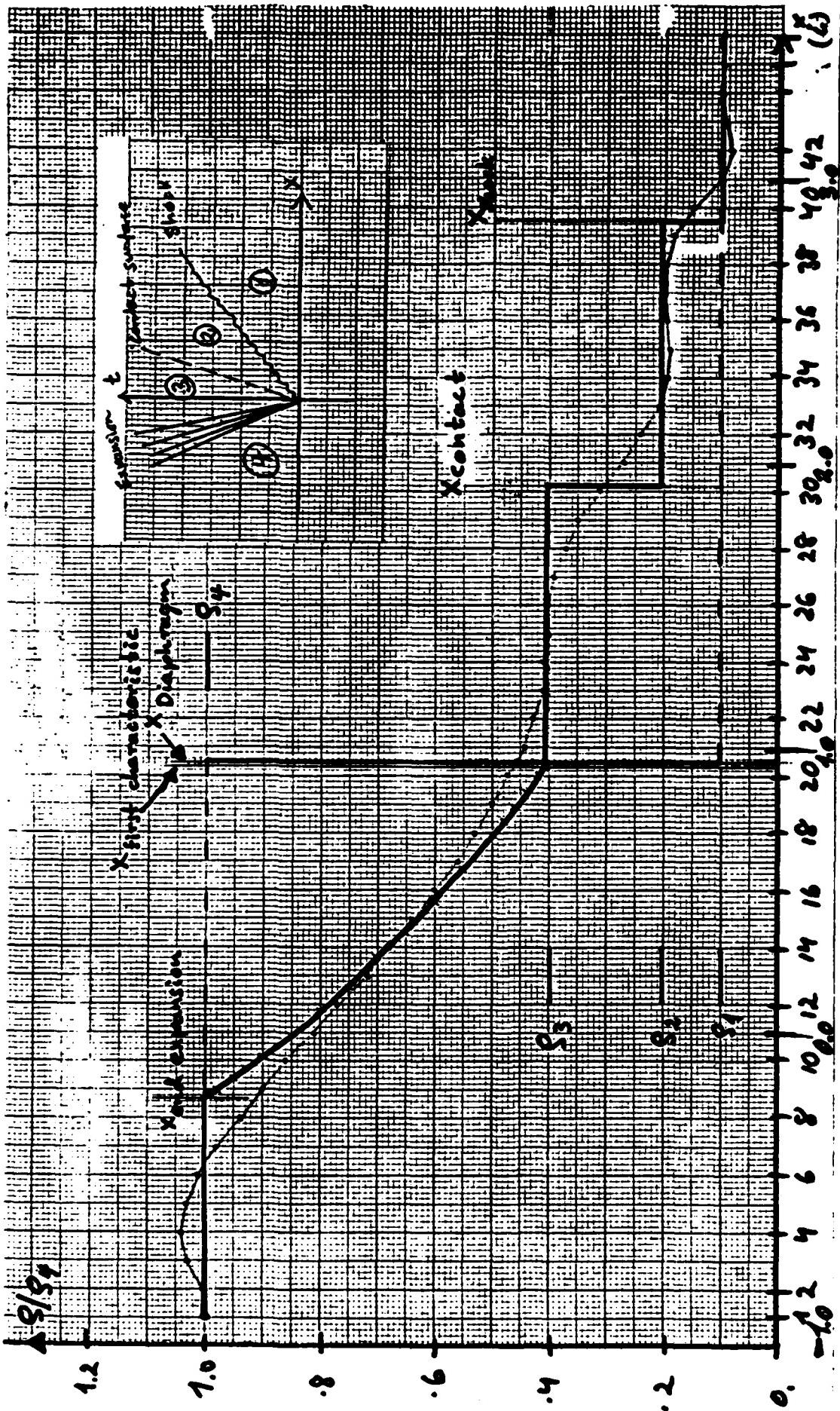


Fig. 5.1-1. Shock tube solution with second order spatial accuracy.
 Initial pressure ratio of 10, diaphragm situated at $x=0.95$.

Shock Tube

- Density before diaphragm is burst.
- Exact solution at time $t=1.0000$.
- Numerical solution at time $t=0.9954$.

5.2. Shock Oscillation Induced By Time Varying Back Pressure.

5.2.1. Validation of the Method

Adamson et al have developed analytical small perturbation theories to the problem of oscillated back pressure in transonic one and two dimensional nozzles /39-45/. Their results indicate that the unsteady shock oscillation amplitude, as well as the time-averaged shock position, depends not only on the steady-state (or average back pressure) but also on the amplitude of the oscillation and, largely, on the oscillation frequency (and, of course, the nozzle geometry). As these solutions are of an analytical nature, comparisons with the present, fully numerical, methodology is of interest.

The Adamson et al nozzles are prescribed by the following function of the area /44/:

$$A(x) = 1 + \epsilon^2 \cdot f(x)$$

where $f(x)$ is a function describing the wall shape and ϵ is a constant defining the small perturbation. In ref. /44/ the function $f(x)$ is defined as, with the entrance of the subsonic part of the nozzle situated at $x=-0.5$, the throat at $x=+0.5$ and the exit at $x=1.5$:

$$f(x) = \begin{cases} 3 & -0.5 \leq x \leq -1/6 \\ \{27[3(x-0.5)+2]^4 - 48[3(x-0.5)+2]^3\}/13+3 & -1/6 \leq x \leq 1/6 \\ 18[3(x-0.5)]^2/13 & 1/6 \leq x \leq 5/6 \\ \{27[3(x-0.5)-2]^4 + 48[3(x-0.5)-2]^3\}/13+3 & 5/6 \leq x \leq 7/6 \\ 3 & 7/6 \leq x \leq 1.5 \end{cases}$$

Furthermore, the unsteady flow is introduced by varying the back pressure according to

$$P = P_e + P_{e,amp} \sin(\omega(t-t_0))$$

with

$$\omega = \text{circular frequency of oscillation} = 2\pi/t_{\text{cycle}}$$

The first results presented compare the numerically computed shock position with the analytical location from ref. /44/, with the following (dimensionless) parameters:

$$\begin{aligned}\epsilon &= 0.1 \\ p_0 &= 0.626474 \\ p_{e,amp} &= 0.014032 \quad (\text{i.e. } p_{e,amp}/p_0 = 2.2\%) \\ t_{cycle} &= 18.2 \Rightarrow k = [\omega]_{l_r}/[2q_r] \\ &= [2\pi]/[2t_{cycle}] \cdot l_r/[t_r q_r] \\ &= [2\pi]/[2t_{cycle}] \\ &= 0.173\end{aligned}$$

(If the following reference values are employed:

$$\begin{aligned}T_r &= 300K \\ l_r &= \text{reference length} = 0.1 m \\ q_r &= \text{reference velocity} = \sqrt{RT} \approx 293 \text{ m/s} \\ t_r &= l_r/q_r \approx 3.41 \cdot 10^{-4} \text{ s}\end{aligned}$$

we find the physical values to be:

$$\begin{aligned}t_{cycle,physical} &= t_{cycle} \cdot t_r \approx 0.006207 \text{ s} \\ f &= 1/t_{cycle} \approx 161 \text{ Hz}\end{aligned}$$

Based on a reference length of $l_r = 1 \text{ m}$, the frequency would instead be $f = 16.1 \text{ Hz}$.)

In Fig. 5.2-1a the numerical (121 grid points) and exact steady state pressure distributions are given. As for the previous steady state solutions (section 3.5) the shock is captured sharply and accurately. If the position of the sonic line within the structure of the numerical shock is defined as the shock location (as pointed out in /43/ to be a reasonable assumption), it is concluded that the exact and numerical shock positions agree well.

As the backpressure then starts to oscillate (at a dimensionless time of $t \approx 41.1$, Fig. 5.2-1b), the shock will not react until the disturbances wave has travelled the distance from the outlet ($x = 1.5$) to the shock ($x = 1.00$). The shock then starts to react, in the beginning slowly, to the change in

pressure at an approximate time of $t \approx 44$ (Fig. 5.2-1c). As the pressure increases in the beginning of the cycle (Fig. 5.2-1b) the shock moves, as expected, upstream. It is seen that the shock position as determined by the numerical method agrees well with the analytical small perturbation from Adamson et al /44/, although the numerical solution displaces the average shock location slightly downstream ($\Delta x_s \approx 0.012$, corresponding to ≈ 0.7 mesh elements with the 121 grid points used).

Both methods illustrate the important factor that the average shock position of an unsteady shock does not have to be the steady state position. In the example presented in Fig. 5.2-1c the steady state and the averaged unsteady (based on the first cycle only) shock positions are as follows:

	Steady state shock position	Unsteady average shock position
Analytical ¹	1.000	0.960
Numerical	0.998	0.972

The corresponding Mach number distributions for different time levels during the first cycle are given in Fig. 5.2-1d. This figure illustrates the shock displacement in the channel. It is also seen that the flow upstream of the shock is not, as expected, influenced by the back pressure oscillations. Also in this figure it is clearly seen that the average shock location is not identical to the steady state position.

The reason for this is probably the variation in the flow velocity relative to the shock, as well as the phase lag between the post shock pressure change and the shock position, combined with the pressure fluctuation downstream of the shock. As the shock moves upstream in the sample case shown, the flow velocity relative to the shock increases (as for this sample case the shock velocity becomes larger than the change in the velocity upstream of the shock due to the area change (see ref. /44/ as well as the later discussion on shock velocity)). This increases the pressure jump over the shock, at the same time as the disturbance wave train from the exit introduces a compression in the post shock flow field,

¹ Please note that it is not entirely clear from ref. /44/ if the analytical solution was performed over several cycles or if it was stopped when the pressure returned to the steady state value.

slightly (as the change in nozzle area is small) counteracted by an expansion due to the increase in the nozzle section up to $x=7/6$ (Fig. 5.2-1d,e).

After the shock has reached its minimum position ($x_{s,\min} \approx 0.930$), it starts to move downstream again. At a certain time it passes again over its unsteady average location ($x_{s,\text{unsteady average}} \approx 0.972$, see Fig. 5.2-1c). In this position the shock has reached its maximum speed going downstream, wherefore the flow velocity relative to the shock has its minimum value. Simultaneously, the disturbance wave train from the nozzle exit introduces an expansion downstream of the shock. The pressure jump at the shock is thus smaller than the jump when the shock moved upstream (Fig. 5.2-1e).

With these two phenomena acting together (in different ways, depending on the nozzle geometry, pressure amplitude and frequency) it is not to be expected that the average of the unsteady shock position should coincide with the steady state shock location.

If the numerical calculation is continued over several periods it is seen that a periodic shock movement is found after approximatively two cycles (Fig. 5.2-1f).

For a lower frequency of the imposed exit pressure oscillation, but with the same amplitude as previous ($f=32\text{Hz}$, $k=0.035$ based on, as before, $i_r=0.1\text{m}$), the shock movement increases drastically (compare Figs. 5.2-1f and 5.2-2a). This can be explained by the fact that, for high reduced frequencies, the shock has not got time to fully react to the disturbances (for example a compression wave), before there is another disturbance (for example an expansion wave) counteracting the effect of the first one. As in the previous sample case, it is determined that the unsteady flow is practically periodic after two cycles. Furthermore, the unsteady average value of the shock position has again changed, and the following values are obtained:

	Average shock position (numerical, based on first cycle)	$\Delta x_s =$ $x_{s,\text{unsteady}} - x_{s,\text{steady}}$
Steady state	0.998	-
$k=0.035$	1.013	0.015
$k=0.173$	0.972	-0.026

The increase in shock movement can also be seen by studying the Mach number distribution along the nozzle at the steady state, maximum and minimum positions for the first cycle for the two sample cases (Figs. 5.2-1d, 5.2-2b). In the low reduced frequency case the maximum shock position extends well into the part of the nozzle where the area is constant ($x \approx 7/6$). The minimum and maximum Mach numbers are approximatively 1.11 and 1.20 resp., compared to the steady state value of 1.18, and the shock moves over approximatively 36% of the nozzle distance downstream of the throat, compared to 8% for the higher reduced frequency.

In both cases the imposed pressure oscillation is 2.2%.

Also for the lower reduced frequency the unsteady shock position, as calculated with the flux vector splitting method, agrees well with analytical results from Adamson and Liou /44/ (see Fig. 5.2-2c).

As a final validation, and before applying the flux vector splitting method to a few different one dimensional sample cases, the shock **velocity** is compared with the analytical results in /44/. It should here be noted that the numerically determined shock velocity is the time derivative, calculated as a centered difference, of the shock location, i.e.

$$u_s = \Delta x_s / \Delta t$$

Furthermore, x_s is an interpolated value, given by the position of the sonic line within the numerical shock. It is thus not expected that the numerical shock velocity should be uniform, but rather that its fundamental frequency should coincide with the analytical shock velocity from /44/.

This comparison is made in Figs. 5.2-3a,b for $k=0.173$ and $k=0.035$, respectively. In both figures the curve from Adamson and Liou /44/ agrees well with the average of the numerical results. However, the bandwidth of the numerical solution is considerable, which can be explained, in a physical manner considering the numerical scheme, by looking at Fig. 5.3-2a.

It must be recognized that, although the numerical shock is fairly sharp, it still consists of a few intermediate grid points. The disturbances moving upstream from the exit will, as they approach the two or three

grid points immediately downstream of the shock position x_s (which is, we repeat, determined as the position of the sonic line within the numerical shock structure), find a higher flow velocity (see steady state solution, Fig. 5.2-1a). The speed of propagation of the disturbance signals ($=u-a$) will thus slow down. As the last point upstream of the shock starts to be influenced, the shock velocity rapidly increases (at $t \approx 44.1$), until $t \approx 45.7$. At $t \approx 46.4$ the Mach number in grid point $I=90$ passes from supersonic to subsonic. The pressure in grid point $I=89$ starts then to build up (with an initial low shock velocity) until, at $t \approx 47.9$, the Mach number in this grid point becomes subsonic. At this time, the flow in grid point $I=88$ starts to be influenced, etc. A close look on the shock position curve in Fig. 5.2-1c reveals also this jump every time the Mach number passes the sonic value in a grid point.

The shock velocity traces at the lower reduced frequency ($k=0.035$, Fig. 5.2-3b) does not show an identical behaviour. However, this is just due to the fact that only each 100th time step was used to compute the shock velocity (and also the shock position in Fig. 5.2-2a).

Another important aspect of the oscillating shock is when it reacts as regards to the imposed pressure fluctuation. It has been shown analytically (for small perturbation pressure) by Adamson and Liou /44/ that the two sample cases presented previously corresponds to two different classes of solutions:

- The first corresponds to a case when the disturbance wave from the exit reaches the shock in a time comparable to the time the imposed pressure performs a cycle.
- The second corresponds to the case when the period of the imposed pressure is much longer than the time it takes for the disturbance wave to reach the shock².

Each of these two classes has a different analytical solution (see for ex. ref. /44/, p.25), with the implication that, for the first solution (i.e. $t_{cycle}/t_{sh} \approx 0(1)$), the shock **velocity** is essentially in phase (apart from the time lag t_{sh}) with the imposed pressure fluctuation, whereas for the

² In the first sample case the time for the disturbance wave to reach the shock is approximatively $t_{sh} \approx 43.4 - 41.1 \approx 2.3$ (see Fig. 5.2-1.c) and the period $t_{cycle} \approx 18.2$, i.e. $t_{cycle}/t_{sh} \approx 8$. In the second sample case, t_{sh} is still the same, whereas $t_{cycle} \approx 91$. Thus, $t_{cycle}/t_{sh} \approx 40$.

second solution (i.e. $t_{cycle}/t_{sh} \gg 1$) the phase lag depends upon other terms, such as the nozzle geometry and average exit pressure.

This implies that, for the case presented in Fig. 5.2-1, the shock position³ should be displaced as regards to the pressure fluctuation at the outlet approximatively $\Delta t \approx t_{cycle}/4 + t_{sh} \approx 7$. As the maximum pressure ($p_{e,max}$) appears at $t_{pe,max} \approx 45.7$ (Fig. 5.2-1b), the minimum shock position should be reached at $t_{min.shock} \approx t_{pe,max} + \Delta t \approx 52.7$. This is the case (obviously for the analytical solution, but also for the numerical), as can be seen from Fig. 5.2-1c.

However, as explained in /44/, for the second sample case (Fig. 5.2-2) another phase lag should, and does indeed, exist. The analytical solution by Adamson and Liou (ref. /44/, p.29) shows that the shock velocity for low reduced frequencies ($t_{cycle}/t_{sh} \gg 1$) does not respond instantaneously to a pressure disturbance, although the signals from the imposed pressure fluctuation at the exit reaches the shock "instantaneously" (as t_{sh} now is very small compared to our time scale of interest, i.e. the period of oscillation). This is due to some terms in the small perturbation analysis, which are dependent on the nozzle form, pressure amplitude and frequency, etc. /44/. It is important to note that the numerical solution accurately predicts this phase lag, together with the amplitude of the shock oscillation (Fig. 5.2-2.c).

³ Note: $p \approx \sin(t) \Rightarrow u_s \approx \sin(t) \Rightarrow x_s \approx \cos(t)$ for this case.

RUN NUMBER = 90

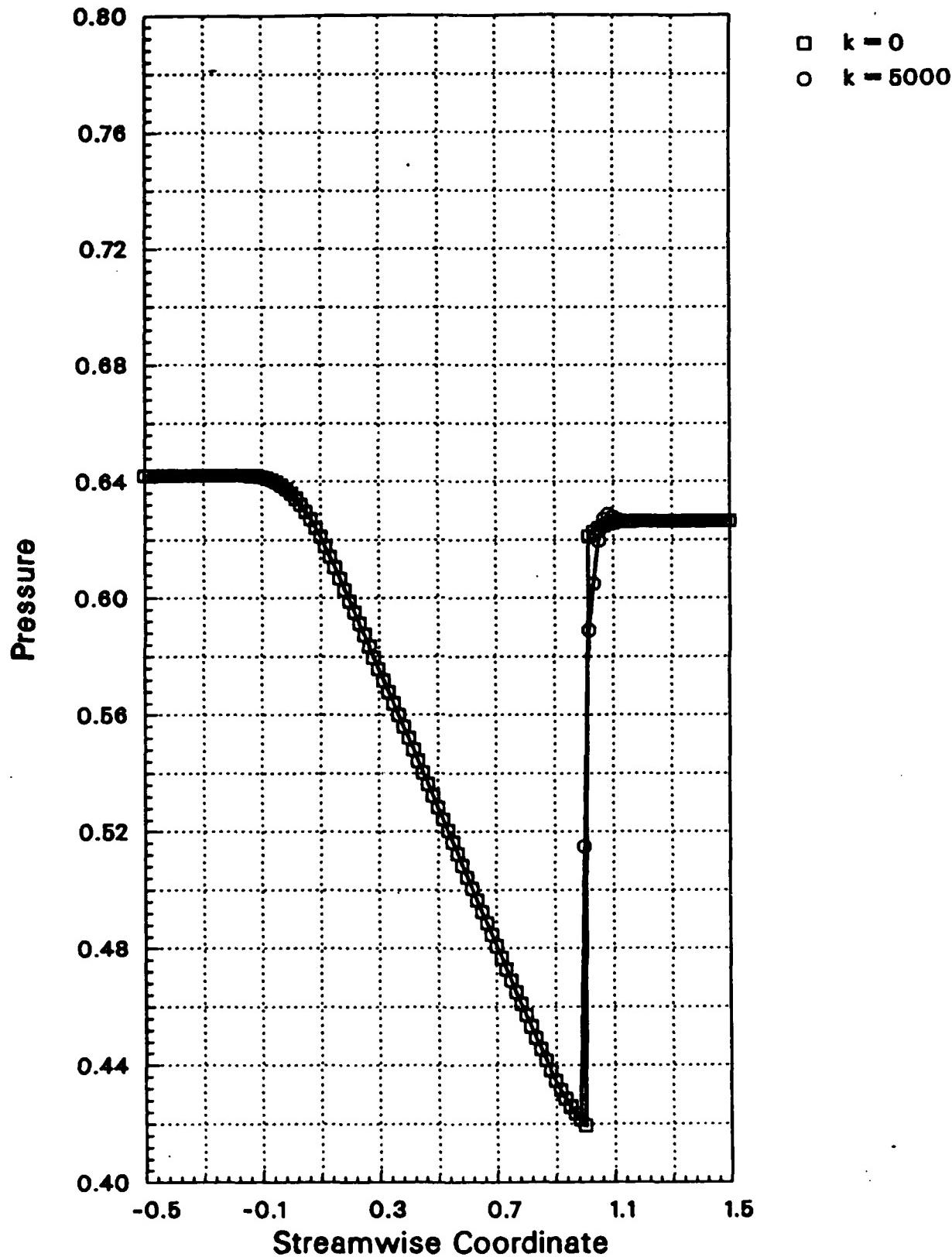
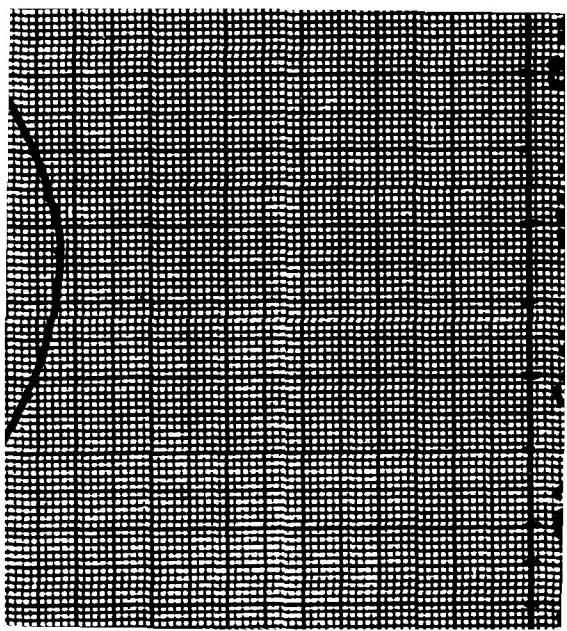


Fig. 5.2-1a. Comparison of exact and numerically computed steady state solution for Adamson's /44/ first sample case. $k=0.173$, $P_{e,amp}=0.0140$ (Grid: 121 points).



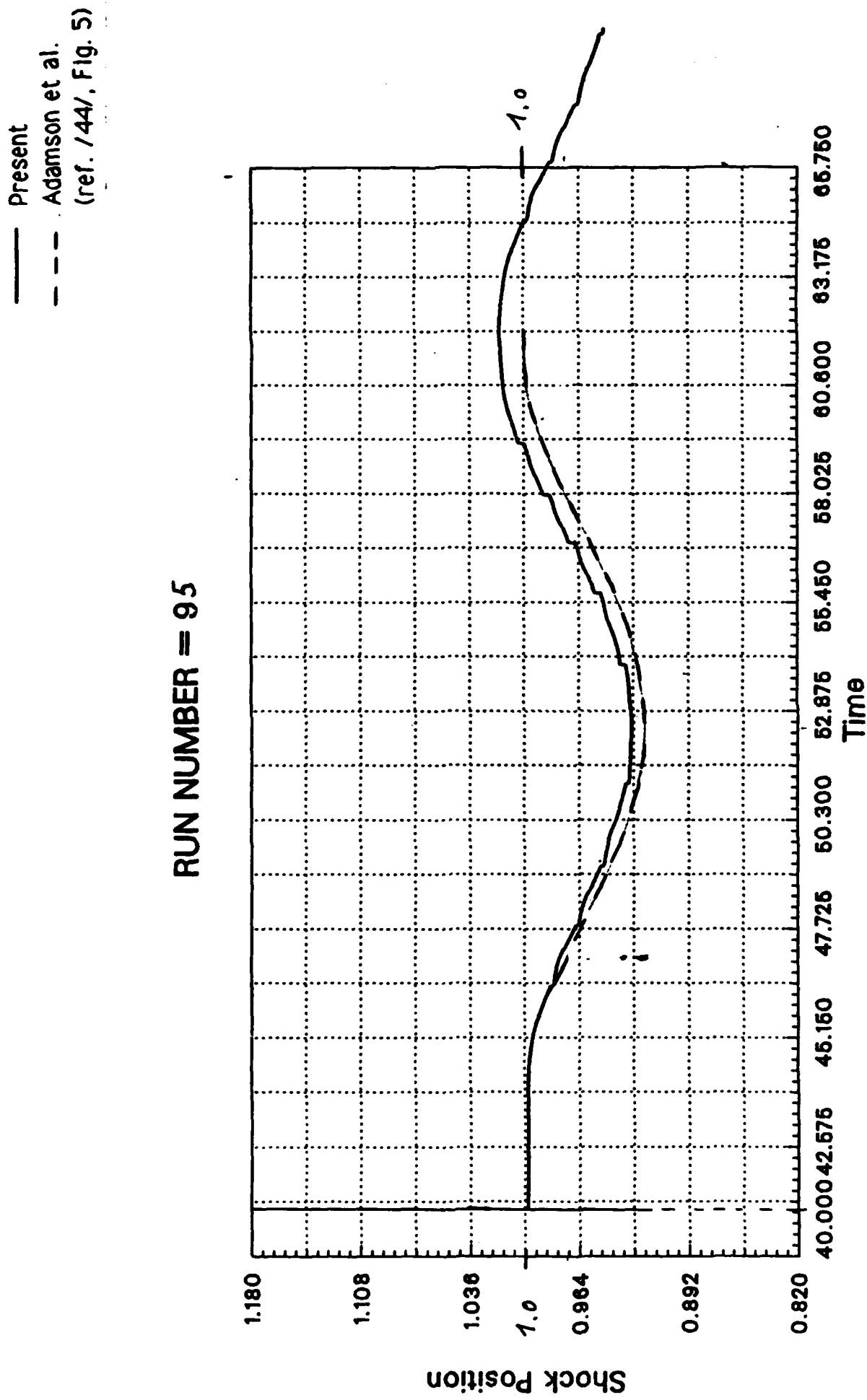


Fig. 5.2-1c. Computed displacement of shock position in time for Adamson's /44/ first sample case. $k=0.173$, $\rho_{e,amp}=0.0140$.

RUN NUMBER = 95

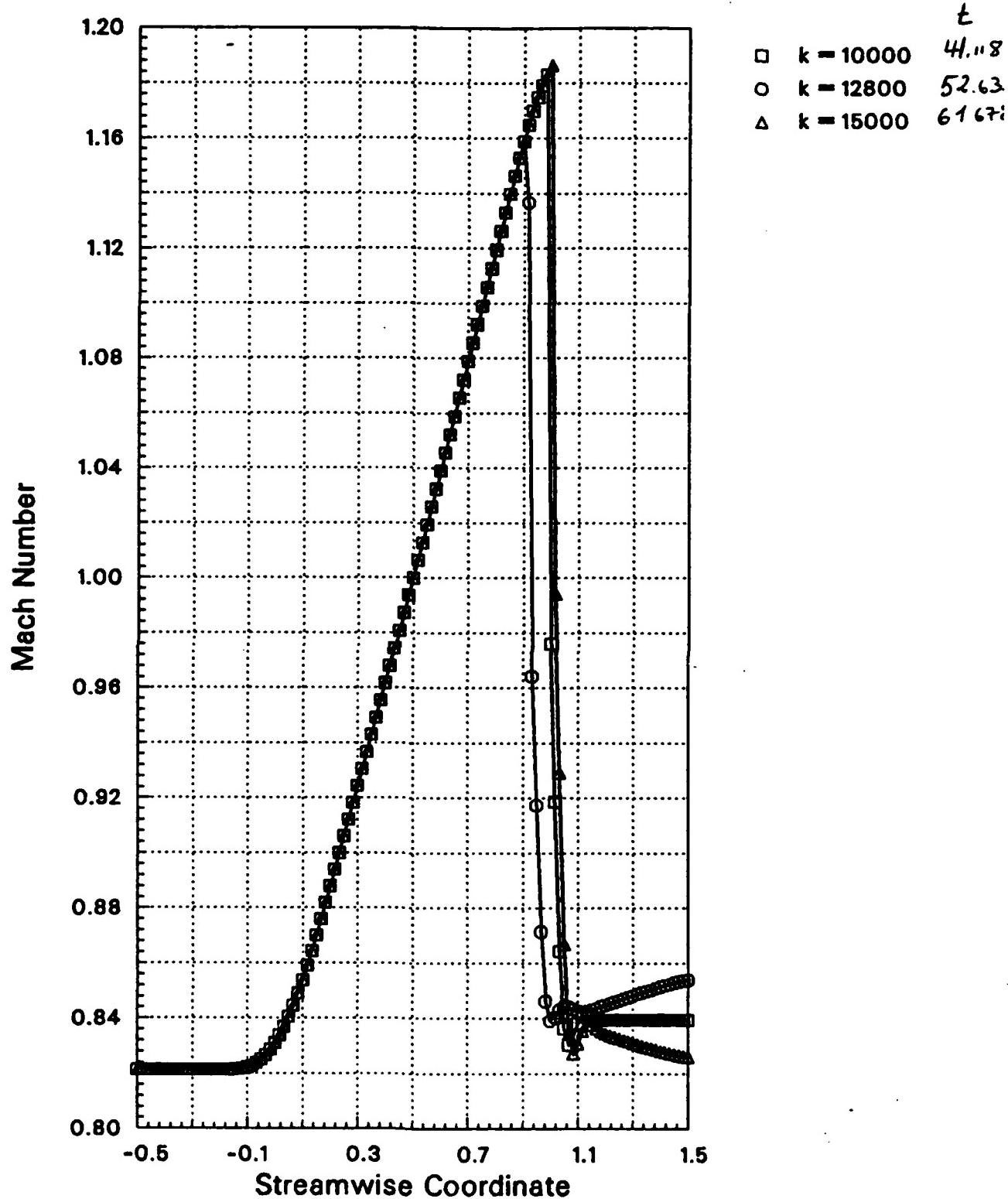


Fig. 5.2-1d. Mach number distribution for steady state (at $t=41.118$) as well as approximate minimum (at $t=52.632$) and maximum (at $t=61.678$) unsteady shock positions during the first cycle. Adamson's /44/ first sample case. $k=0.173$, $D_{e,amp}=0.0140$.

RUN NUMBER = 97-1

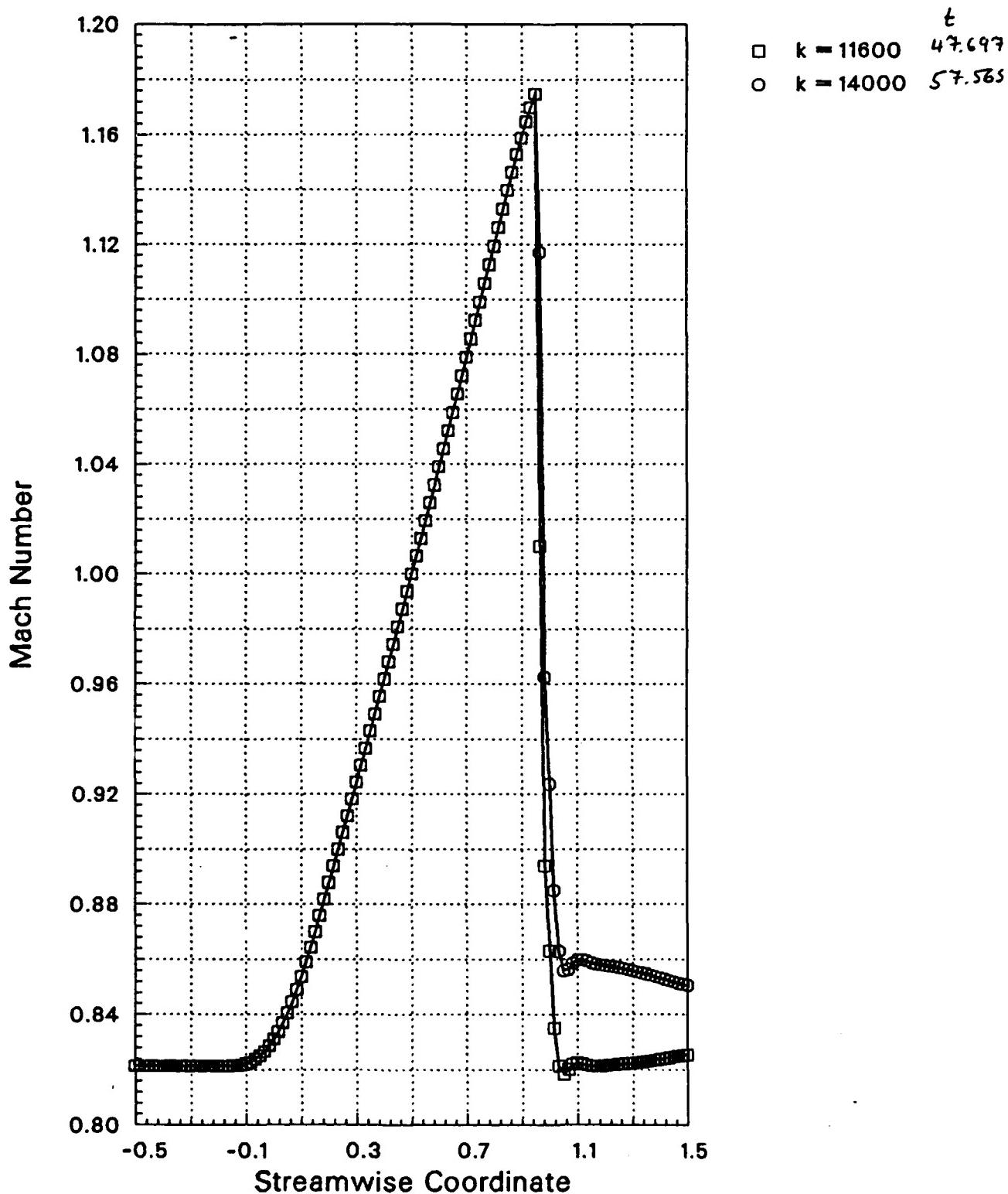


Fig. 5.2-1e. Mach number distribution for approximate unsteady average shock positions during the first cycle ($x_{s,\text{unsteady,average}} \approx 0.972$). Adamson's /44/ first sample case. $k=0.173$, $\rho_{\text{e,amp}}=0.0140$.

RUN NUMBER = 95 + $q_3/1 + q_4/2$

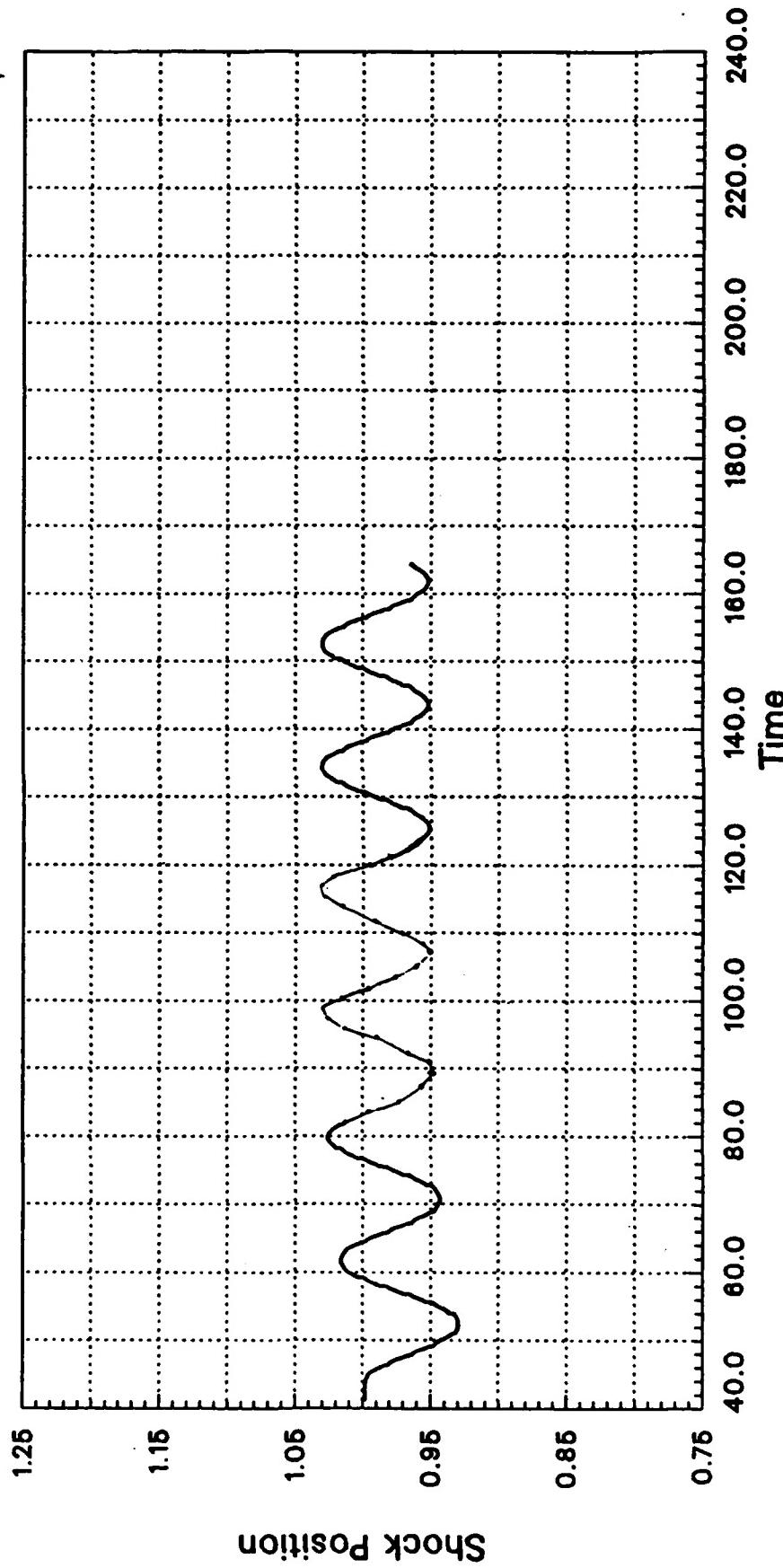


Fig. 5.2-1f. Computed displacement of shock position in time, over 6 periods, for Adamson's /44/ first sample case. $k=0.173$, $P_{e,amp}=0.0140$.

5.2.2 Numerical Results.

As seen from the two comparisons with ref. /44/ the shock may move considerably, even if the imposed pressure fluctuation at the exit is relatively small. In such a case, for a given nozzle geometry, the shock movement and, in some cases as will be seen later, the flow throughout the entire nozzle depends on the reduced frequency of the prescribed disturbance. In the following we will, for the same nozzle geometry as previously, investigate the flow field throughout the channel for a higher back pressure fluctuation in three sample cases:

Sample $p_e[-]$ case	$p_{e,amp} [-]$	$p_{e,amp}/p_e$ [%]	$k [-]$	$f [Hz]$ (with $l_r=1m$)	Fig.
3	0.6265	0.05	8.0	0.318	30
4	"	0.10	16.0	"	30
5	"	0.05	8.0	0.106	10

Sample Case 3:

As previous, the imposed pressure fluctuation is sinusoidal, with an initial increase at $t=t_0$ (Fig. 5.2-4.1). The pressure fluctuation is such that if a steady state pressure was kept at the maximum exit pressure, the flow would have been subsonic in the whole nozzle.

The change in pressure distribution in the nozzle throughout the oscillation is shown in the sequence of Figs. 5.2-4.2 to 5.2-4.32, with 12 plots per period of oscillation. Initially the imposed fluctuation at the exit travels upstream (Fig. 5.2-4.3). The pressure downstream of the shock is thus modified, essentially according to the imposed pressure oscillation (since the nozzle has a constant cross section for $x \geq 7/6$). At the approximate time $t \approx \pi/2$ (where the time has been referenced to the start of the pressure oscillation for easier identification), the wave train has reached the shock (Fig. 5.2-4.5) and has influenced all the post shock computational points (as well as the first supersonic point, which is situated within the numerical shock structure). At the next time level presented ($t=4\pi/6$) the post shock pressure has increased as the wave

train has propagated upstream (Fig. 5.2-4.6). The shock has started to move slightly upstream. At $t \approx 5\pi/6$ the pressure just downstream of the shock has reached its maximum level (Fig. 5.2-4.7), whereafter the expansion part of the wave train decreases this value. The shock is now displaced faster upstream, although the post shock pressure is now decreasing according to the imposed wave train.

The shock reaches its minimum location at $t \approx 10\pi/6$ (Fig. 5.2-4.12), whereafter it starts to move downstream. At $t \approx (15-16)\pi/6$ it has again reached its steady state position (Figs. 5.2-4.17 and 5.2-4.18), which approximatively, for this sample case, corresponds to the maximum shock position for the first cycle.

The procedure is then repeated, although with some slight differences in the time, shock location and pressure level as the flow adapts itself to the periodic pressure fluctuation at the outlet (these plots are not shown in the sequence of figures). Then, after about two full cycles, the flow is periodic. Such a periodic cycle is shown in the sequence of Figs. 5.2-4.20 to 5.2-4.32. The minimum shock position (Fig. 5.2-4.23,24) is reached at $t \approx 33.5\pi/6$ (which corresponds to a time lag towards the exit pressure of $\Delta t \approx 0.8 \cdot t_{cycle}$) and the maximum (Figs. 5.2-4.29,30) at $t \approx 39.5\pi/6$ (time lag towards exit pressure $\Delta t \approx 0.3 \cdot t_{cycle}$).

As this sample case falls into the cathegory $t_{cycle}/t_{sh} \approx 0(1)$ according to the classification in section 5.2.1, we would expect the minimum shock position to appear at

$$\begin{aligned} t &= [\text{time for disturbances to travel from the exit to the shock}] \\ &\quad + [\pi/2 \text{ phase lag of shock position towards post shock pressure}] \\ &\quad + [\text{time for exit pressure to reach its maximum level}] \\ &\approx \pi/2 + \pi/2 + \pi/2 = 0.75 \cdot 2\pi = 0.75 \cdot t_{cycle} \end{aligned}$$

and the maximum at 1/2 period later, i.e. at $t \approx 0.25 \cdot t_{cycle}$. It is seen that both of these values agree well with the numerically determined results. Again it should be pointed out that the fully developed periodic solution has a maximum shock position $x_{s,max} \approx 0.92$ and a minimum $x_{s,min} \approx 0.83$, compared to the steady state solution of $x_{s,steady} = 1.00$.

It is also interesting to note that although the maximum pressure is such that it would have given subsonic flow throughout the nozzle in steady state, the shock still stays well behind the throat ($x_{throat} = 0.50$) during

the whole period. This is clearly a fact because the fluctuation frequency is in the same order of magnitude as the time t_{sh} .

Furthermore, as showed in section 5.2.1, although the shock is in the same position twice during its oscillation, the pressure distributions at these times are not the same. This is again illustrated by the average shock position. At time $t=31\pi/6$ (Fig. 5.2-4.21) the shock is moving forward and at $t=37\pi/6$ (1/2 period later, Fig. 5.2-4.27) it is moving downstream. The shock location is approximatively the same, but the unsteady lift and moment introduced downstream of the shock are very different.

Most of the difference in the pressure jump across the shock can, in this sample case, be attributed to the shape of the imposed wave train, and some to the change in relative shock velocity (see section 5.2.1).

Sample Case 4.

If the pressure amplitude is increased from $p_{e,amp}=0.05$ to $p_{e,amp}=0.10$, with all the other parameters the same, the resulting flow through the nozzle will be completely different. We will here only discuss the periodic result, beginning at the time $t=5\pi$ after the imposed pressure fluctuation at the exit started (Fig. 5.2-5.1). At this time, the exit pressure is decreasing and has its average level. The shock is situated at $x_s \approx 0.83$ at an intermediate location (Fig. 5.2-5.3) for the geometry under consideration. As in the previous sample case, the steady state shock position is $x_{s,steady}=1.00$.

As the exit pressure decreases further, the shock moves upstream (Figs. 5.2-5.4,5) and the pressure jump across the shock decreases. The exit pressure reaches its minimum value at $t=11\pi/2$, but the post shock pressure continues to decrease because of the time lag between the exit and post shock pressures, counteracted by the increase in pressure jump as the shock moves upstream, i.e. the relative velocity the shock sees is larger than in a steady state case (Fig. 5.2-5.6). The pressure just downstream of the shock does therefore not decrease as much as would be expected from the expansion only. This can be the explanation for the local peak in post shock pressure. It is also probable that the plateau at point "3" in the figures is the plateau of maximum exit pressure that has now been transported to be located just downstream of the shock.

Simultaneously, the shock has moved close to the throat and the flow is barely supersonic upstream of it. However, the pressure jump is still considerable. Thereafter the pressure at the exit increases again, and a compression -wave moves upstream from the exit (Figs. 5.2-5.7,8,9) Simultaneously, the shock has now moved upstream of the throat and it is slowly weakened by the decrease in flow velocity upstream of it (as the area changes the relative shock velocity will become subsonic), as well as by the fact that the post shock pressure is still decreasing (due to the finite time it takes for the disturbances from the exit to propagate upstream). It is also smoothed out towards a compression wave (see later discussion). Between the shock and the last compression wave at the exit the pressure distribution indicates a complicated mixture of compression and expansion waves. The flow immediately downstream of the shock builds now up the velocity on its way to expand towards the steady state solution, which it would eventually reach if the exit pressure was now to be kept constant at the average value (=level of Fig. 5.2-5.9).

Downstream of this a small compression and another expansion lies before the large compression wave at the outlet. A part of this consists of the upstream moving signals being reflected at the shock, a part by the phase lag between the response of the shock to the post shock pressure changes, and a part can be attributed to the increase in pressure jump over the upstream moving unsteady shock.

As the time increases (Figs. 5.2-5.10,11,12), the upstream moving unsteady shock wave (by now so smoothed out that it can be considered as a compression wave instead) approaches the inlet and the flow behind it builds up towards choking. Downstream of this build up, a small compression wave is forced to steepen, probably because of the main expansion build up and the compression build up at the exit. The final compression steepens fairly soon into a shock wherefore, at $t=39\pi/5$, three small shocks can be found at three different locations in the nozzle. A further increase in time pushes the first shock out through the inlet (Figs. 5.2-5.13,14,15), without any noticeable reflection. Simultaneously, the main expansion is built up and the two last shocks merge into one large instead. In this procedure it appears that the first of those is moving downstream (pushed by the main expansion build up) and the second is moving upstream (pushed by the imposed pressure at the outlet). Although the pressure distribution is now fairly like the steady state solution, the flow is still not sonic at the throat. The blockage appears

somewhat later, at $t=44\pi/6$, just before the shock is again pushed upstream of the throat due to the next period of the pressure variation. As the flow is now periodic, the same resulting pressure distributions will repeat themselves.

In the present sample case it is hard to define an "average shock position", but it is still of interest to compare two times during the cycle. As the reduced frequency is the same as in sample case 3, the pressure distributions at $t=31\pi/6$ (Fig. 5.2-5.4) and $t=37\pi/6$ (Fig. 5.2-5.10) are compared. It should again be stated that these two positions do not correspond to the average unsteady exit pressure.

The two pressure distributions look very different, which again (compare the third sample case) give unsteady lifts and moments quite different from the steady-state values.

It should also be pointed out that, although the supersonic shocks are sharply captured¹, the unsteady shocks in the subsonic flow are spread out a bit more. Two reasons, one physical and one numerical, may be given. Firstly, as the shock travels upstream the relative shock velocity may eventually become subsonic. The decrease in Mach number then will counteract the shock. The unsteady upstream moving expansion wave downstream of the shock (introduced by the shock moving into a section with increasing area) will catch up with the shock, and it will start to spread out. Secondly, it is probable that, as the pre-shock Mach number is subsonic, the numerical dissipation associated with a supersonic shock does not manifest itself. A more sophisticated flux limiter, based on the gradients instead of just the present crude way of determining the passage over the sonic line, would certainly improve the subsonic shock structure. It is also possible that the van Leer flux vector splitting approach may improve the accuracy.

Sample Case 5.

Obviously, it is also possible to drive the shock from its steady state position into the subsonic part of the nozzle while keeping the exit pressure fluctuation amplitude at $p_{e,amp}=0.05$, as in the third sample case.

¹ Indications in ref. /49,50/ are that the unsteady shocks may be captured even more sharply with the van Leer splitting and some more sophisticated flux limiter.

This can be done by reducing the frequency of the oscillation. Here we will show the first cycle of a case with a three times slower fluctuation (Fig. 5.2-6.) than previously ($k=0.106$ and $k=0.318$ resp.). Out of the sequence four time levels are shown ($t=0$, $t=[17/36]\cdot 2\pi$, $t=[26/36]\cdot 2\pi$, $t=[29/36]\cdot 2\pi$).

As for sample case 4 the change in exit pressure drives the shock upstream. An important difference towards the previous two cases is though that the post shock pressure distribution is now much flatter (at the frequency is lower), see Figs. 5.2-C.2,3. There is thus no second shock being built up before the first has dissapeared through the inlet due to the compression wave from the exit. However, as for the previous sample case, it is seen that the flow builds up to become supersonic before it is choked /Fig. 5.2-6.3).

The flow becomes sonic at the throat (Fig. 5.2-6.4) and the shock appears as a combination of this build up and the compression from the exit of the nozzle. The fact that the flow becomes supersonic again before it is choked is also noted by looking at the shock position (where x_s is, as before, defined as the value where the Mach number within the numerical shock structure is 1) in Fig. 5.2-6.5. It is concluded that the shock is driven forward until it is completely subsonic (at $t \approx 35$). This appears at the throat. Thereafter it is not possible to compute a shock location according to the definition that $M_s=1.00$, until the flow once again becomes supersonic. This happens at $t \approx 41.6$ (compare Fig. 5.2-6.3), before the flow is choked and slightly before the compression wave has built up to a shock. Note that $M_s=1$. first appears at $x_s \approx 0.72$ (compare Figs. 5.2-6.3,5), i.e. well ($\Delta x \approx 0.22$) downstream of the throat.

As the exit pressure amplitude is larger in sample case 4 than in 3 and 5, the shock moves faster in this case. For the two cases with identical fluctuation amplitude the average shock speed is approximatively the same (slightly larger for the highest frequency). This can be expected from the fact that the shock velocity in a shock tube increases with increasing pressure ratio.

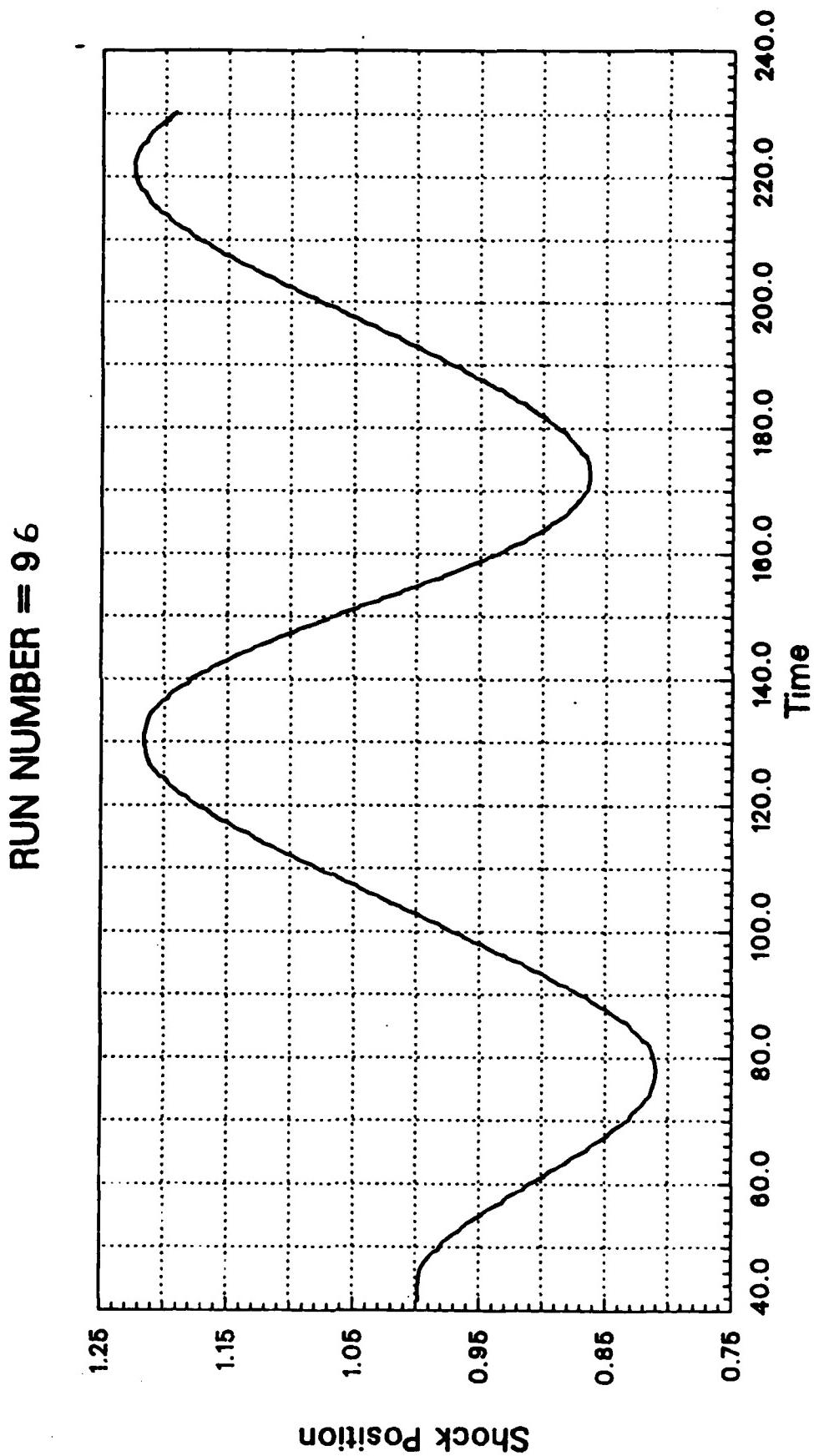


Fig. 5.2-2a. Computed displacement of shock position in time for Adamson /44/ second sample case. $k=0.035$, $\rho_{e,0}=\rho_0=0.0140$.

RUN NUMBER = 96

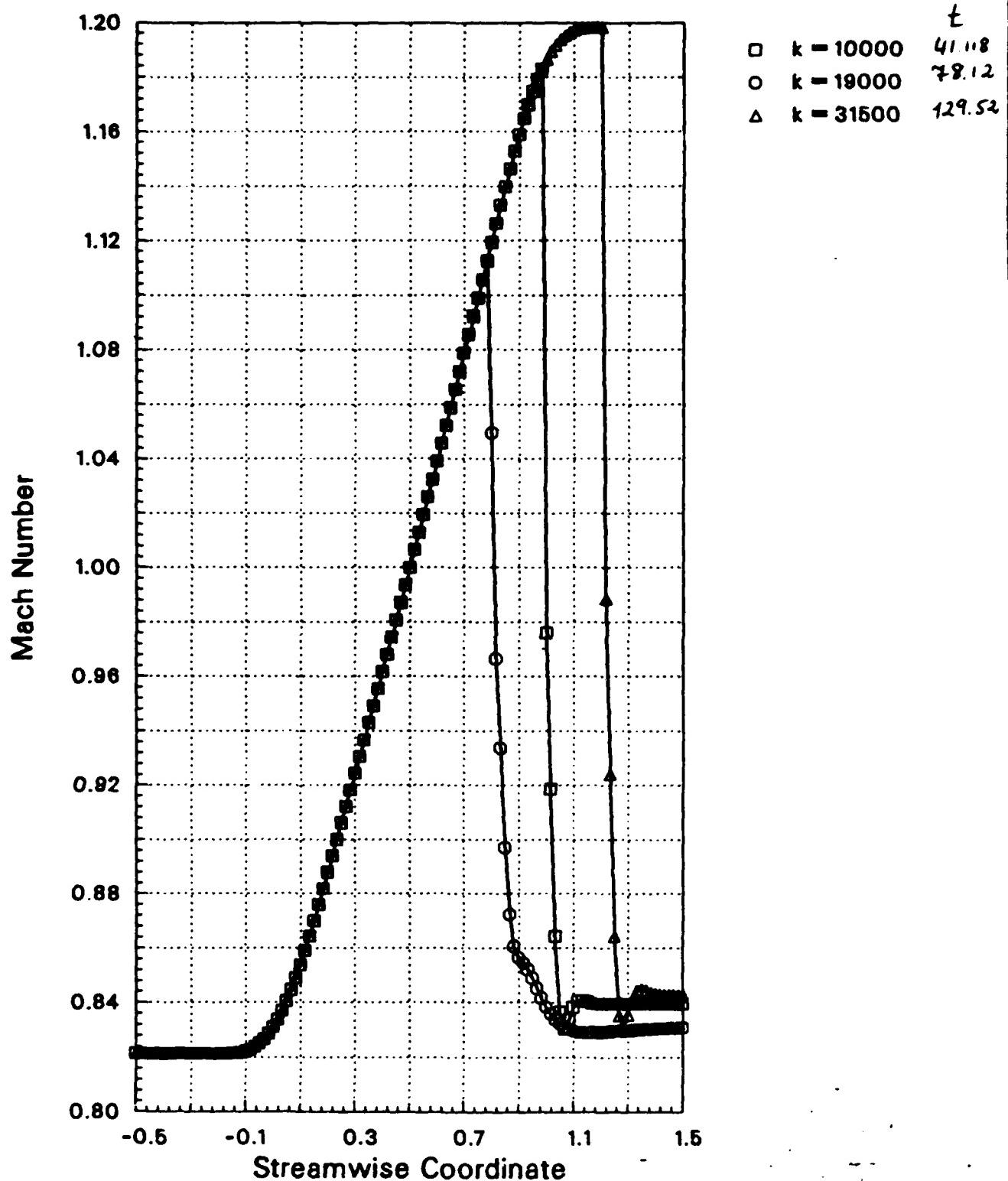


Fig. 5.2-2b. Mach number distribution for steady state (at $t=41.118$, $x_s=0.998$) as well as approximate minimum (at $t=78.12$, $x_s=0.810$) and maximum (at $t=129.52$, $x_s=1.215$) unsteady shock positions during the first cycle. Adamson's /44/ second sample case. $k=0.035$, $p_{e,amp}=0.0140$.

RUN NUMBER = 96

Present
 Adamson et al.
 (ref. /44/, Fig. 7)

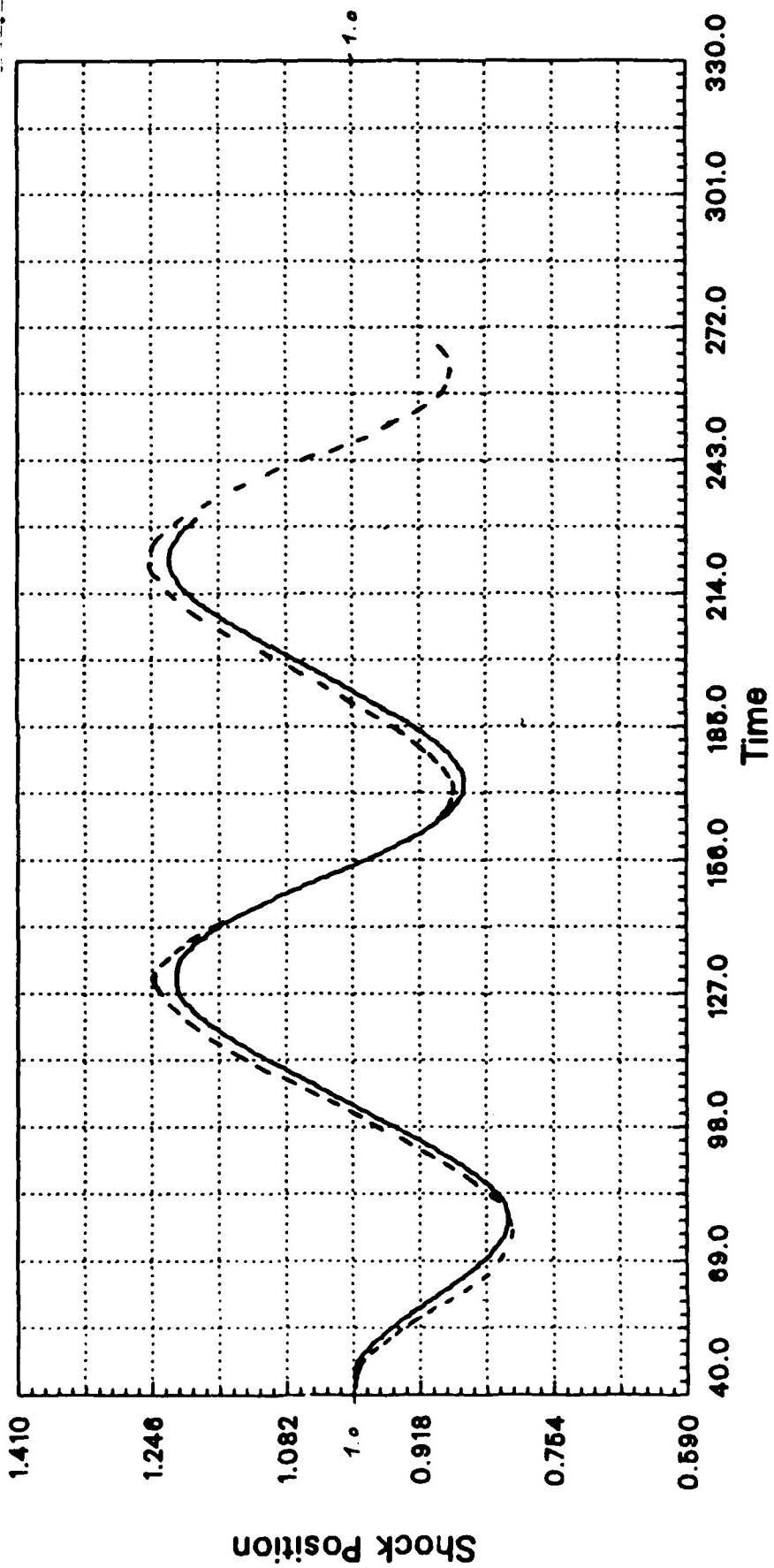


Fig. 5.2-2c. Comparison of unsteady shock position, as calculated with the flux vector splitting and an analytical (ref. /44/) method for Adamson's /44/ second sample case. $k=0.035$, $p_{e,\text{amp}}=0.0140$. Note: Only each 100th time step plotted.

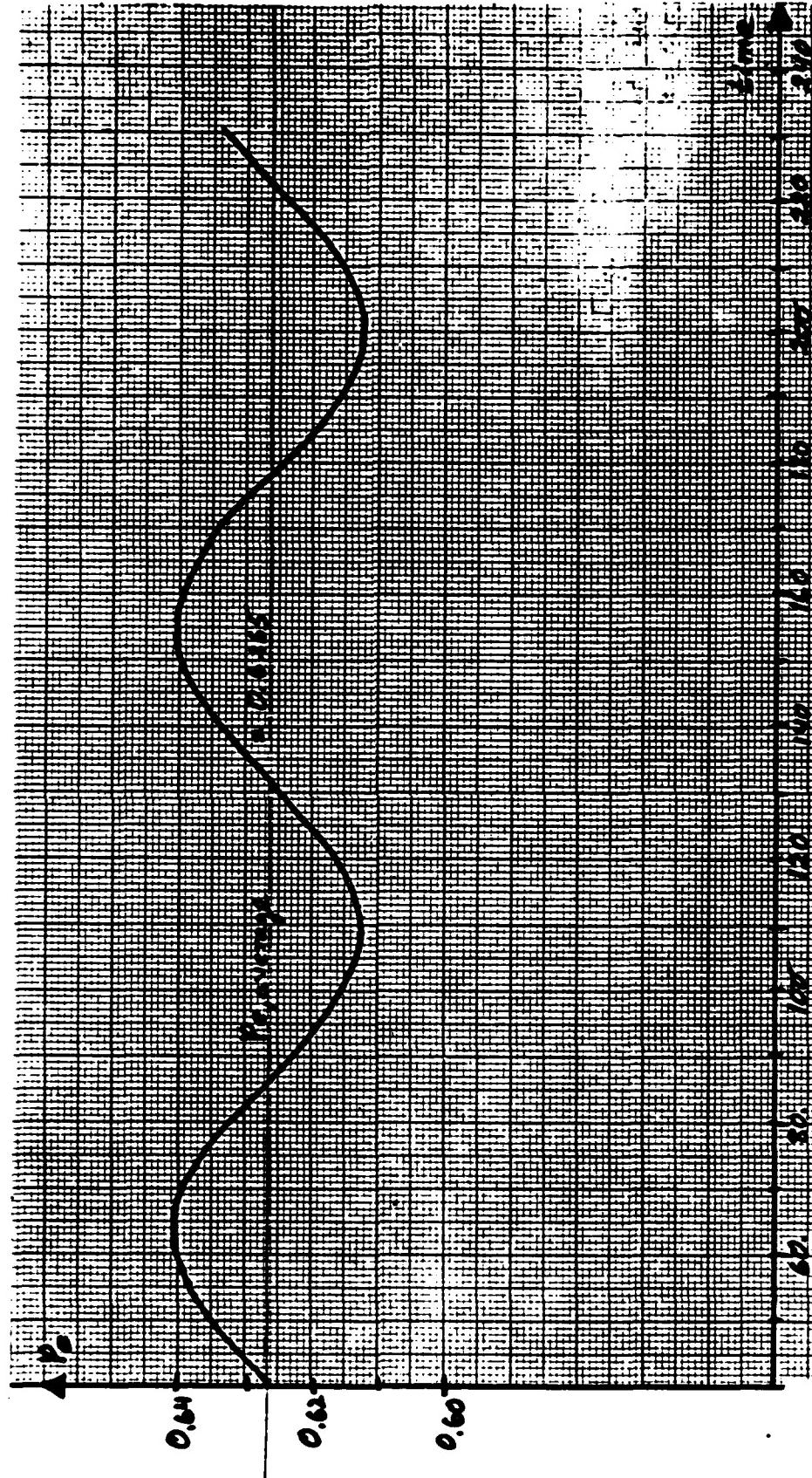
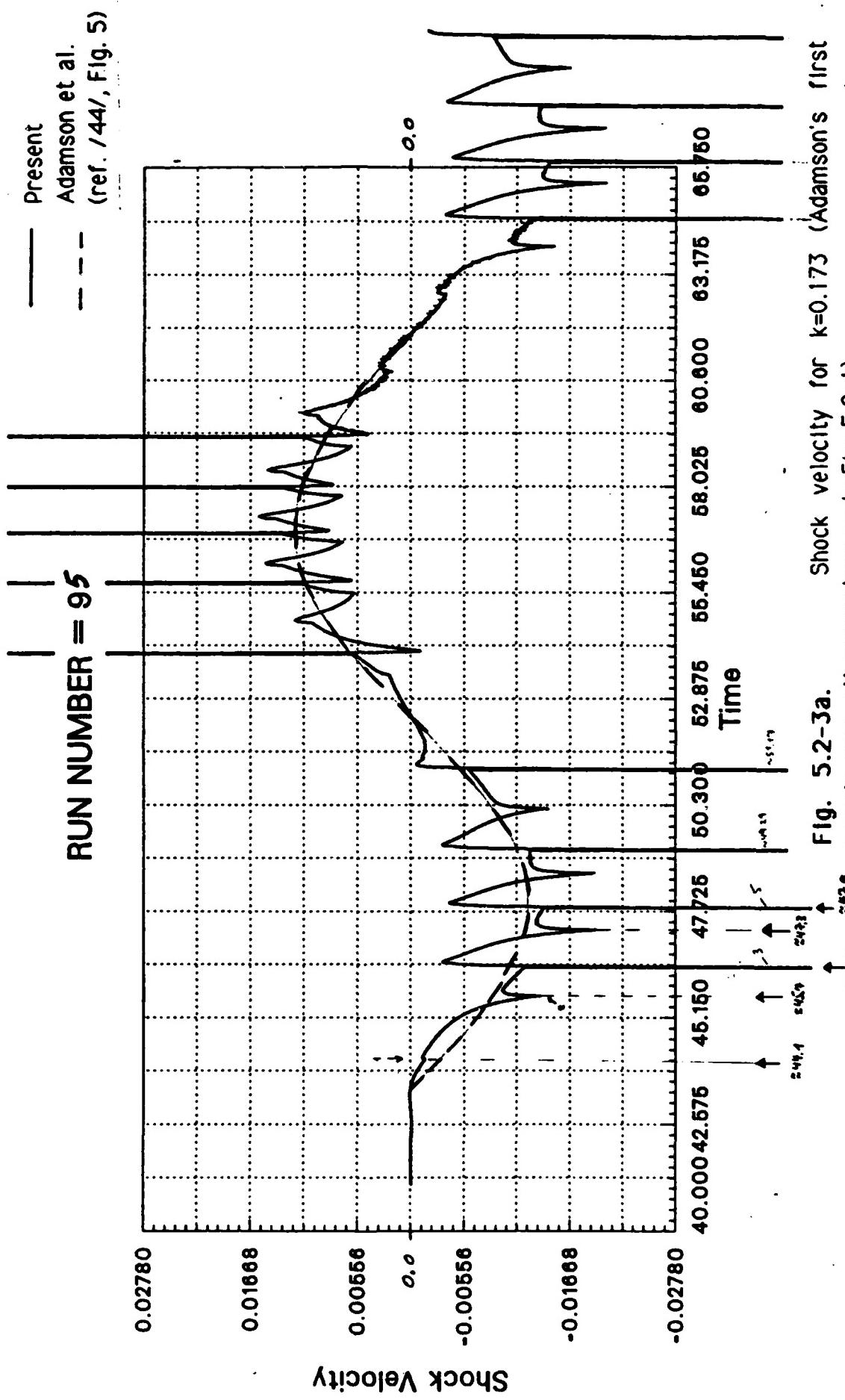


Fig. 5.2-2d. Imposed oscillation of back pressure for Adamson's /44/ second sample case. $k=0.035$, $\rho_{e,amp}=0.0140$.



RUN NUMBER = 96

Present

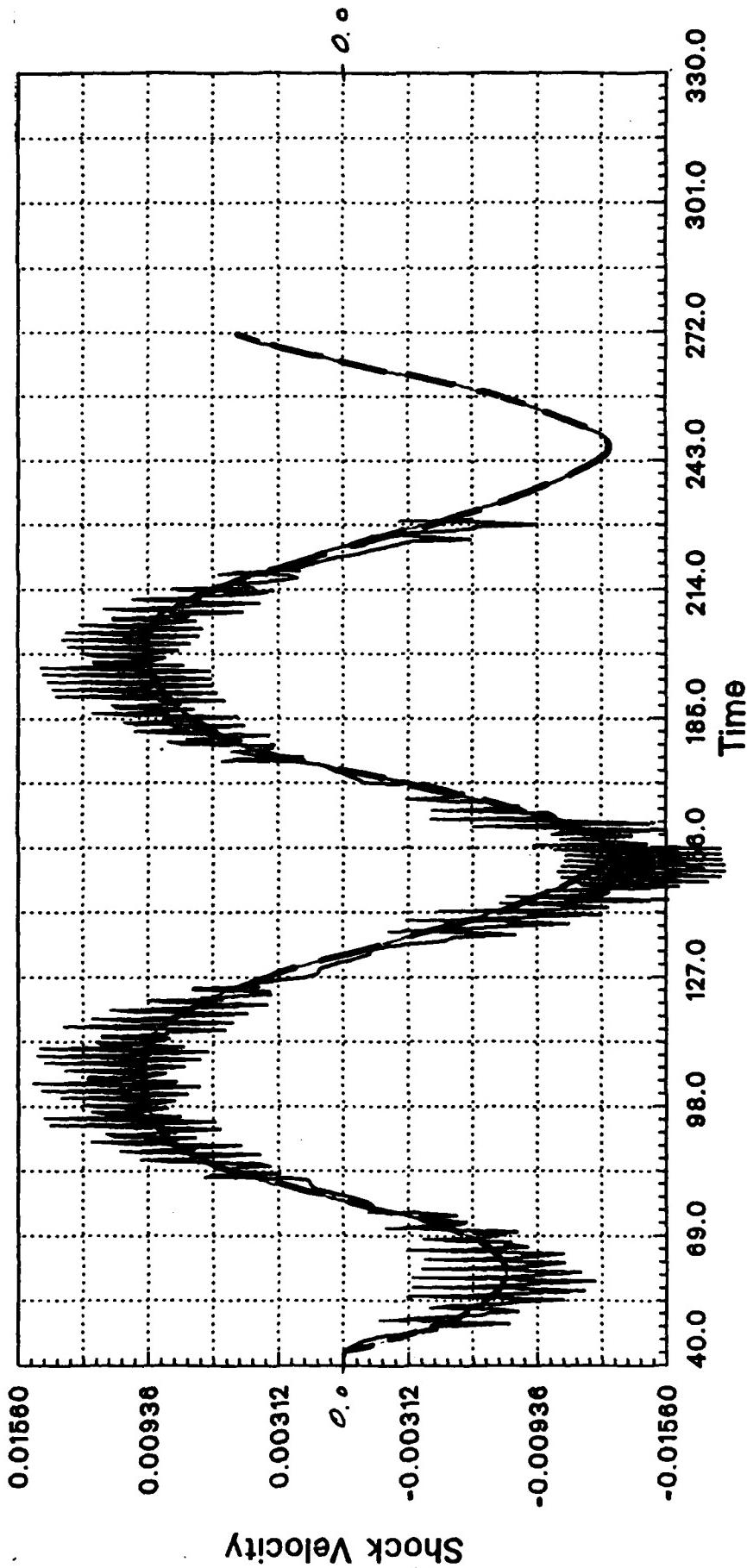
Adamson et al
(ref. /44/, Fig

Fig. 5.2-3b. Shock velocity for $k=0.035$ (Adamson's second sample case, all parameters as in Fig. 5.2-1). Note: Only each 100th time step used to calculate the shock velocity.

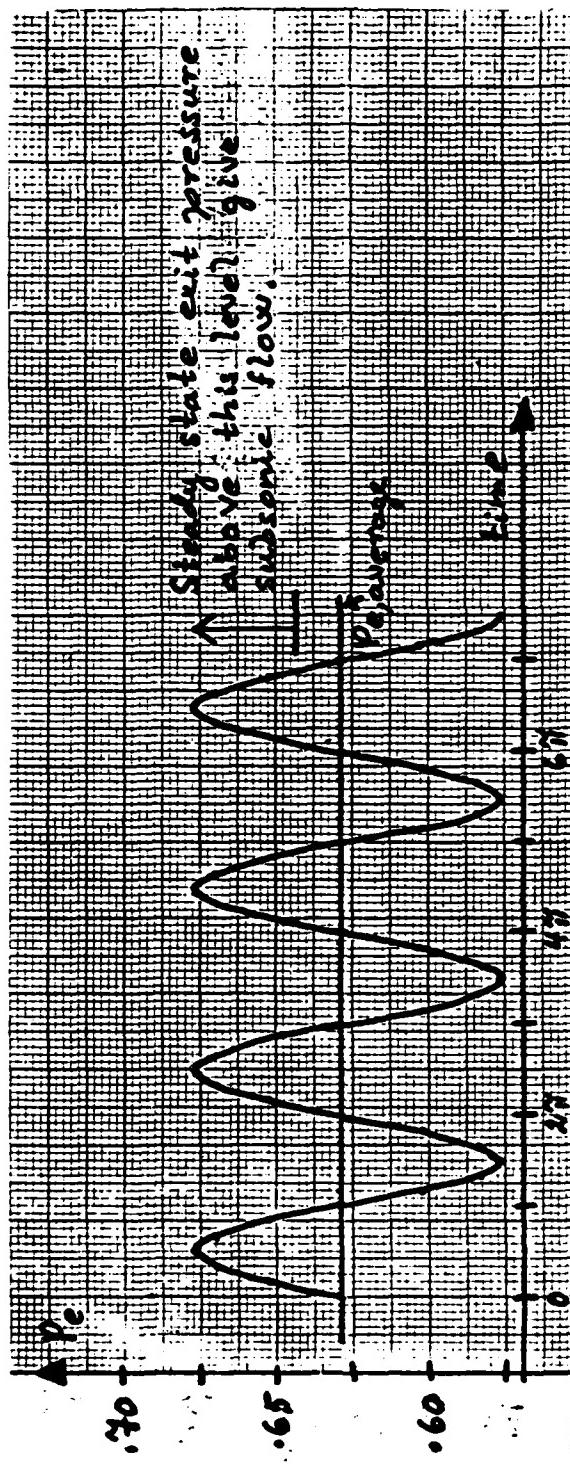


Fig. 5.2-4. Imposed exit pressure fluctuation for $k=0.318$,
 $p_{e,amp}=0.05$. All other parameters as in Figs. 5.2-1.

RUN NUMBER = 90

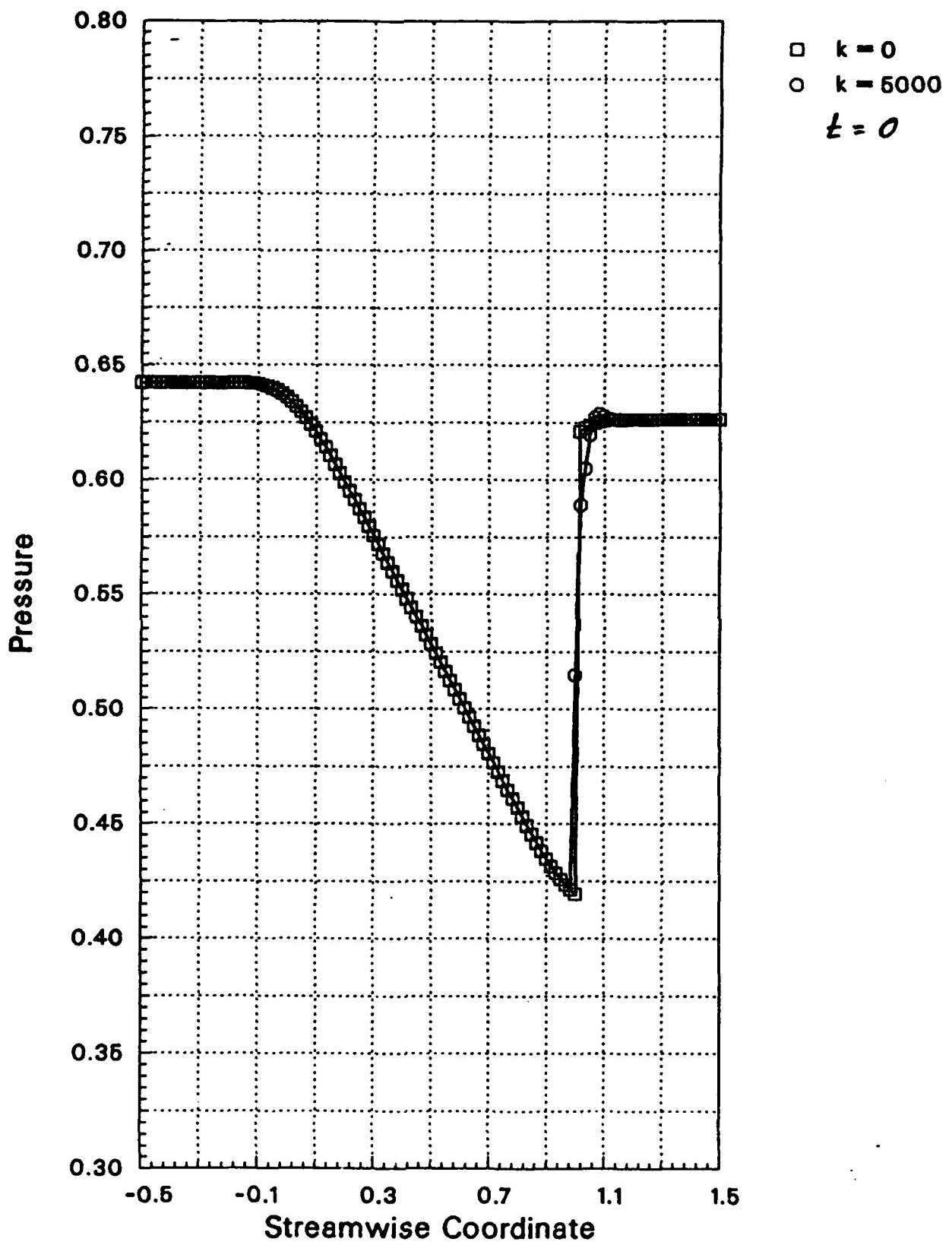


Fig. 5.2-4.2. Steady state pressure distribution in a nozzle for $k=0.318$, $Pe_{amp}=0.05$. All other parameters as in Figs. 5.2-1.

RUN NUMBER = 427

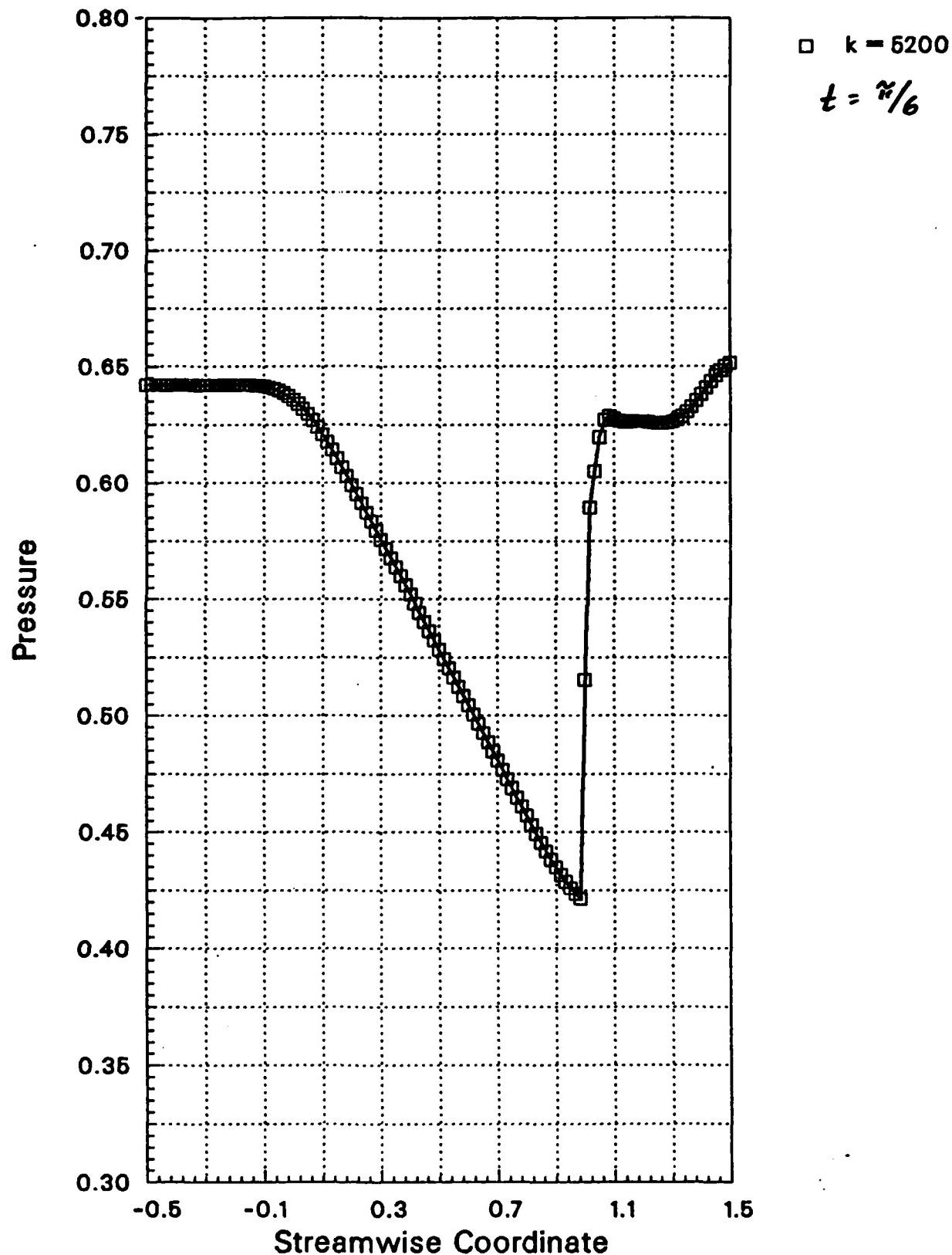


Fig. 5.2-4.3. Unsteady pressure distribution in a nozzle for $k=0.318$, $p_{e,amp}=0.05$. All other parameters as in Figs. 5.2-1.

RUN NUMBER = 427

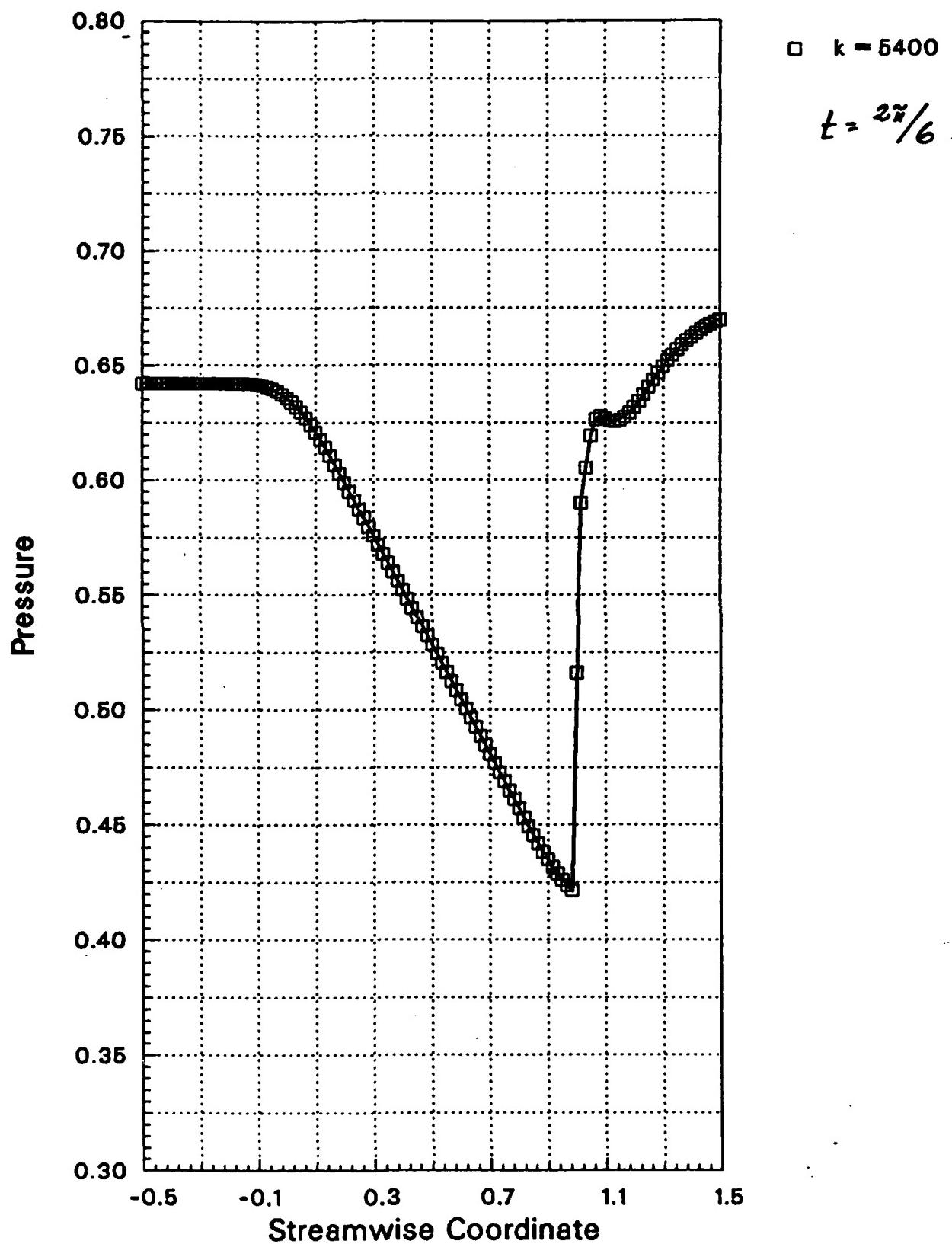


Fig. 5.2-4.4. Unsteady pressure distribution in a nozzle for $k=0.318$, $Pe_{amp}=0.05$. All other parameters as in Figs. 5.2-1.

RUN NUMBER = 427

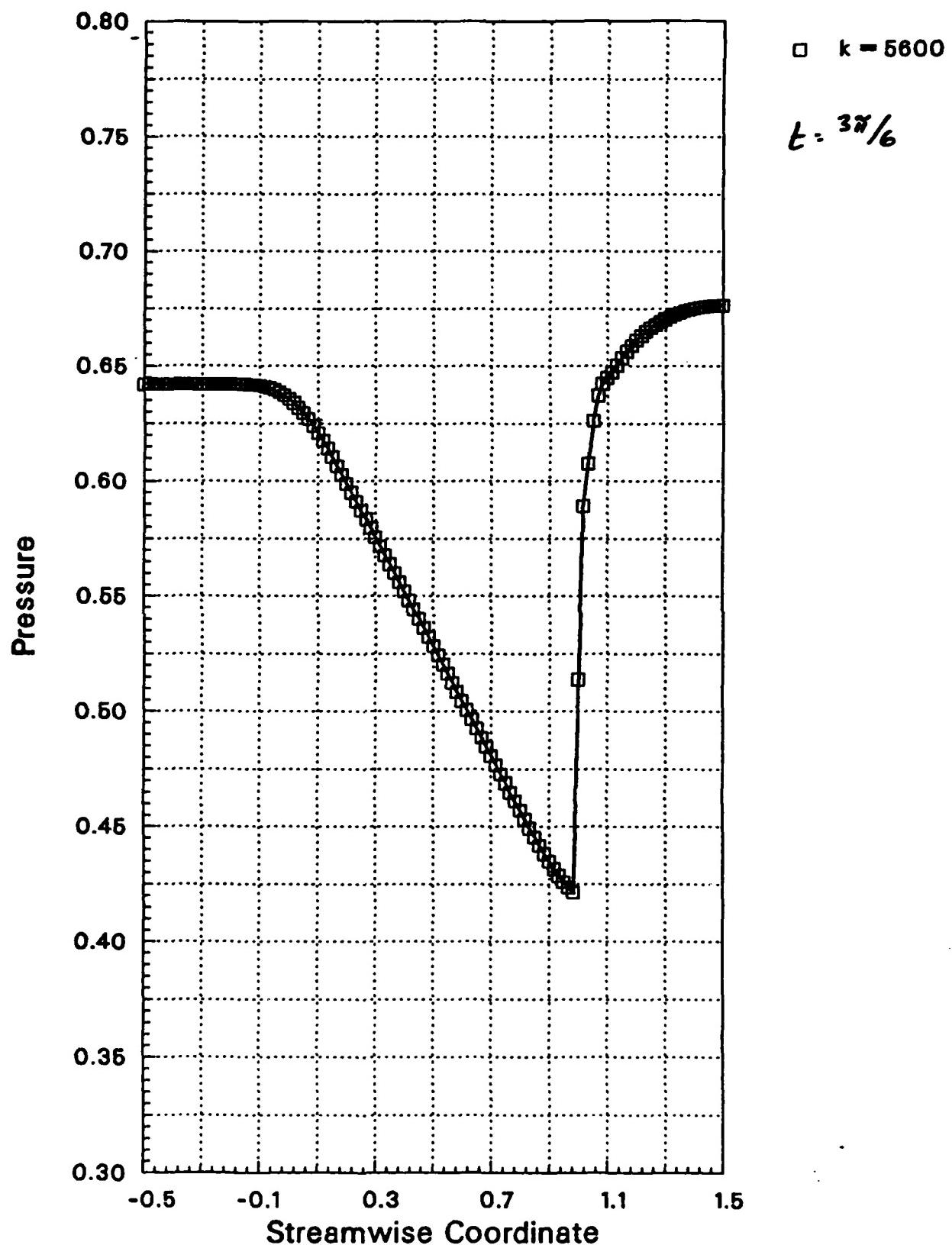


Fig. 5.2-4.5. Unsteady pressure distribution in a nozzle for $k=0.318$, $P_{e,amp}=0.05$. All other parameters as in Figs. 5.2-1.

RUN NUMBER = 427

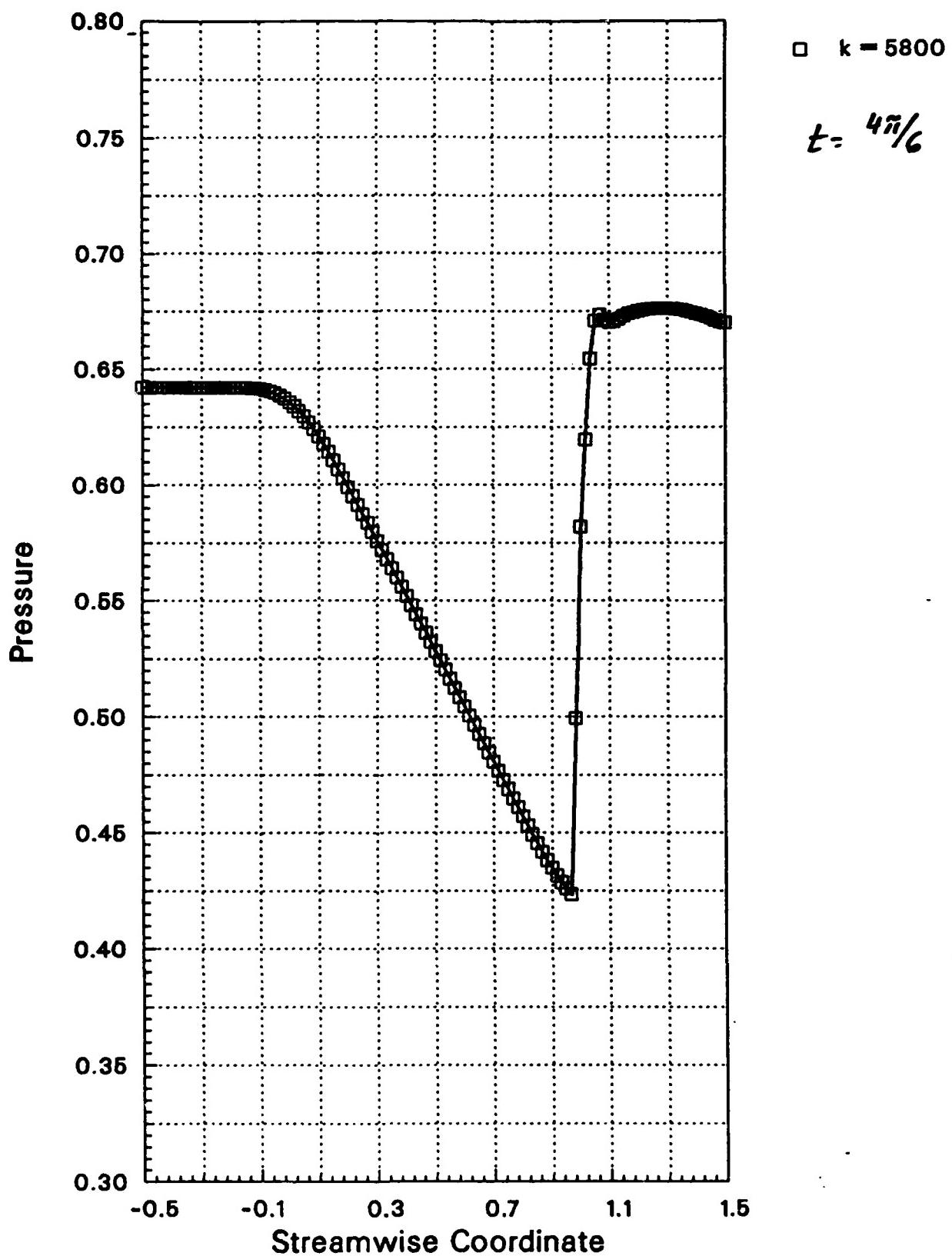


Fig. 5.2-4.6. Unsteady pressure distribution in a nozzle for $k=0.318$, $P_{e,amp}=0.05$. All other parameters as in Figs. 5.2-1.

RUN NUMBER = 427

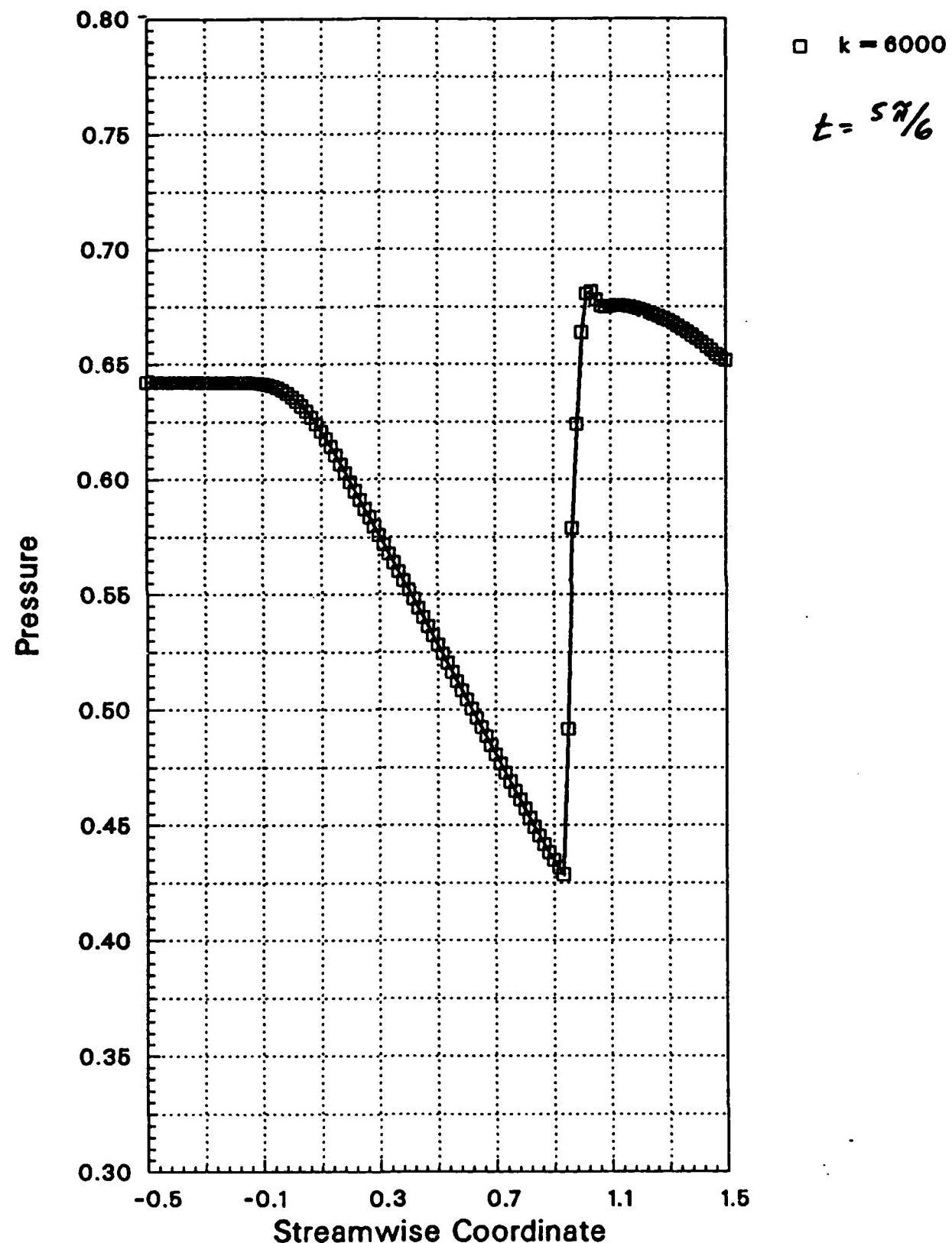


Fig. 5.2-4.7. Unsteady pressure distribution in a nozzle for $k=0.318$, $P_{e,amp}=0.05$. All other parameters as in Figs. 5.2-1.

RUN NUMBER = 427

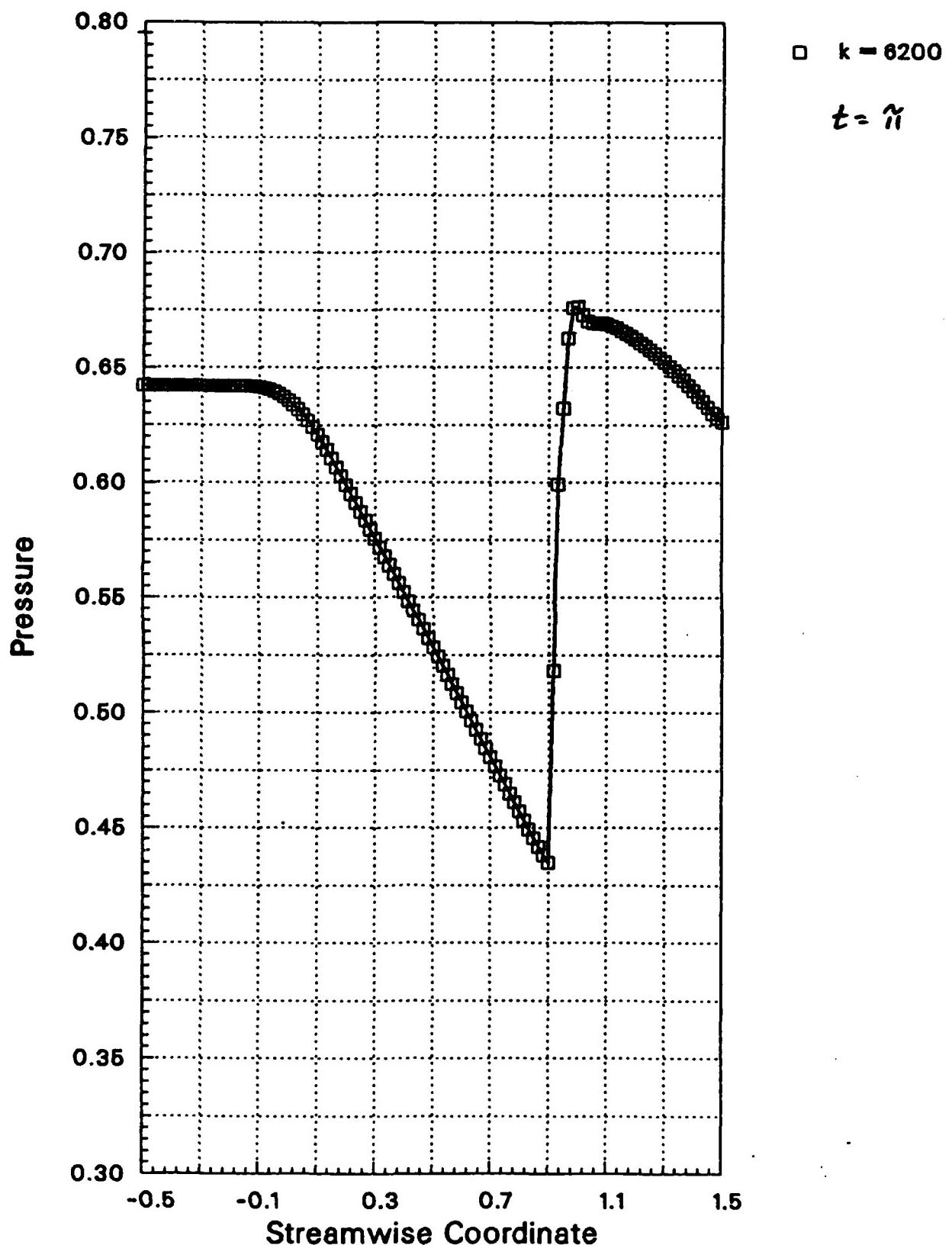


Fig. 5.2-4.8. Unsteady pressure distribution in a nozzle for $k=0.318$, $P_{e,amp}=0.05$. All other parameters as in Figs. 5.2-1.

RUN NUMBER = 427

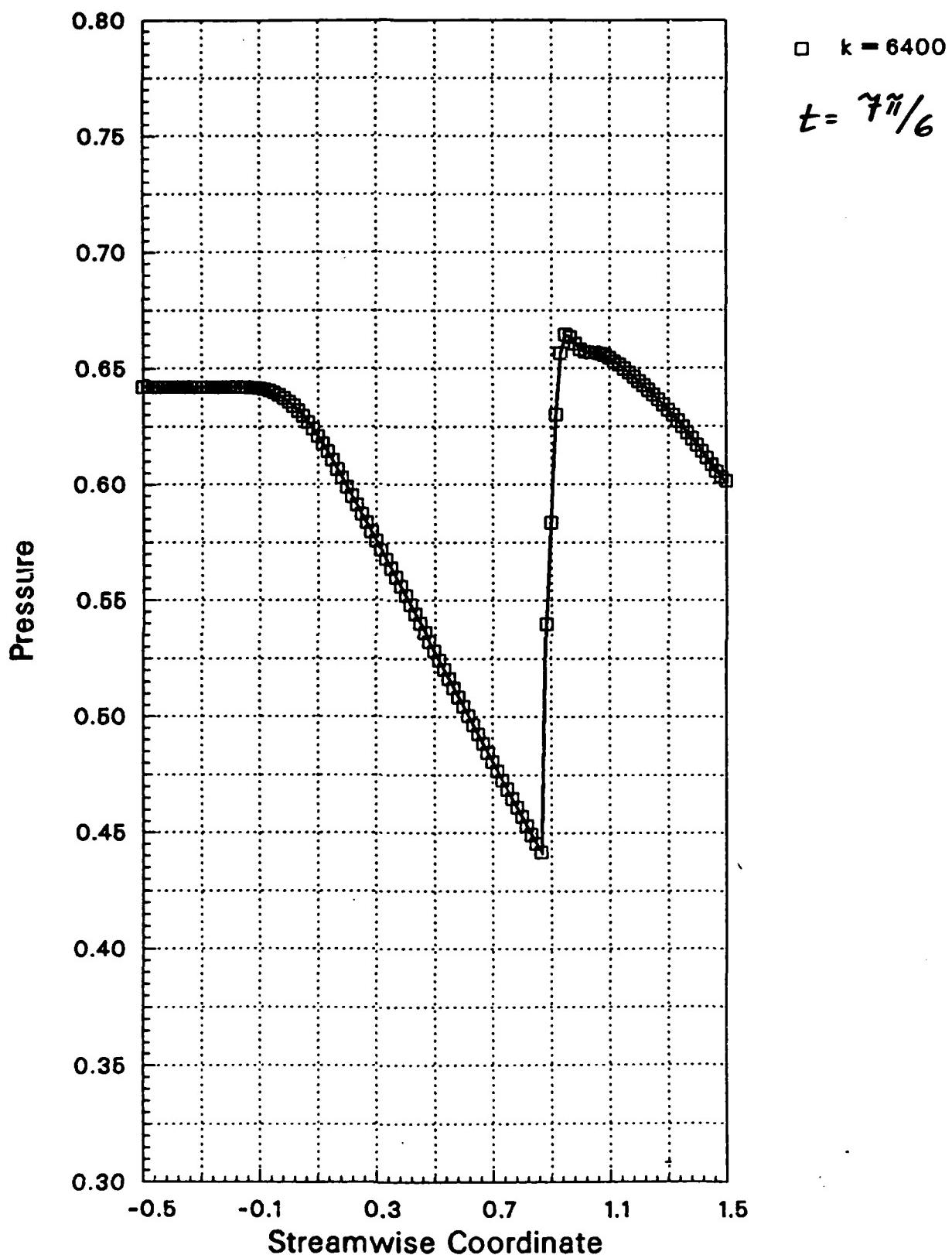


Fig. 5.2-4.9. Unsteady pressure distribution in a nozzle for $k=0.318$, $\rho_{e,amp}=0.05$. All other parameters as in Figs. 5.2-1.

RUN NUMBER = 427

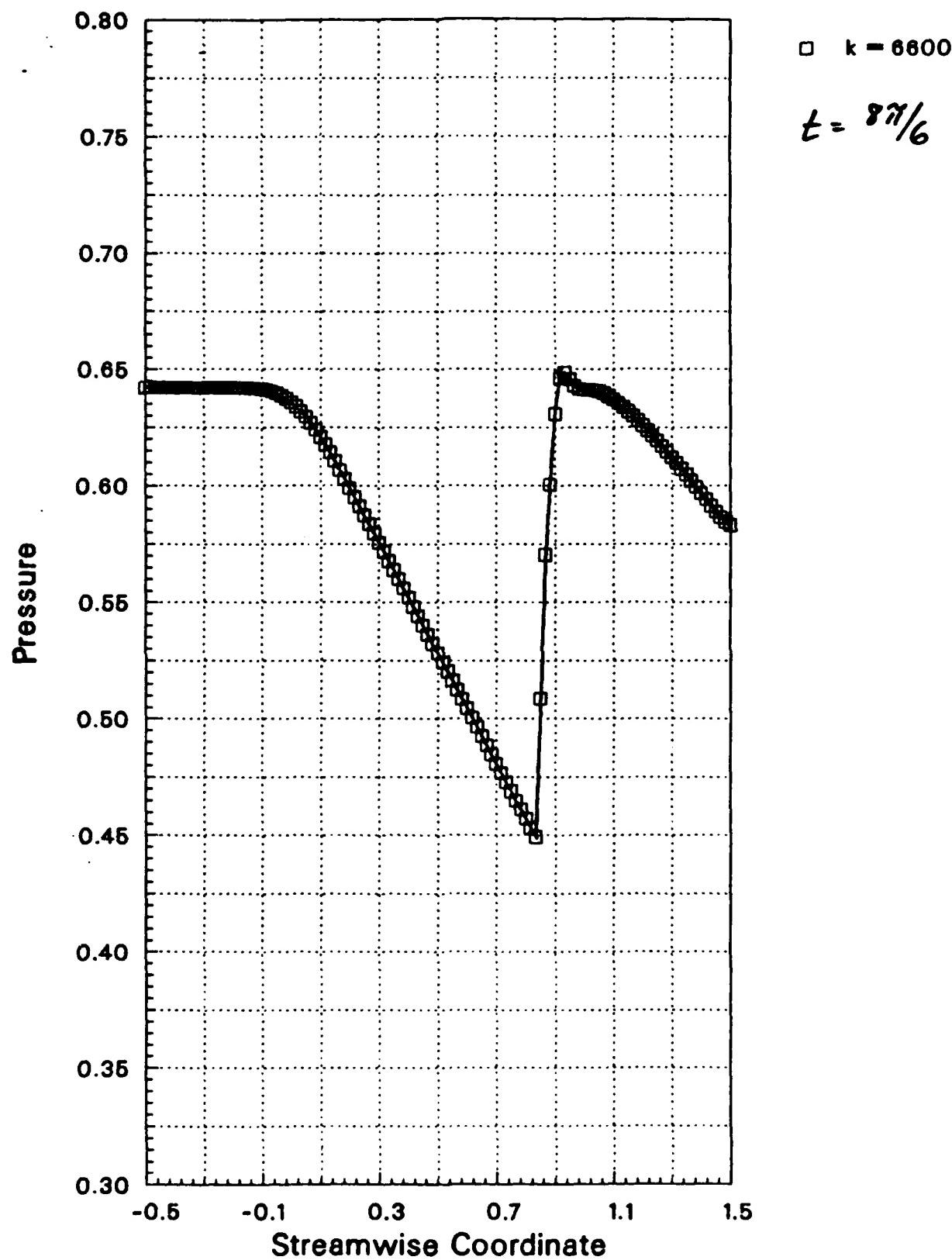


Fig. 5.2-4.10. Unsteady pressure distribution in a nozzle for $k=0.318$, $P_{e,amp}=0.05$. All other parameters as in Figs. 5.2-1.

RUN NUMBER = 427

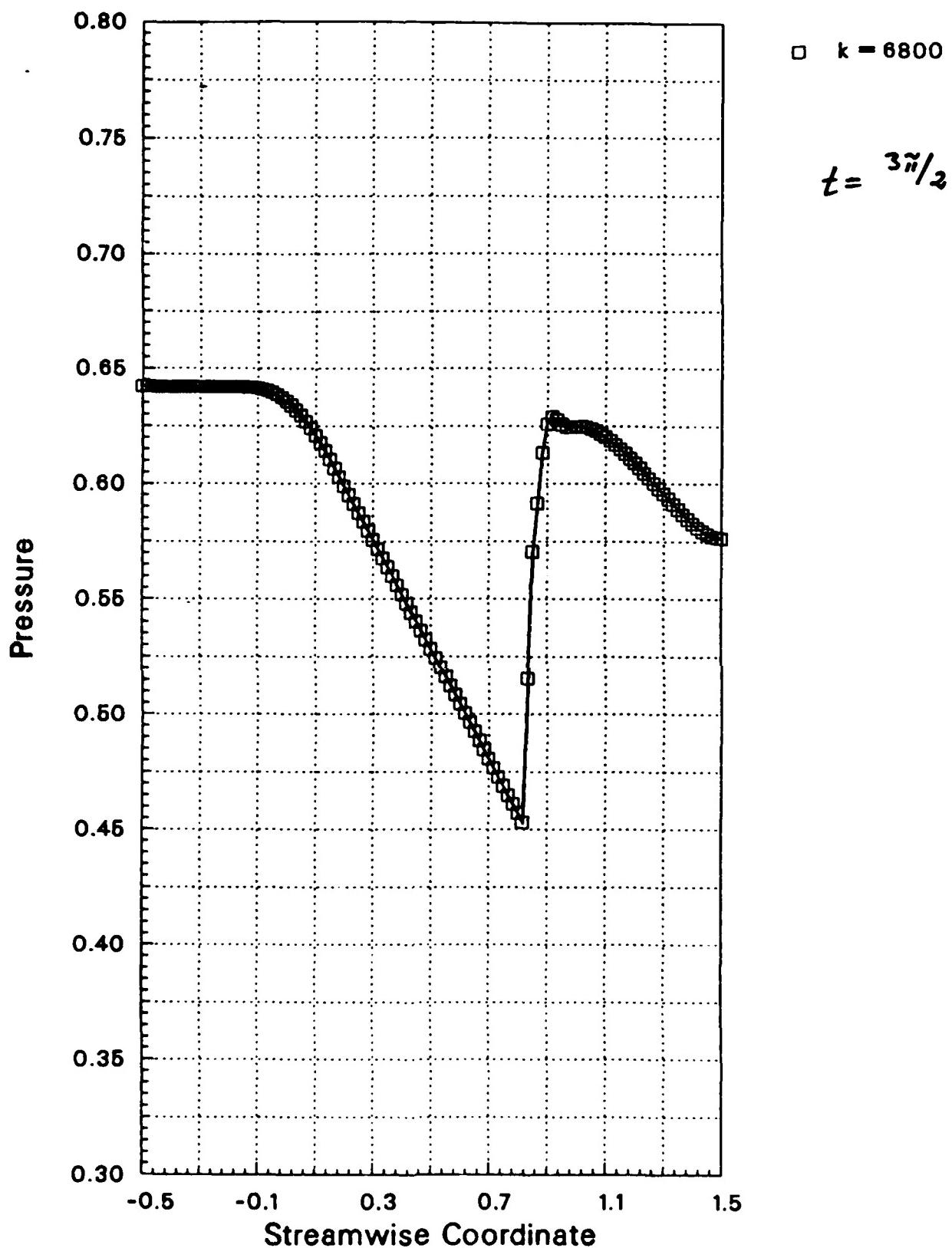


Fig. 5.2-4.11. Unsteady pressure distribution in a nozzle for $k=6800$
 $\rho_{e,temp}=0.05$. All other parameters as in Figs. 5.2-1

RUN NUMBER = 427

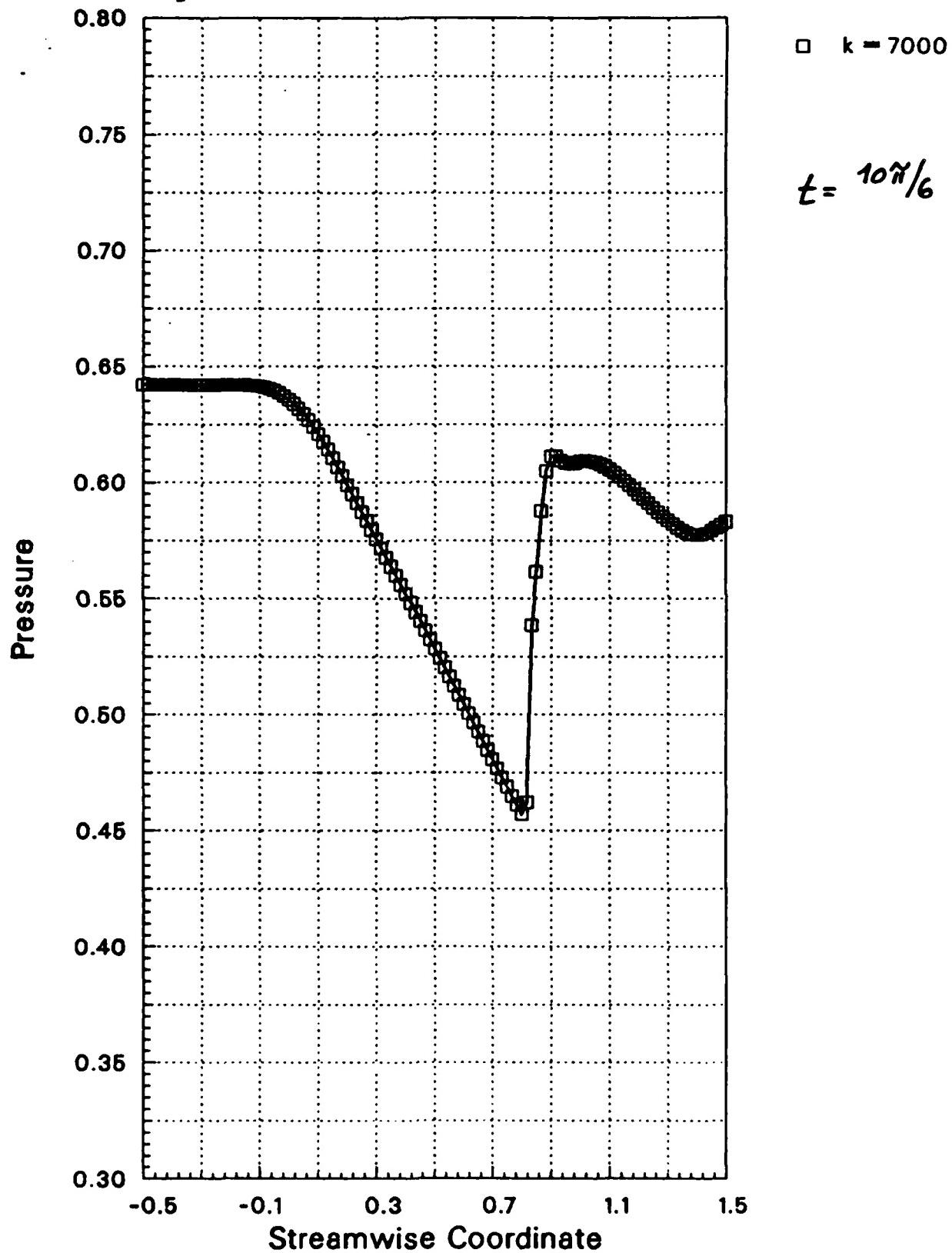


Fig. 5.2-4.12. Unsteady pressure distribution in a nozzle for $k=0.318$, $\beta_{e,amp}=0.05$. All other parameters as in Figs. 5.2-1.

RUN NUMBER = 427

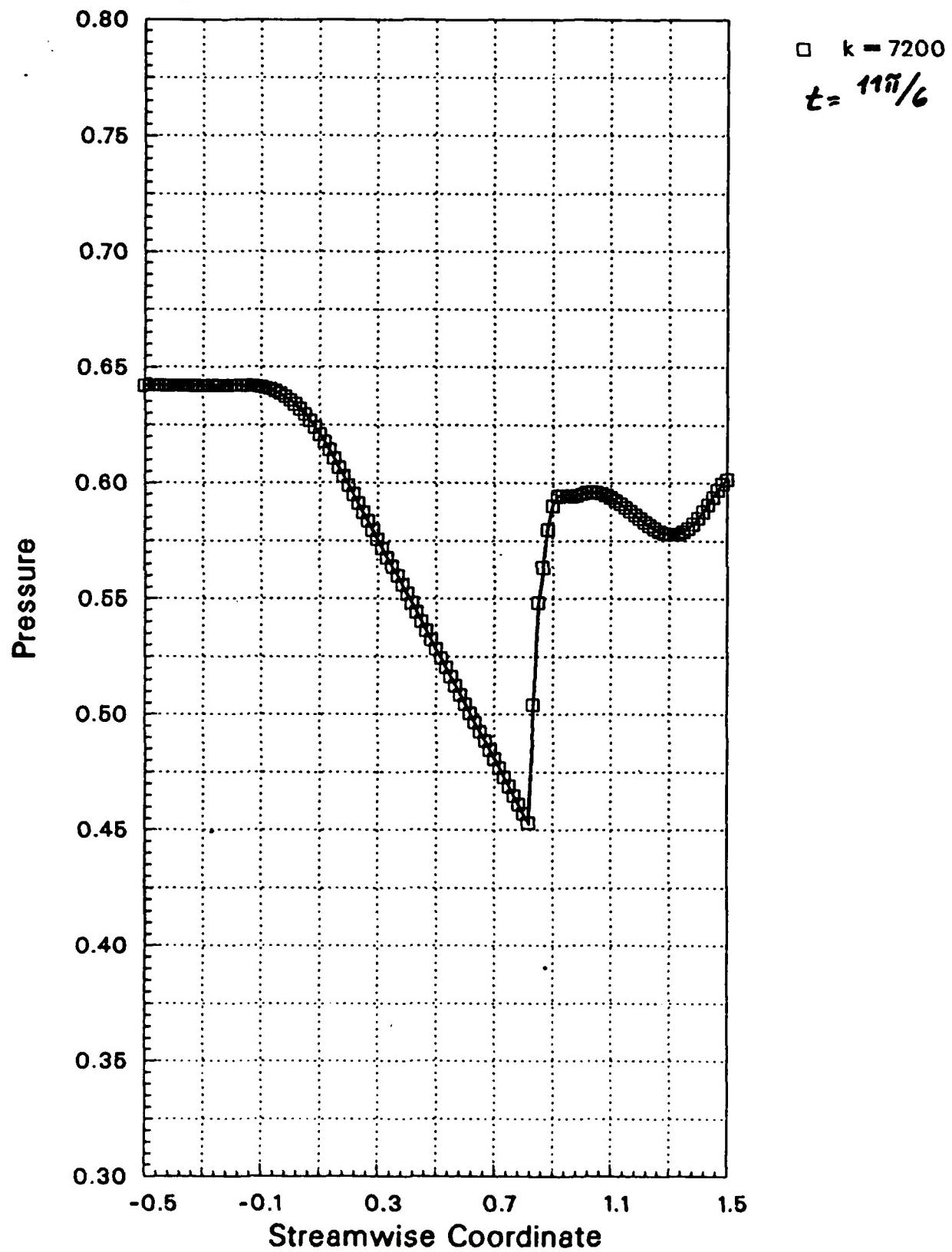


Fig. 5.2-4.13. Unsteady pressure distribution in a nozzle for $k=0.318$
 $P_{e,amp}=0.05$. All other parameters as in Figs. 5.2-1.

RUN NUMBER = 427

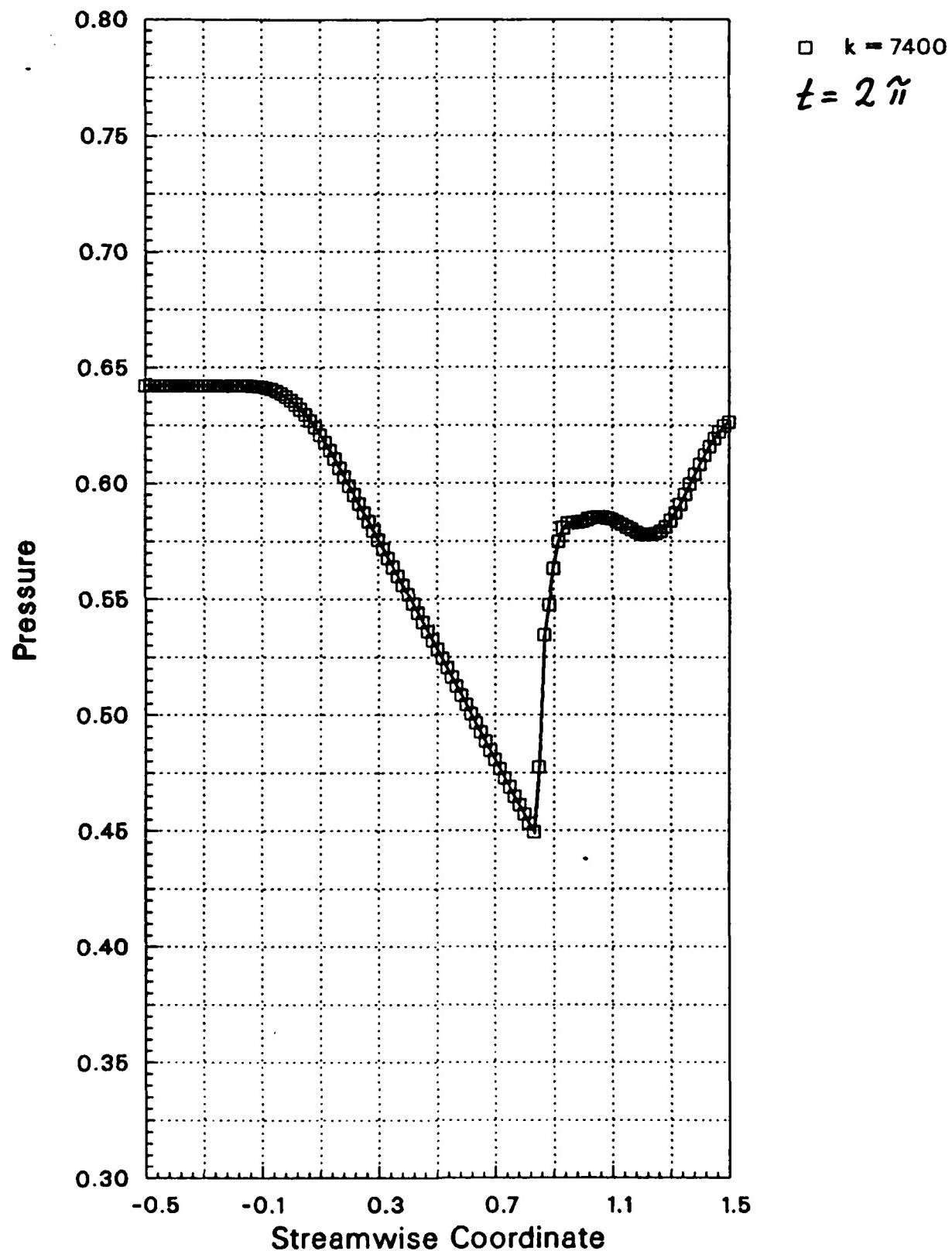


Fig. 5.2-4.14. Unsteady pressure distribution in a nozzle for $k=0.318$, $\bar{\rho}_{e,amp}=0.05$. All other parameters as in Figs. 5.2-1.

RUN NUMBER = 427

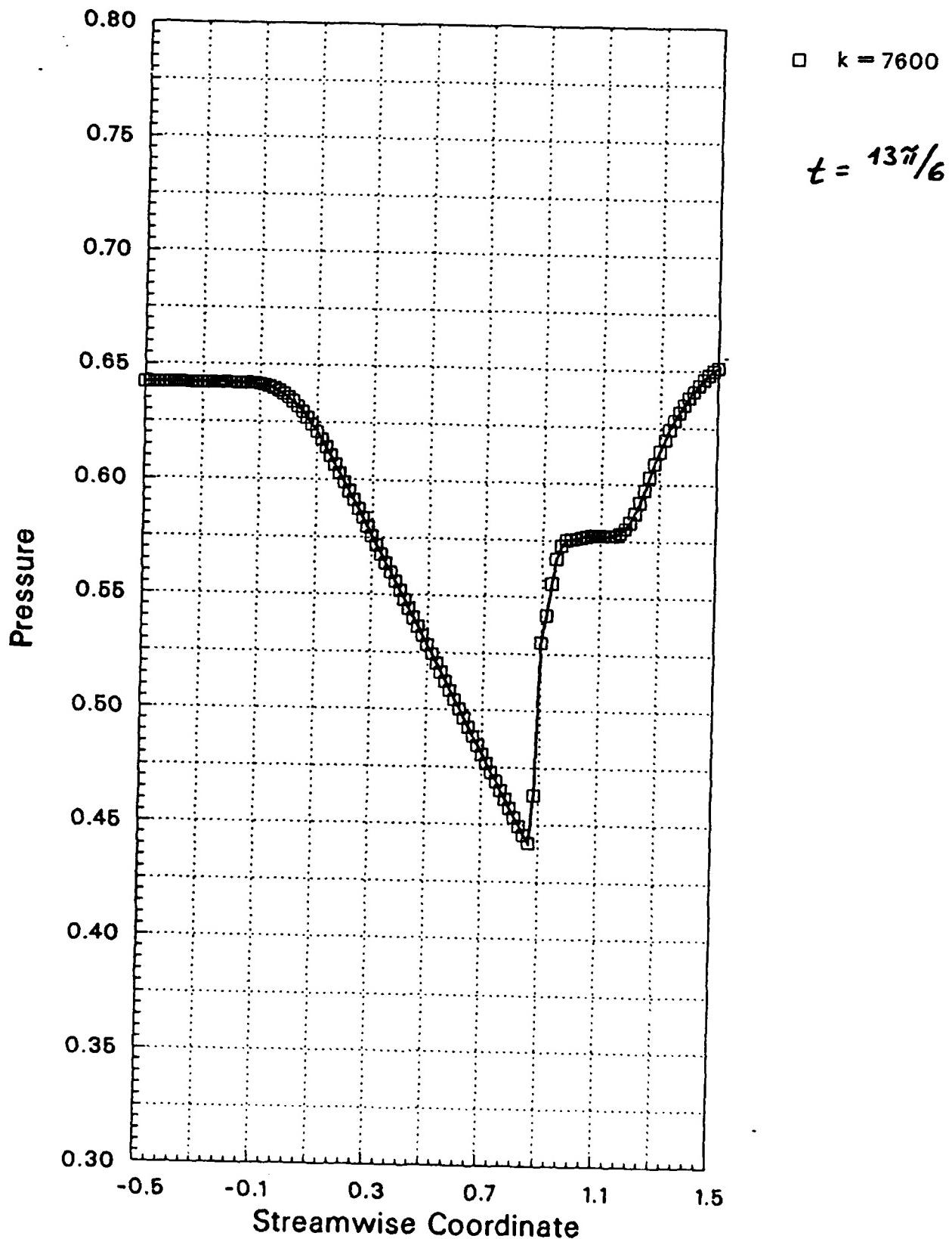


Fig. 5.2-4.15. Unsteady pressure distribution in a nozzle for $k=0.510$
 $\rho_{e,amp}=0.05$. All other parameters as in Figs. 5.2-1

RUN NUMBER = 427

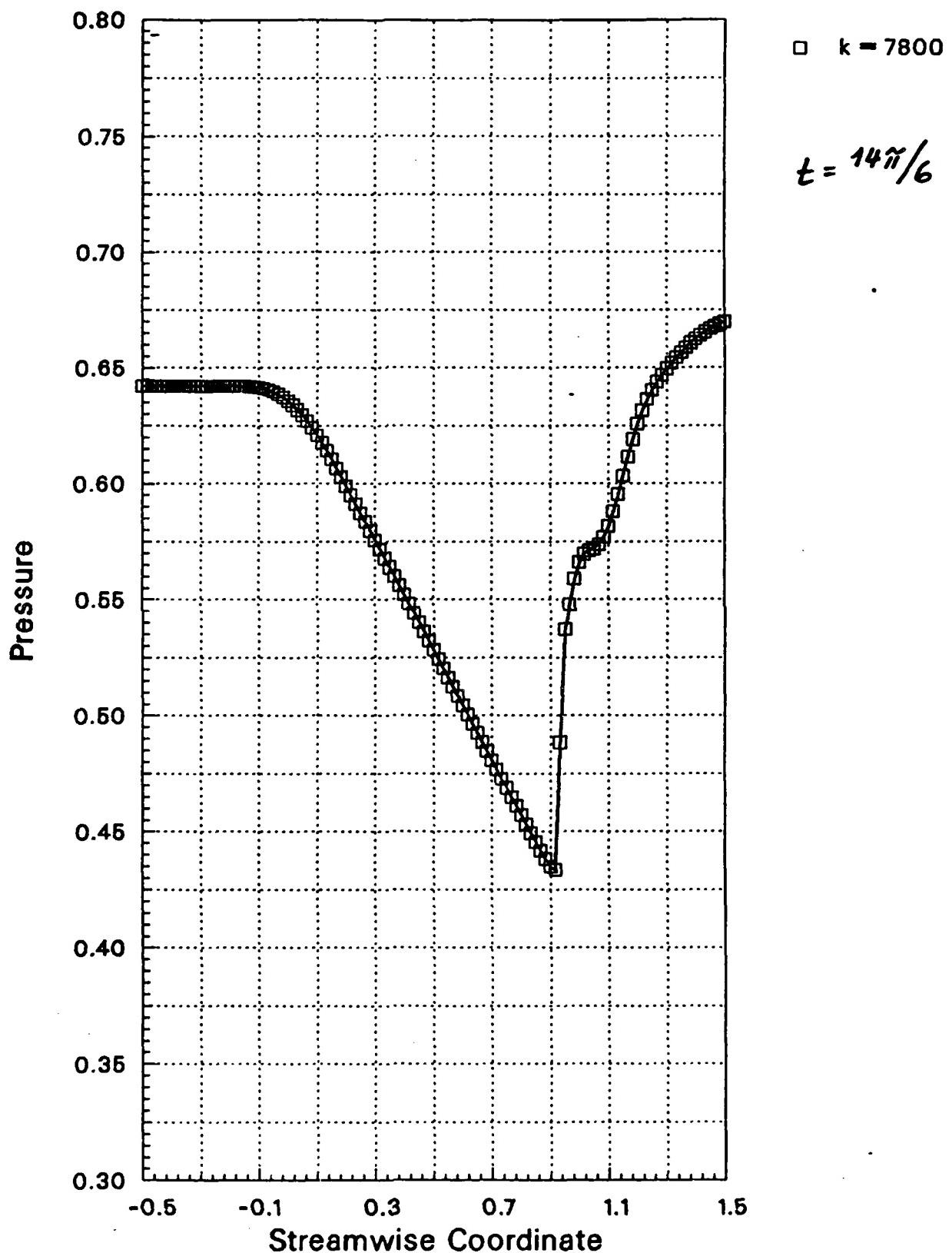


Fig. 5.2-4.16. Unsteady pressure distribution in a nozzle for $k=0.318$, $P_{e,am0}=0.05$. All other parameters as in Figs. 5.2-1.

RUN NUMBER = 427

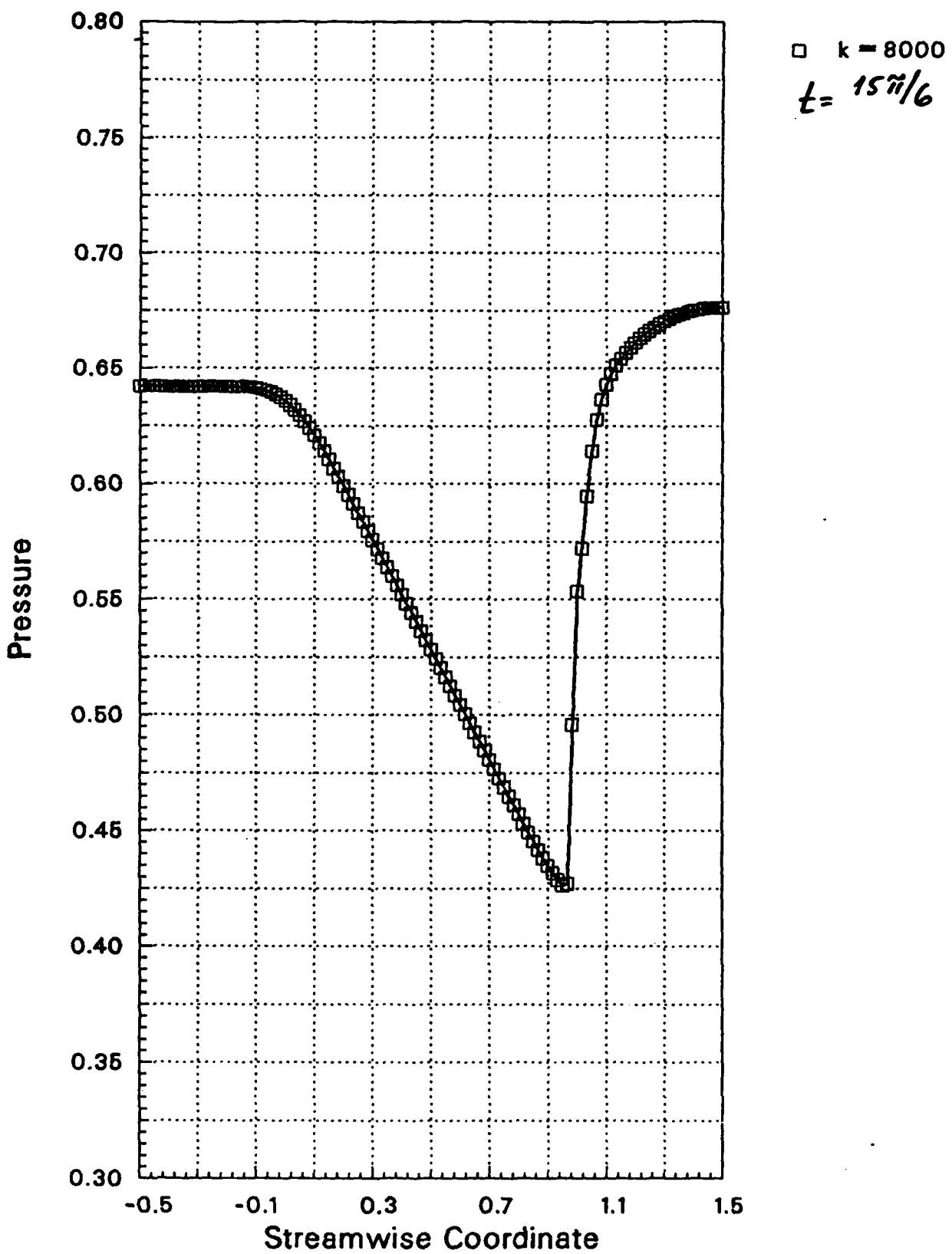


Fig. 5.2-4.17. Unsteady pressure distribution in a nozzle for $\kappa=0.316$, $P_{e,amp}=0.05$. All other parameters as in Figs. 5.2-1.

RUN NUMBER = 427

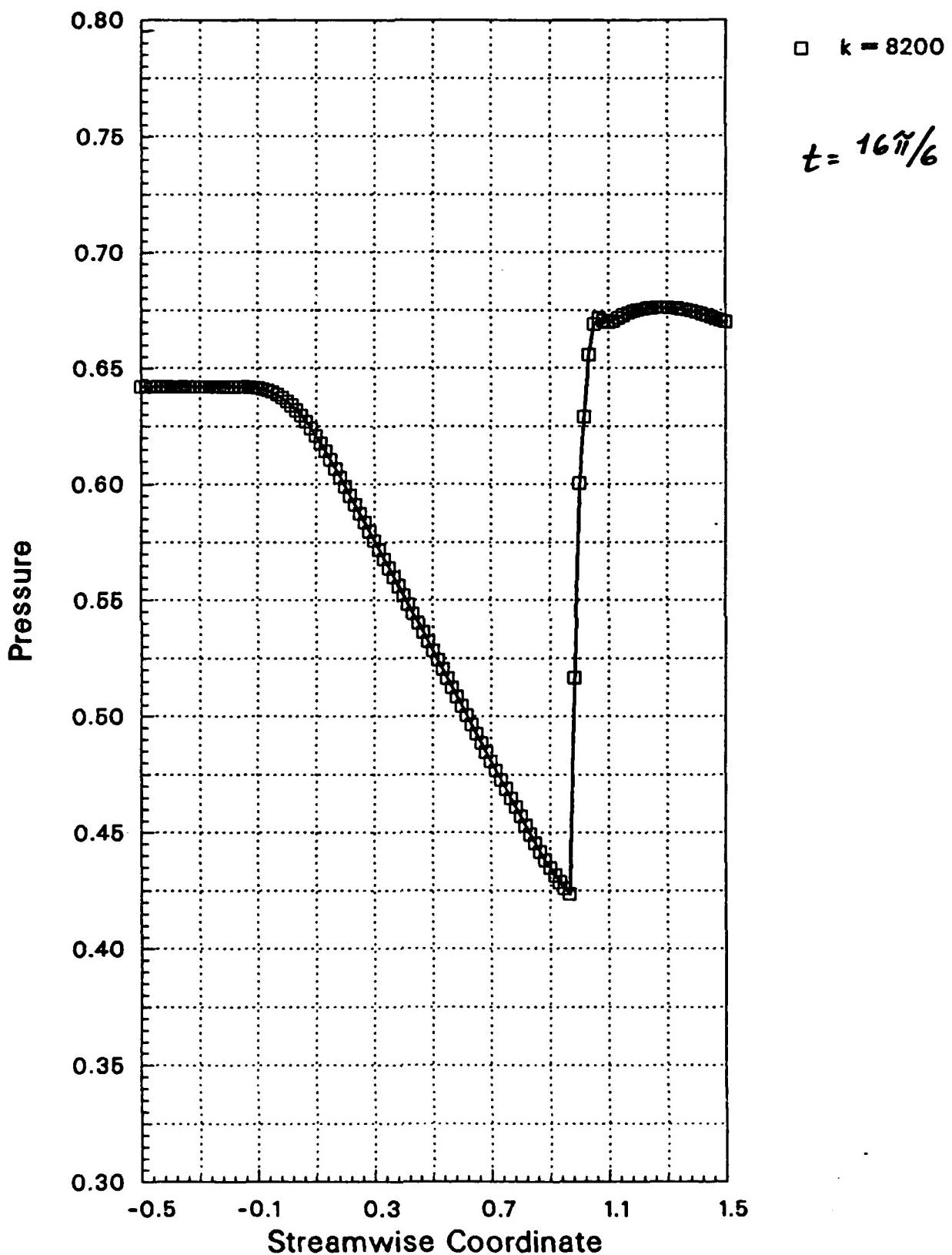


Fig. 5.2-4.18. Unsteady pressure distribution in a nozzle for $k=0.318$, $\delta_{e,amp}=0.05$. All other parameters as in Figs. 5.2-1.

RUN NUMBER = 427

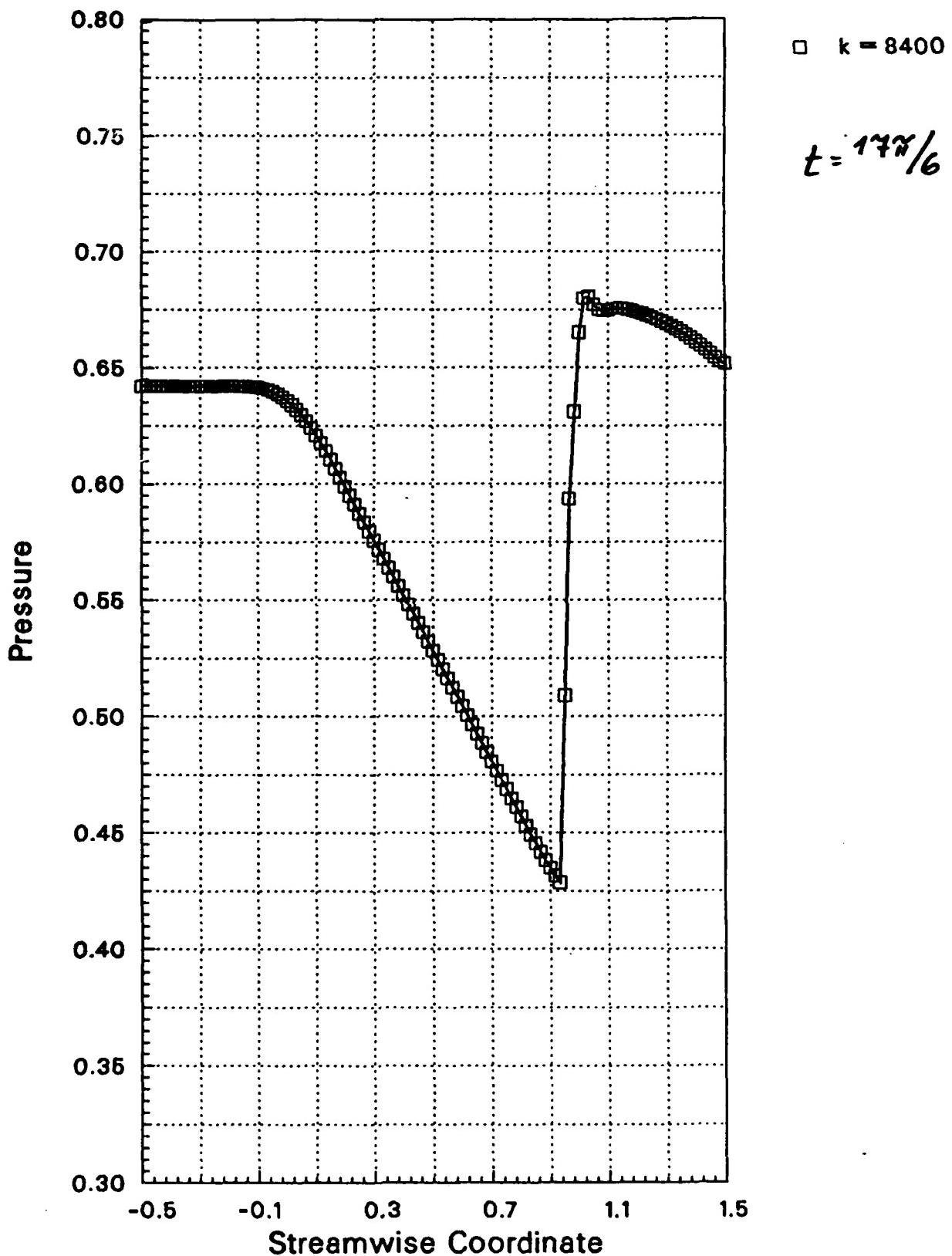


Fig. 5.2-4.19. Unsteady pressure distribution in a nozzle for $k=0.318$, $P_{e,amp}=0.05$. All other parameters as in Figs. 5.2-1.

RUN NUMBER = 427

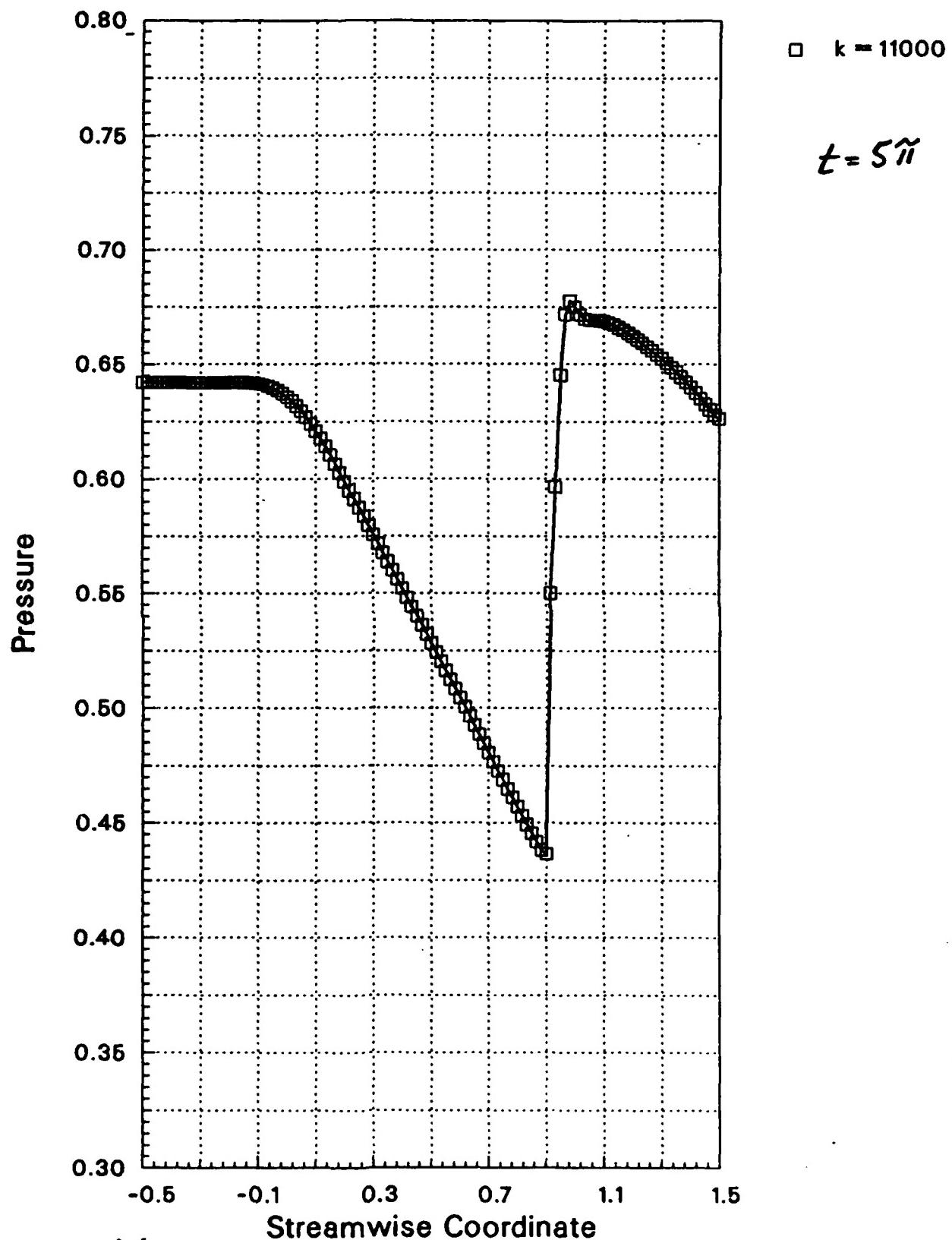


Fig. 5.2-4.20. Unsteady pressure distribution in a nozzle for $k=0.318$, $P_{e,amp}=0.05$. All other parameters as in Figs. 5.2-1.

RUN NUMBER = 427

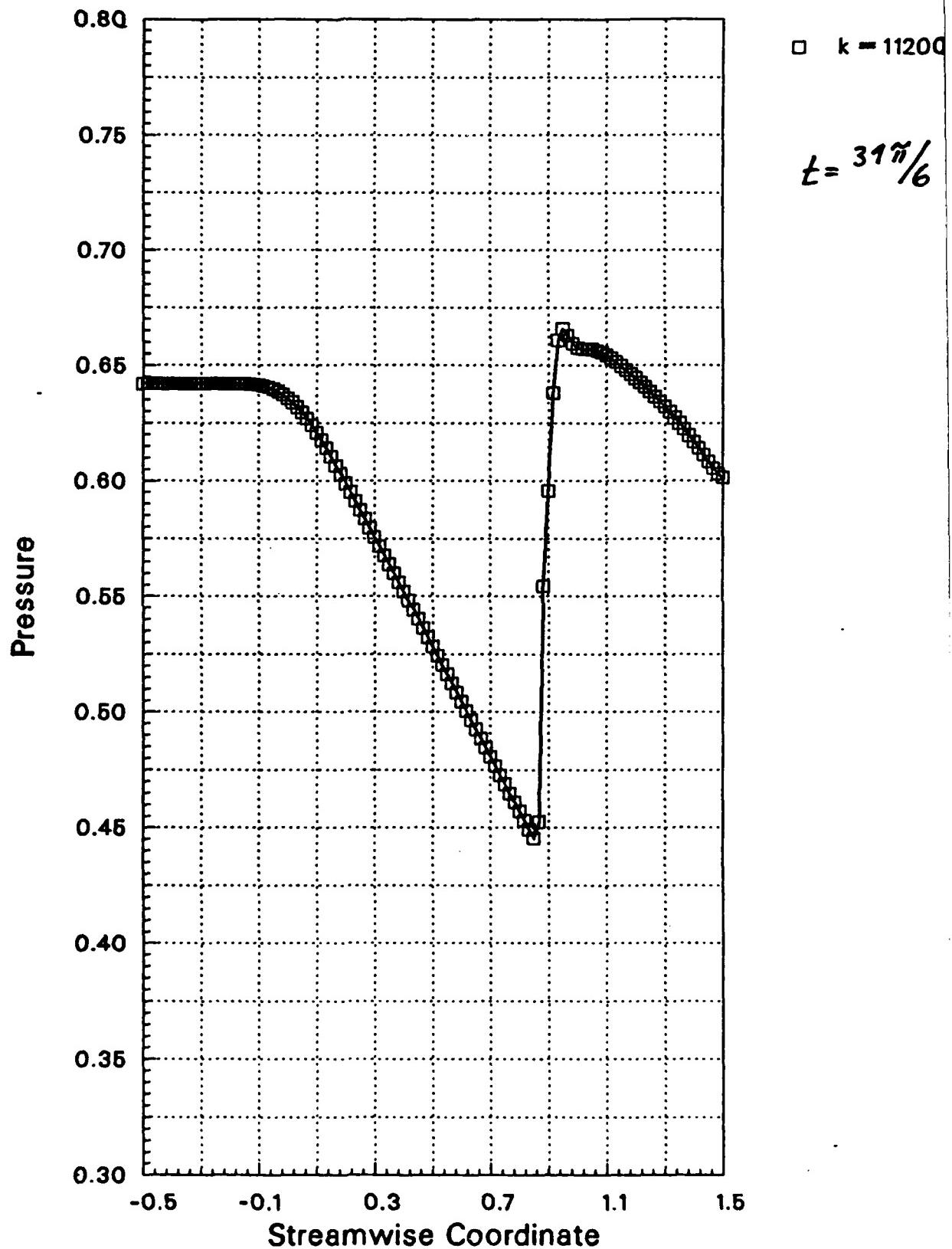


Fig. 5.2-4.21. Unsteady pressure distribution in a nozzle for $k=0.318$.
 $P_{e,amp}=0.05$. All other parameters as in Figs. 5.2-1.

RUN NUMBER = 427

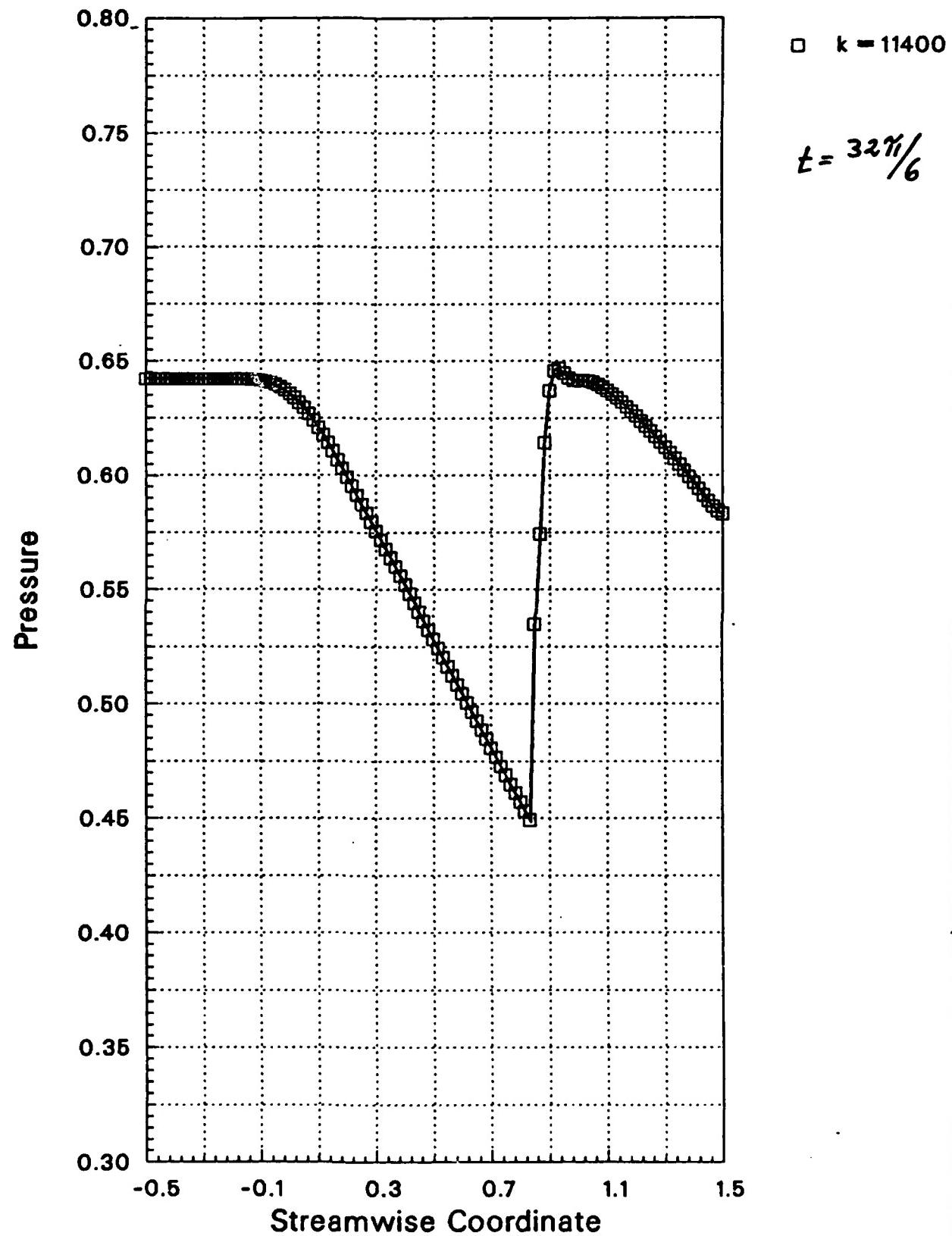


Fig. 5.2-4.22. Unsteady pressure distribution in a nozzle for $k=0.318$, $\rho_{e,amp}=0.05$. All other parameters as in Figs. 5.2-1.

RUN NUMBER = 427

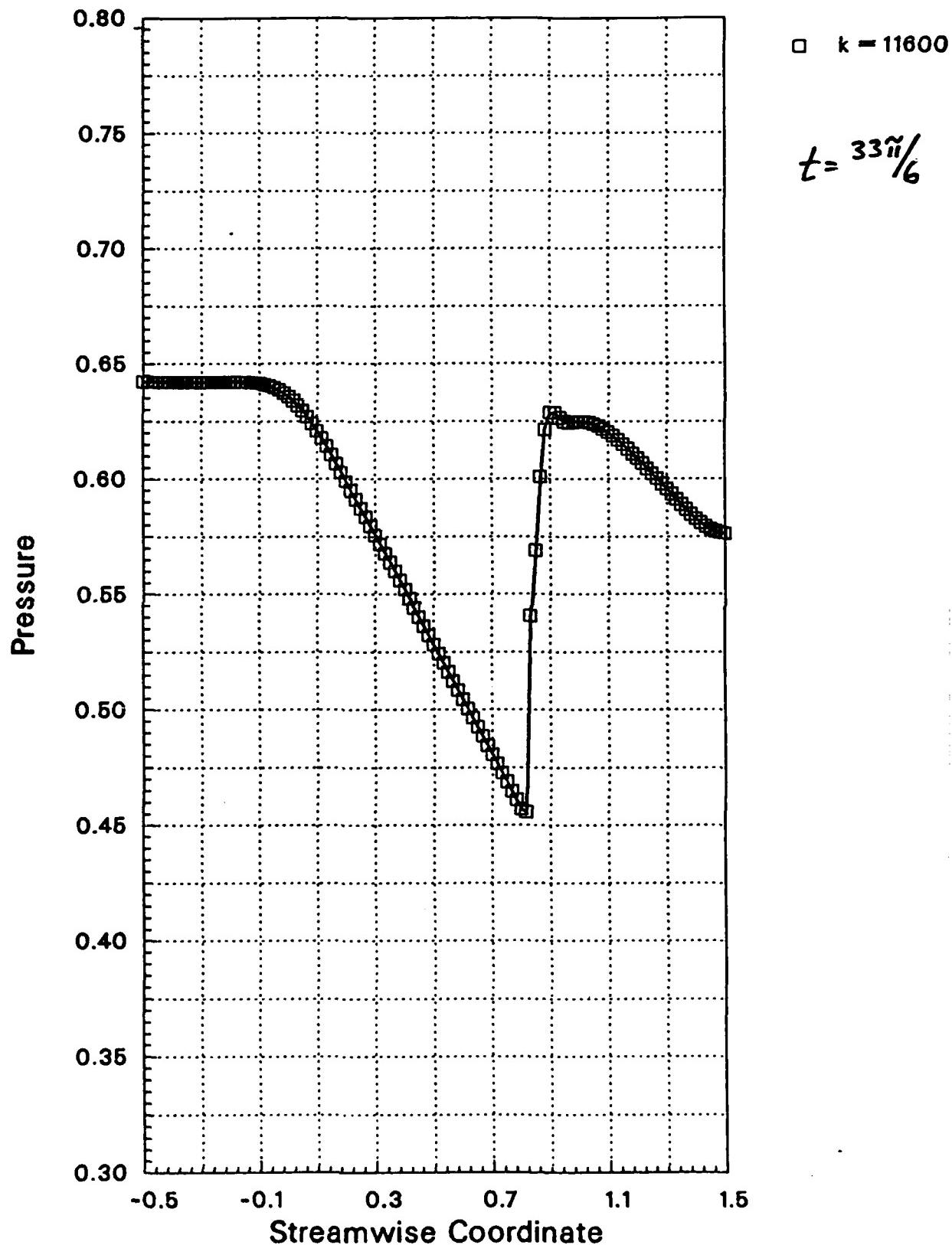


Fig. 5.2-4.23. Unsteady pressure distribution in a nozzle for $k=0.518$, $P_{e,amp}=0.05$. All other parameters as in Figs. 5.2-1.

RUN NUMBER = 427

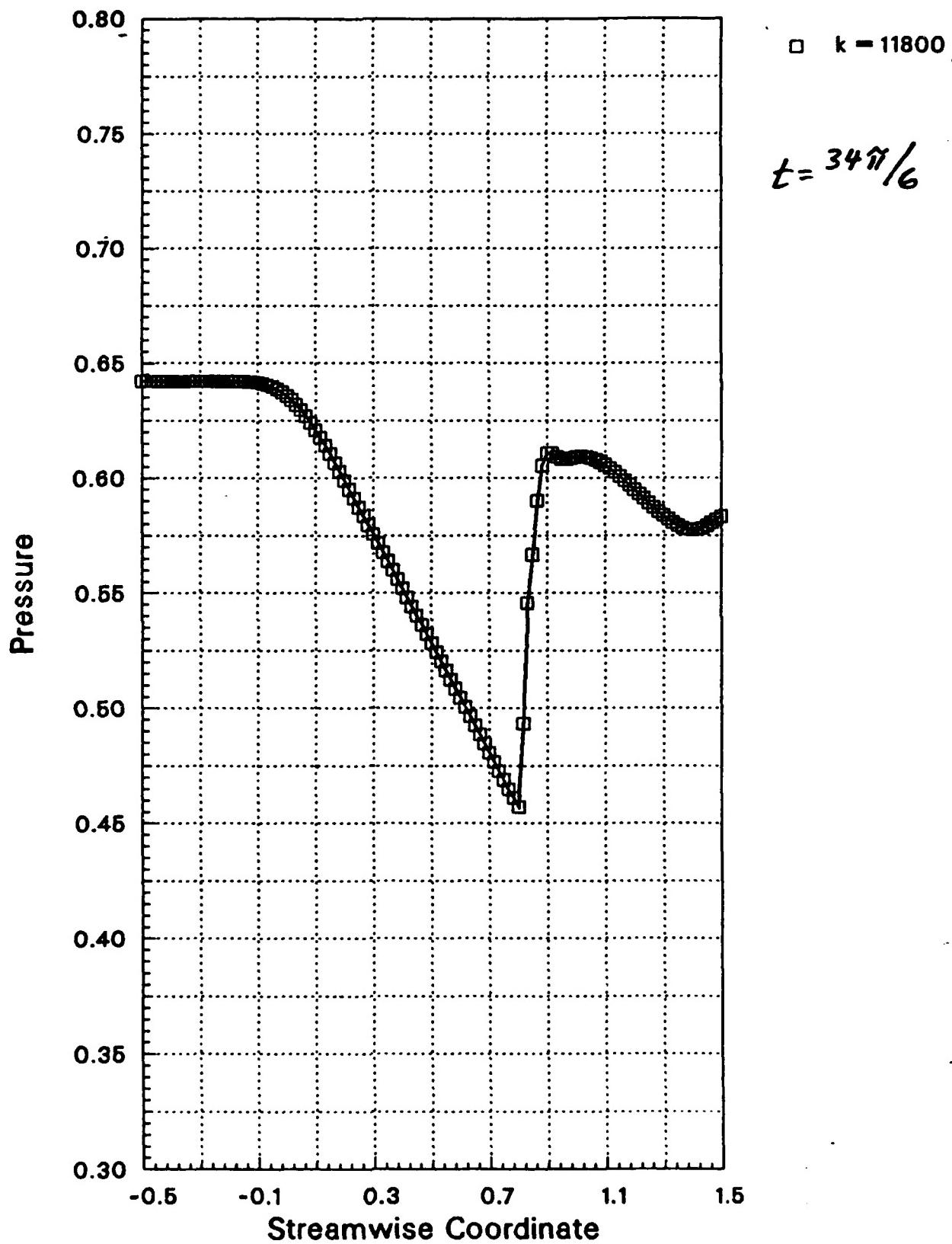


Fig. 5.2-4.24. Unsteady pressure distribution in a nozzle for $k=0.318$, $P_{e,amp}=0.05$. All other parameters as in Figs. 5.2-1.

RUN NUMBER = 427

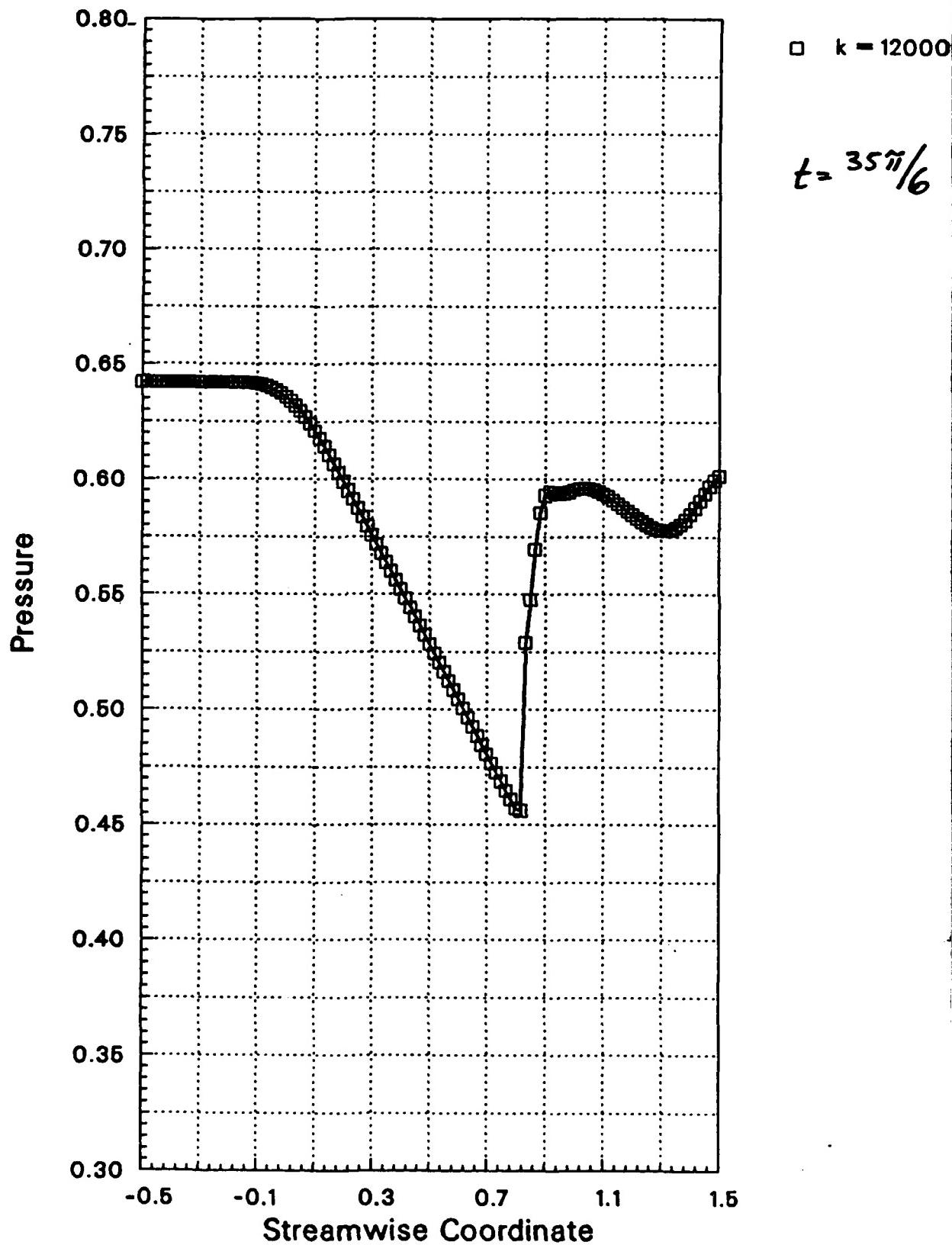


Fig. 5.2-4.25. Unsteady pressure distribution in a nozzle for $k=0.318$, $Pe_{amp}=0.05$. All other parameters as in Figs. 5.2-1.

RUN NUMBER = 427

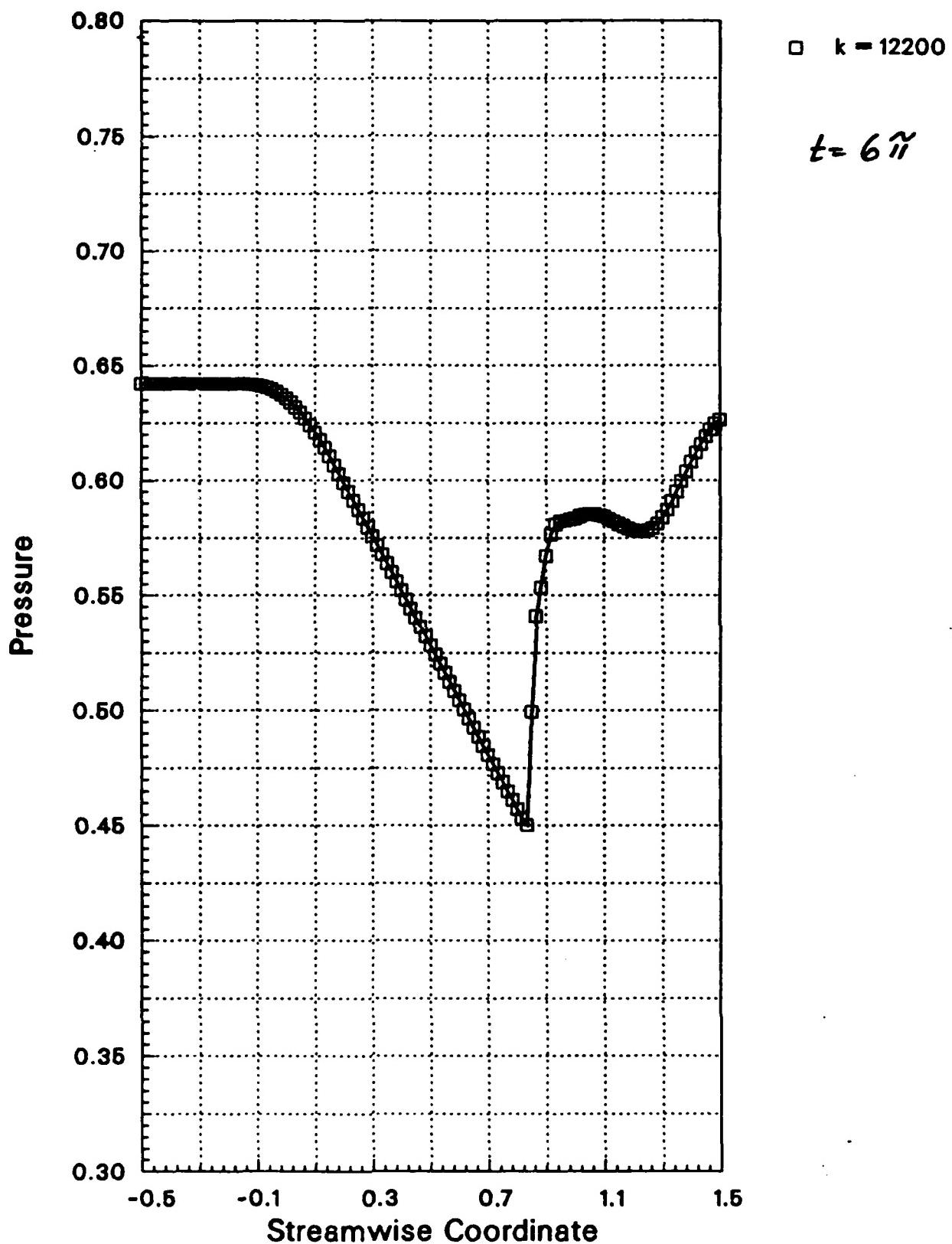


Fig. 5.2-4.26. Unsteady pressure distribution in a nozzle for $\kappa=0.318$, $P_{e,amp}=0.05$. All other parameters as in Figs. 5.2-1.

RUN NUMBER = 427

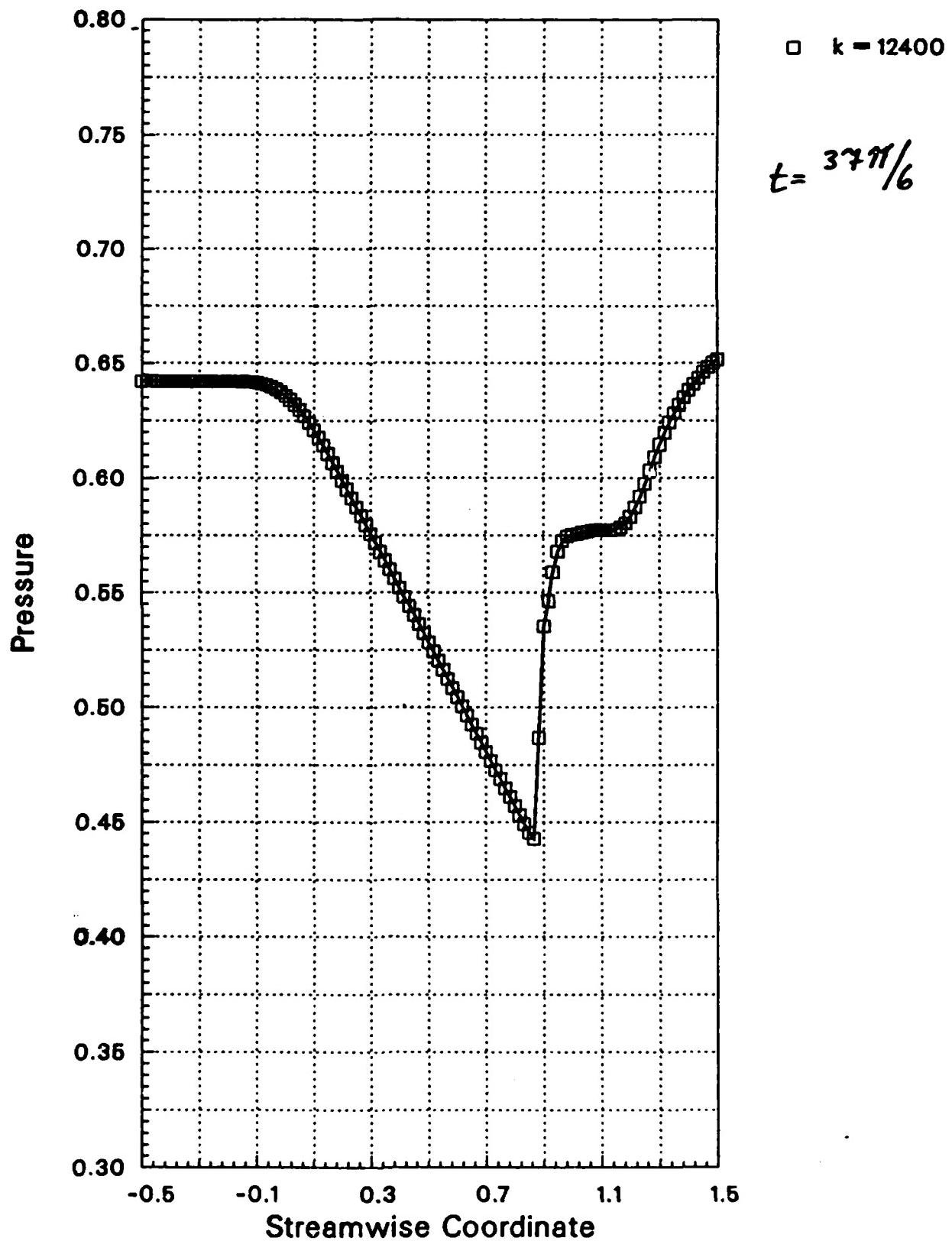


Fig. 5.2-4.27. Unsteady pressure distribution in a nozzle for $k=0.318$, $P_{e,amp}=0.05$. All other parameters as in Figs. 5.2-1.

RUN NUMBER = 427

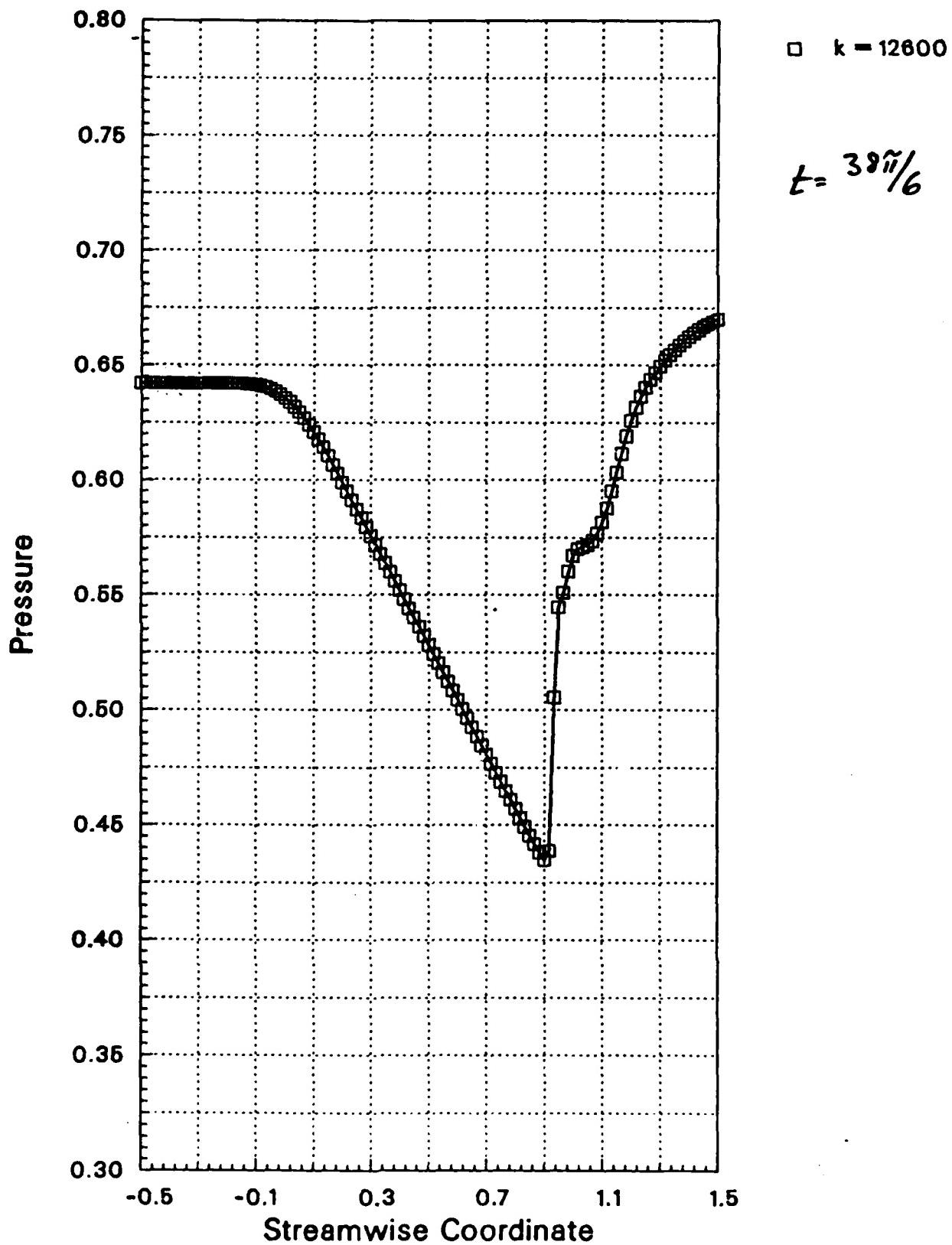


Fig. 5.2-4.28. Unsteady pressure distribution in a nozzle for $k=0.318$.
 $\rho_{e,amp}=0.05$. All other parameters as in Figs. 5.2-1.

RUN NUMBER = 427

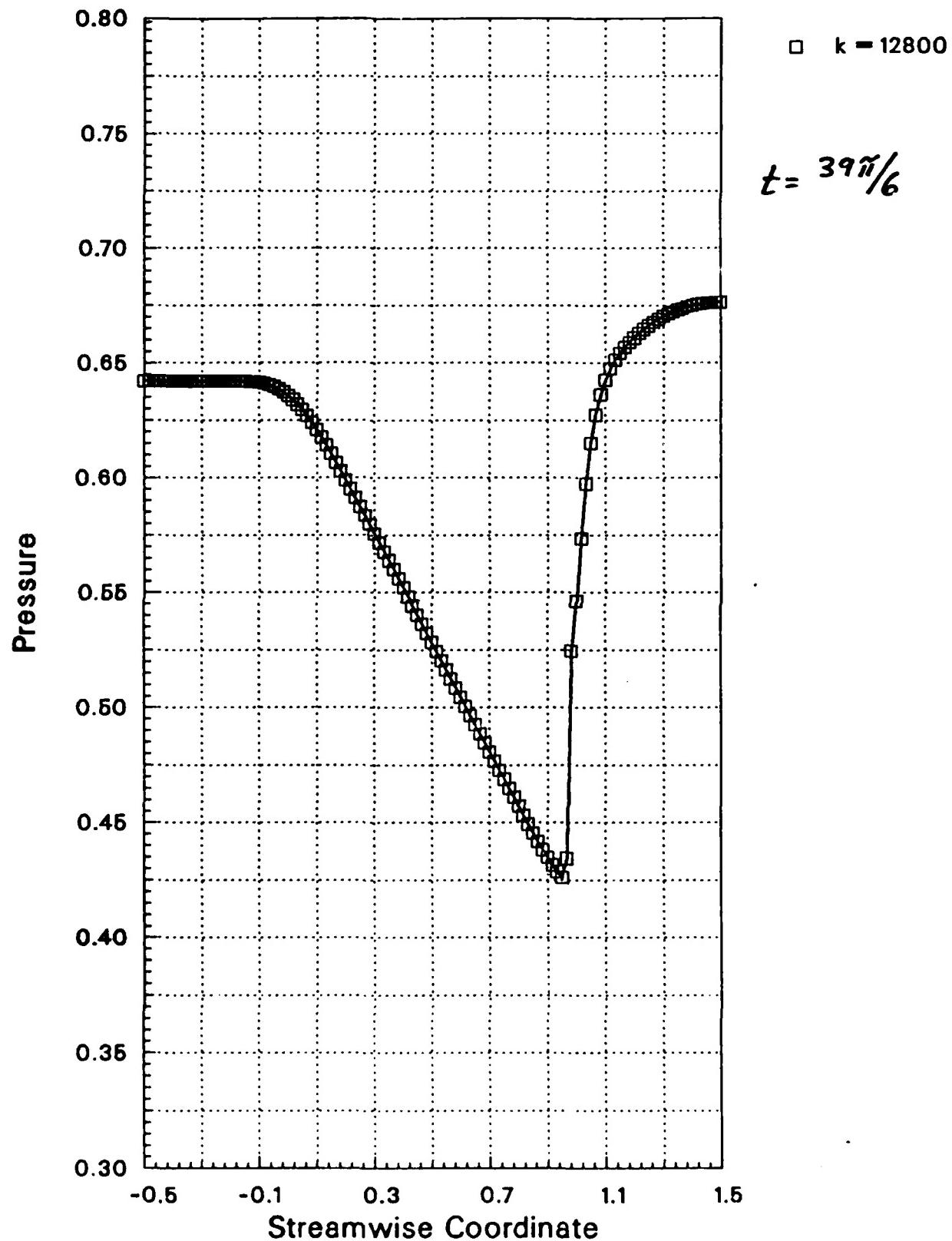


Fig. 5.2-4.29. Unsteady pressure distribution in a nozzle for $k=0.318$, $\rho_{e,amp}=0.05$. All other parameters as in Figs. 5.2-1.

RUN NUMBER = 427

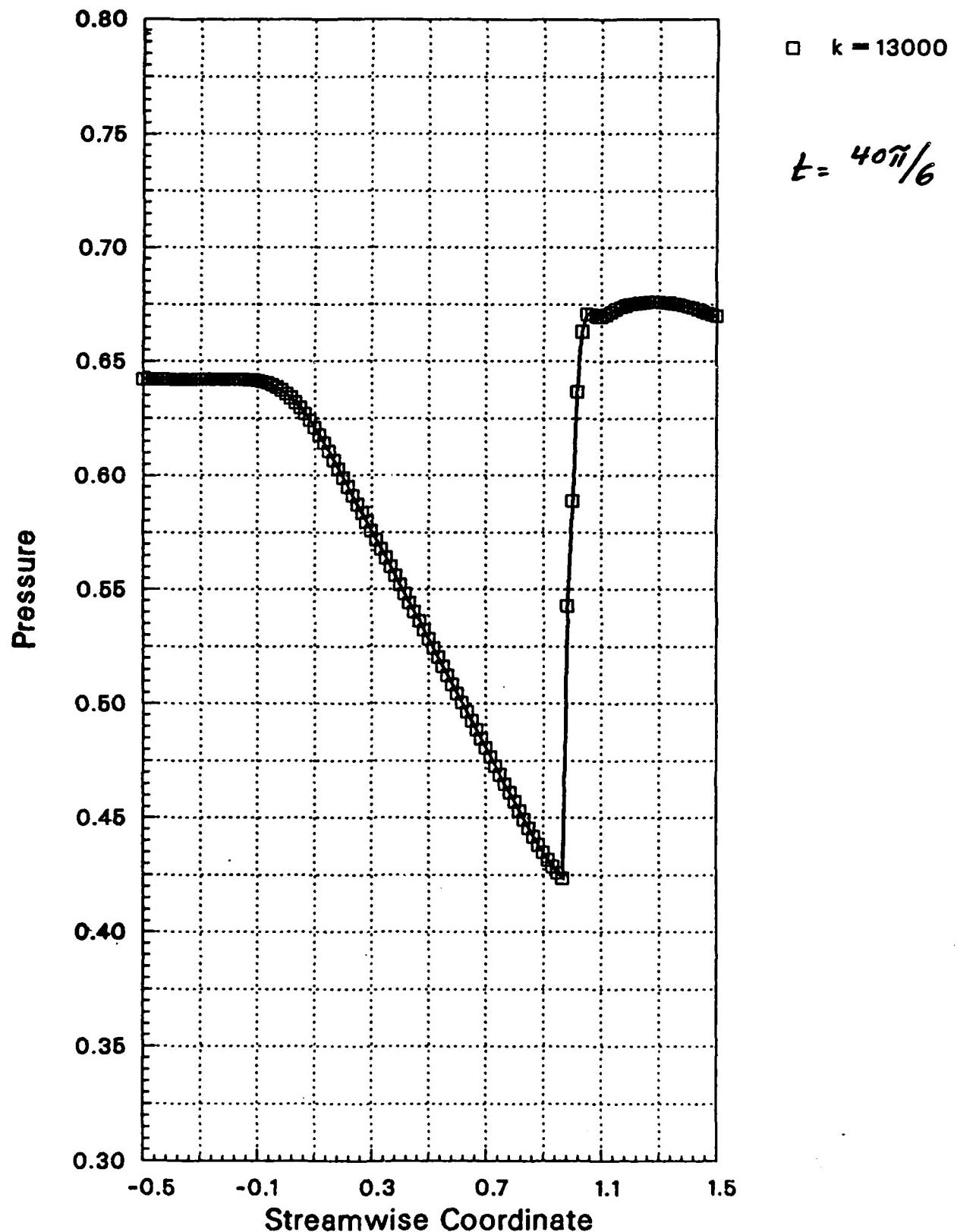


Fig. 5.2-4.30. Unsteady pressure distribution in a nozzle for $k=0.318$, $\rho_{e,amp}=0.05$. All other parameters as in Figs. 5.2-1.

RUN NUMBER = 427

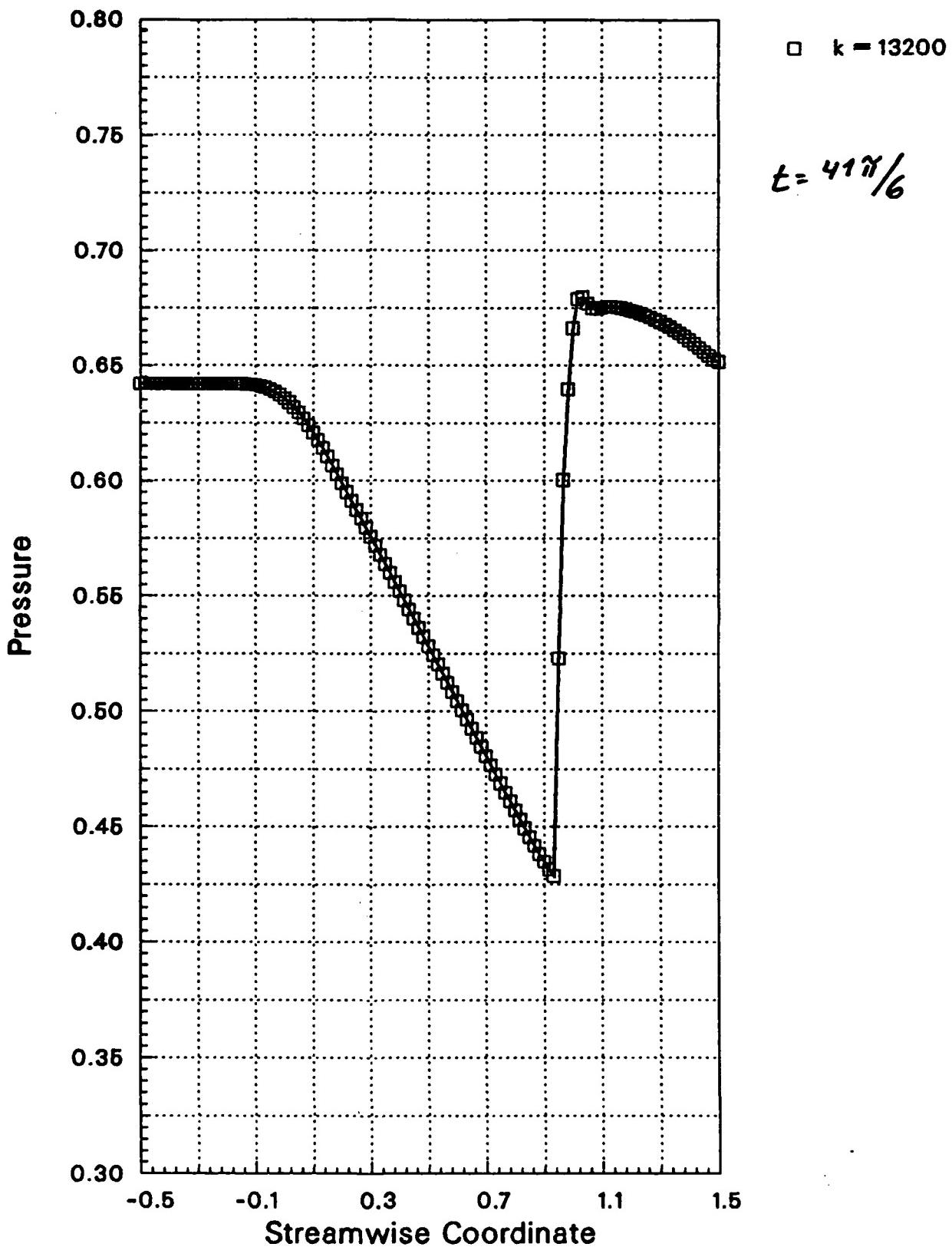


Fig. 5.2-4.31. Unsteady pressure distribution in a nozzle for $k=0.318$, $D_{e,amp}=0.05$. All other parameters as in Figs. 5.2-1.

RUN NUMBER = 427

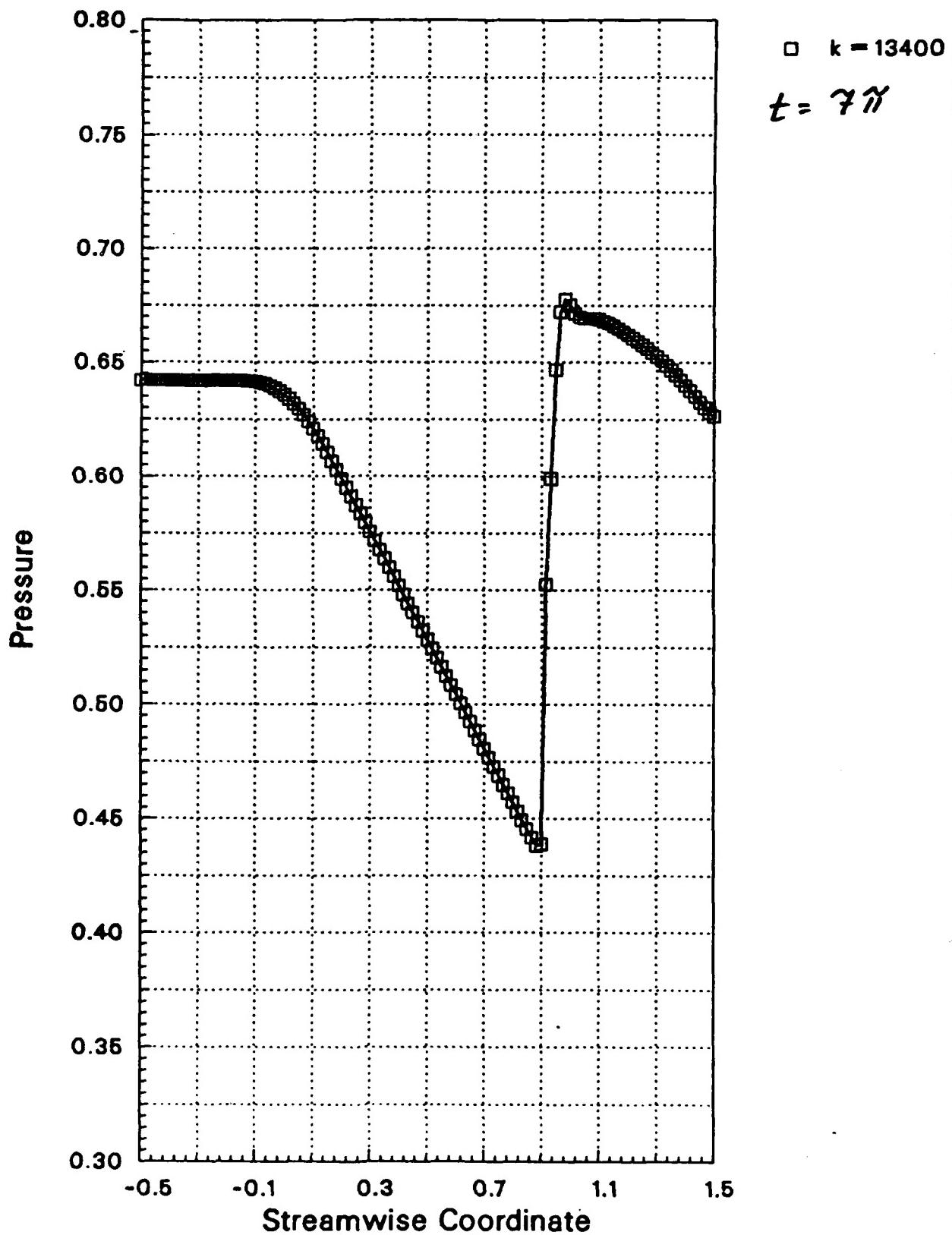


Fig. 5.2-4.32. Unsteady pressure distribution in a nozzle for $k=0.318$, $P_{e,amp}=0.05$. All other parameters as in Figs. 5.2-1.

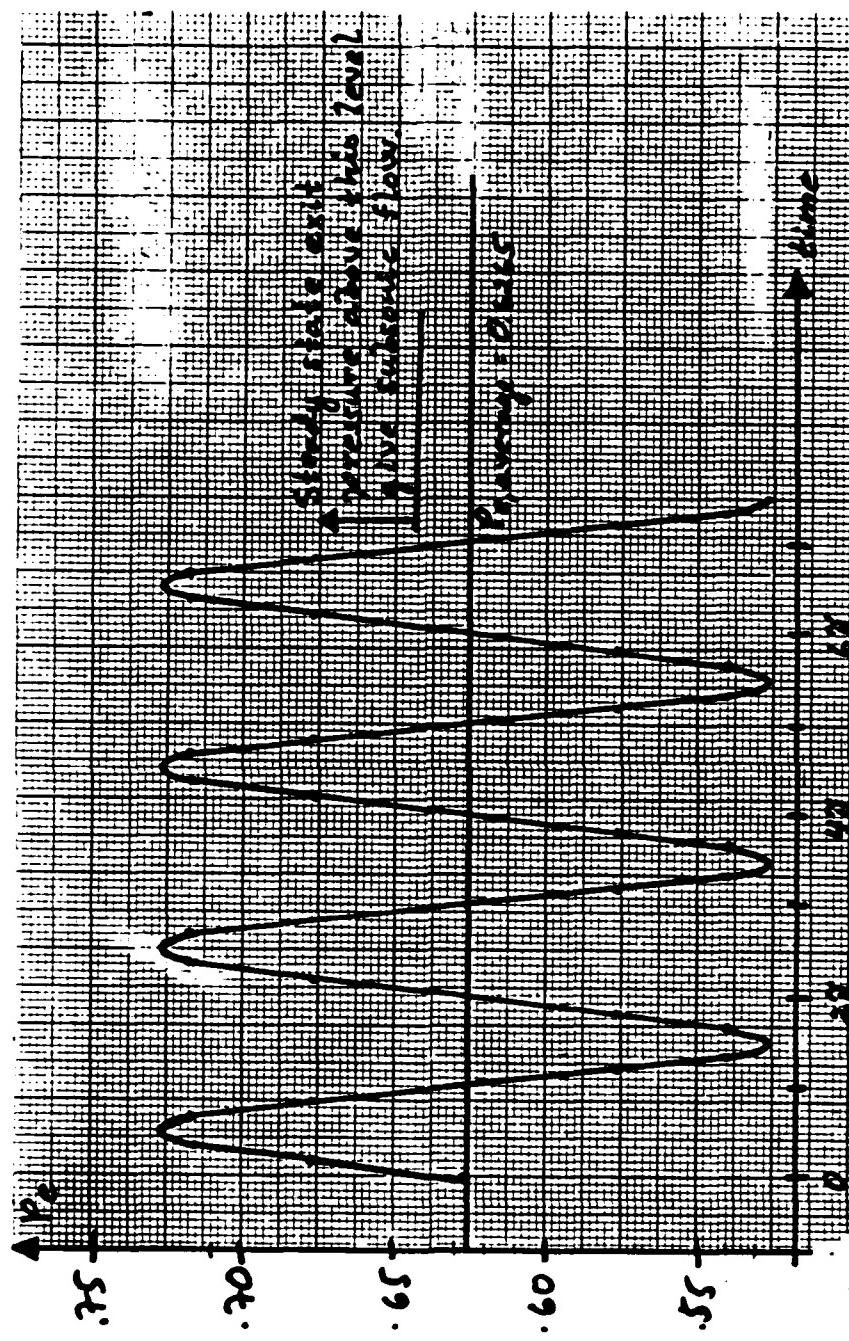


Fig. 5.2-5. Imposed exit pressure fluctuation for $k=0.318$,
 $P_{e,amp}=0, 10$. All other parameters as in Figs. 5.2-1.

RUN NUMBER = 426

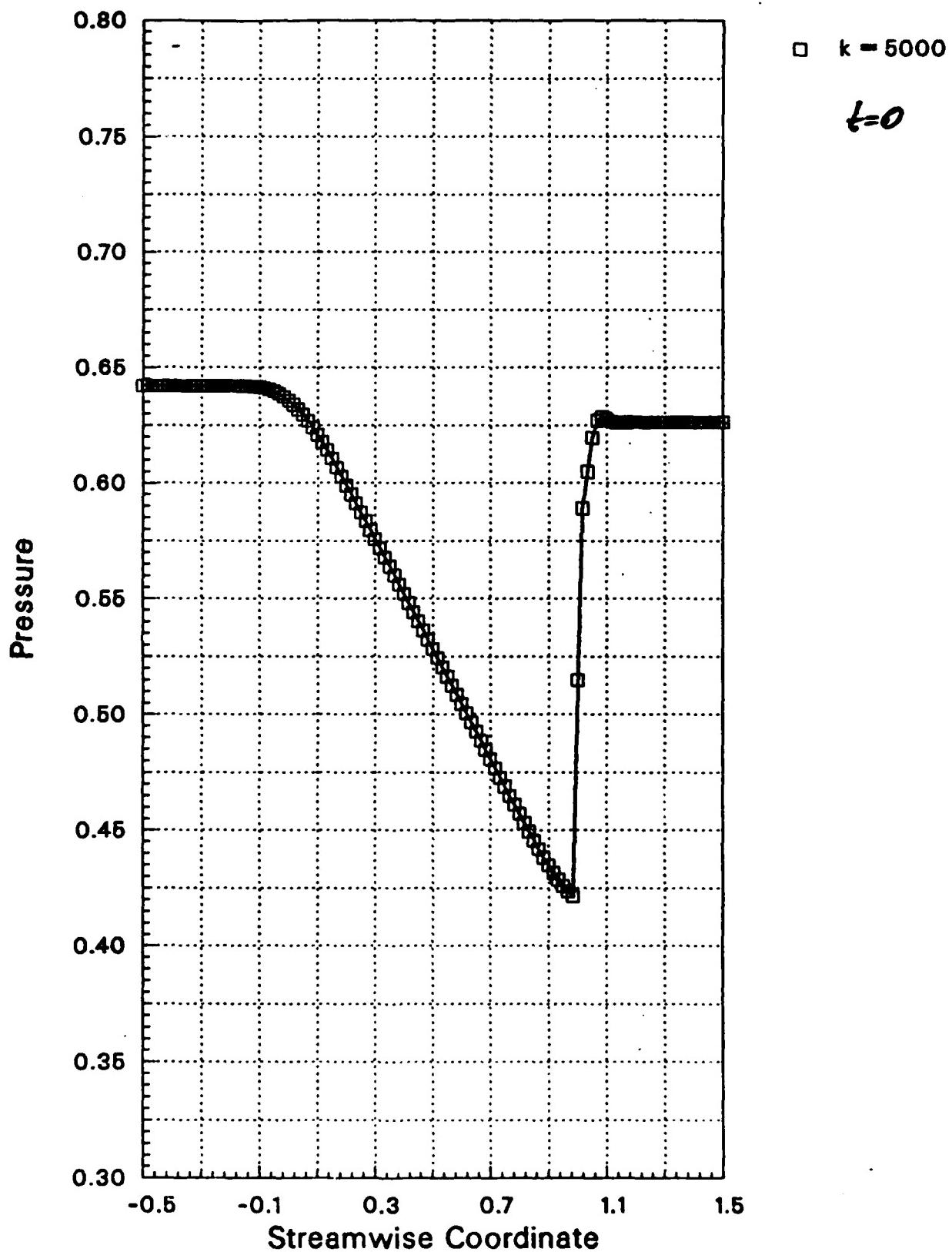


Fig. 5.2-5.2. Steady state pressure distribution in a nozzle for $k=0.318$, $P_{e,amp}=0.10$. All other parameters as in Figs. 5.2-1.

RUN NUMBER = 426

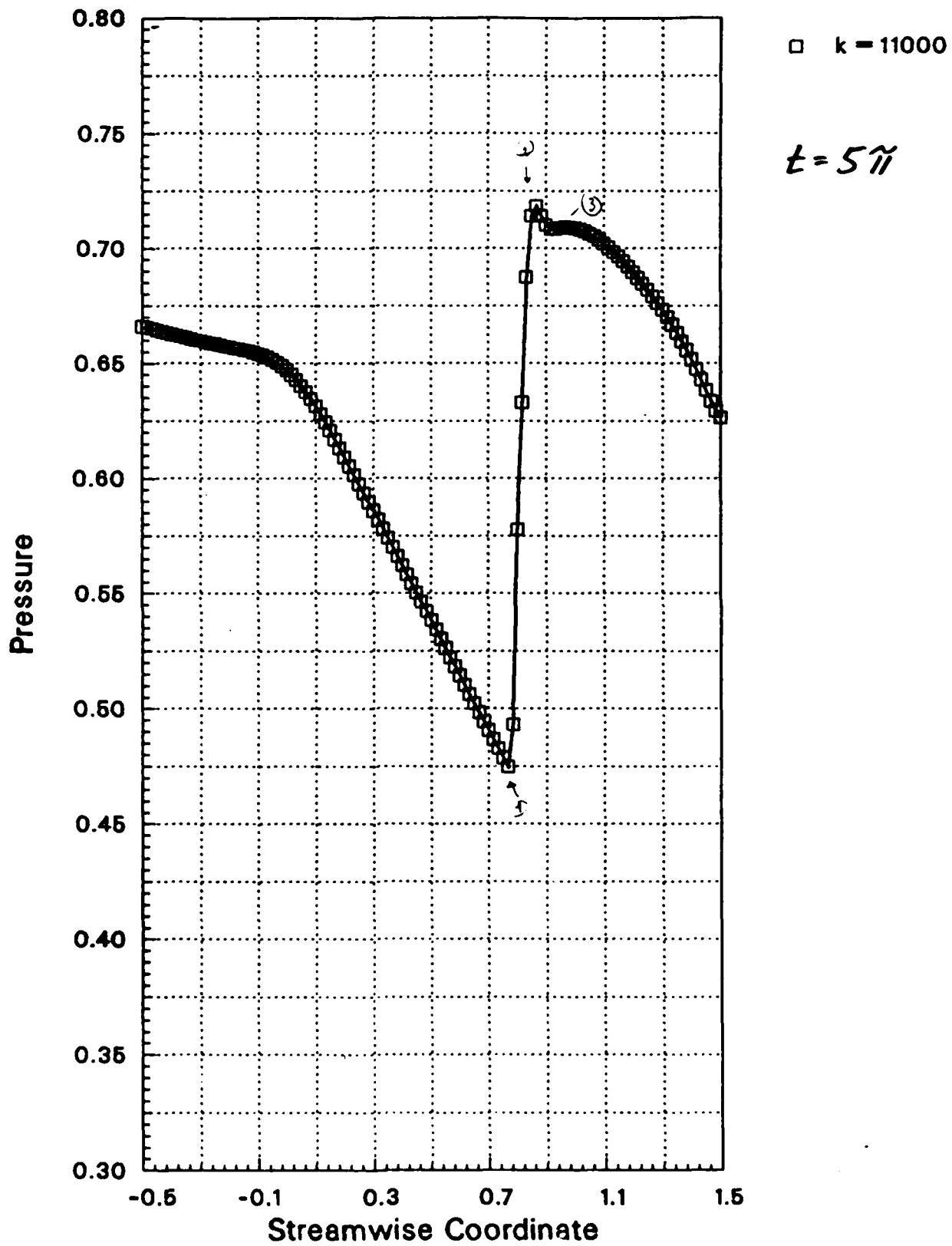


Fig. 5.2-5.3. Unsteady pressure distribution in a nozzle for $k=0.318$, $P_{e,amp}=0.10$. All other parameters as in Figs. 5.2-1.

RUN NUMBER = 426

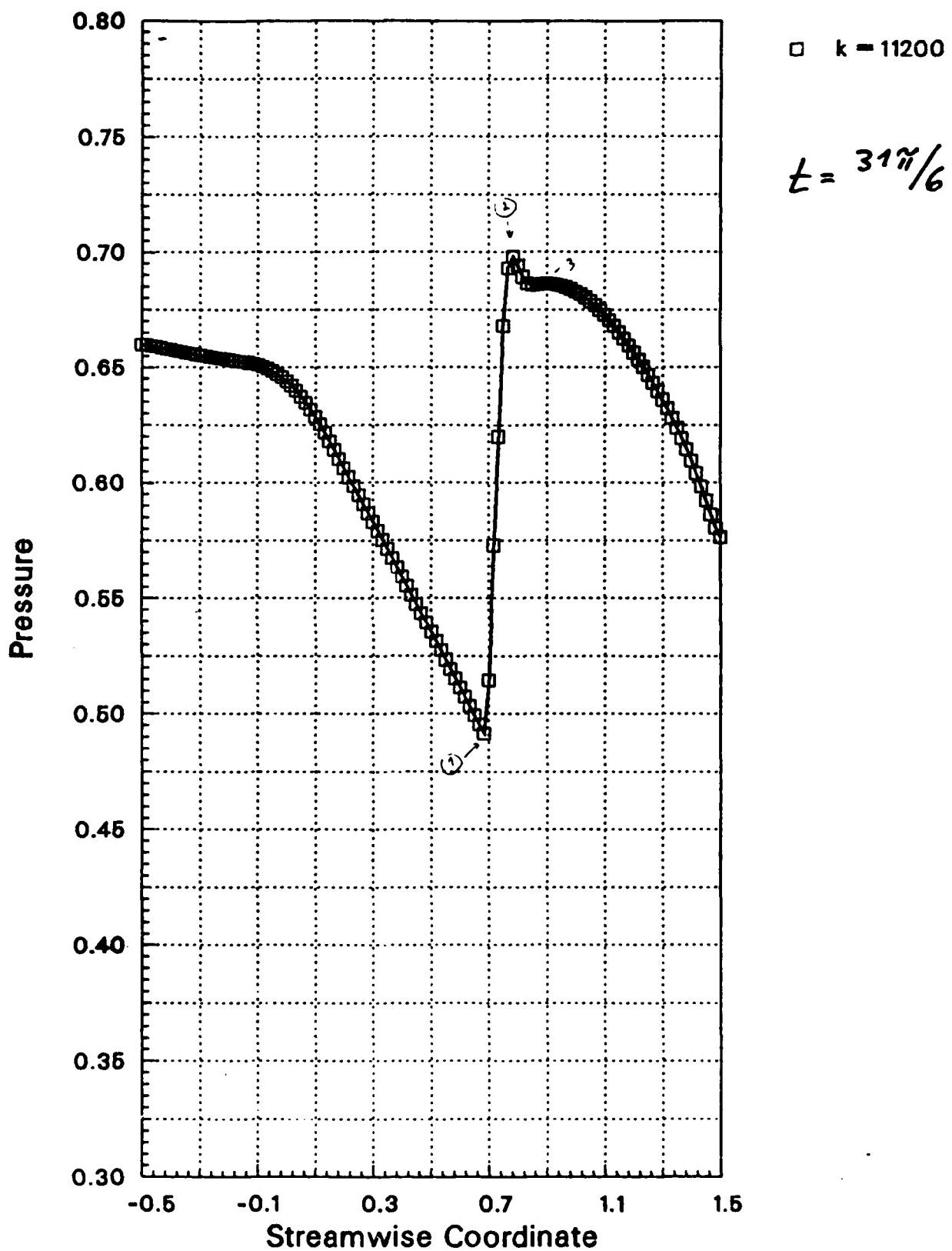


Fig. 5.2-5.4. unsteady pressure distribution in a nozzle for $k=0.516$,
 $\rho_{e,emp}=0.10$. All other parameters as in Figs. 5.2-1.

RUN NUMBER = 426

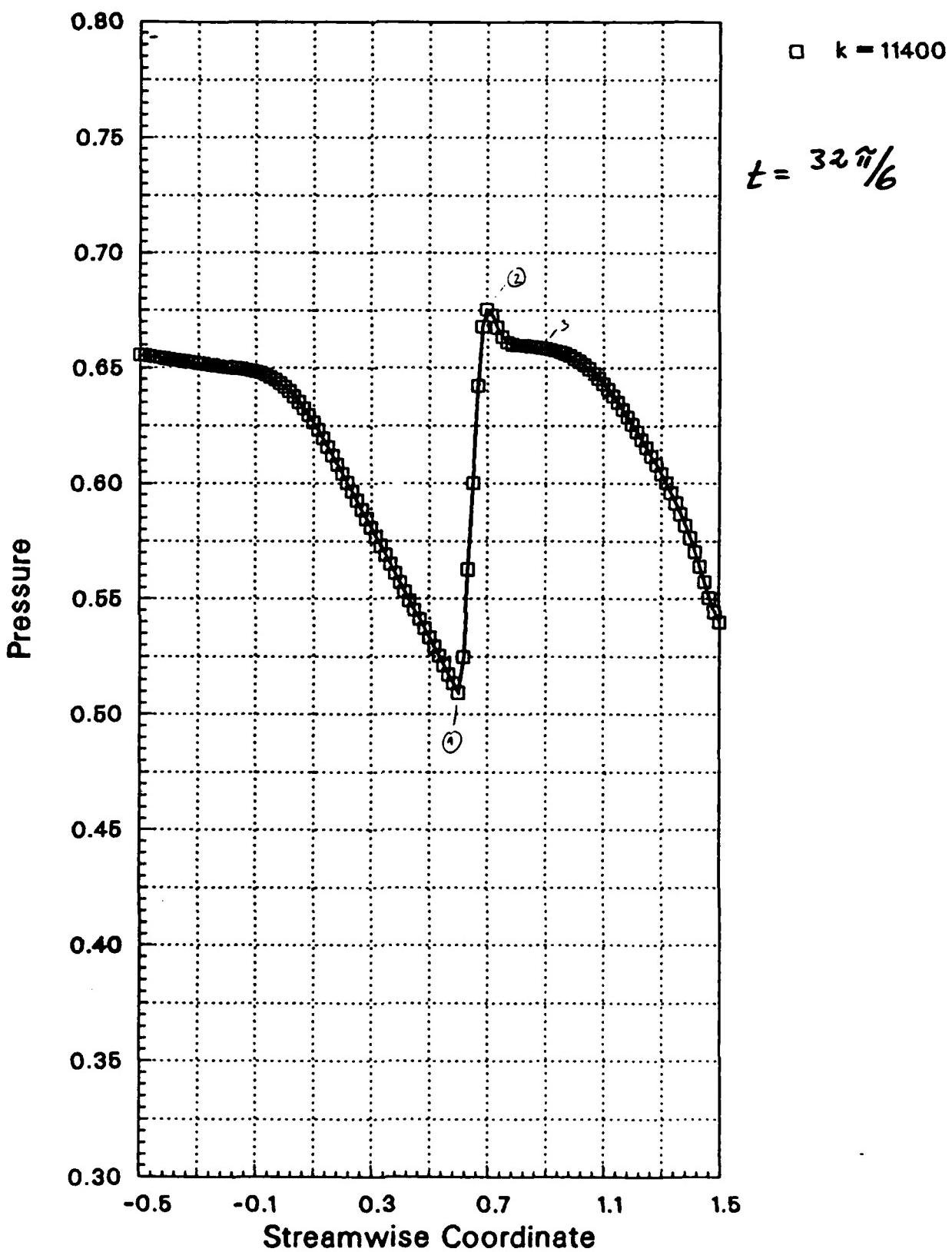


Fig. 5.2-5.5. Unsteady pressure distribution in a nozzle for $k=0.318$, $P_{e,amp}=0.10$. All other parameters as in Figs. 5.2-1.

RUN NUMBER = 426

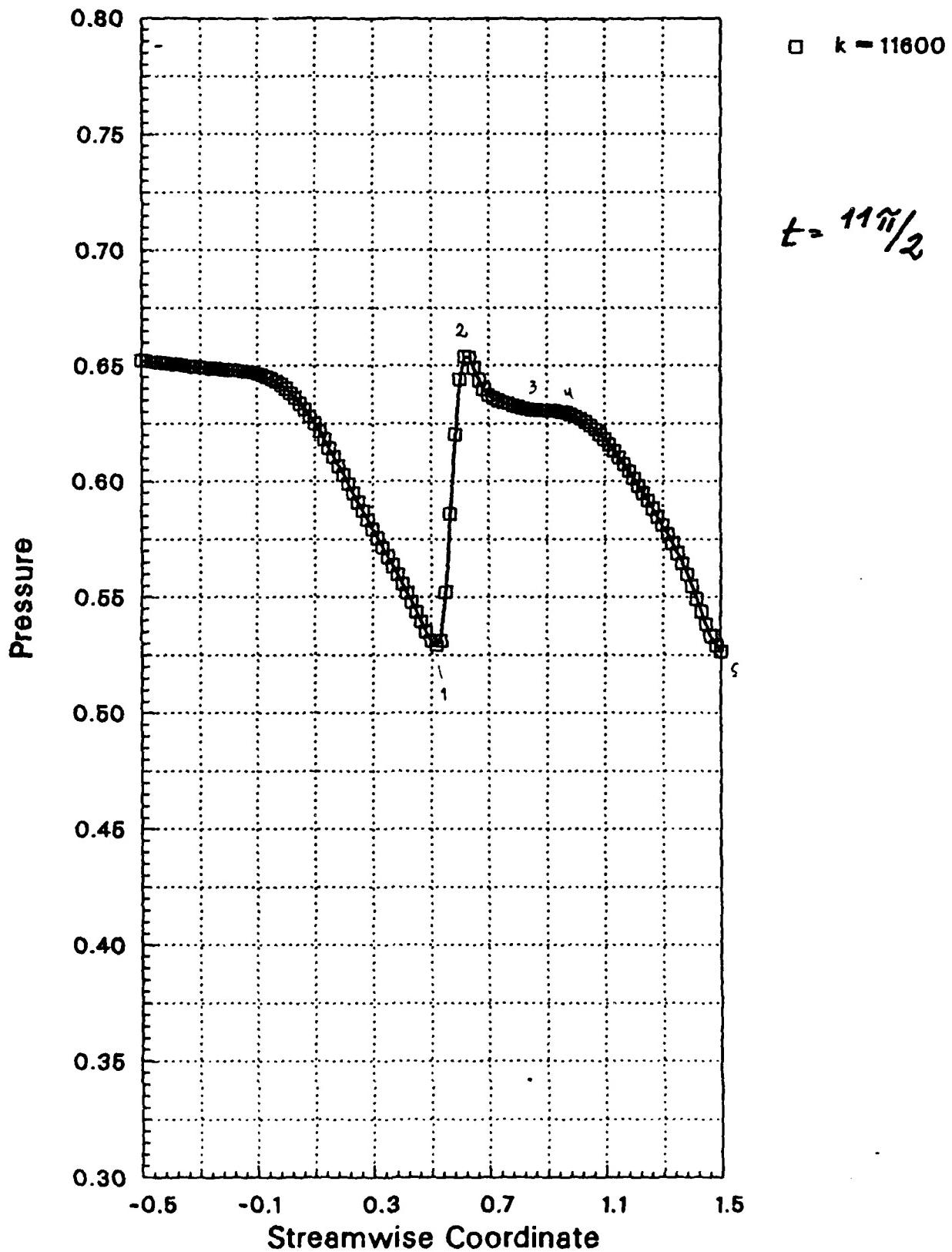


Fig. 5.2-5.6. Unsteady pressure distribution in a nozzle for $k=0.318$, $P_{e,amp}=0.10$. All other parameters as in Figs. 5.2-1.

RUN NUMBER = 426

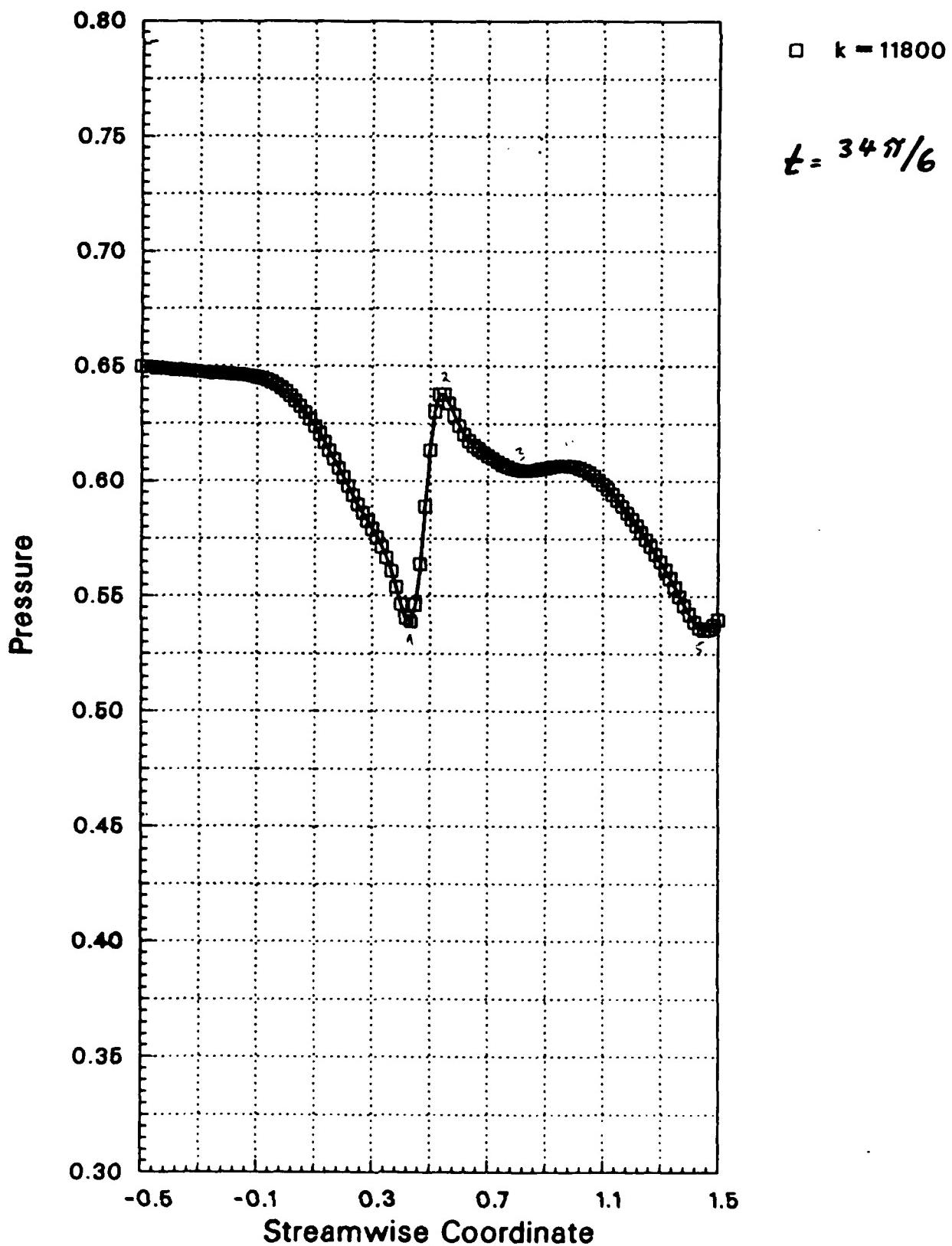


Fig. 5.2-5.7. Unsteady pressure distribution in a nozzle for $k=0.318$, $\rho_{e,amp}=0.10$. All other parameters as in Figs. 5.2-1.

RUN NUMBER = 426

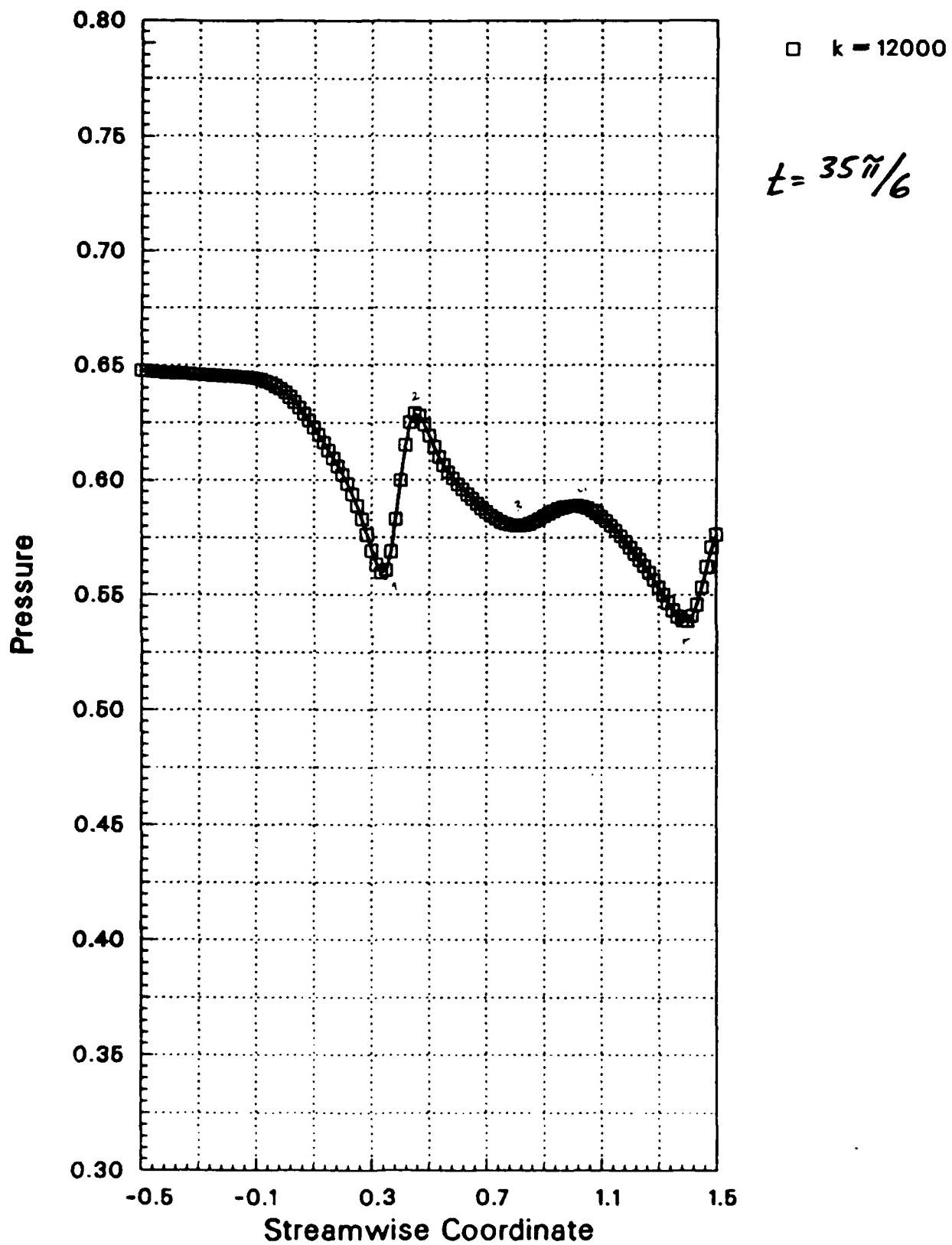


Fig. 5.2-5.8. unsteady pressure distribution in a nozzle for $k=0.318$, $\rho_{e,amp}=0.10$. All other parameters as in Figs. 5.2-1.

RUN NUMBER = 426

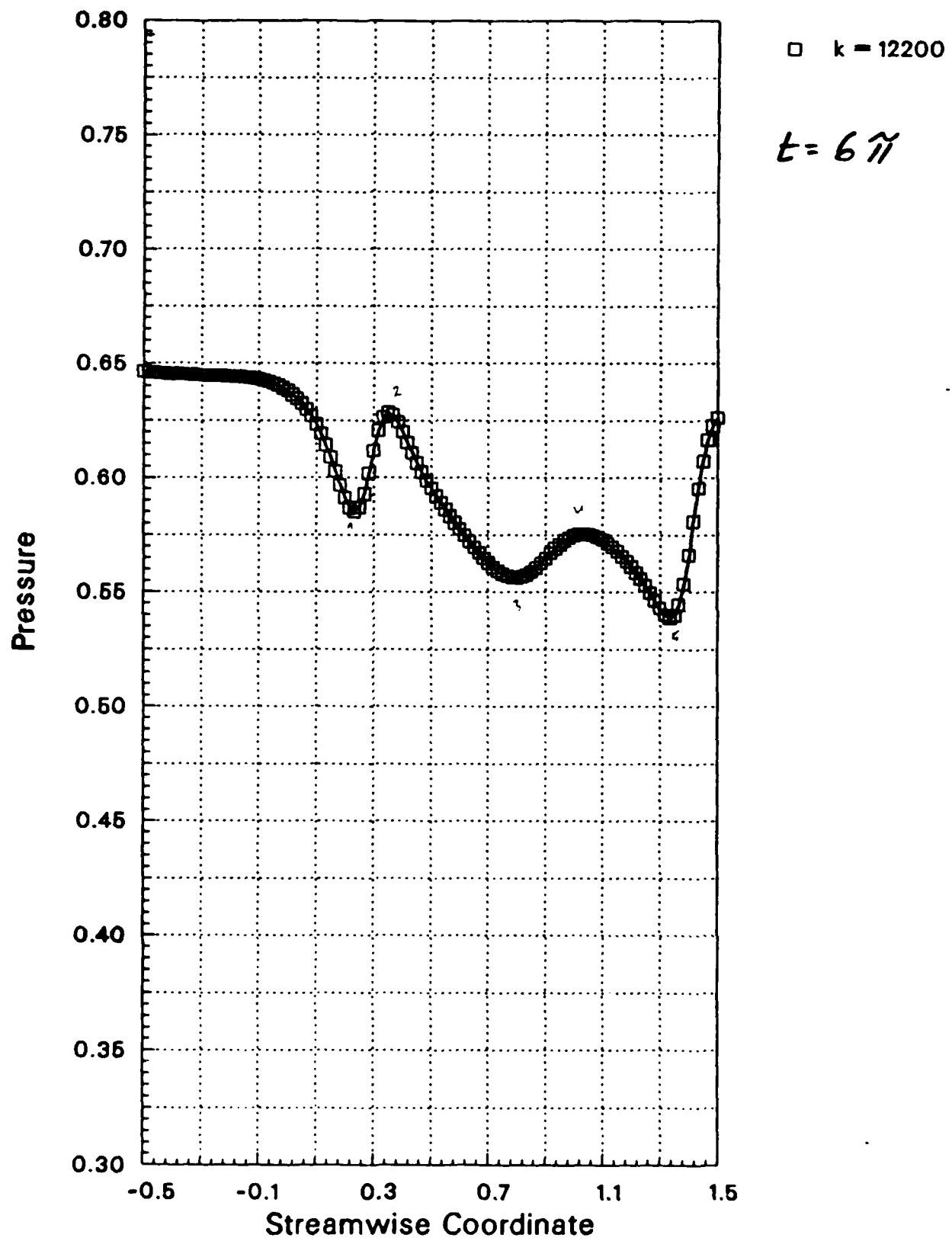


Fig. 5.2-5.9. Unsteady pressure distribution in a nozzle for $k=0.313$, $De_{amp}=0.10$. All other parameters as in Figs. 5.2-1.

RUN NUMBER = 426

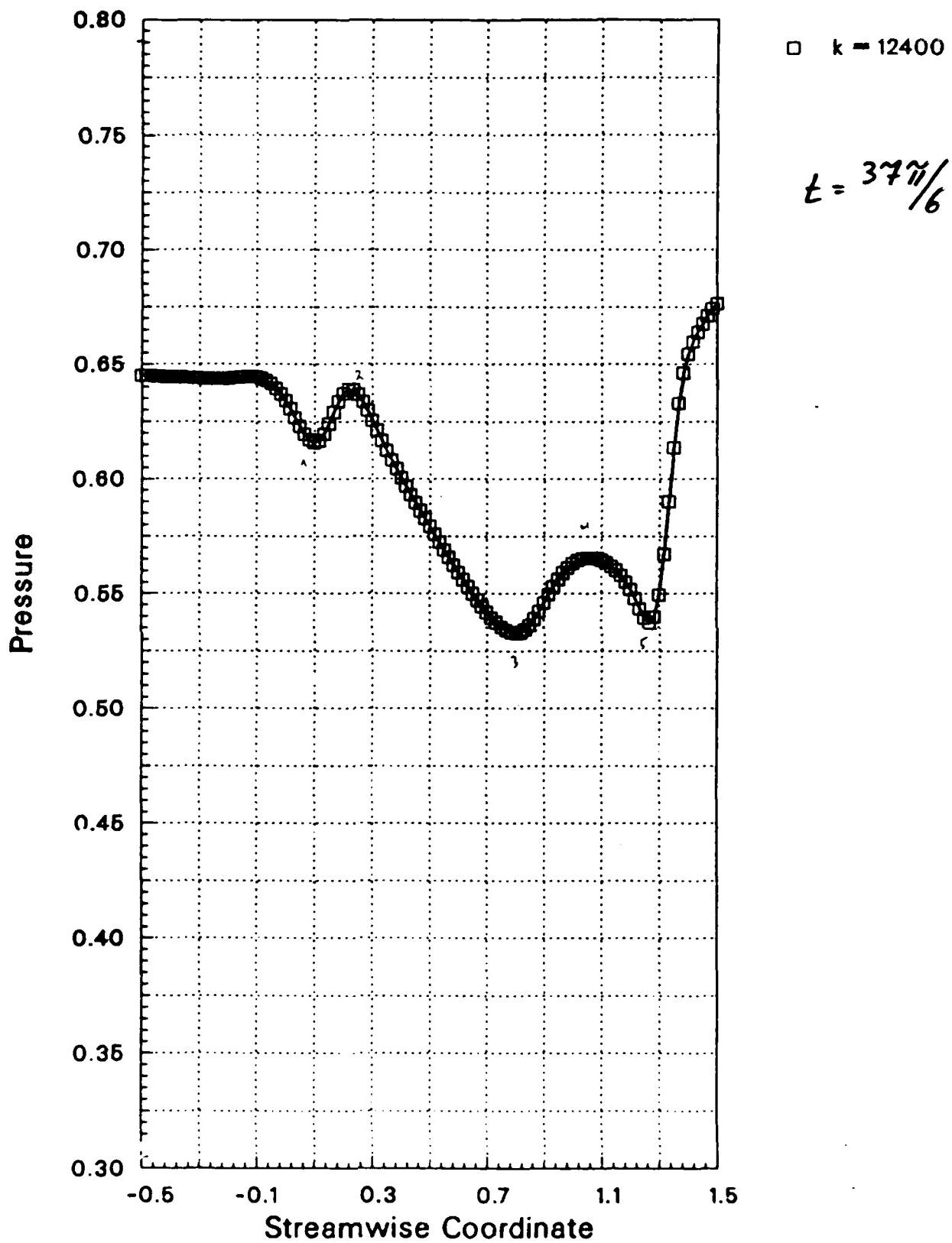


Fig. 5.2-5.10. Unsteady pressure distribution in a nozzle for $k=0.318$, $P_{e,amp}=0.10$. All other parameters as in Figs. 5.2-1.

RUN NUMBER = 426

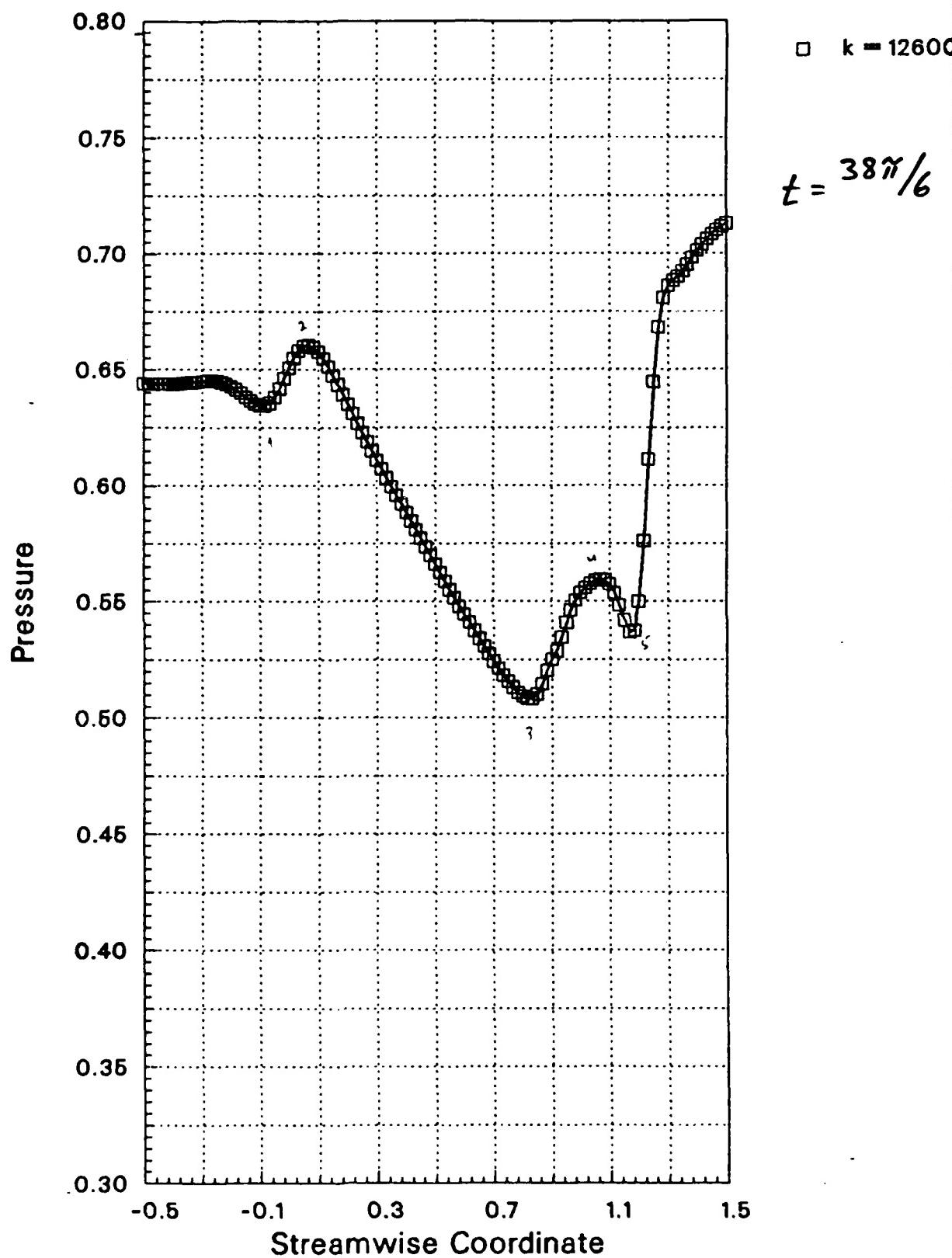


Fig. 5.2-5.11. Unsteady pressure distribution in a nozzle for $k=0.318$, $P_{e,amp}=0.10$. All other parameters as in Figs. 5.2-1.

RUN NUMBER = 426

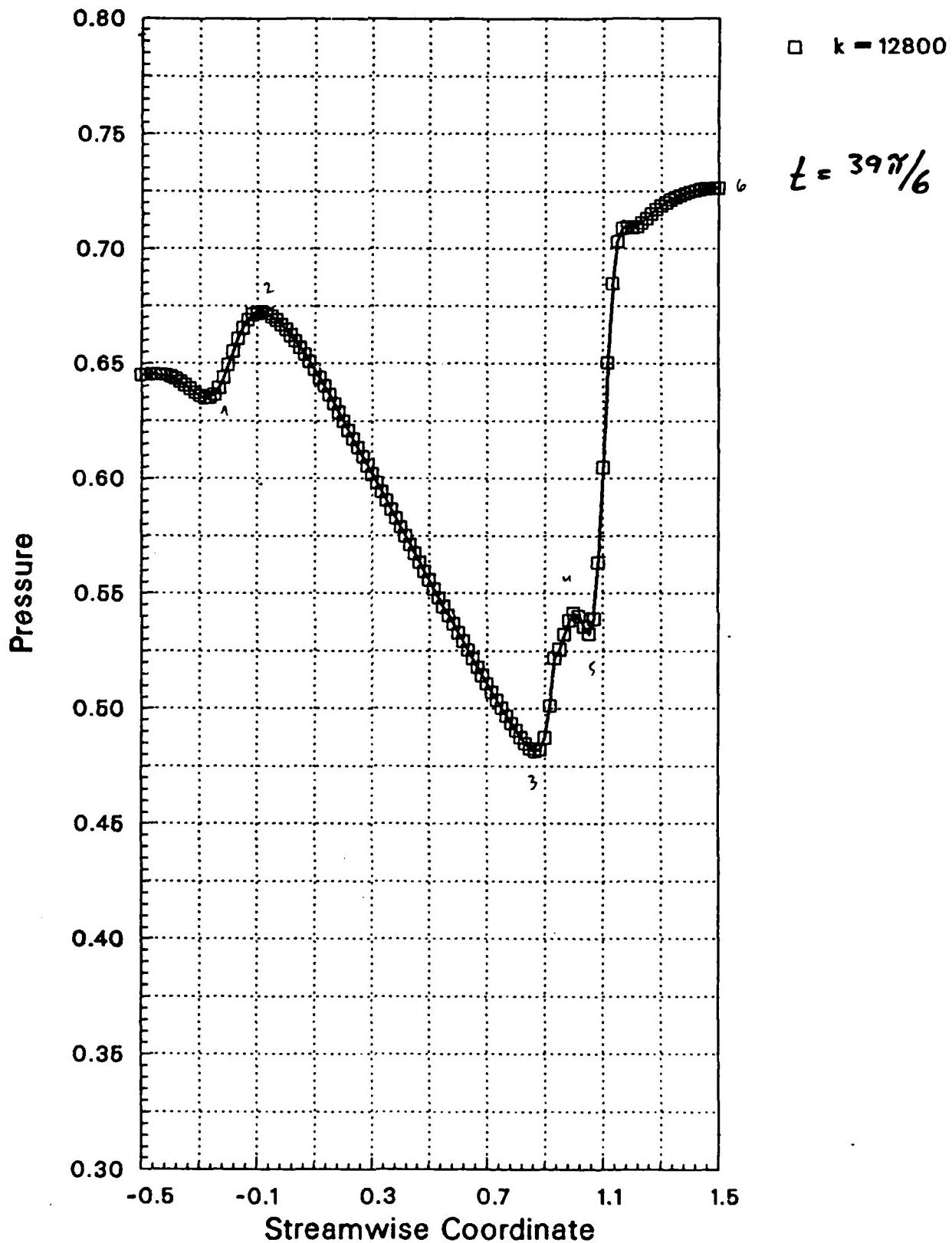


Fig. 5.2-5.12. Unsteady pressure distribution in a nozzle for $k=0.318$, $p_{\theta,\text{amp}}=0.10$. All other parameters as in Figs. 5.2-1.

RUN NUMBER = 426

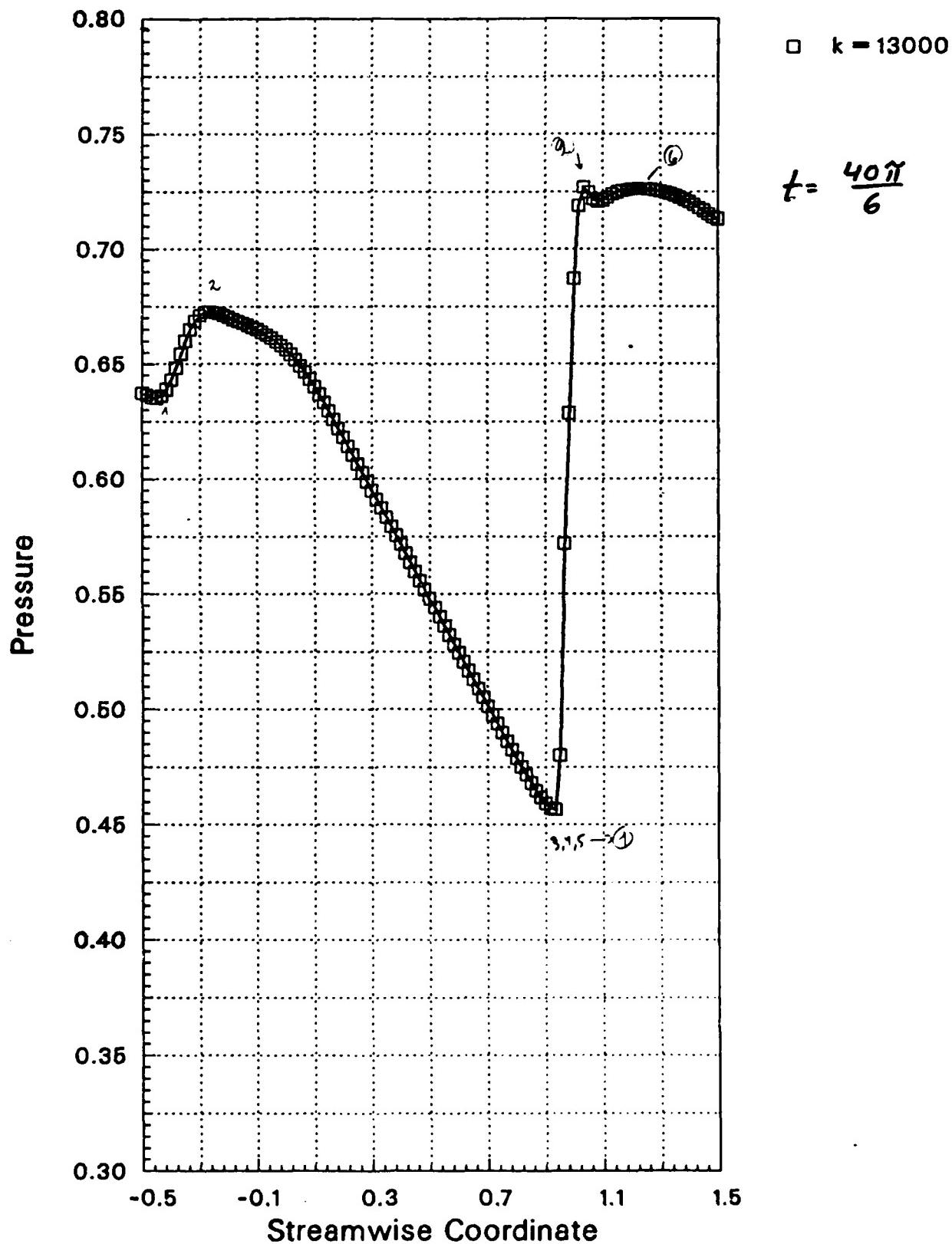


Fig. 5.2-5.13. Unsteady pressure distribution in a nozzle for $k=0.518$. $P_{e,amp}=0.10$. All other parameters as in Figs. 5.2-1.

RUN NUMBER = 426

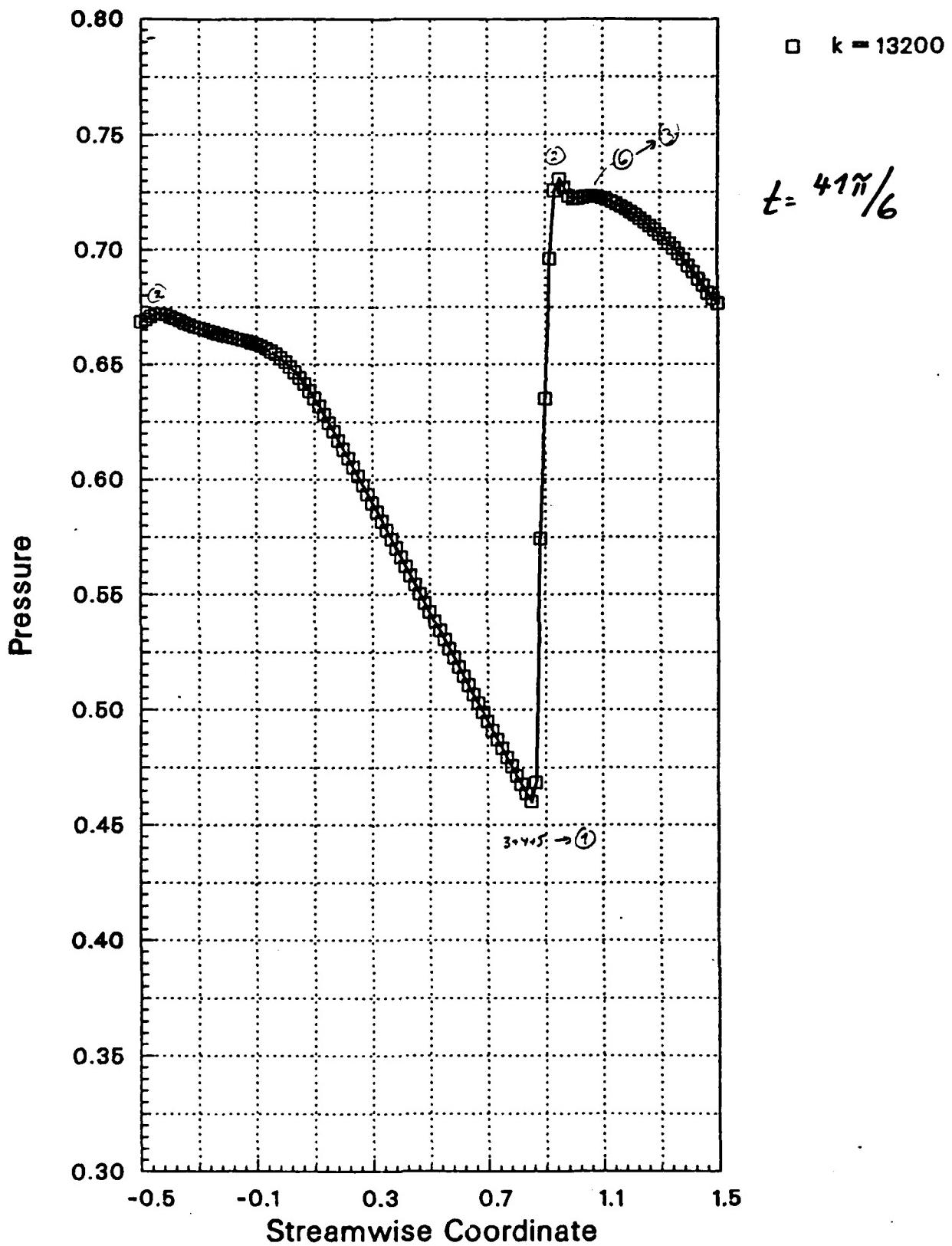


Fig. 5.2-5.14. Unsteady pressure distribution in a nozzle for $k=0.318$, $P_{e,amp}=0.10$. All other parameters as in Figs. 5.2-1.

RUN NUMBER = 426

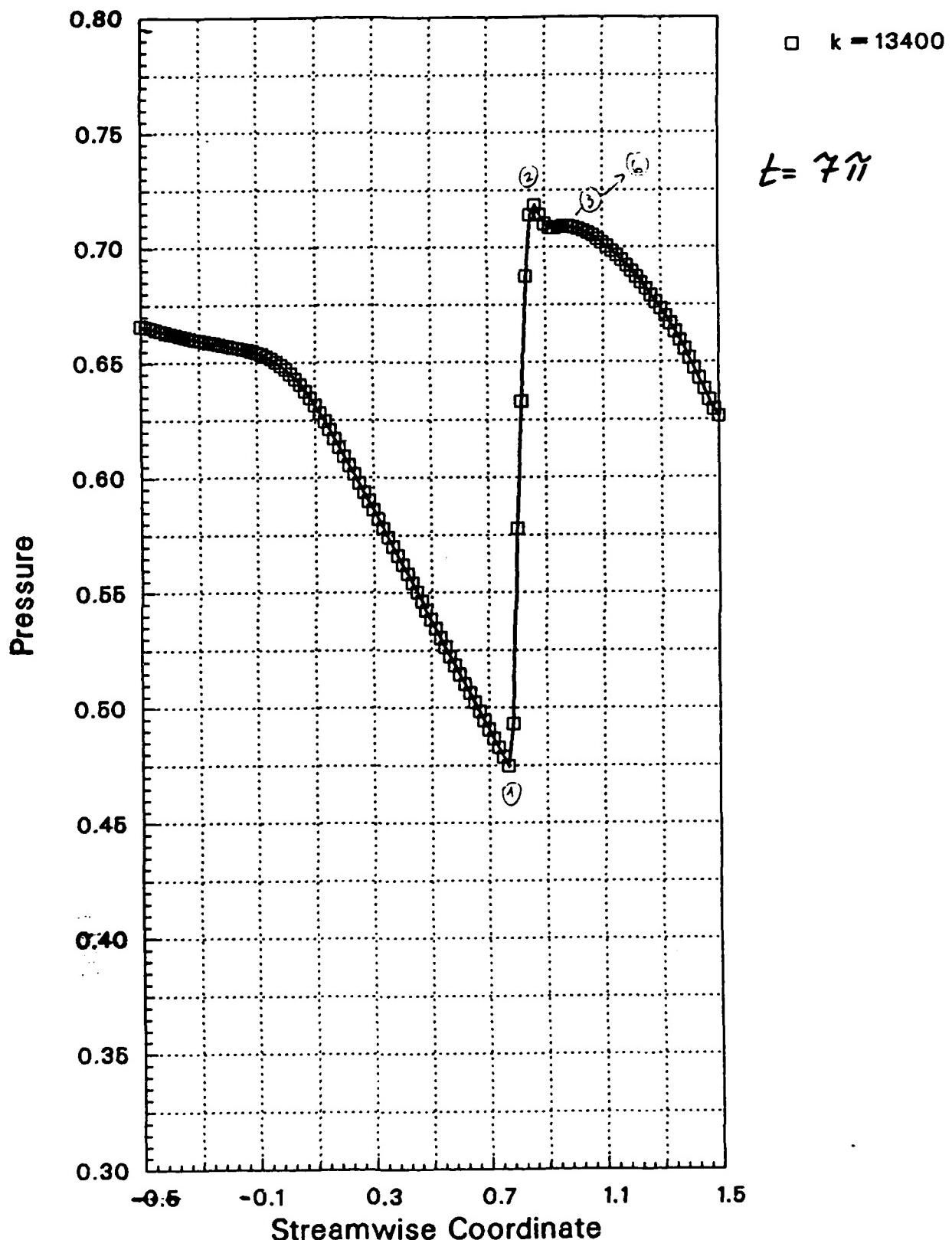


Fig. 5.2-5.15. Unsteady pressure distribution in a nozzle for $k=0.318$, $P_{e,amp}=0.10$. All other parameters as in Figs. 5.2-1.

RUN NUMBER = 426

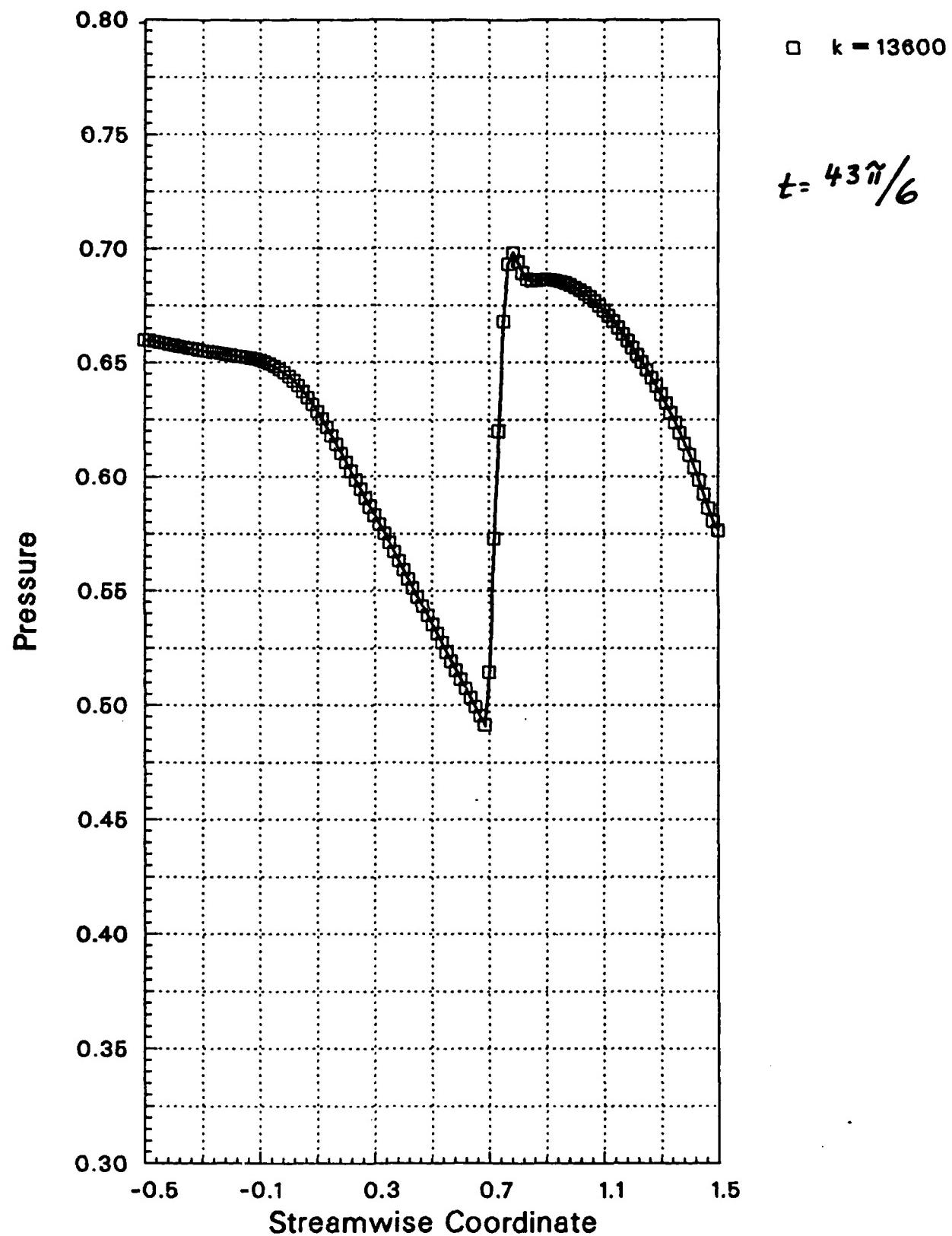


Fig. 5.2-5.16. Unsteady pressure distribution in a nozzle for $k=0.318$, $P_{e,amp}=0.10$. All other parameters as in Figs. 5.2-1.

RUN NUMBER = 426

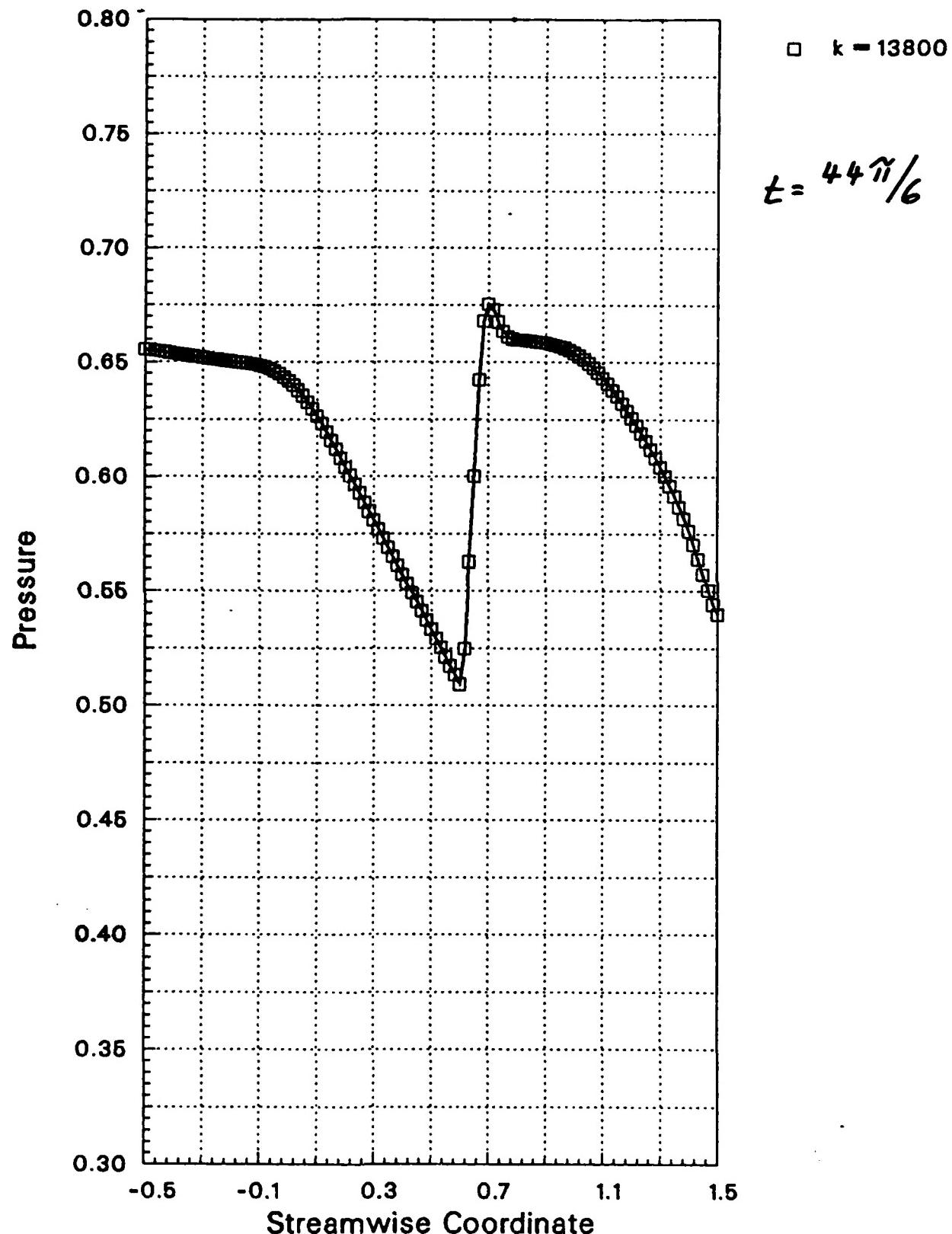


Fig. 5.2-5.17. Unsteady pressure distribution in a nozzle for $k=0.318$, $p_{e,amp}=0.10$. All other parameters as in Figs. 5.2-1.

RUN NUMBER = 426

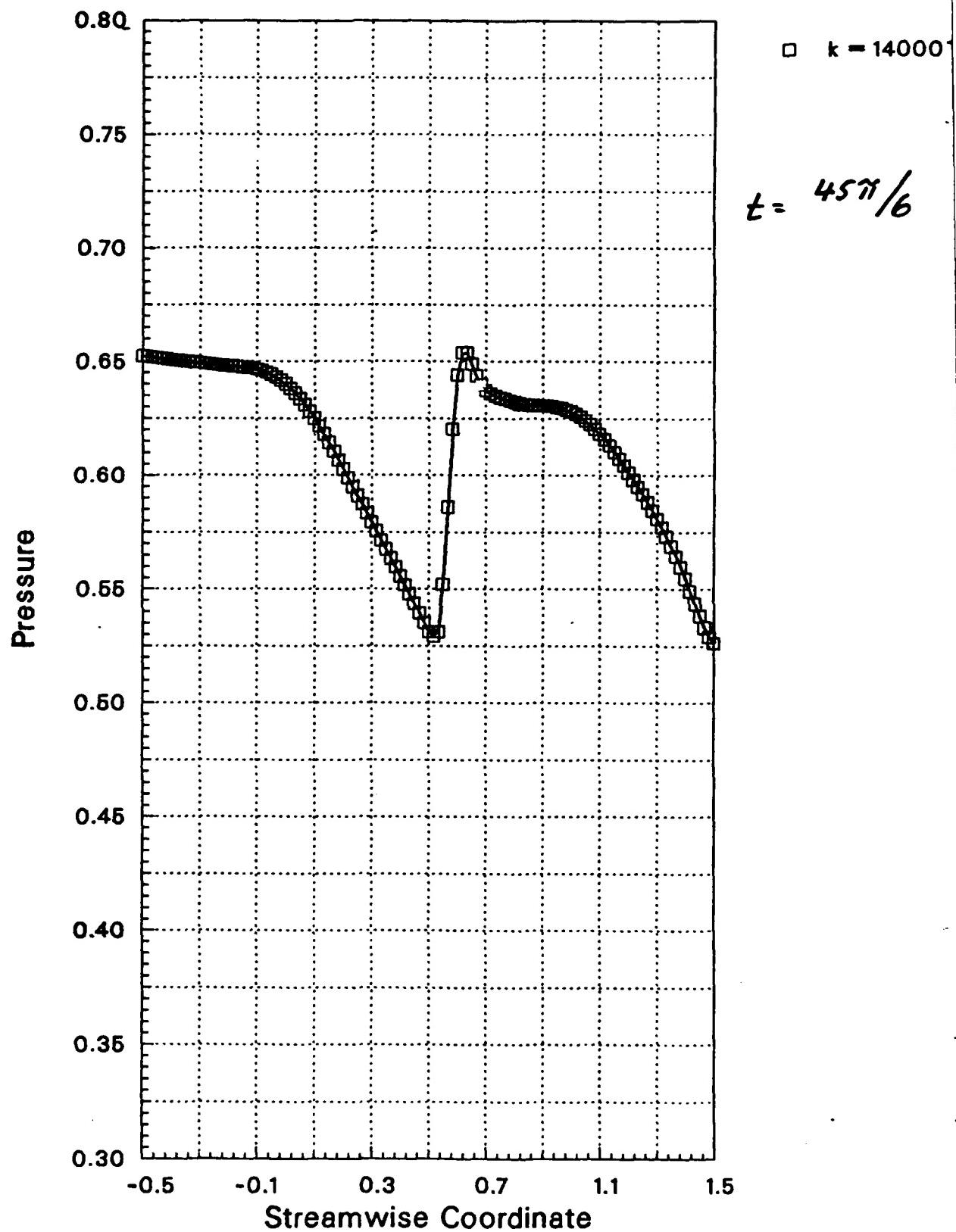


Fig. 5.2-5.18. Unsteady pressure distribution in a nozzle for $k=0.318$, $p_{e,amp}=0.10$. All other parameters as in Figs. 5.2-1.

RUN NUMBER = 433

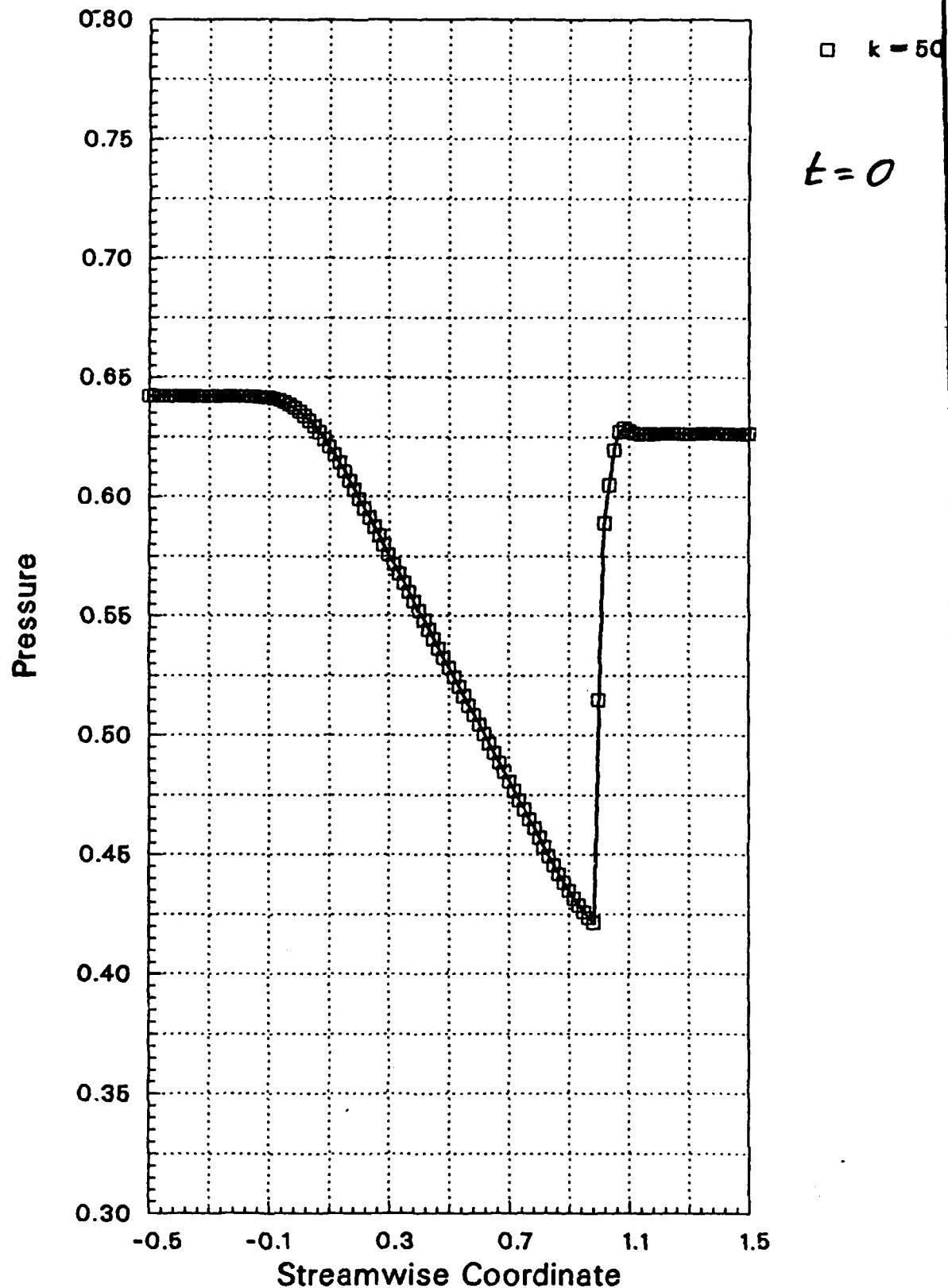


Fig. 5.2-6.1. Steady state pressure distribution in a nozzle for $k=0.106$, $P_{e,amp}=0.05$. All other parameters as in Figs. 5.2-1.

RUN NUMBER = 433

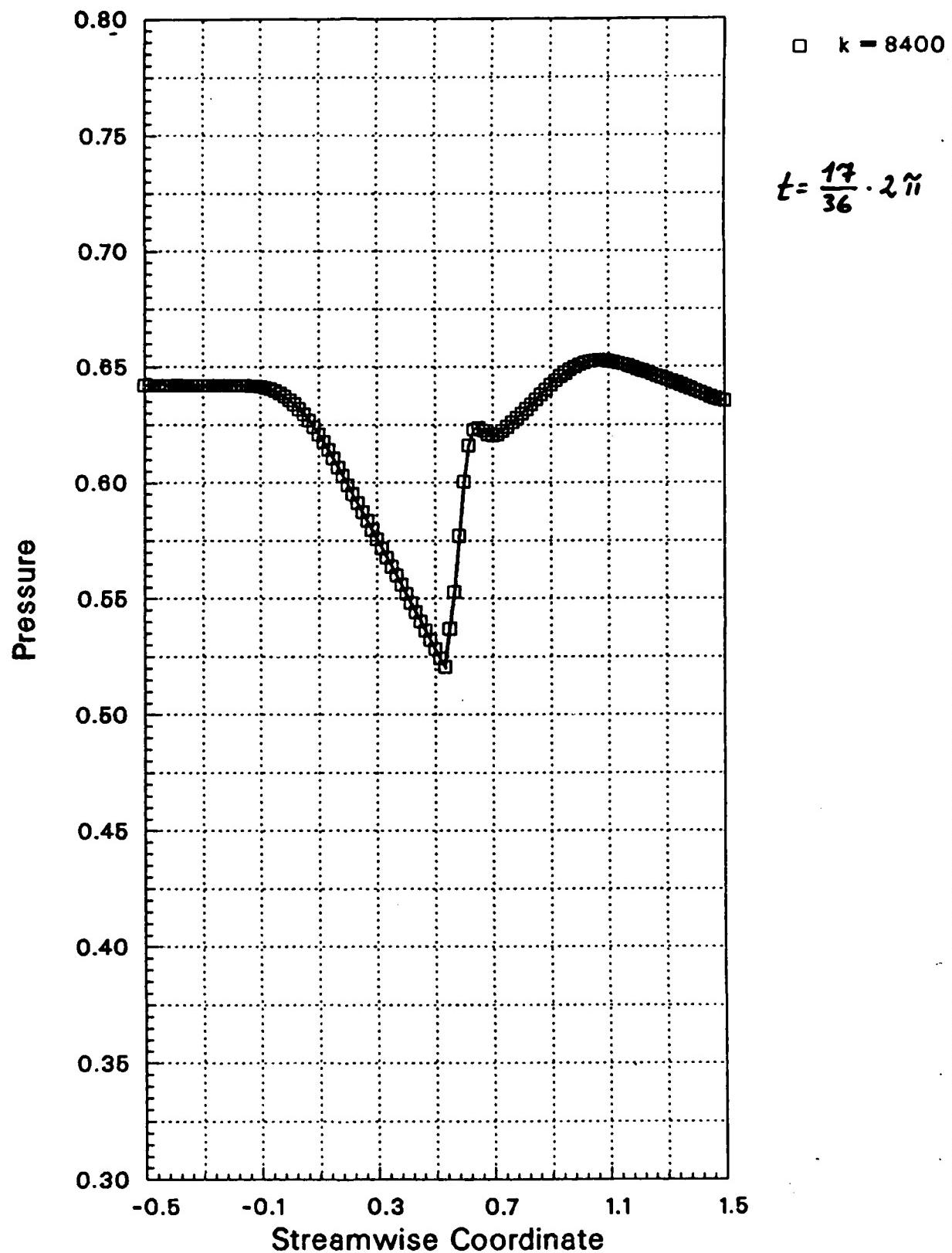


Fig. 5.2-6.2. Unsteady pressure distribution in a nozzle for $k=0.100$, $p_{e,amp}=0.05$. All other parameters as in Figs. 5.2-1.

RUN NUMBER = 433

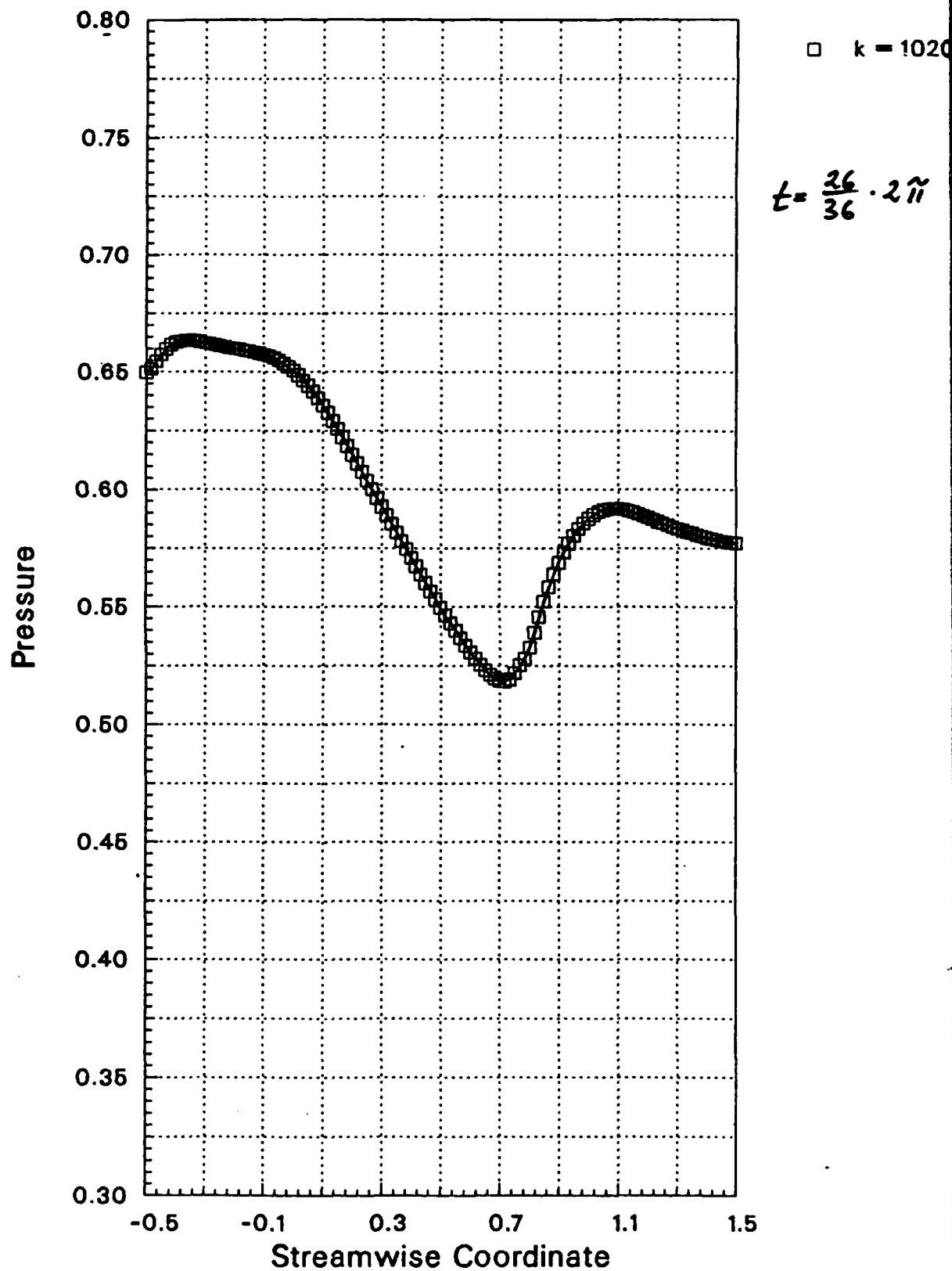


Fig. 5.2-6.3. Unsteady pressure distribution in a nozzle for $k=0.106$. $P_{e,amp}=0.05$. All other parameters as in Figs. 5.2-1.

RUN NUMBER = 433

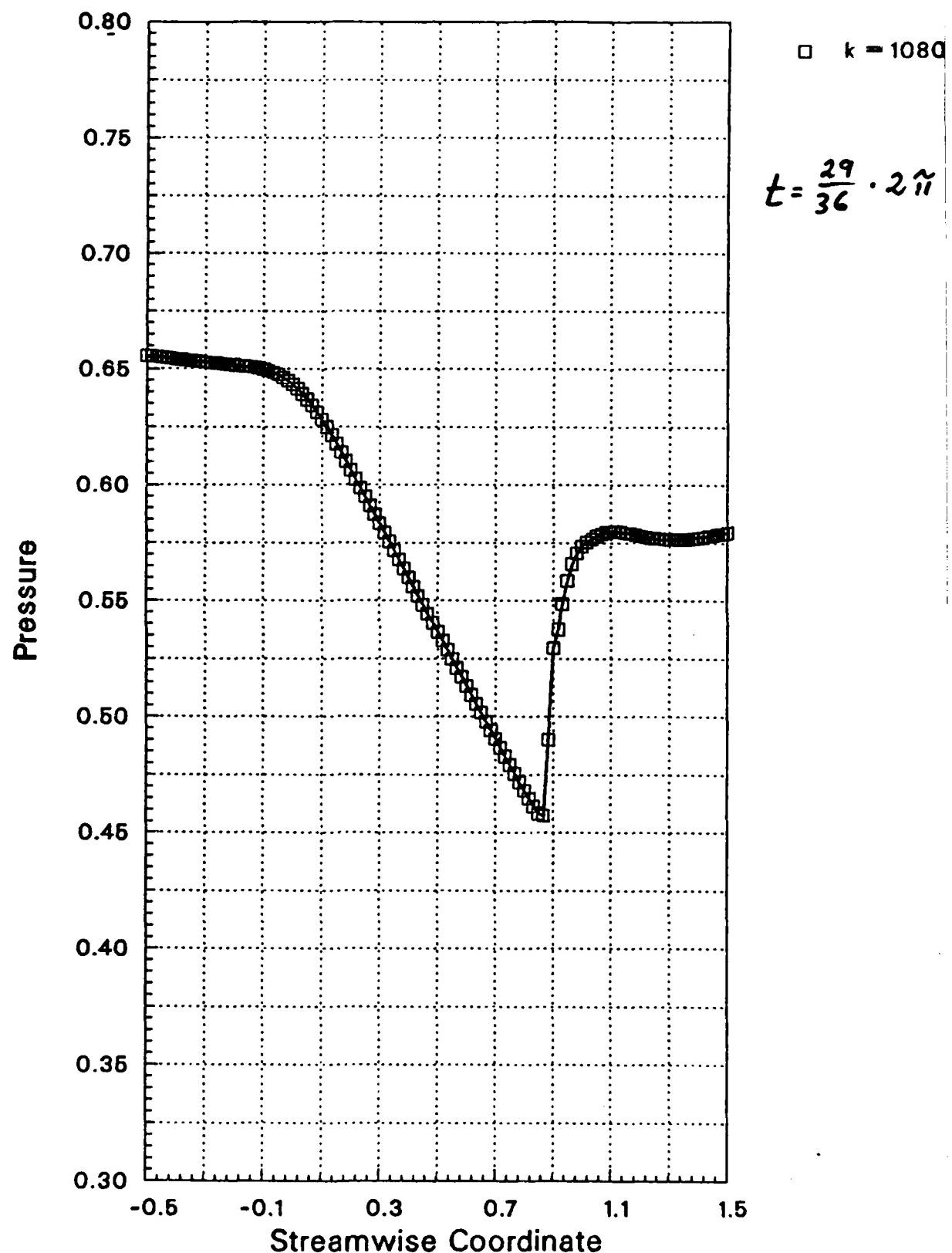


Fig. 5.2-6.4. Unsteady pressure distribution in a nozzle for $k=0.106$, $\rho_{e,amp}=0.05$. All other parameters as in Figs. 5.2-1.

RUN NUMBER = 433

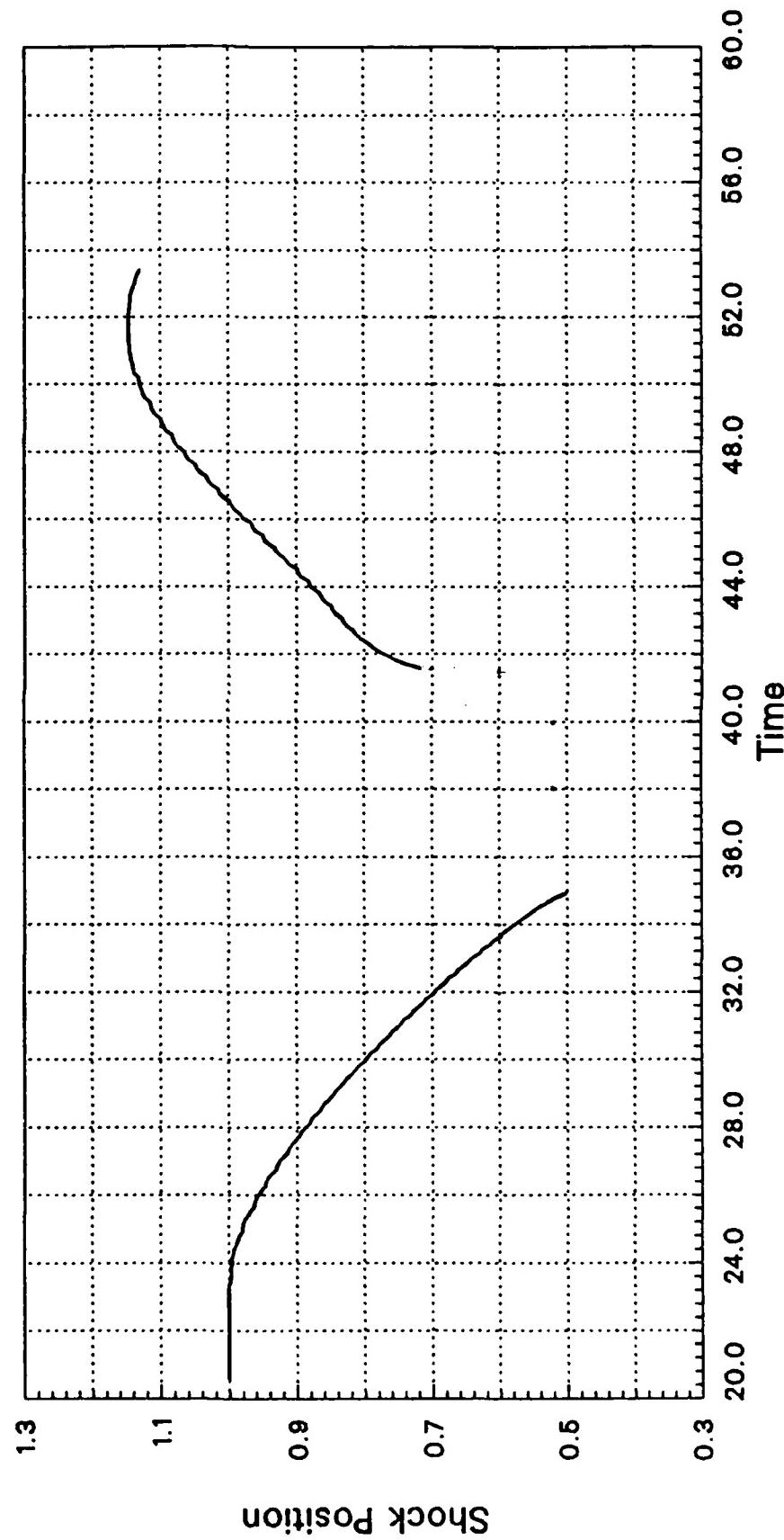


Fig. 5.2-6.5. Shock position in a nozzle for $k=0.106$, $\rho_{e,amp}=0.05$. All other parameters as in Figs. 5.2-1.

6. Two Dimensional Unsteady Results.

Unsteady two dimensional results will be presented for a channel flow with a 10% "bump" on the upper wall. The geometry is similar to the steady state case presented in section 4.6.2, apart from the fact that the "bump" has now a sinusoidal, instead of a circular arc, form. This change is deliberately introduced in order not to create any numerical disturbances at the corners of the "bump" in cases when the unsteady shock propagates thereover.

Two sample cases will be presented. Both cases consider the same steady state flow field as in section 4.6.2, i.e. $p_e=0.7369$ ($M_{\infty}=0.675$). The first treats an exit pressure amplitude of $p_{e,amp}=0.12$, with a reduced frequency (calculated with c_r as in the previous section) of $k=0.396$ (corresponding to $f=369\text{Hz}$ for a profile length of $l_p=0.1\text{m}$). The second case has a lower amplitude, $p_{e,amp}=0.06$, with the same reduced frequency.

In both sample cases the imposed exit pressure is the same over the width of the channel, and the variation of pressure starts, as in the quasi one dimensional cases, with a sinusoidal increase.

First Sample Case.

In the first sample case we will present, starting from the beginning of the variation of exit pressure, about 1.5 periods. The steady state solution is given in Fig. 6-1, and the unsteady sequence is studied in Figs. 6-2 to 6-31. It should be pointed out that the grid used for this computation consists of (14×60) cells, and the shock is captured within two cells, i.e. with one intermediate computational point (see for example Fig. 6-1).

As the exit pressure increases, the lines of constant Mach number close to the outlet are pushed upstream, especially at the lower wall (Figs. 6-2 to 6-4). During this time there is no change in the flow up to $x \approx 0.7$. At $t=\pi/2$ the exit pressure has reached its maximum value (Fig. 6-5), whereafter it decreases (Fig. 6-6 to 6-8). The lines of constant Mach number close to the exit now become turned in the other direction (towards the upper wall), and the shock starts simultaneously to move upstream. The maximum Mach number upstream of the shock decreases rapidly as the shock moves upstream. At the same time the velocity decreases also on the lower wall of the nozzle, and the isomach lines

which were bent towards the outlet in the steady state (see for example $M=0.70$ in Fig. 6-1) are now bent forward instead ($M=0.70$ in Fig. 6-8).

At time $t=\pi$ (Fig. 6-9) the exit pressure has again reached its steady state level but, due to the time lag between the pressure at the exit and the pressure in the nozzle, the velocity throughout the nozzle continues to decrease. At this time the shock is pushed into the subsonic part of the nozzle and the flow is completely subsonic. At an approximate time of $t \approx 9.2\pi/16$ the velocity has reached its minimum value throughout the nozzle, and the flow starts finally to react to the previous decrease in outlet pressure (i.e. the decrease that started at $t=\pi/2$, Fig. 6-5). Thus the flow velocity begins to increase. Before this, as in one dimensional flow, the unsteady shock moves upstream in the subsonic flow domain (Figs. 6-9 to 6.10). It is however not, in contrast to the quasi-one dimensional results from section 5.2.2, pushed all the way to the inlet, but reaches instead a minimum position and is then moved downstream, starting at $t \approx 9.2\pi/16$.

The increase in flow velocity appears over the whole channel width, but obviously with a larger value at the bump. As the imposed decrease in the pressure wave train approaches the bump, the flow velocity at the upper wall will again reach a sonic value ($t=11.2\pi/16$, Fig. 6-12), and the shock steepens again (Fig. 6-13). At time $t=3\pi/2$ (Fig. 6-13) the exit pressure has reached its minimum level, and at time $t \approx 13.2\pi/16$ (Fig. 6-14) the shock has reached its steady state position, however with a lower pre shock Mach number and a lower pressure jump than in the steady state flow field. The pressure at the outlet is now increasing, but the shock is still moving downstream (because of the finite time it takes for disturbances to travel upstream). The shock at the upper wall reaches maximum position at $t \approx 19.2\pi/16$, with a maximum pre shock pressure significantly higher than the corresponding steady state maximum position is reached well after the exit pressure has reached its average (=steady state) level at $t=22\pi/16$. Simultaneously, the pressure increase at the exit propagates upstream, and this compression wave is slowly building up also over the lower wall also and, indeed, over the whole channel width ($t=19.2\pi/16$, Fig. 6-20). Although this shock is located on the lower wall, it can still be considered to be reflected from the upper wall cells ($t=20.2\pi/16$, Fig. 6-21). The shock then moves back upstream and, at $t=22.2\pi/16$ (Fig. 6-22),

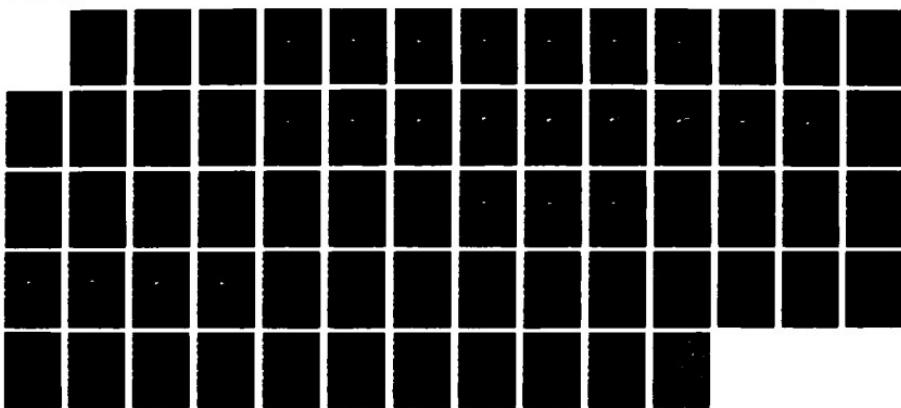
AD-A189 500 APPLICATION OF A FLUX VECTOR SPLITTING METHODOLOGY
TOWARDS THE SOLUTION O (U) NAVAL POSTGRADUATE SCHOOL
MONTEREY CA T H FRANSSON JUL 87 NPS67-87-006

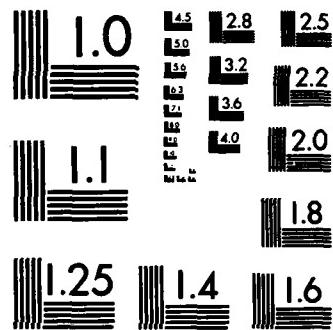
3/3

UNCLASSIFIED

F/G 20/4

NL





MICROCOPY RESOLUTION TEST CHART
NATIONAL BUREAU OF STANDARDS-1963-A

lower wall is still moving upstream, but is in the subsonic field of the flow. At $t=21 \cdot 2\pi/16$ the shock at the upper wall has again reached its steady state location (half a period after it reached the same position moving downstream). The pre-shock Mach number is now much higher than the corresponding value for the downstream moving shock (Fig. 6-14), and also considerably higher than the steady state value (Fig. 6-1). The rest of the flow field in the nozzle is also very different between these three time levels.

The shock at the lower wall is pushed further into the subsonic part of the nozzle and becomes weaker because of the decrease in upstream flow velocity, at the same time as the shock at the upper wall also is moved upstream (Figs. 6-23 to 6-25). The upper part of the shock is thereafter finally again pushed into the subsonic part of the nozzle (Fig. 6-26). The shock that extended over the whole nozzle width at time $t=20 \cdot 2\pi/16$ (Fig. 6-21) is now so weak that it is only noticed as a shock (unsteady, although in the subsonic flow) close to the upper wall. As we are now considering the second period of the oscillation, the flow field in the nozzle is far from identical to the flow during the first cycle (compare Fig. 6-10, 6-26). However, as the shock now again begins to move upstream at $t=26 \cdot 2\pi/16$, the flow field is slowly built up towards a periodic solution. Thus, the flow during the second cycle is fairly close to the flow field of the first cycle (compare Figs. 6-12, 6-28; 6-13, 6-29; and 6-14, 6-30), and the same pattern of shock build up as seen during the first cycle is repeated. In fact, the flow becomes periodic so fast that already the second period can almost be considered as the periodic solution. This can be seen by comparing the flow field at $t=25 \cdot 2\pi/16$ and one period later, at $t=41 \cdot 2\pi/16$ (Figs. 6-26 and 6-31), as well as the corresponding solution at later periods (not shown here).

Second Sample Case.

The second sample case treats the flow in the same nozzle, with the same steady state solution ($i \cdot i_{\infty} = 0.675$, $p_e = 0.7369$) and the same reduced frequency of the imposed exit pressure fluctuation. The difference towards the first sample case is the amplitude of the pressure oscillation which is now $p_{e,amp} = 0.06$, towards the previous $p_{e,amp} = 0.12$.

The steady state flow field is given in Fig. 6-32, and a few time steps of the first unsteady period are presented in Figs. 6-33 to 6-42.

As the pressure increases at the exit the Isomach lines are again turned, as in the first sample case, upstream, although to a lesser extent as the pressure increase is smaller (compare Figs. 6-5 and 6-33). As the physical time for the disturbance wave train to travel from the exit to the shock is the same in both sample cases, the shock will start to react at the same time. It will however move much slower in the case with the lower pressure amplitude. This is confirmed by comparing, for example Figs. 6-6 and 6-34.

At time $t=\pi$ the exit pressure is again at its steady state value (Fig. 6-35), and at $t \approx 10.2\pi/16$ the shock at the upper wall has reached its minimum position (Fig. 6-36). This is at approximatively the same time as the shock had reached its minimum location in the first sample case (Fig. 6-10). There are a fundamental difference though between the high and low pressure amplitude cases. As was concluded for $p_{e,amp}=0.12$ the pre-shock Mach number was well below 1.00 before the shock started to move downstream again (Fig. 6.10), whereas for $p_{e,amp}=0.06$ the pre-shock Mach number is still supersonic, and the supersonic zone around the location of maximum bumpthickness is clearly manifested (Fig. 6-36). The flow velocity in the nozzle starts thereafter to increase because of the decrease in exit pressure that started at $t=\pi/2$. The shock at the upper surface of the bump picks up in strength (Fig. 6-37 to 6-41), and reaches its maximum position at $t \approx 20.2\pi/16$, sligthly after the time the higher pressure amplitude shock reached its maximum location (Fig. 6-20). As expected, for the lower amplitude case the compression from the outlet can not build itself up to a shock wave at the lower wall, wherefore the flow is completely subsonic there (Fig. 6-41). This is in contrast to the high amplitude case where the flow was choked during a small part of the period (Fig. 6-21).

The highest pre-shock Mach number (Fig. 6-41) is also in this sample case higner than the steady state value, although not as high as in the high amplitude case (Fig. 6-21), and the supersonic zone reaches out to $\approx 66\%$ from the upper wall (see $M=1.00$ in Fig. 6.41), compared to only $\approx 44\%$ in the steady state solution.

Mach number in physical plane

RUN NUMBER = 213
 $k = 6000$
 $t = 0$

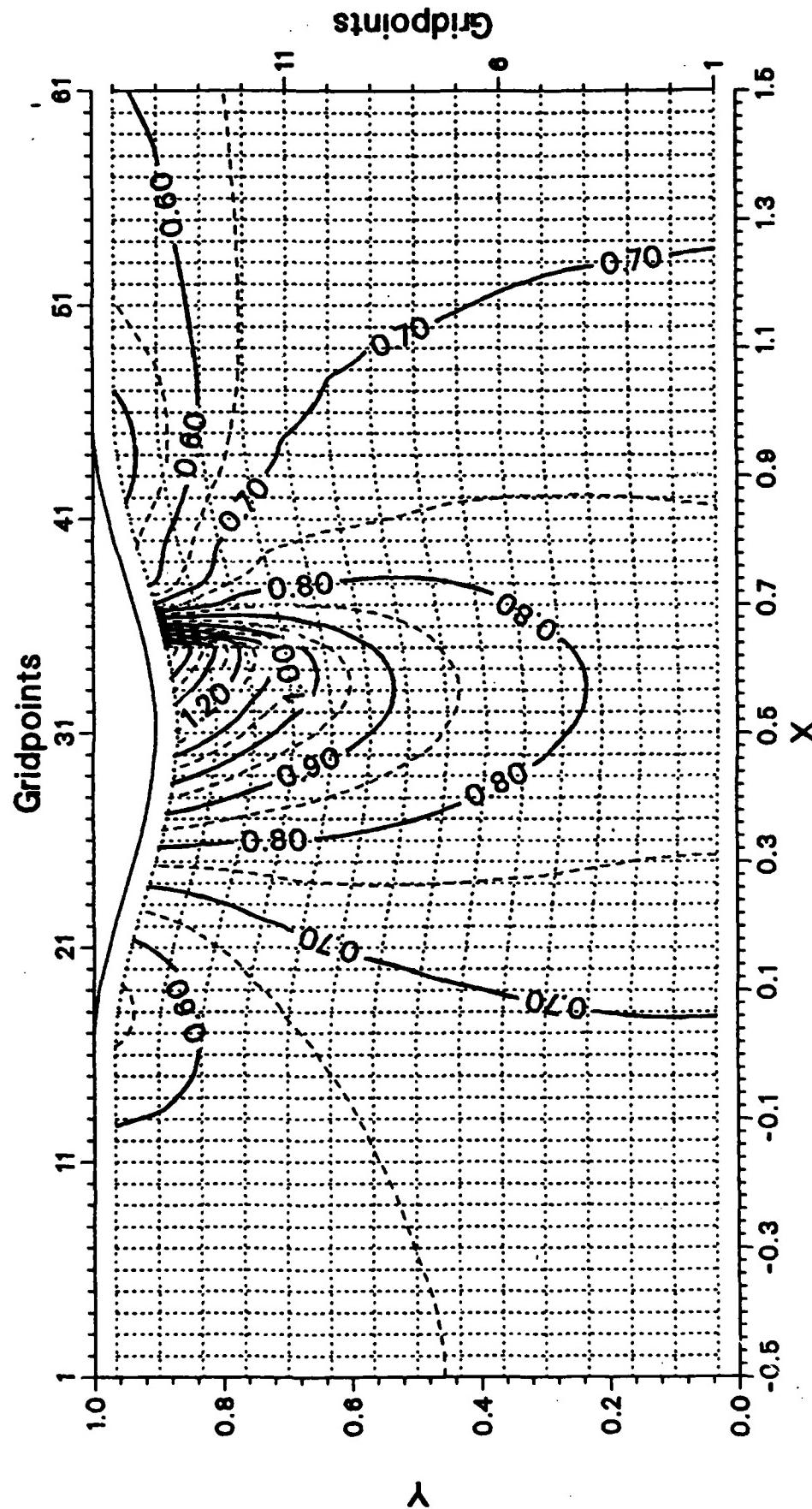


Fig. 6-1. Sinusoidal "bump"-flow. $M_{\infty} = 0.675$, $\rho_{\infty} = 0.7369$. Steady state solution for first two dimensional sample case.

Mach number in physical plane

RUN NUMBER = 213
 $t = \frac{1}{k} \cdot 2\pi$
 $k = 6100$

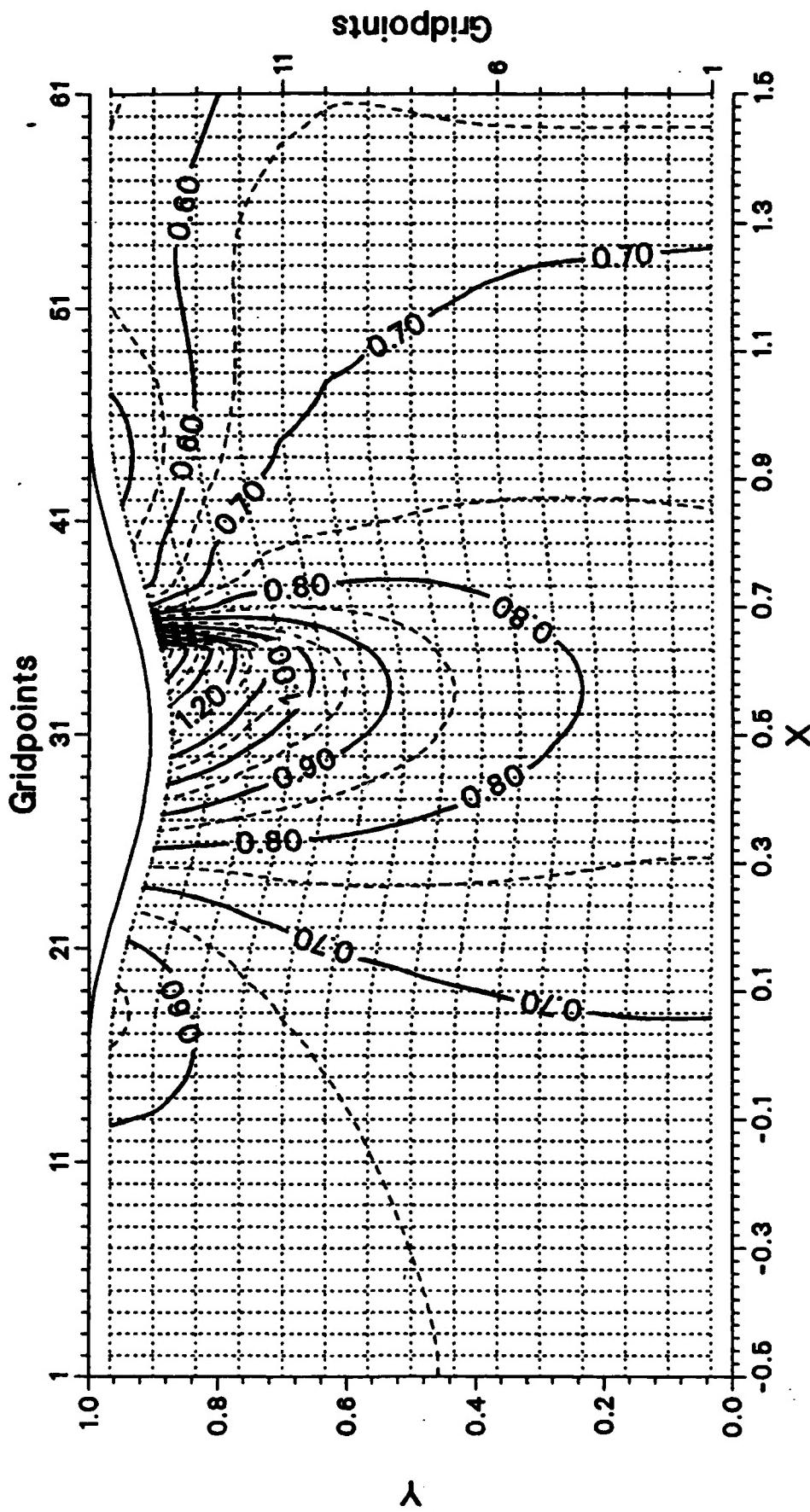


Fig. 6-2. Sinusoidal "bump"-flow. $M_{\infty} = 0.675$, $p_e = 0.7369$. Unsteady solution for first two dimensional sample case.
 $p_{e,amp} = 0.12$, $k = 0.369$.

Mach number in physical plane

RUN NUMBER = 213
 $k = 6200$
 $t = \frac{2}{k} \cdot 2\pi$

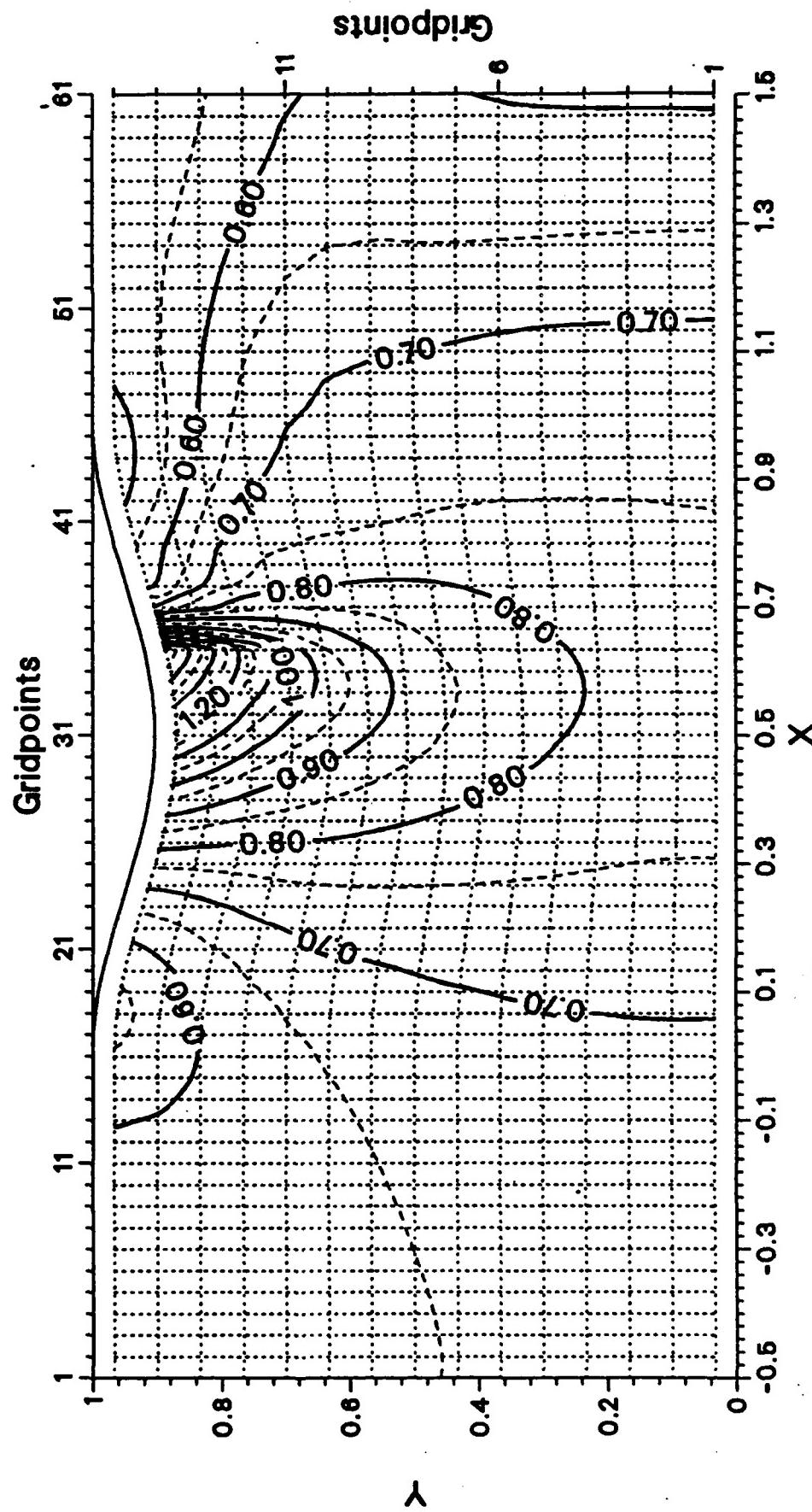


Fig. 6-3. Sinusoidal "bump"-flow. $M_{L\infty}=0.675$, $p_e=0.7369$. Unsteady solution for first two dimensional sample case.
 $p_{e,dmg}=0.12$, $k=0.369$.

Mach number in physical plane

$$t = \frac{3}{16} \cdot 2\pi$$

RUN NUMBER = 213
k = 6300

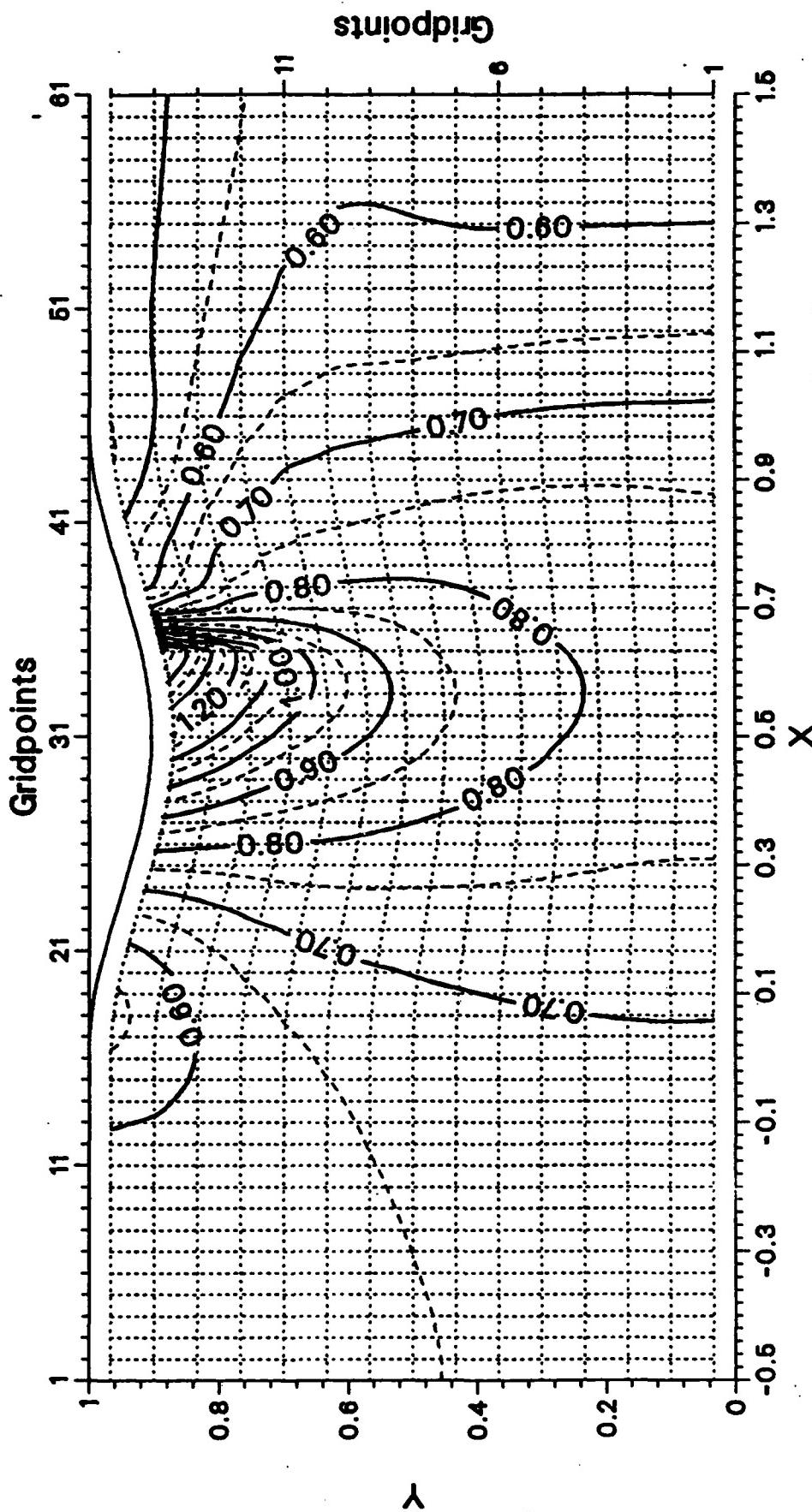


Fig. 6-4. Sinusoidal "bump"-flow. $M_{\infty} = 0.675$, $\rho_e = 0.7369$. Unsteady solution for first two dimensional sample case.
 $D_{max} = 0.12$, $k = 0.369$.

Mach number in physical plane

RUN NUMBER = 213
 $k = 6400$
 $t = \frac{4}{16} \cdot 2\pi$

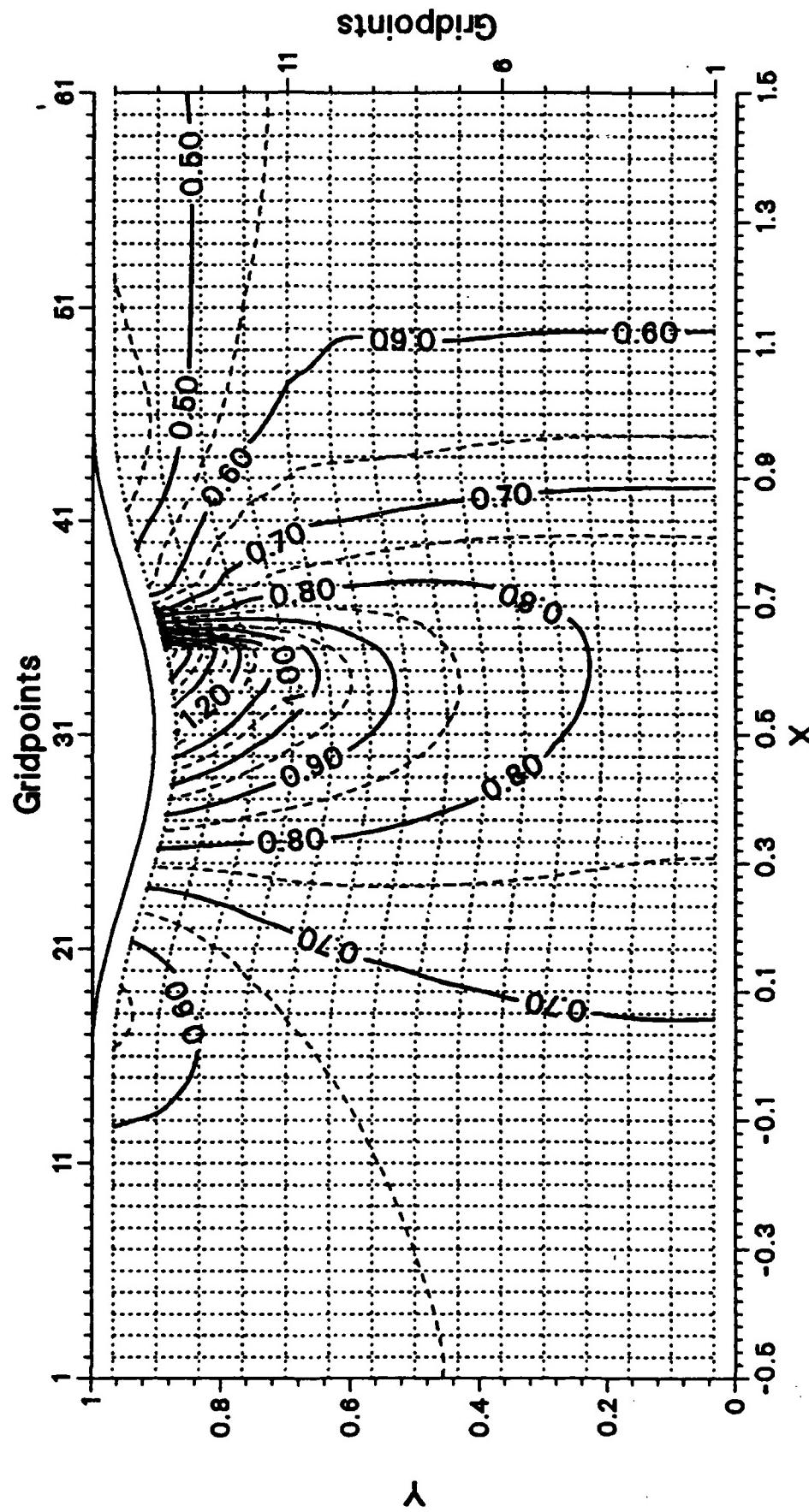


Fig. 6-5. Sinusoidal "bump"-flow. $M_{\infty}=0.675$, $p_e=0.7369$. Unsteady solution for first two dimensional sample case.
 $\rho_{e,amp}=0.12$, $k=0.369$.

Mach number in physical plane

RUN NUMBER = 213
 $k = 6500$
 $t = \frac{5}{16} \cdot 2\pi$

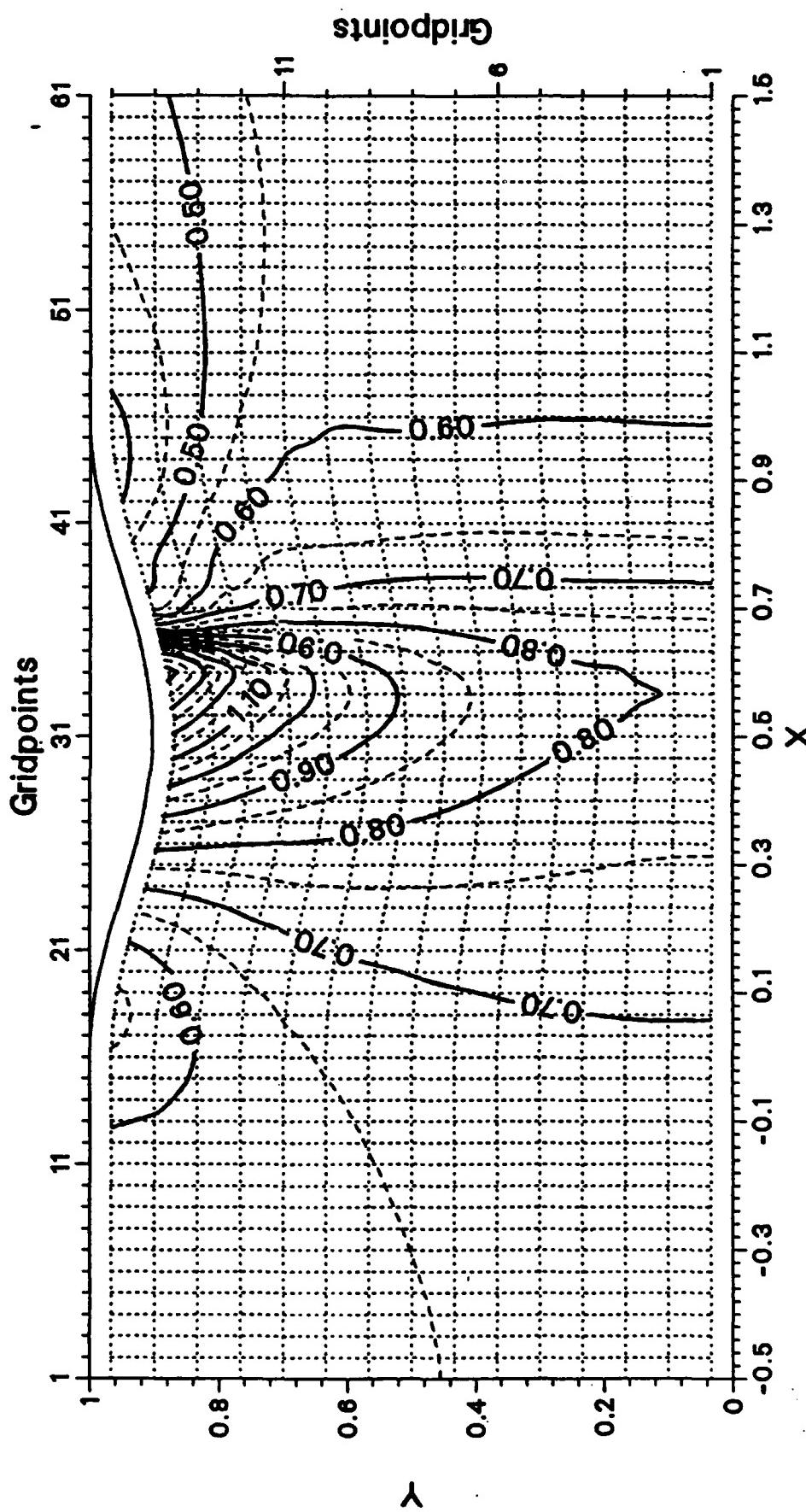


Fig. 6-6. Sinusoidal "bump"-flow. $M_{\infty}=0.675$, $p_0=0.7369$.
 Unsteady solution for first two dimensional sample case.
 $\nu_{e,amp}=0.12$, $k=0.369$.

Mach number in physical plane

$$\text{RUN NUMBER} = 213$$

$$k = 6600$$

$$t = \frac{6}{16} \cdot 2\pi$$

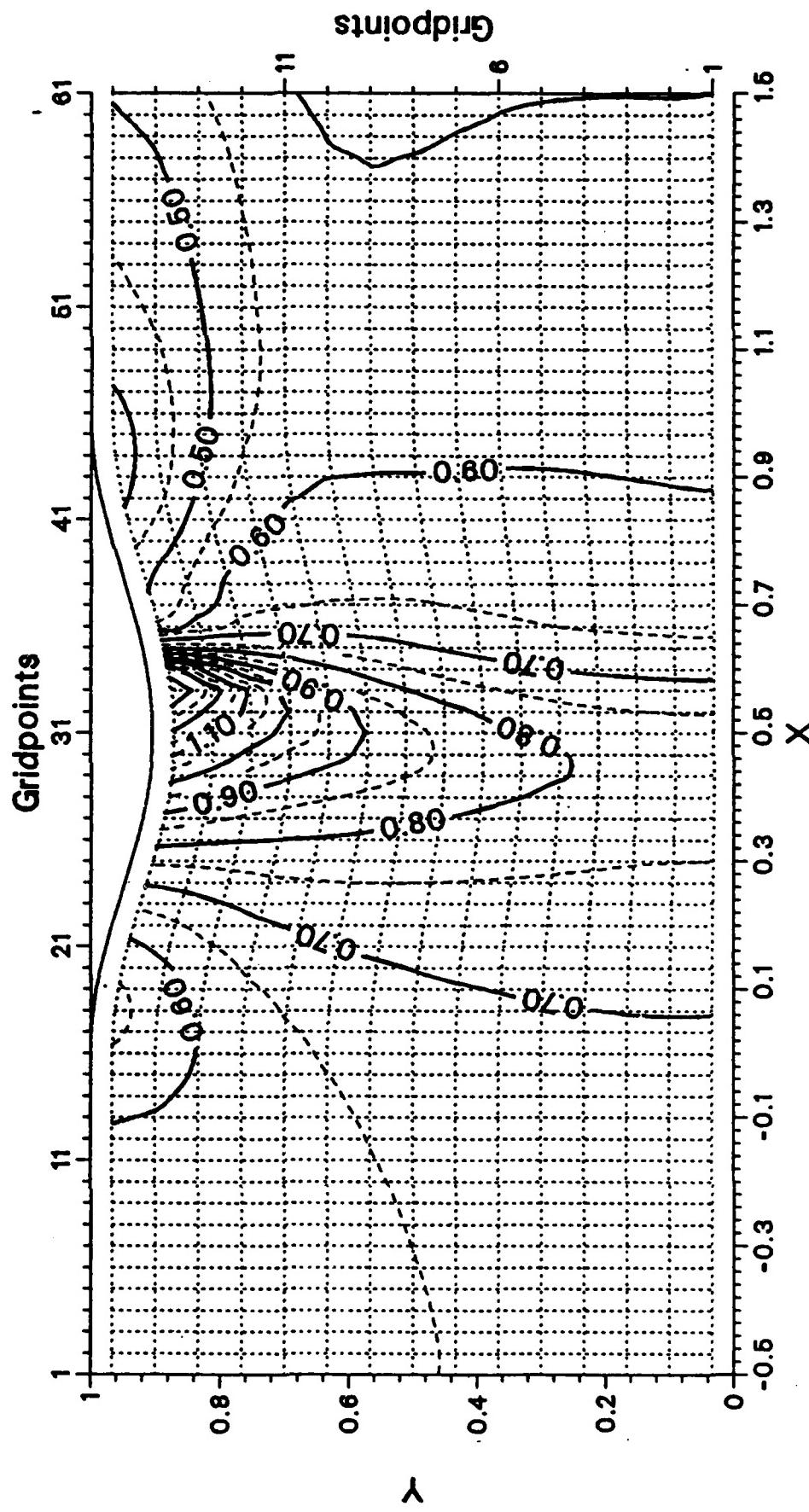


Fig. 6-7. Sinusoidal "bump"-flow. $M_{\infty}=0.675$, $p_e=0.7369$. Unsteady solution for first two dimensional sample case. $p_{e,amp}=0.12$, $k=0.369$.



$$t = \frac{7}{16} \cdot 2\pi$$

RUN NUMBER = 213
k = 6700

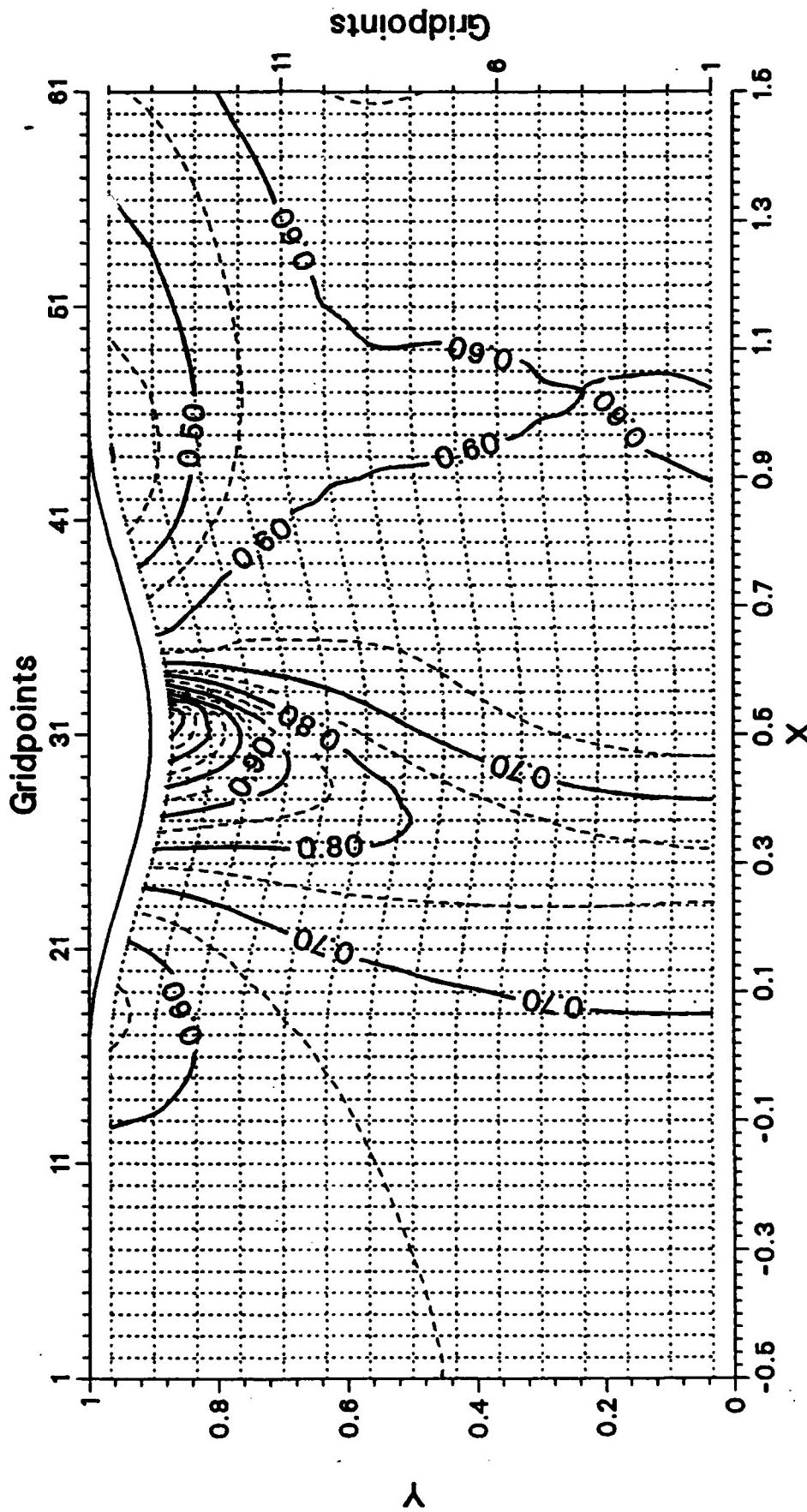


Fig. 6-8. Sinusoidal "bump"-flow. $M_{\infty} = 0.675$, $\alpha_e = 0.7369$. Unsteady solution for first two dimensional sample case.
 $\alpha_{amb} = 0.12$, $\kappa = 0.369$.

Mach number in physical plane

RUN NUMBER = 213
 $k = 6800$
 $t = 777.25$

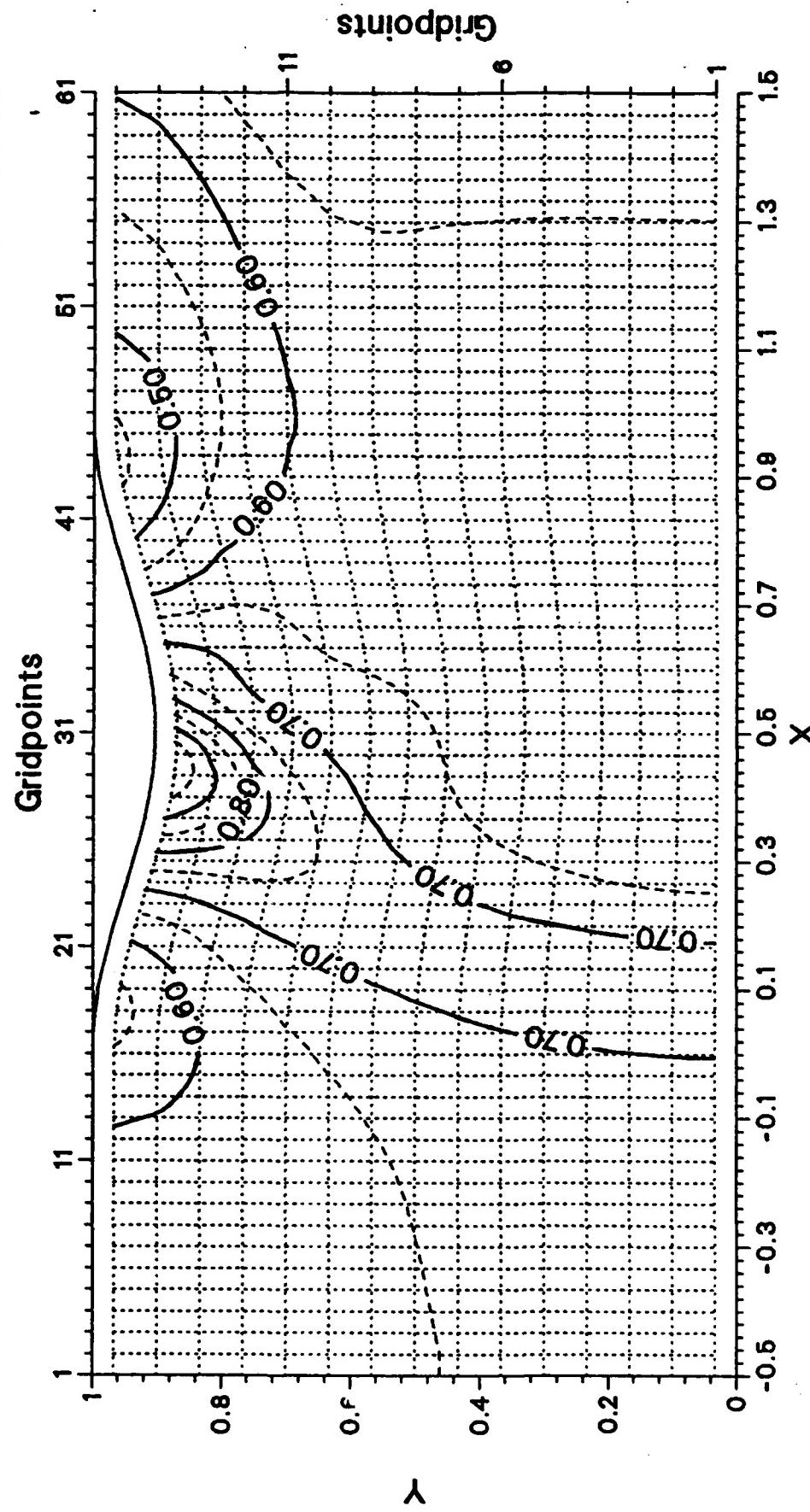


Fig. 6-9. Sinusoidal "bump"-flow. $M_{\infty}=0.675$, $\rho_e=0.7369$.

Unsteady solution for first two dimensional sample case.
 $\rho_{e, \text{ann}}=0.12$, $k=0.369$

Mach number in physical plane

$$t = \frac{9}{16} \cdot 2\pi$$

RUN NUMBER = 213
k = 6900

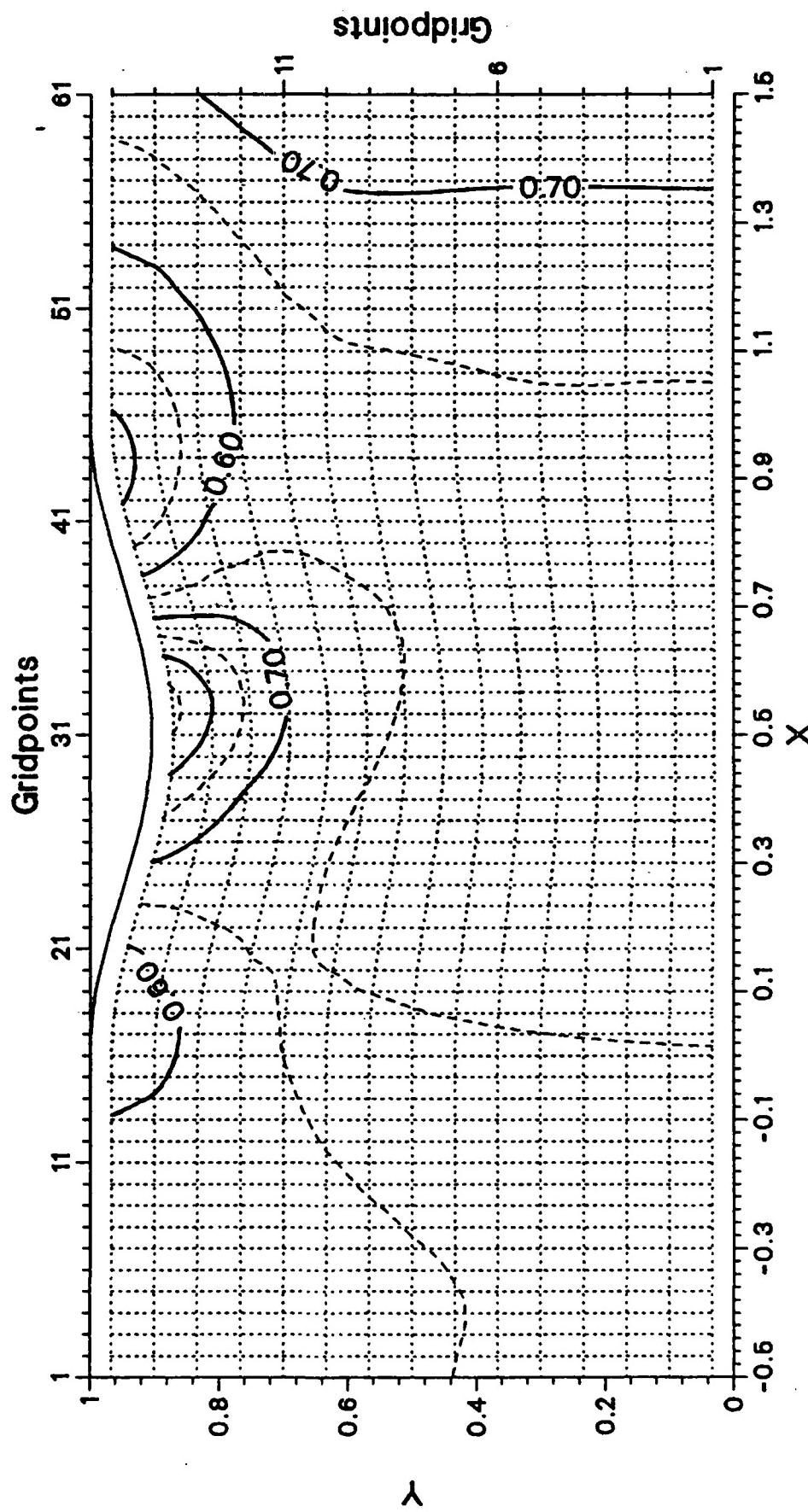


Fig. 6-10. Sinusoidal "bump"-flow. $M_{\infty}=0.675$, $\rho_e=0.7369$. Unsteady solution for first two dimensional sample case.
 $\rho_{e,amp}=0.12$, $k=0.369$.

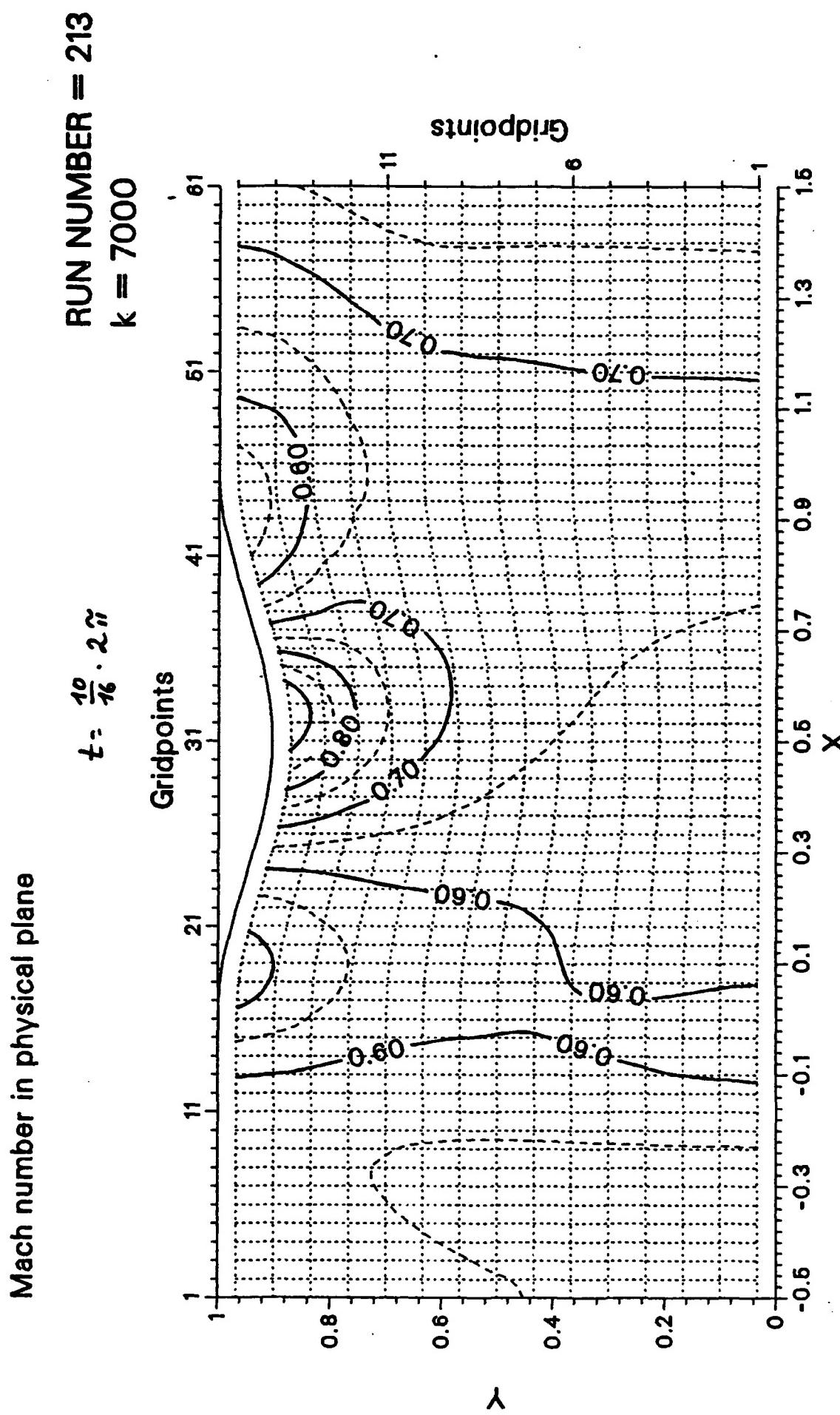


Fig. 6-11. Sinusoidal "dump"-flow. $M_{\infty} = 0.675$, $p_0 = 0.7369$.
Unsteady solution for first two dimensional sample case.
 $D_{\infty} = 0.12$, $k = 0.360$.

Mach number in physical plane

$$t = \frac{11}{16} \cdot 2\pi$$

RUN NUMBER = 213
 $K = 7100$

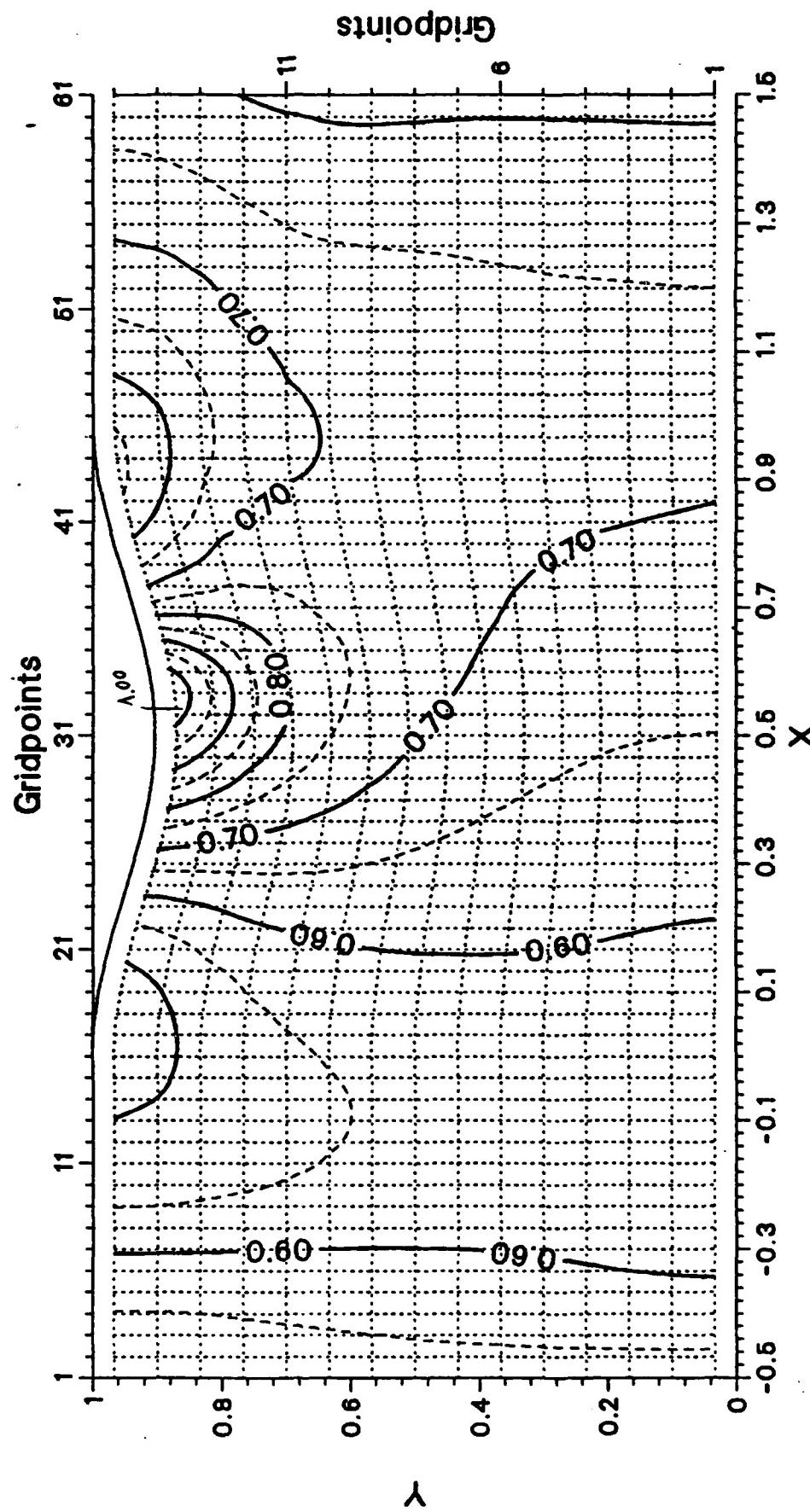


Fig. 6-12. Sinusoidal "bump"-flow. $M_{\infty}=0.675$, $p_e=0.7369$.

Unsteady solution for first two dimensional sample case.

$$p_{e,\text{anno}}=0.12, K=0.369.$$

Mach number in physical plane

$$t_2 = \frac{12}{46} \cdot 2 \pi$$

RUN NUMBER = 213
k = 7200

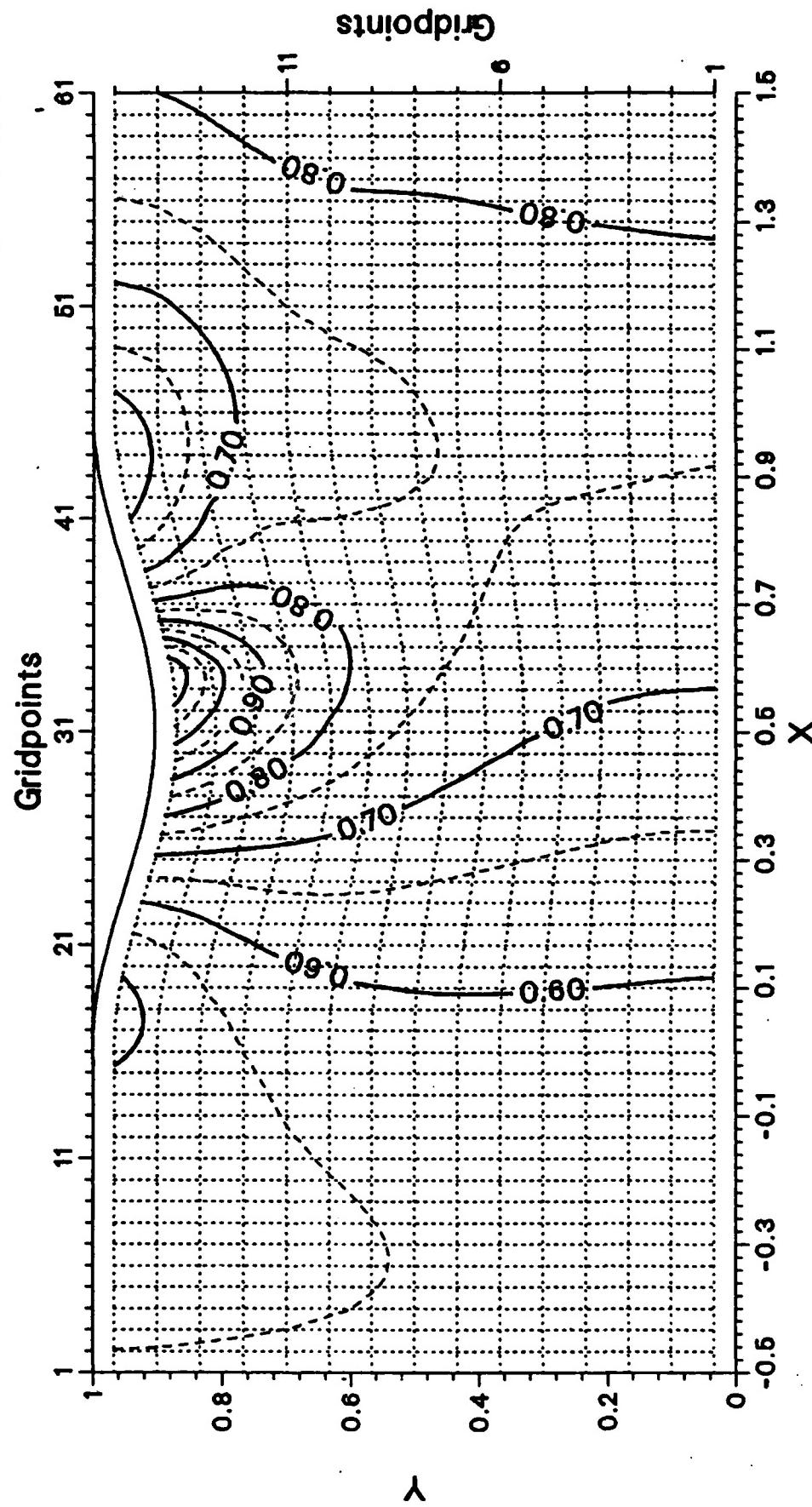


Fig. 6-13. Sinusoidal "bump"-flow. $M_{\infty} = 0.675$, $\beta_e = 0.7369$.

Unsteady solution for first two dimensional sample case.

Mach number in physical plane

RUN NUMBER = 213
 $k = 7300$
 $t = \frac{13}{16} \cdot 2\pi$

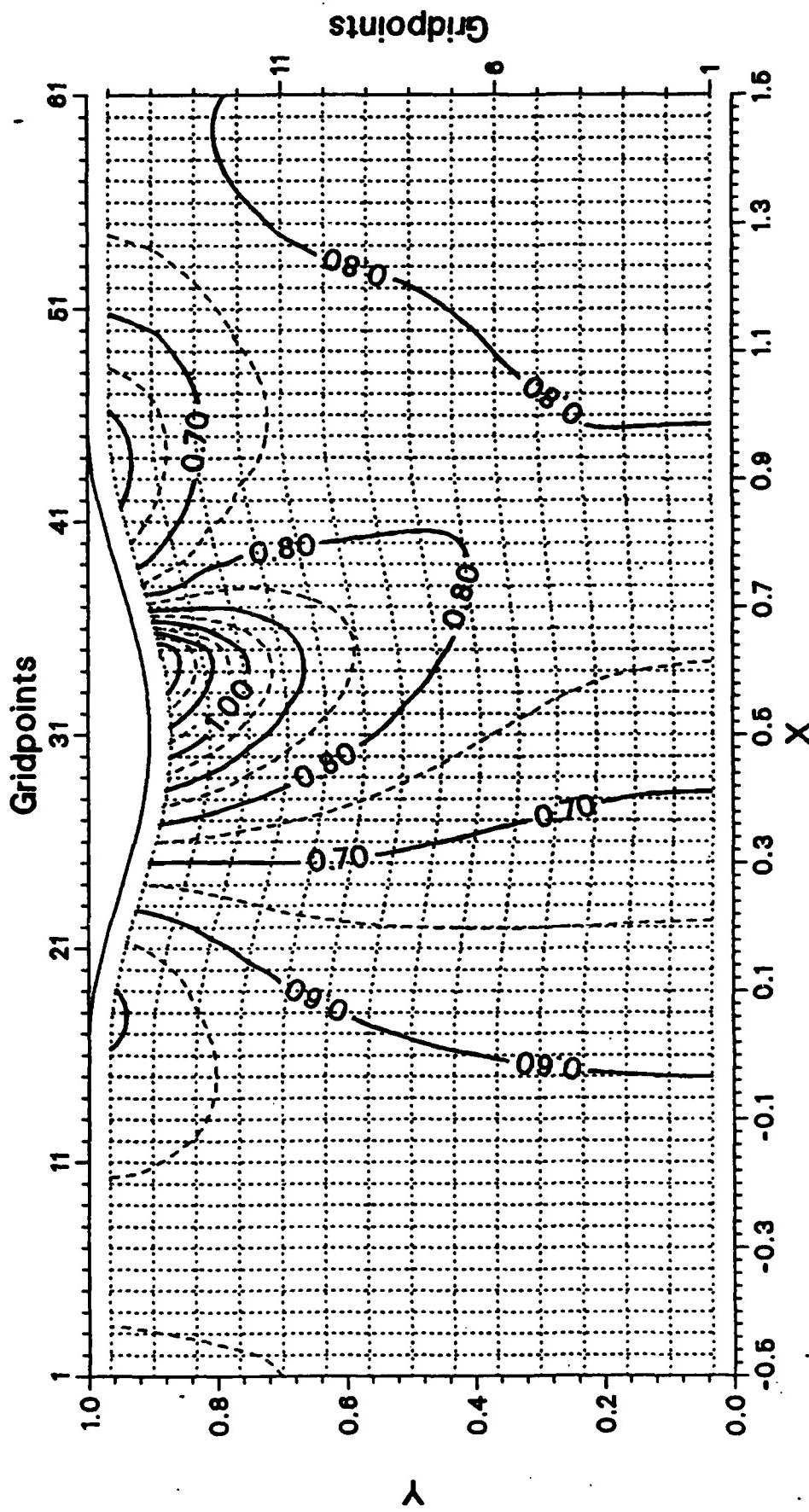


Fig. 6-14. Sinusoidal "bump"-flow. $M_{\infty} = 0.675$, $\rho_0 = 0.7369$.

Unsteady solution for first two dimensional sample case.

$\rho_{0, \text{min}} = 0.12$, $k = 0.369$.

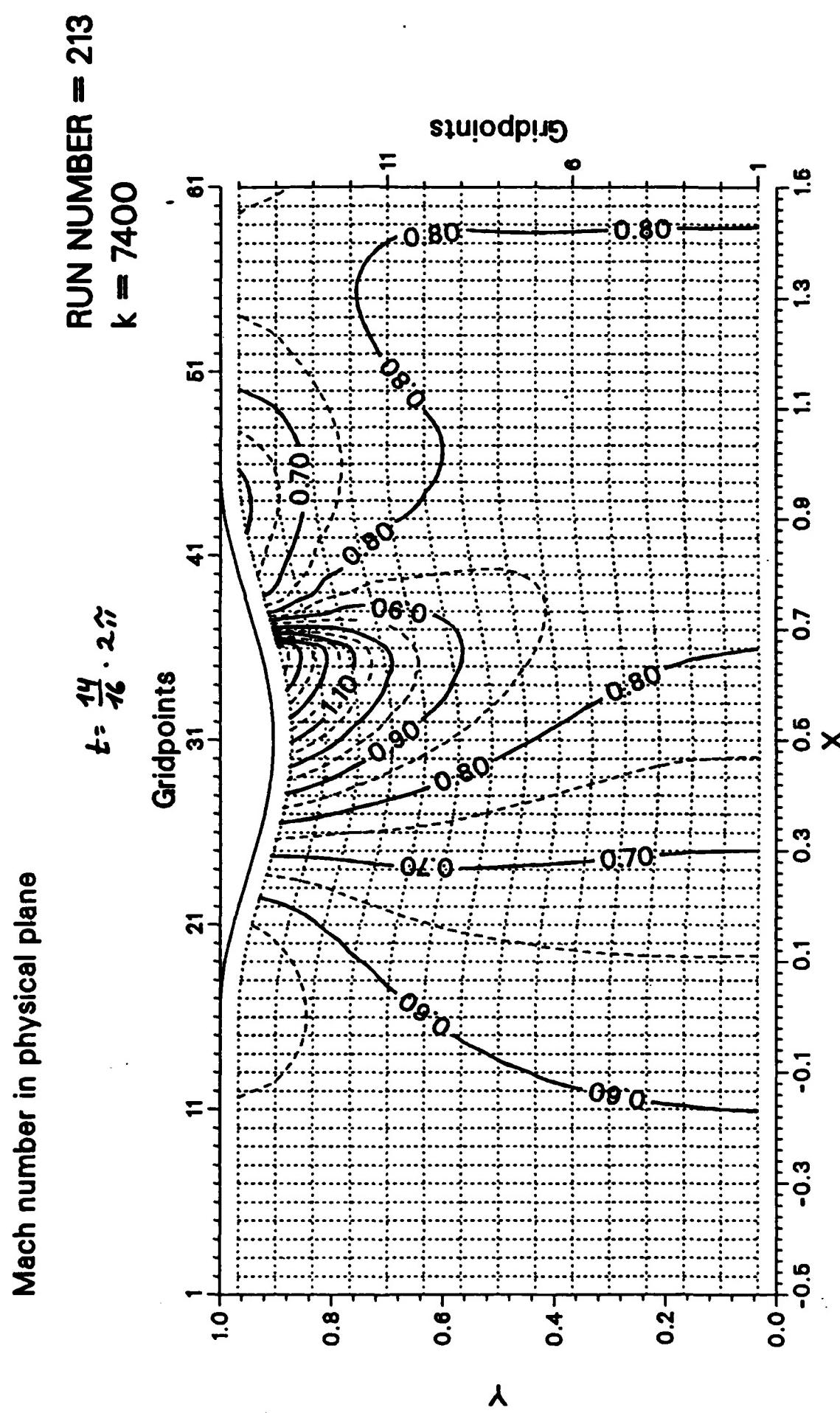


Fig. 6-15. Sinusoidal "bump"-flow. $M_{\infty}=0.675$, $\rho_0=0.7369$. Unsteady solution for first two dimensional sample case.

Mach number in physical plane

RUN NUMBER = 213
 $k = 7500$
 $t = \frac{15}{16} \cdot 2\pi$

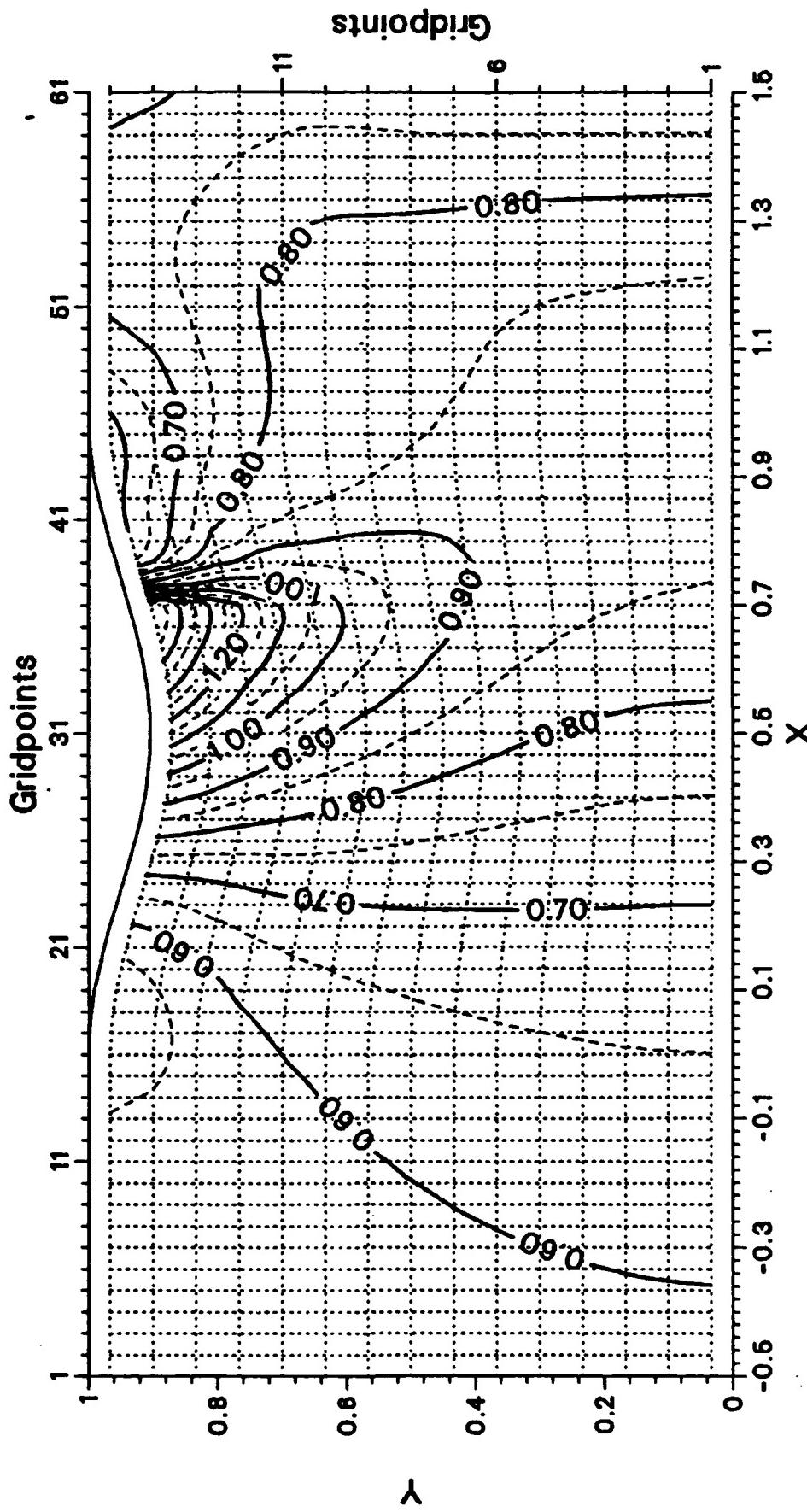


Fig. 6-16. Sinusoidal "bump"-flow. $M_{\infty}=0.675$, $\rho_0=0.7369$. Unsteady solution for first two dimensional sample case.
 $\rho_{e,amp}=0.12$, $k=0.369$.



RUN NUMBER = 213
k = 7600

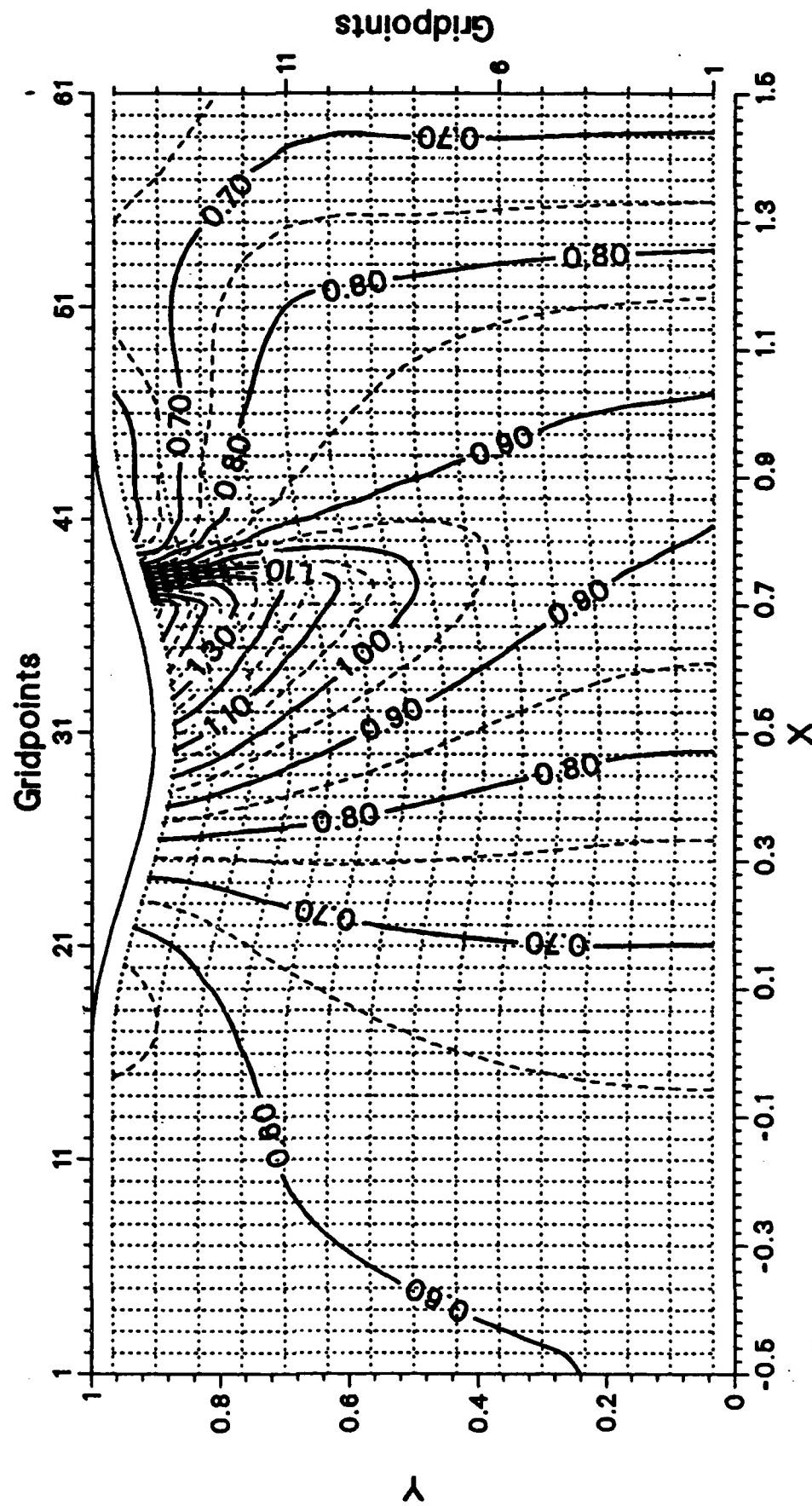


Fig. 6-17. Sinusoidal "bump"-flow. $M_{-\infty}=0.675$, $p_e=0.7369$.

Mach number in physical plane

$$t = \frac{17}{16} \cdot 2\pi$$

RUN NUMBER = 213
 $k = 7700$

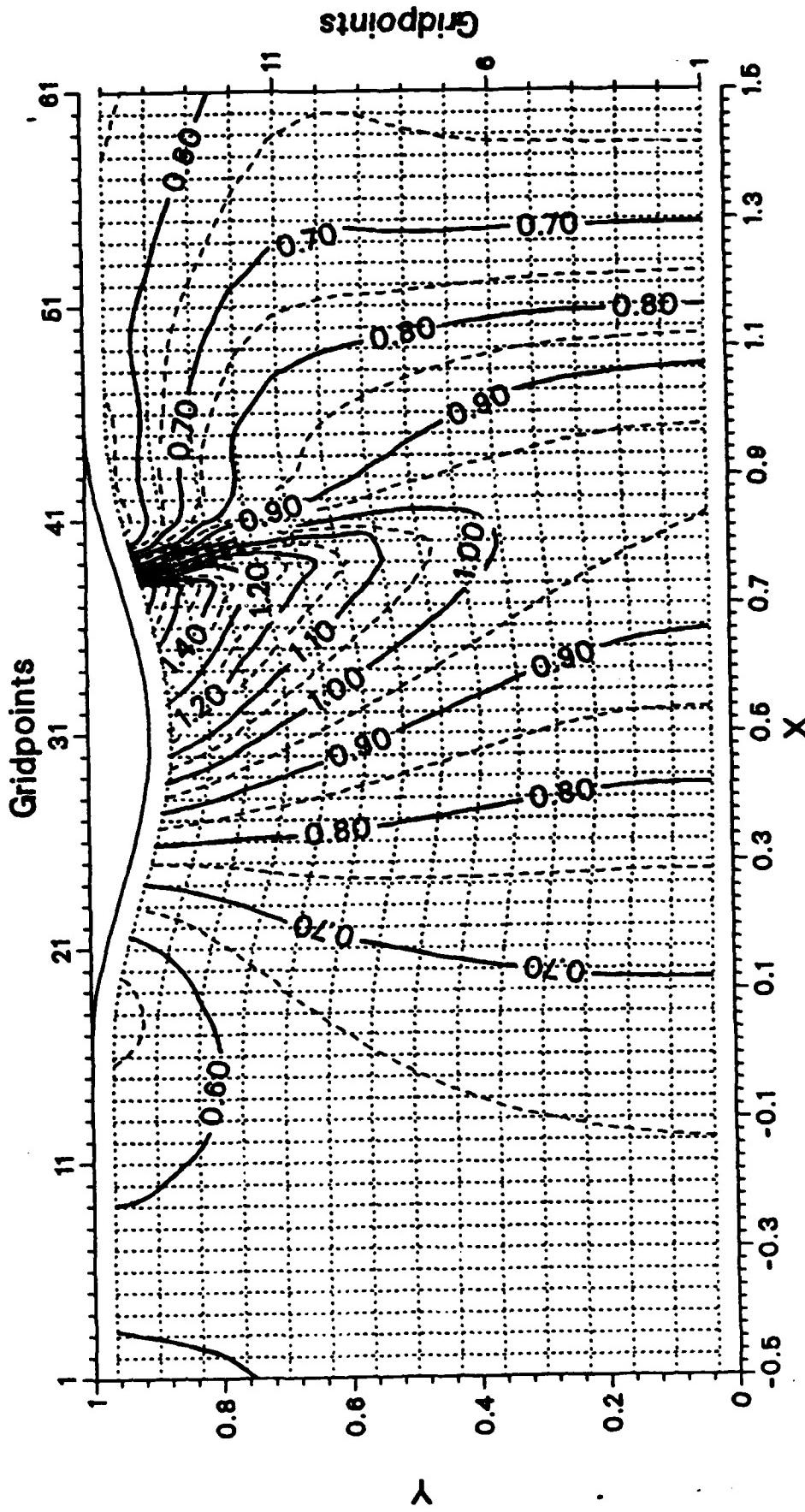


Fig. 6-18. Sinusoidal "bump"-flow. $M_{-\infty} = 0.675$, $\rho_\infty = 0.7369$.

Unsteady solution for first two dimensional sample case.

$D_{max} = 0.12$, $k = 0.369$

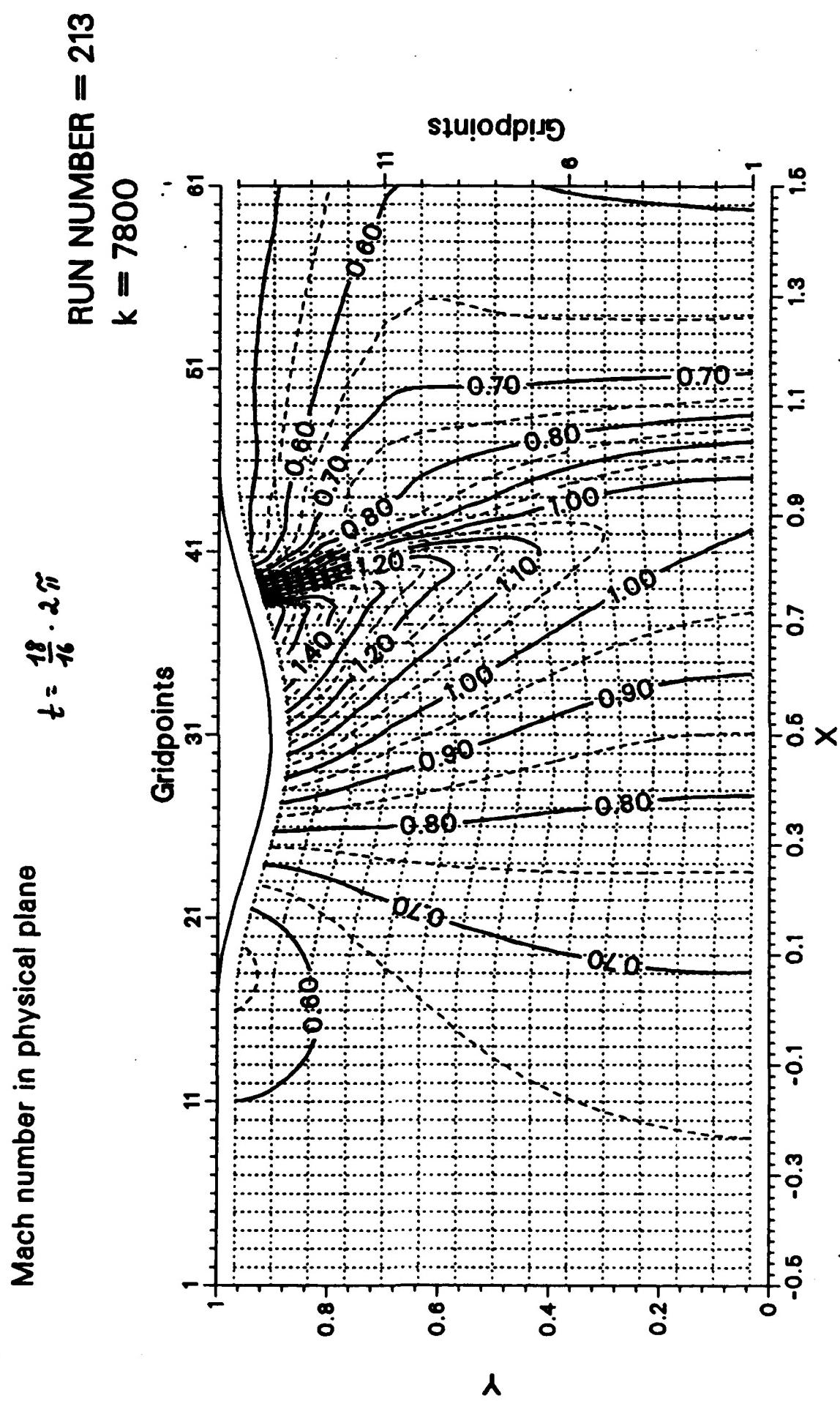


Fig. 6-19. Sinusoidal "bump"-flow. $M_{\infty} = 0.675$, $\rho_0 = 0.7369$.
Unsteady solution for first two dimensional sample case.
 $\nu_{e,amo} = 0.12$, $k = 0.369$.

Mach number in physical plane

RUN NUMBER = 213
 $k = 7900$

$$t = \frac{19}{16} \cdot 2\pi$$

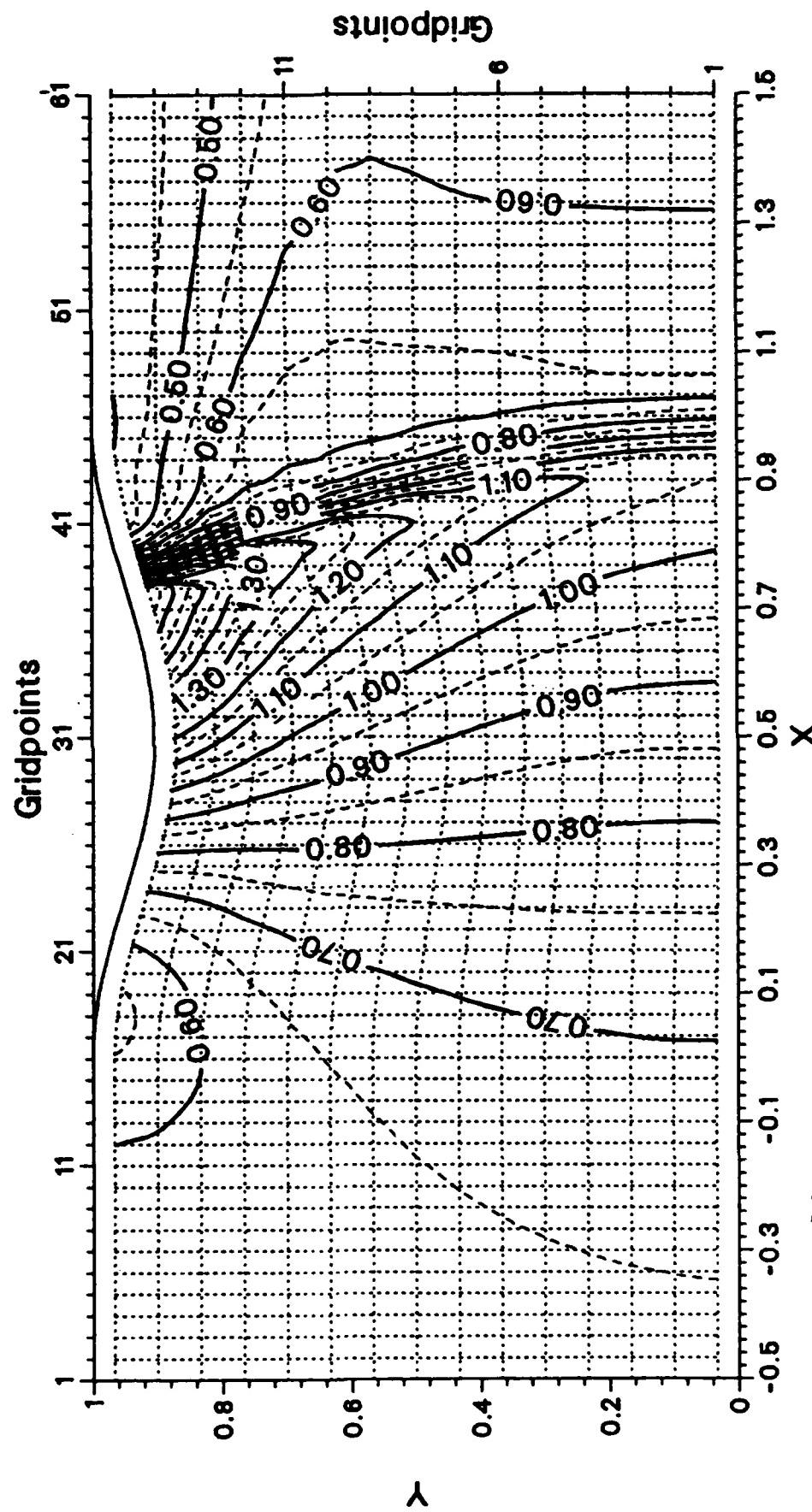
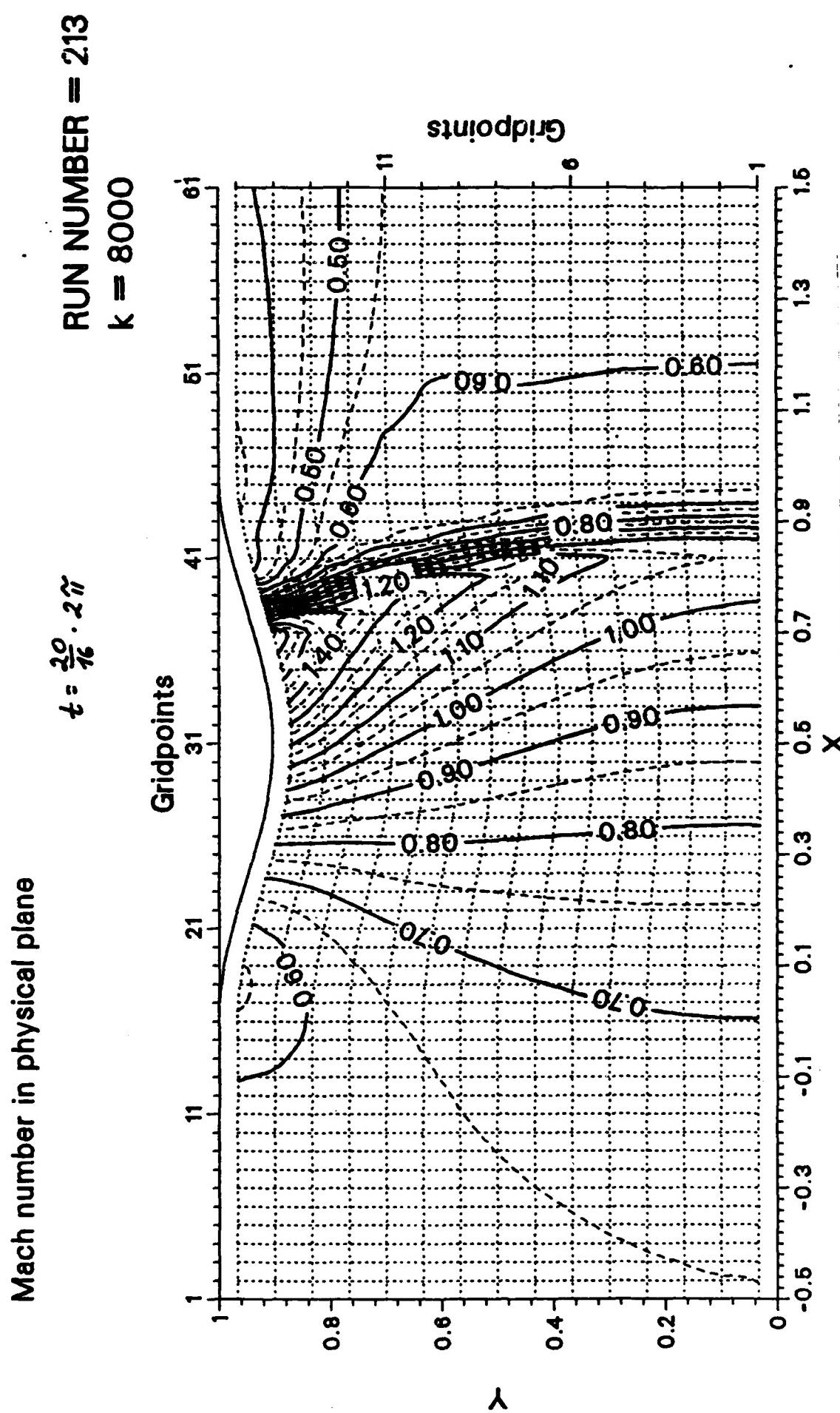


Fig. 6-20. Sinusoidal "bump" flow. $M_{\infty} = 0.675$, $\rho_0 = 0.7369$.

Unsteady solution for first two dimensional sample case.
 $\rho_{e,amp} = 0.12$, $k = 0.369$.



Mach number in physical plane

RUN NUMBER = 213
 $K = 8100$
 $t = \frac{21}{16} \cdot 2\pi$

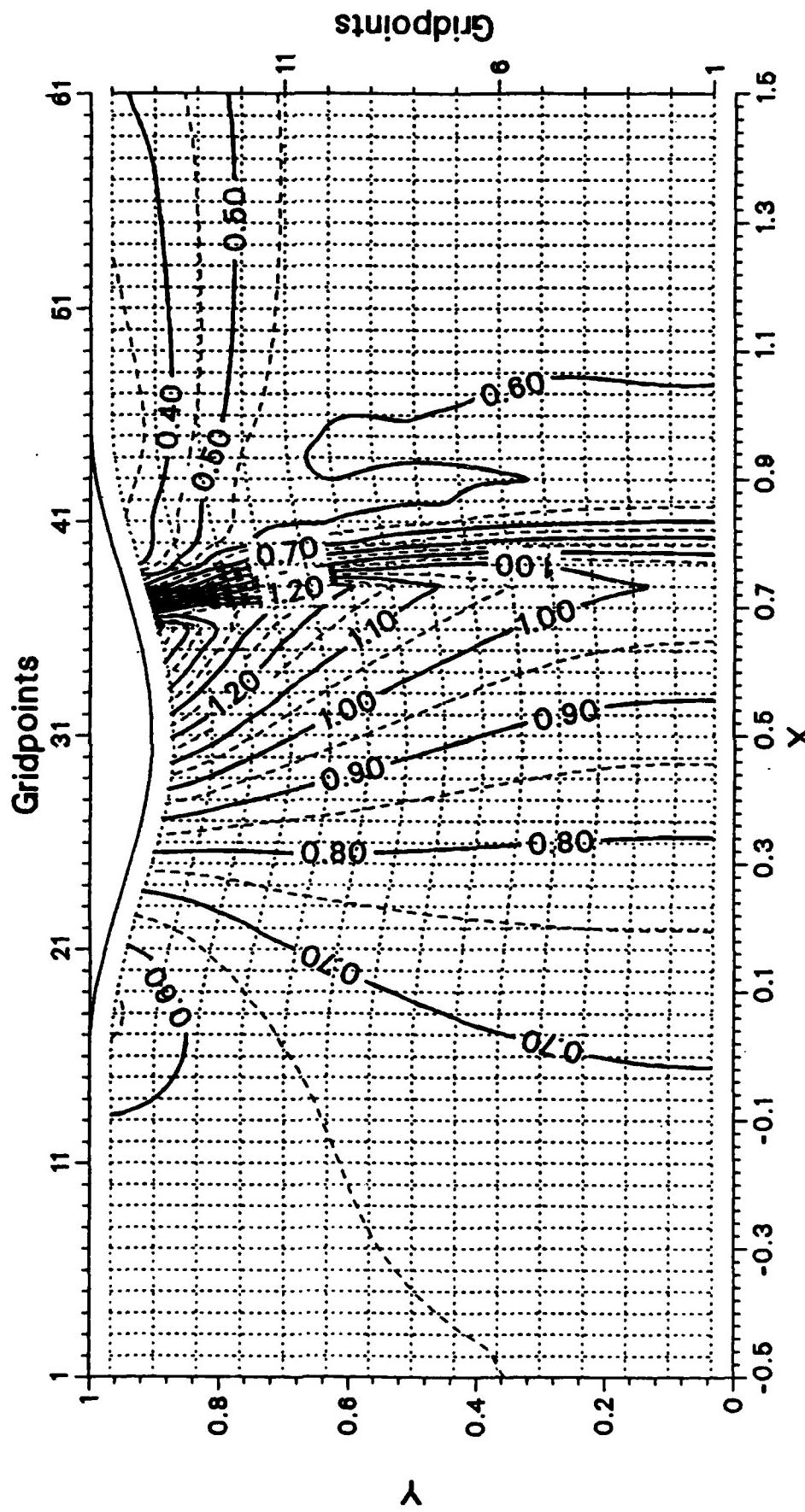


Fig. 6-22. Sinusoidal "bump"-flow. $M_{\infty} = 0.675$, $\rho_e = 0.7369$.

Unsteady solution for first two dimensional sample case.

$\rho_{e,amp} = 0.12$, $K = 0.369$.

Mach number in physical plane

$$t = \frac{2\cdot 2}{\pi} \cdot 2\pi$$

RUN NUMBER = 213
k = 8200

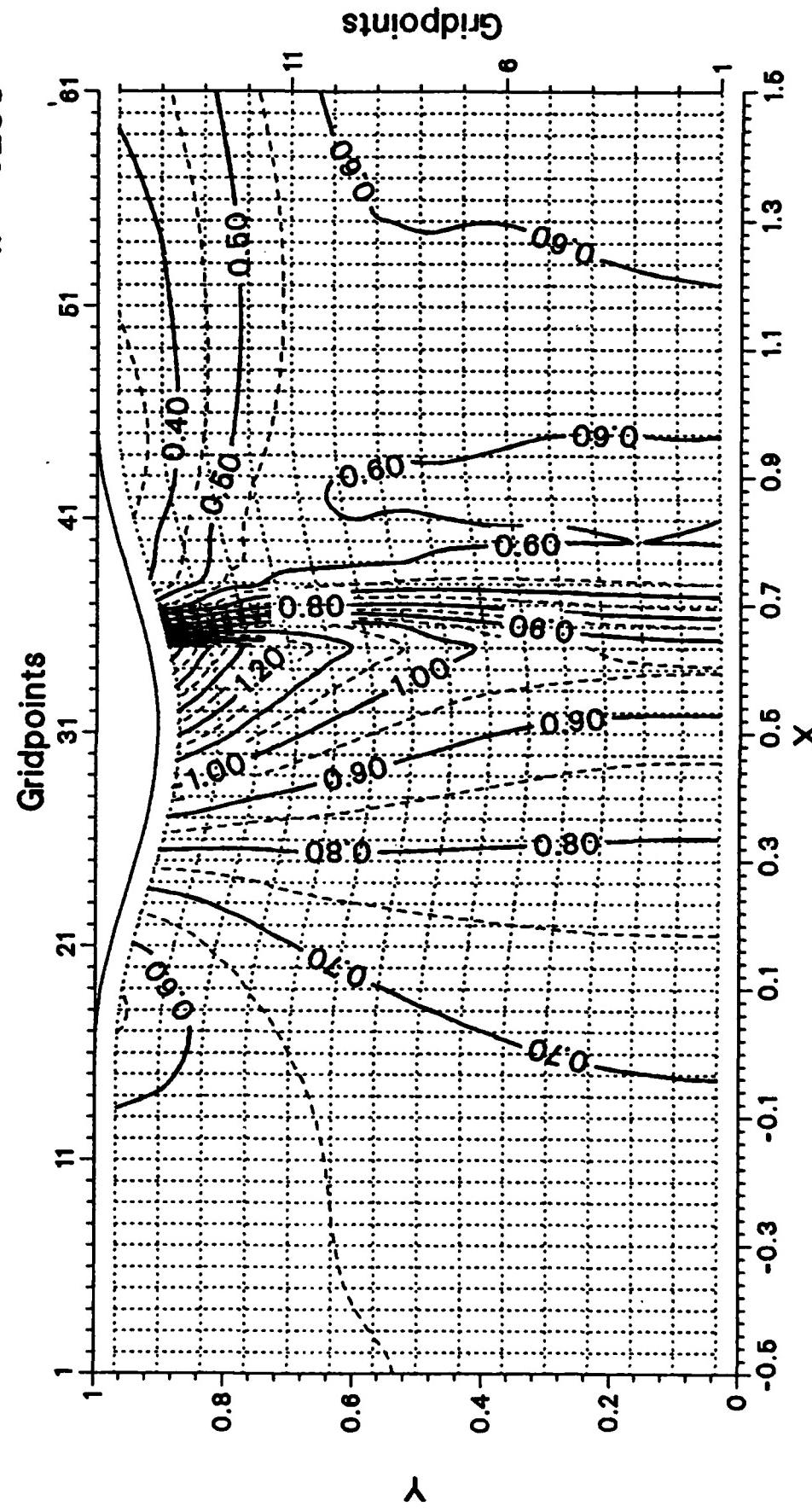


Fig. 6-23. Sinusoidal "bump"-flow. $M_{\infty}=0.675$, $\rho_e=0.7369$.

Unsteady solution for first two dimensional sample case.

$\alpha_1 = 0.12, k = 0.369$

Mach number in physical plane

RUN NUMBER = 213
 $k = 8300$
 $t = \frac{23}{16} \cdot 2\pi$

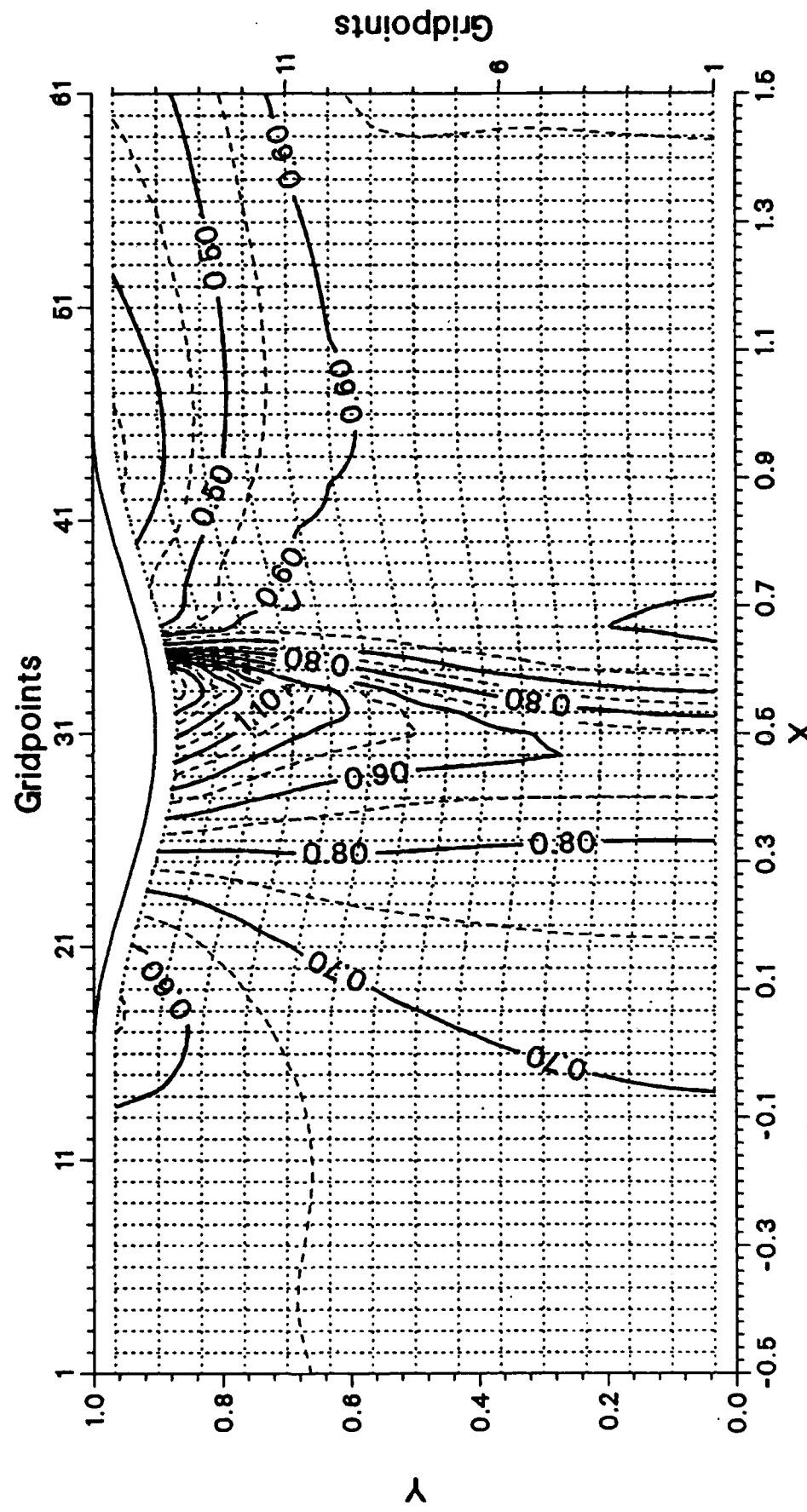


Fig. 6-24. Sinusoidal "bump"-flow. $M_{-\infty}=0.675$, $\rho_e=0.7369$.

Unsteady solution for first two dimensional sample case.

$\rho_{e,\text{amp}}=0.12$, $k=0.369$.

Mach number in physical plane

$$t = \frac{24}{16} \cdot 2\pi$$

RUN NUMBER = 213
k = 8400

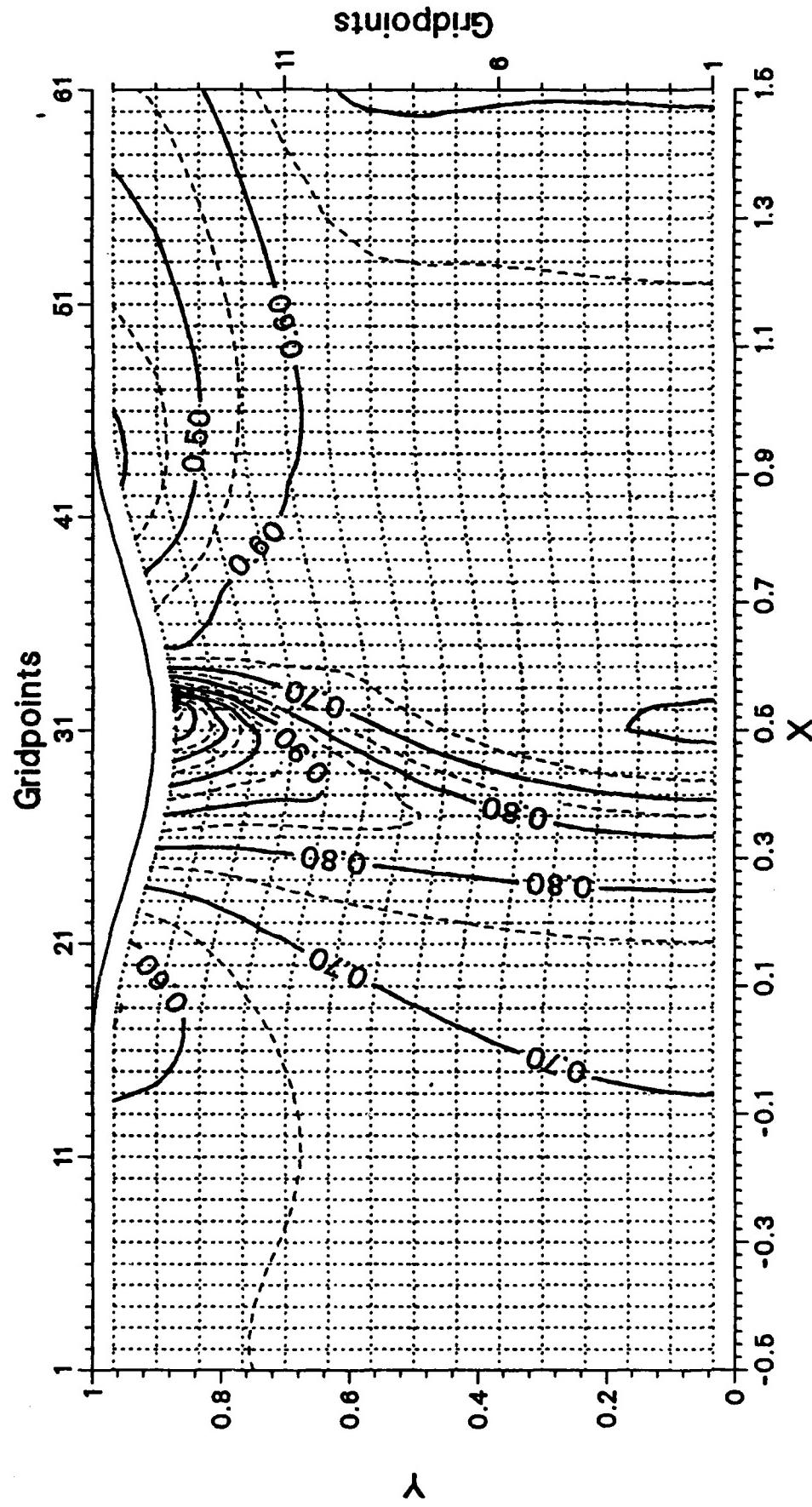


Fig. 6-25. Sinusoidal "bump"-flow. $M_{\infty}=0.675$, $\rho_e=0.7369$.

Unsteady solution for first two dimensional sample case.
 $\rho_{e, \text{am}}=0.12$, $k=0.369$.

Mach number in physical plane

RUN NUMBER = 213
 $k = 8500$
 $t = \frac{25}{16} \cdot 2\pi$

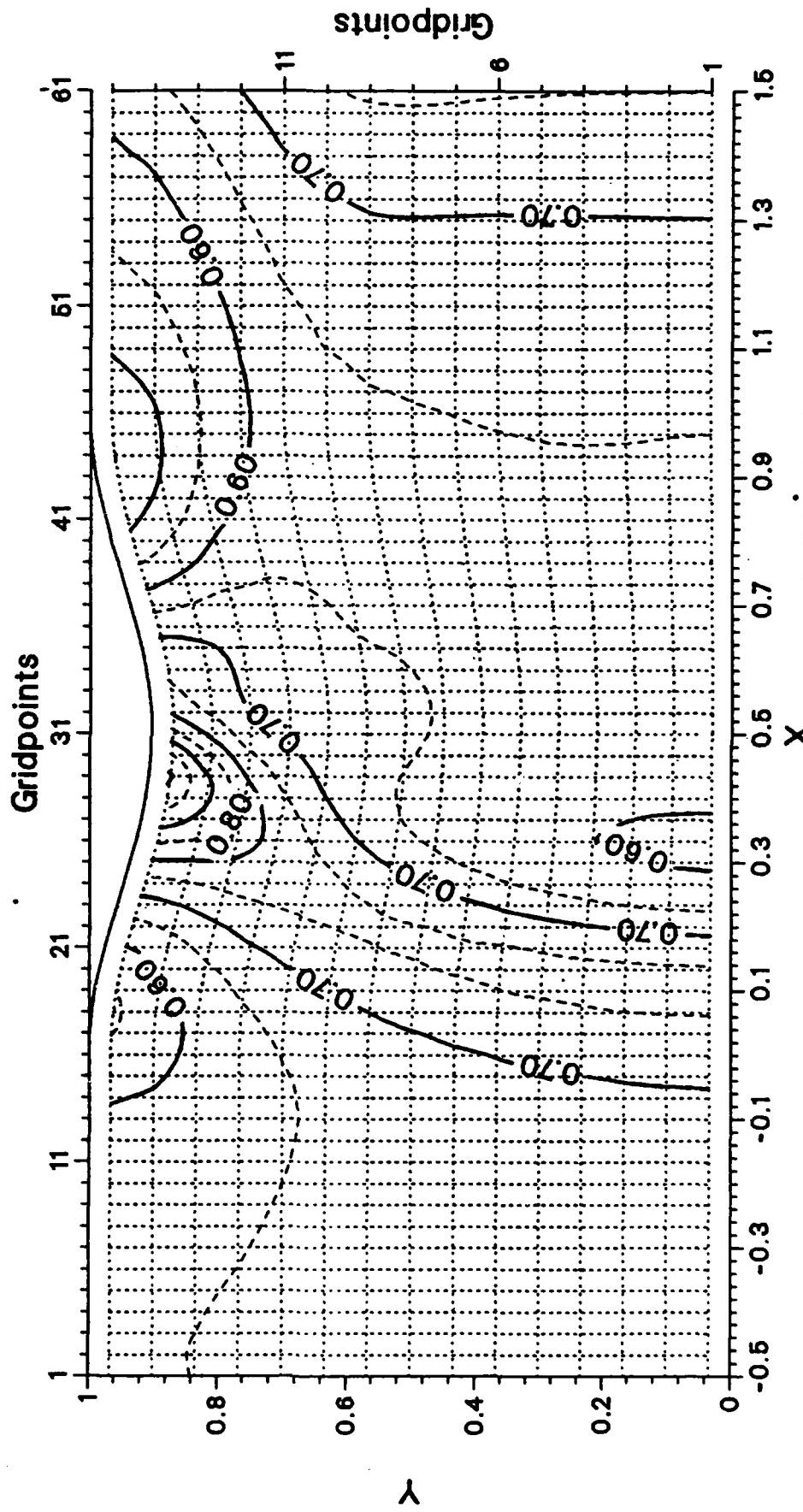


Fig. 6-26. Sinusoidal "bump"-flow. $M_{L\infty}=0.675$, $\rho_e=0.7369$.
 Unsteady solution for first two dimensional sample case.
 $\rho_{e,amp}=0.12$, $k=0.369$.

Mach number in physical plane

$$t = \frac{26}{16} \cdot 2\pi$$

RUN NUMBER = 213
k = 8600

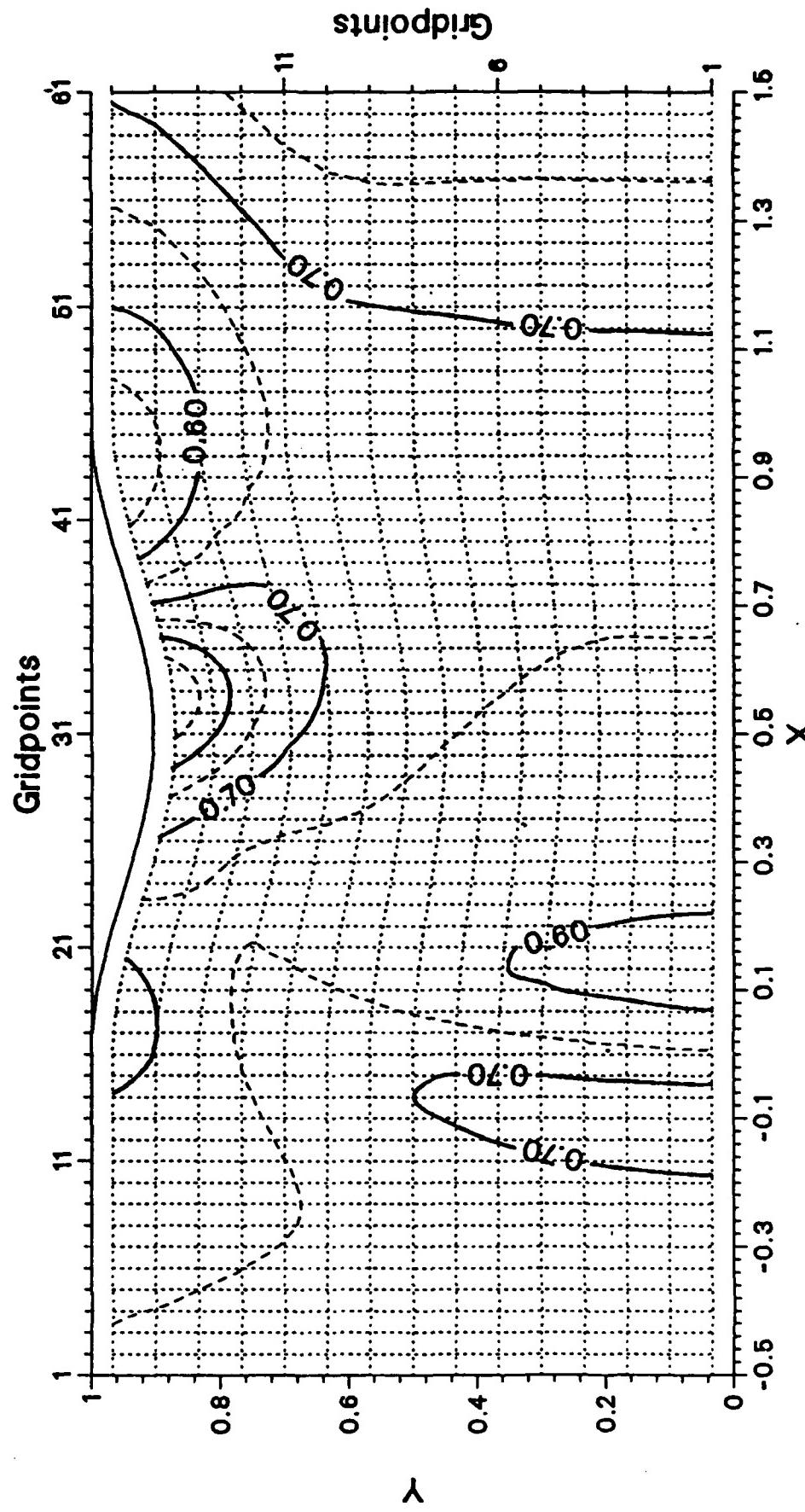


Fig. 6-27. Sinusoidal "bump" flow. $M_{\infty} = 0.675$, $\rho_e = 0.7369$. Unsteady solution for first two dimensional sample case.
 $p_{e,amp} = 0.12$, $k = 0.369$.

Mach number in physical plane

RUN NUMBER = 213
 $k = 8700$
 $t = \frac{2\pi}{16} \cdot 2\pi$

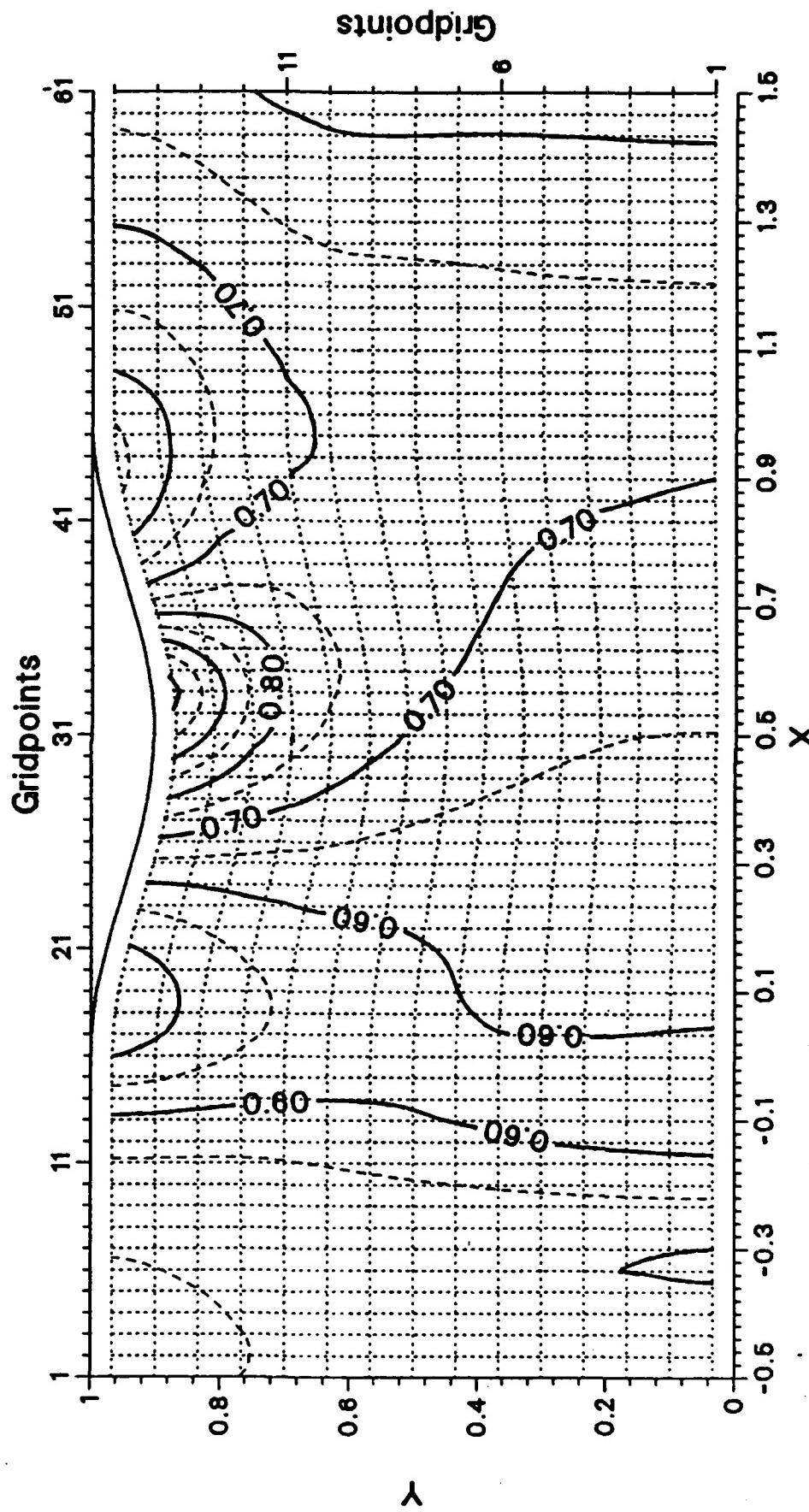


Fig. 6-28. Sinusoidal "hump"-flow. $M_{\infty}=0.675$, $\rho_e=0.7369$. Unsteady solution for first two dimensional sample case.
 $\rho_{e,amp}=0.12$, $k=0.369$.

Mach number in physical plane

RUN NUMBER = 213
 $t = \frac{2\pi}{16} \cdot 2\pi$
 $k = 8800$

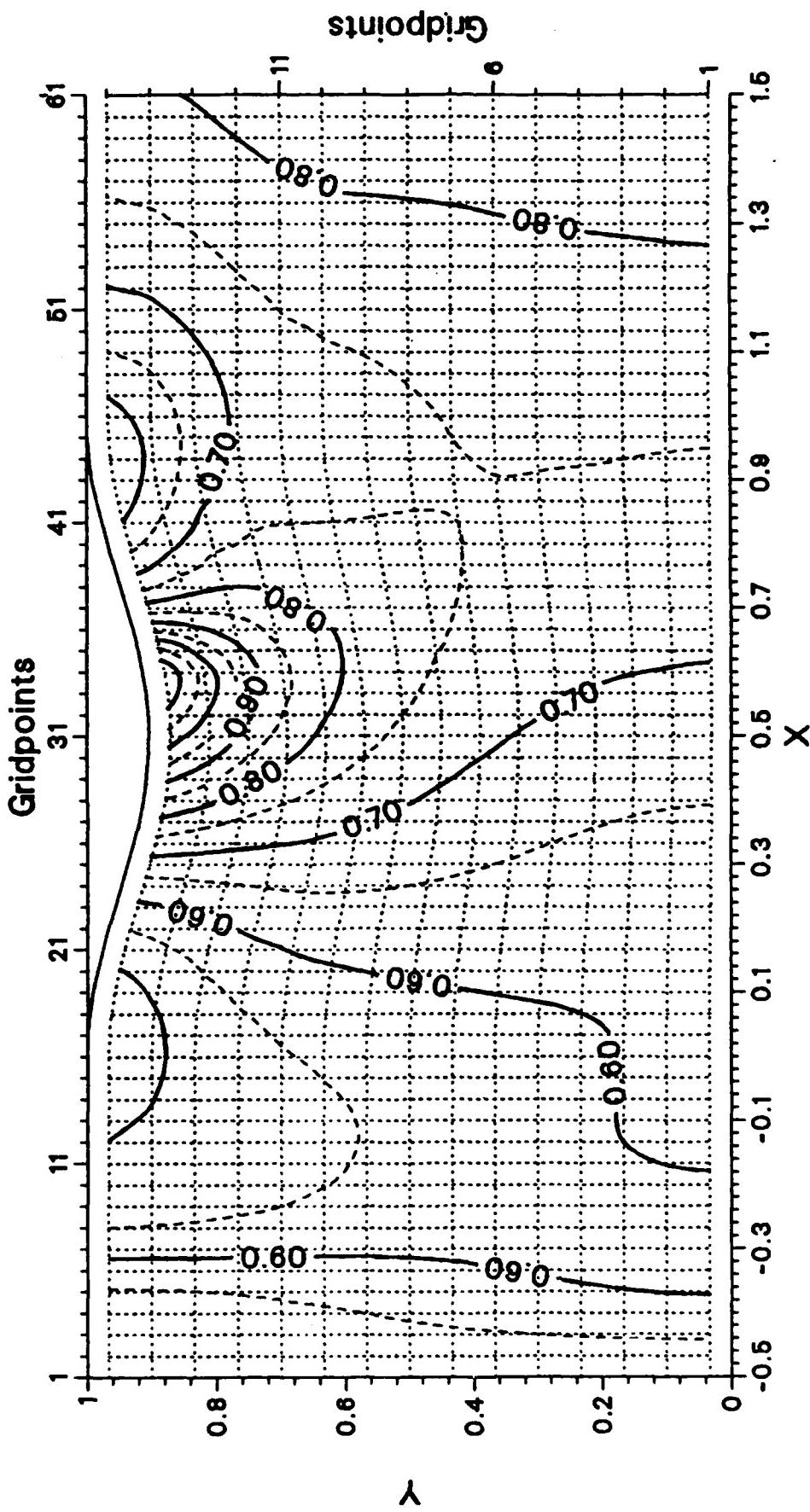


Fig. 6-29. Sinusoidal "bump"-flow. $M_{\infty}=0.675$, $\rho_e=0.7369$.

Unsteady solution for first two dimensional sample case.
 $\rho_{e, \text{avg}}=0.12$, $k=0.369$.

Mach number in physical plane

RUN NUMBER = 213
 $k = 8900$

$$t = \frac{29}{16} \cdot 2\pi$$

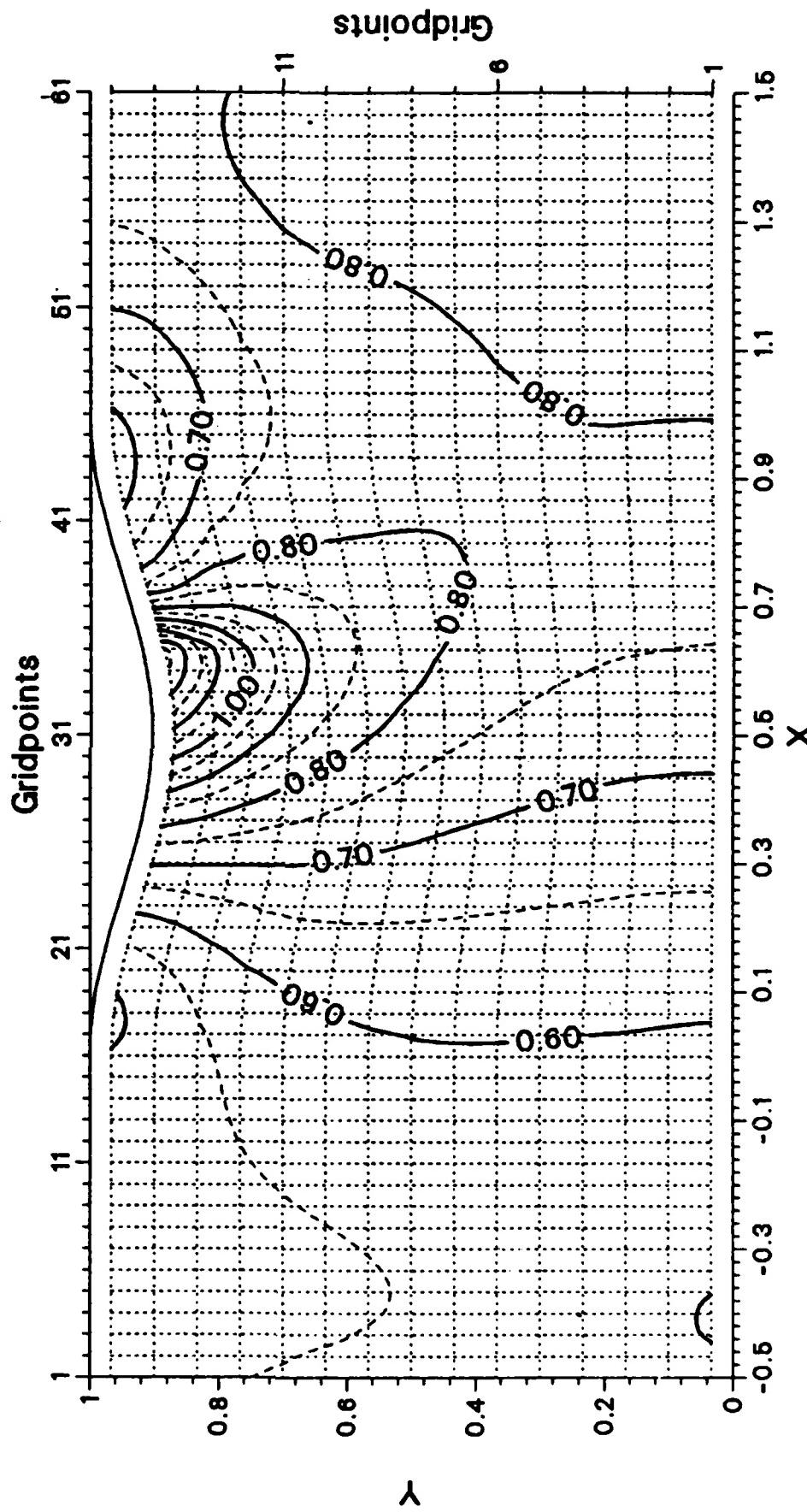


Fig. 6-30. Sinusoidal "bump"-flow. $M_{\infty}=0.675$, $\rho_e=0.7369$.

Unsteady solution for first two dimensional sample case.

$$\rho_{e,amp}=0.12, k=0.369.$$

Mach number in physical plane

RUN NUMBER = 213
 $k = 10100$

$$t = \frac{41}{16} \cdot 2\pi$$

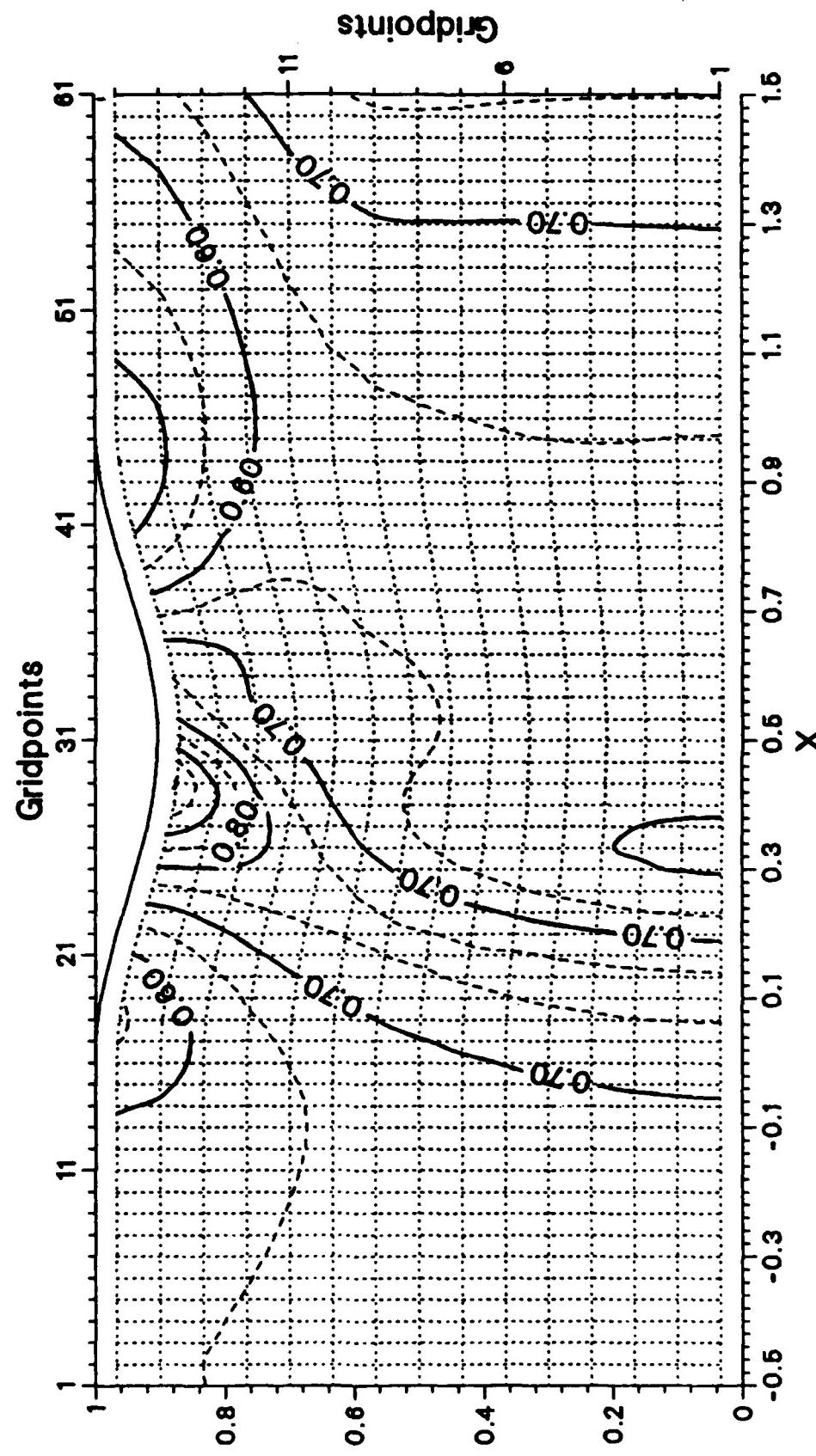


Fig. 6-31. Sinusoidal "bump"-flow. $M_{\infty}=0.675$, $p_e=0.7369$. Unsteady solution for first two dimensional sample case.
 $p_{e,amp}=0.12$, $k=0.369$.

Mach number in physical plane

$t = 0$

RUN NUMBER = 214
 $k = 6000$

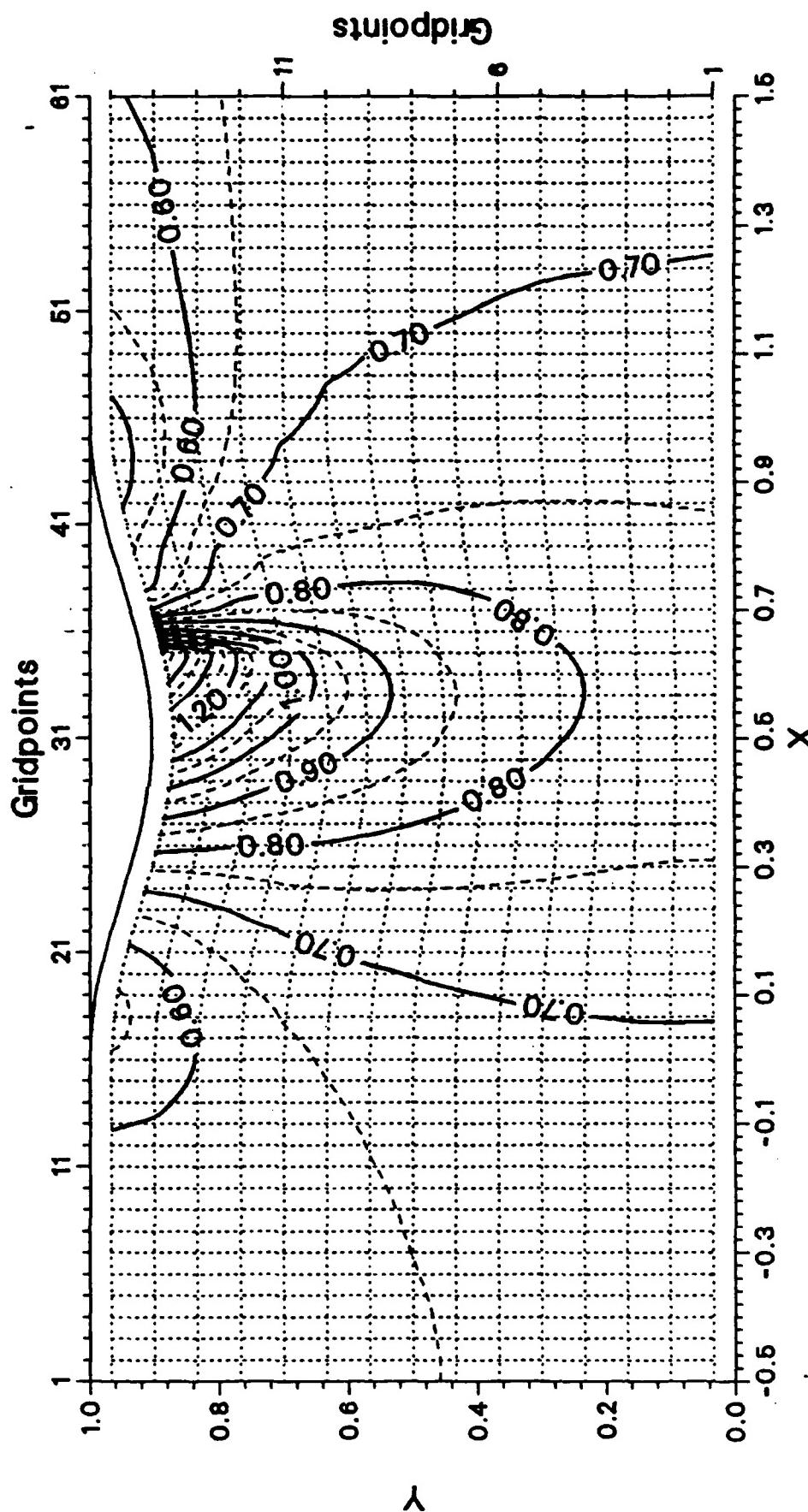


Fig. 6-32. Sinusoidal "bump" flow. $M_{\infty} = 0.675$, $p_0 = 0.7369$.
Steady state solution for second two dimensional sample case.

Mach number in physical plane

RUN NUMBER = 214
 $k = 6400$

$$t = \frac{y}{16} \cdot 2\pi$$

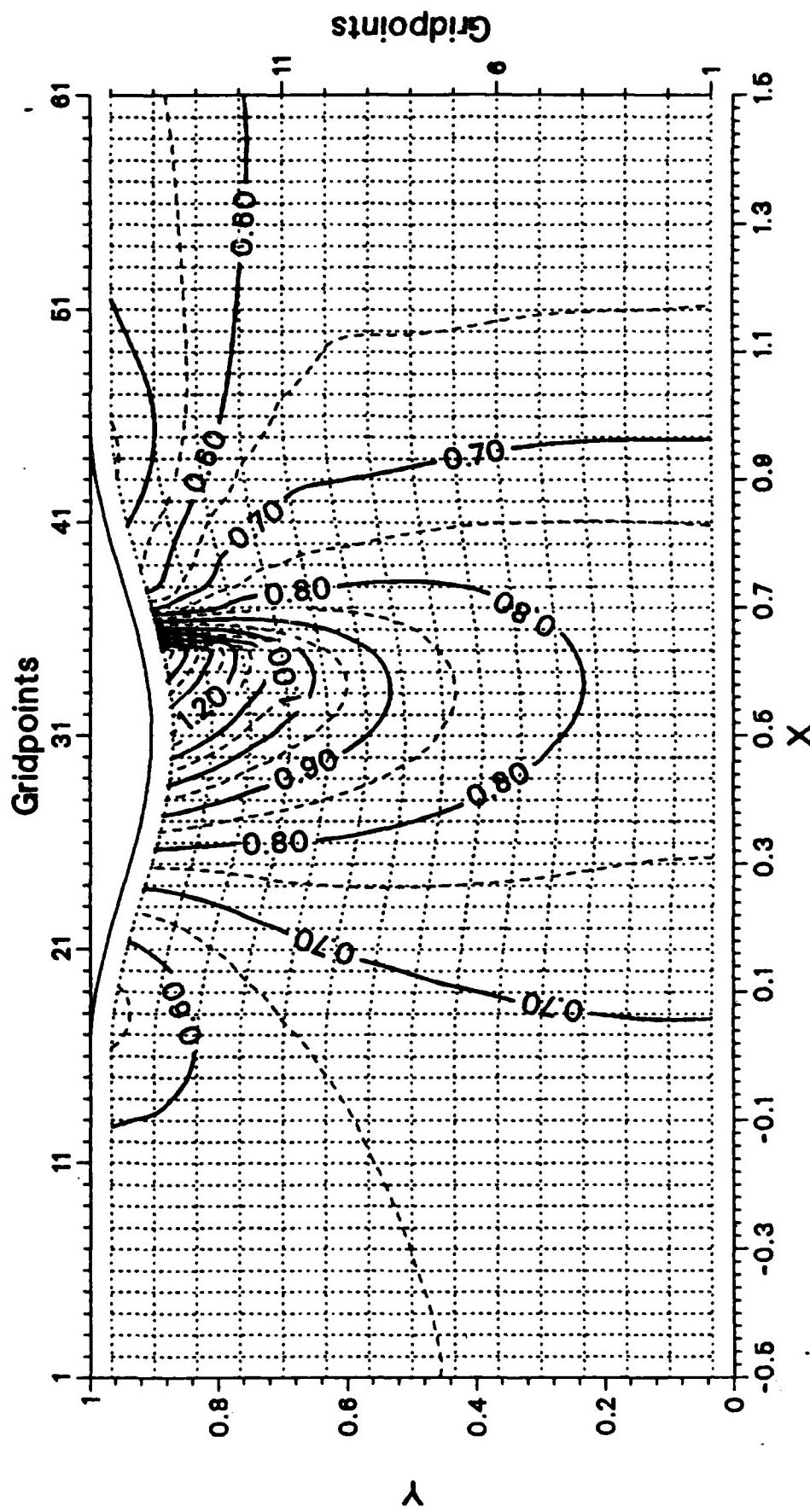


Fig. 6-33. Sinusoidal "bump"-flow. $M_{\infty}=0.675$, $\rho_0=0.7369$.

Unsteady solution for second two dimensional sample case.

Mach number in physical plane

$$t = \frac{5}{\pi} \cdot 2 \tilde{\pi}$$

RUN NUMBER = 214
 $k = 6500$

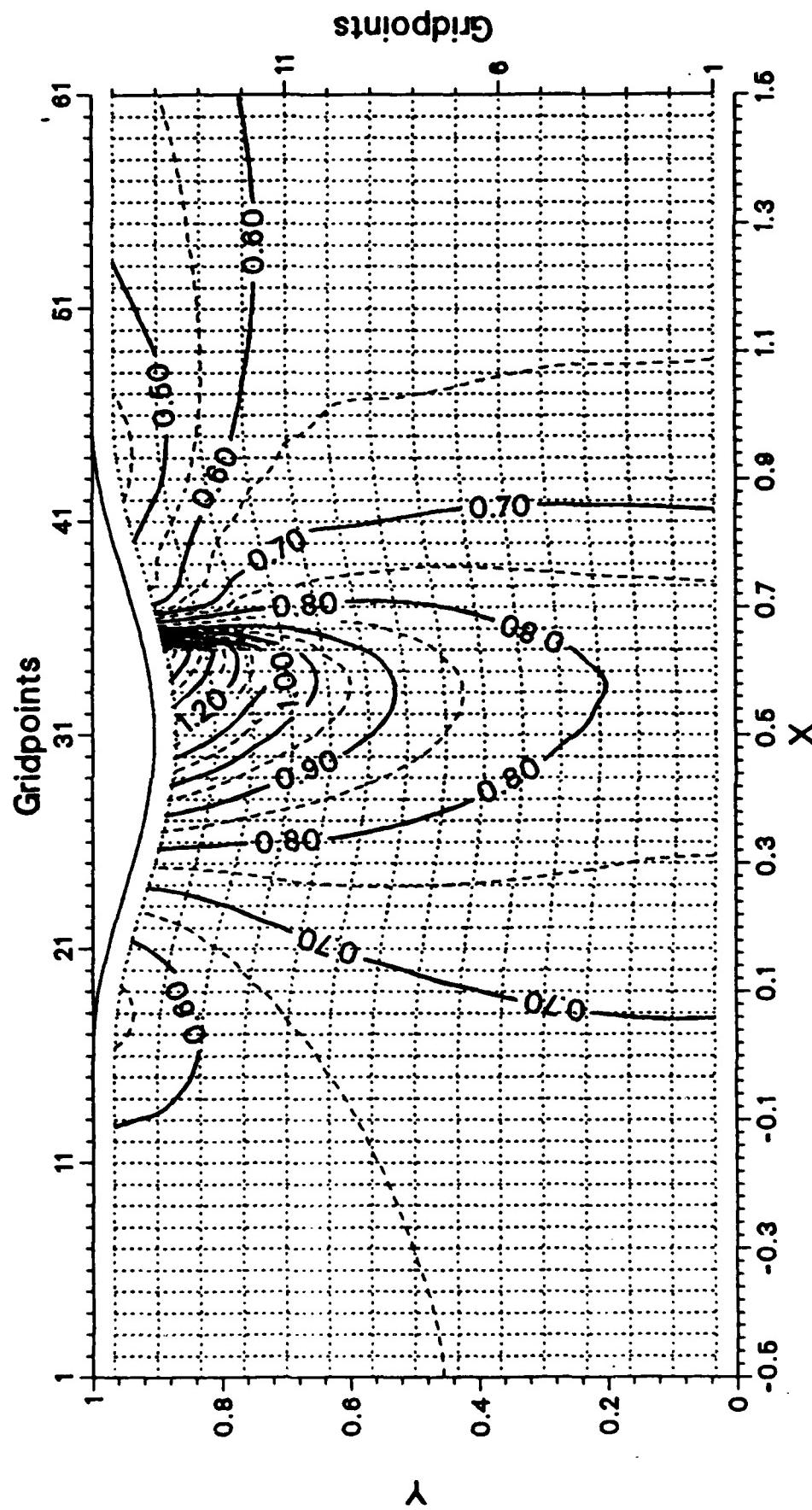


Fig. 6-34. Sinusoidal "bump"-flow. $M_{\infty}=0.675$, $\rho_0=0.7369$.

Unsteady solution for second two dimensional sample case.

$\rho_{e,amp}=0.06$, $k=0.369$.

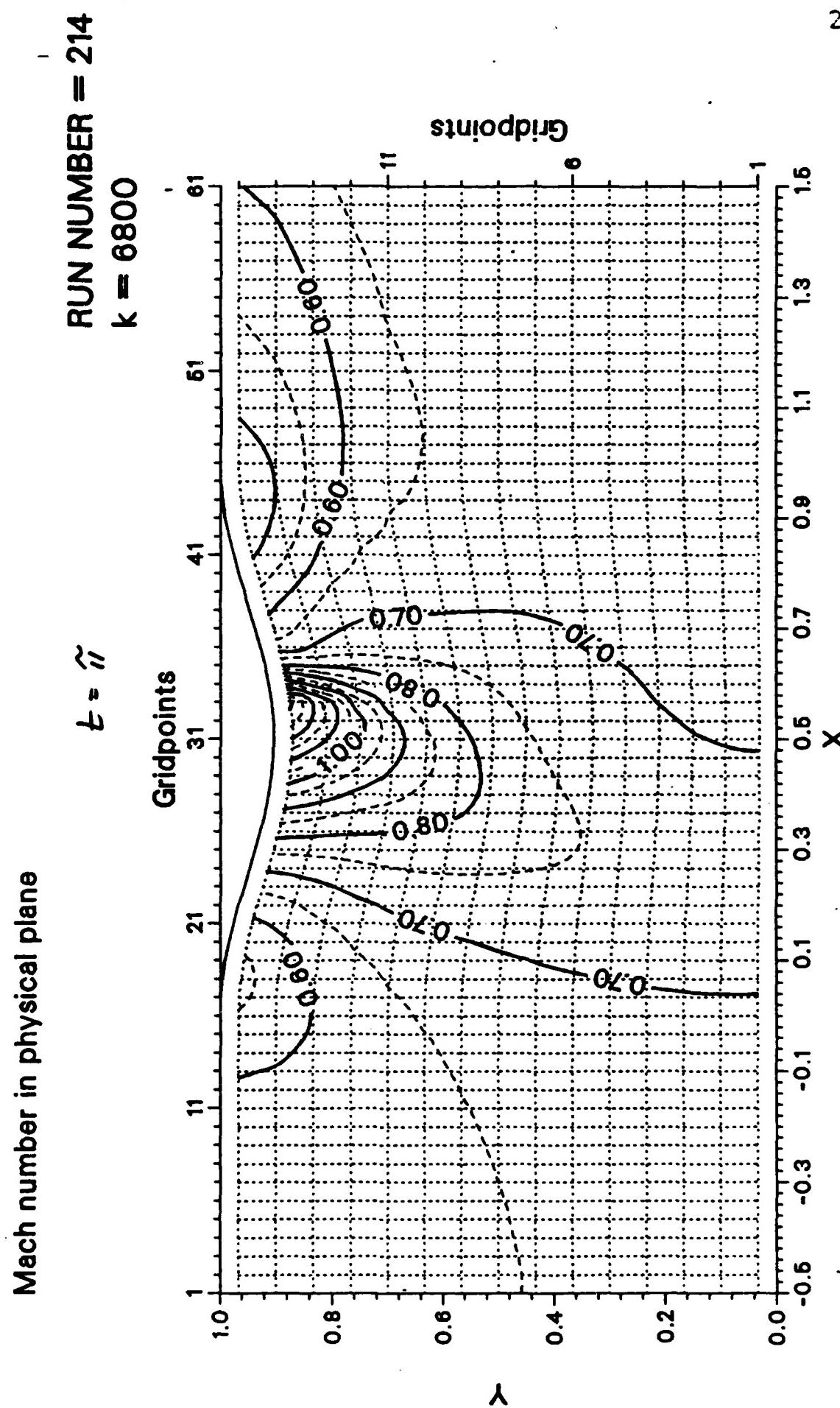


Fig. 6-35. Sinusoidal "bump"-flow. $M_{\infty}=0.675$, $\rho_e=0.7369$. Unsteady solution for second two dimensional sample case.
 $D_a = 0.06$, $K=0.369$.

Mach number in physical plane

RUN NUMBER = 214
 $k = 7000$
 $t = \frac{10}{k} \cdot 2\pi$

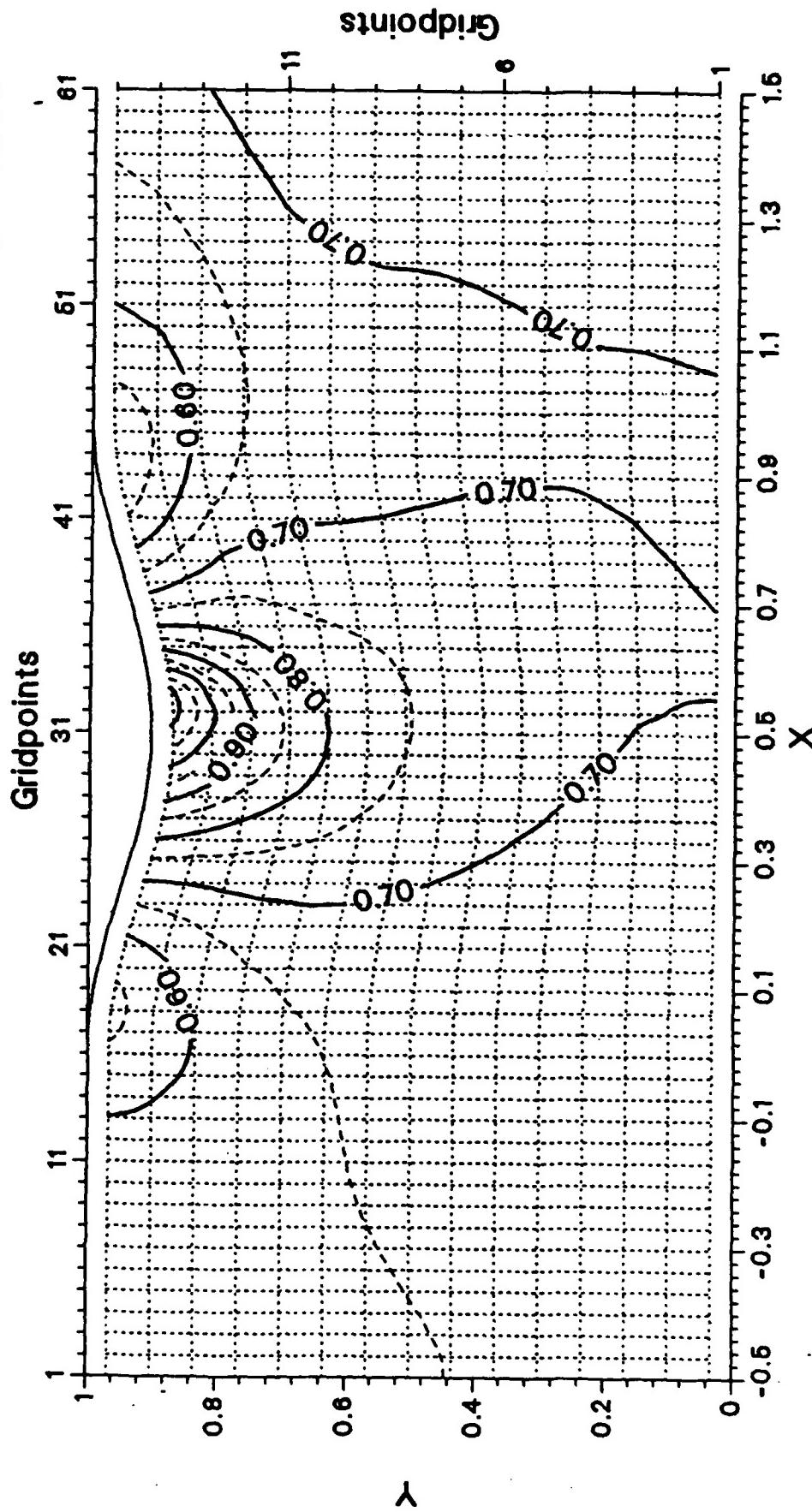


Fig. 6-36. Sinusoidal "bump"-flow. $M_{\infty} = 0.675$, $\rho_e = 0.7369$.

Unsteady solution for second two dimensional sample case.
 $\rho_{e,amp} = 0.06$, $k = 0.369$.

Mach number in physical plane

RUN NUMBER = 214
 $k = 7100$
 $t = \frac{11}{16} \cdot 2\pi$

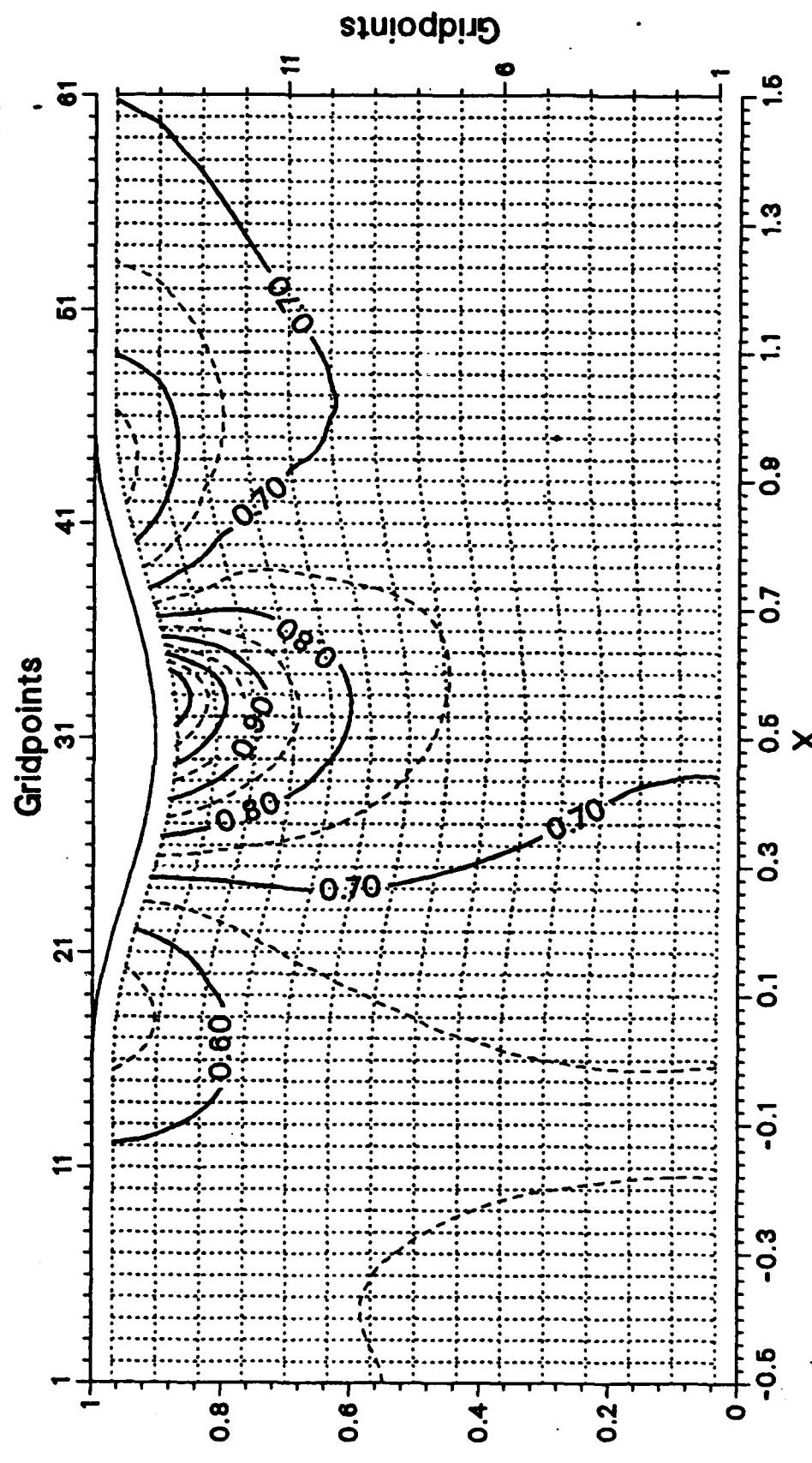


Fig. 6-37. Sinusoidal "bump"-flow. $M_{\infty}=0.675$, $\rho_e=0.7369$.

Unsteady solution for second two dimensional sample case.

$D_{\infty}=0.06$, $k=0.369$

Mach number in physical plane

RUN NUMBER = 214
 $t = \frac{13}{16} \cdot 2\pi$
 $k = 7300$

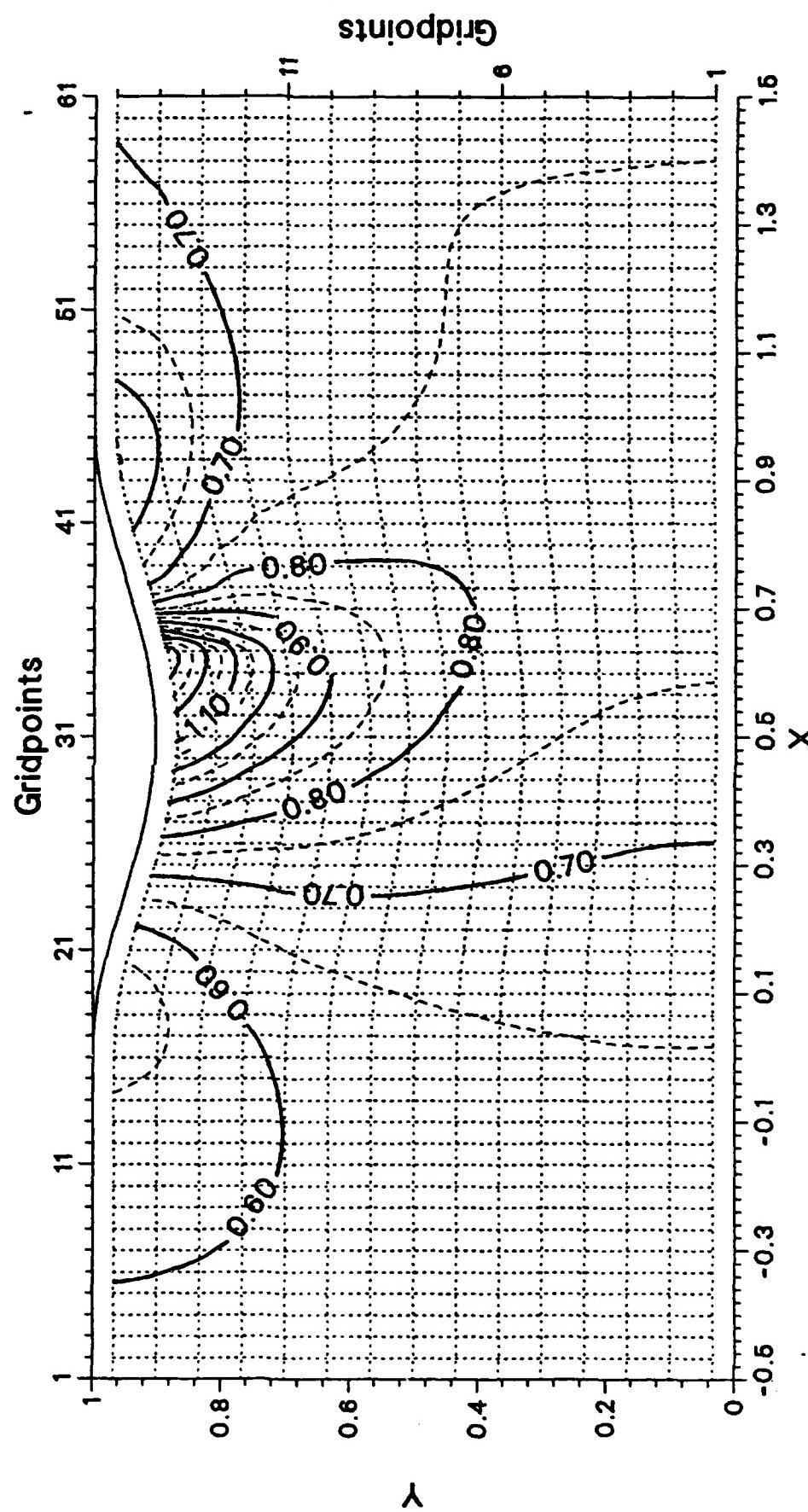


Fig. 6-38. Sinusoidal "bump"-flow. $M_{-\infty} = 0.675$, $p_{\theta} = 0.7369$.

Unsteady solution for second two dimensional sample case.
 $p_{\theta, \text{amp}} = 0.06$, $k = 0.369$.

Mach number in physical plane

RUN NUMBER = 214
 $k = 7800$

$$t = \frac{18}{16} \cdot 2\pi$$

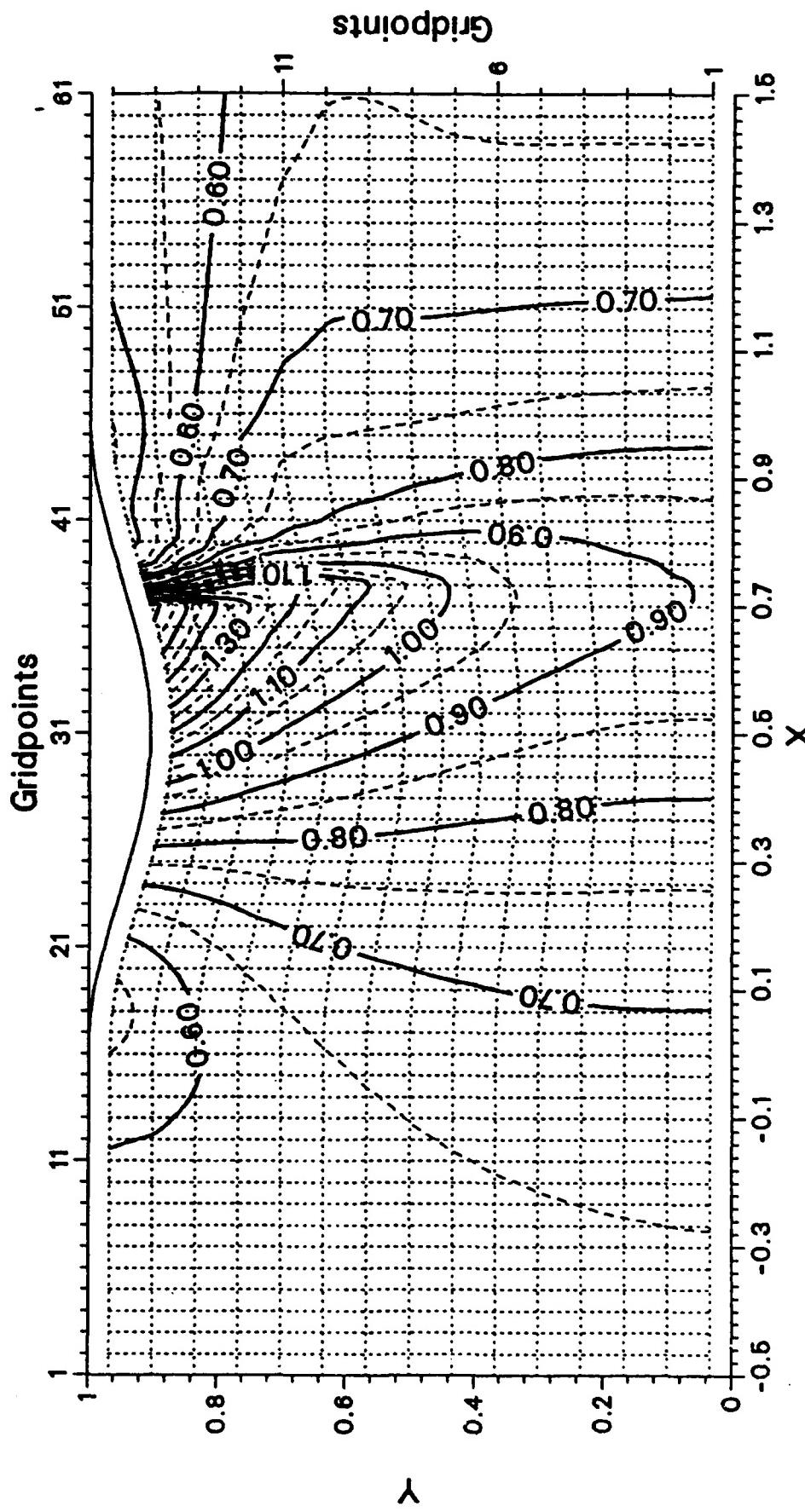


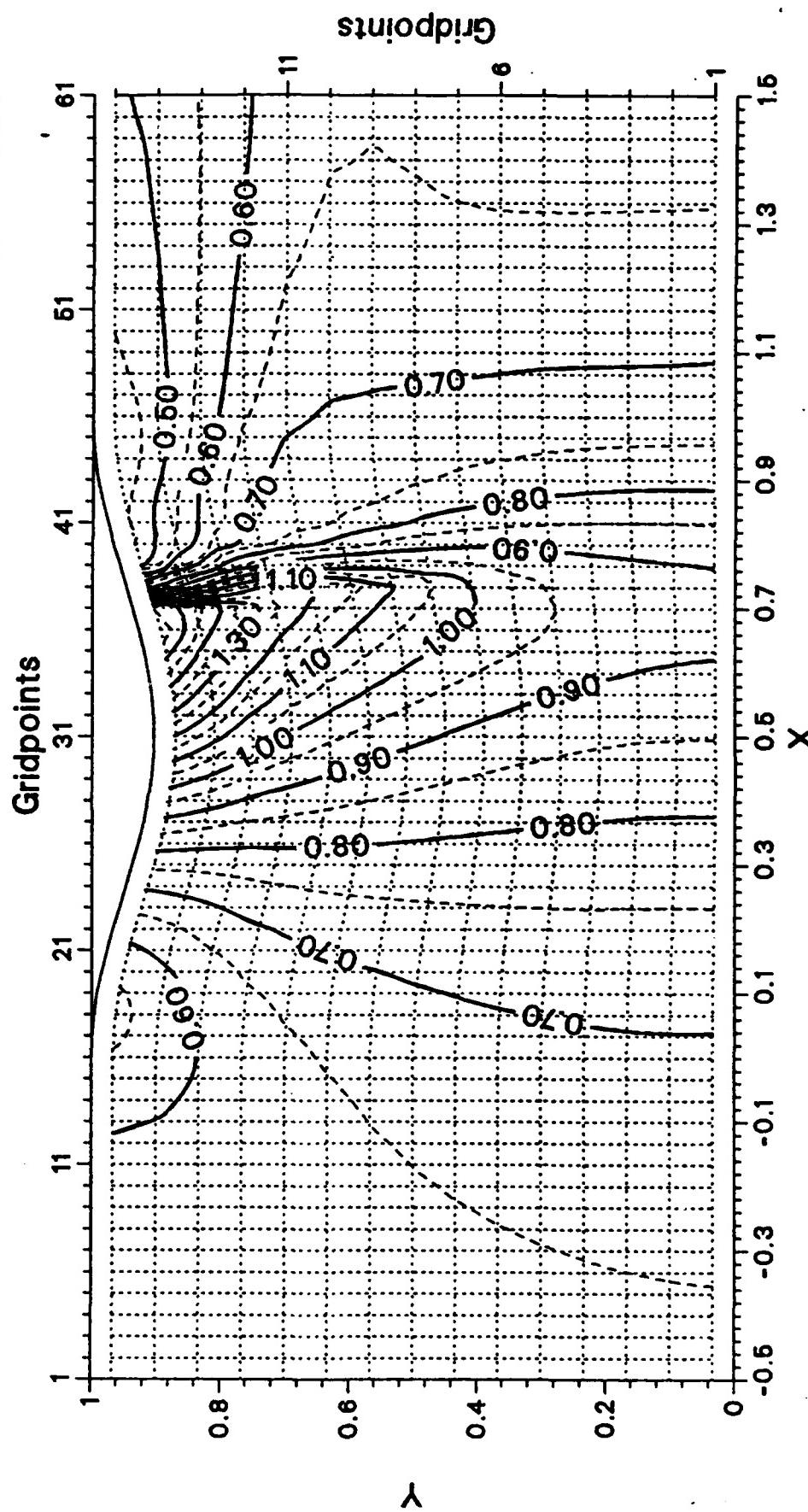
Fig. 6-39. Sinusoidal "bump"-flow. $M_{\infty}=0.675$, $p_e=0.7369$.

Unsteady solution for second two dimensional sample case.

$\rho_{e, \text{ann}}=0.06$, $k=0.369$.

Mach number in physical plane

RUN NUMBER = 214
k = 7900



Sinusoidal "bump"-flow. $M_{-\infty}=0.675$, $p_e=0.7369$.
Unsteady solution for second two dimensional sample case
 $p_e, \alpha, k = 0.06$, $k=0.369$.

Mach number in physical plane

RUN NUMBER = 214
 $t = \frac{20}{16} \cdot 2\pi$
 $K = 8000$

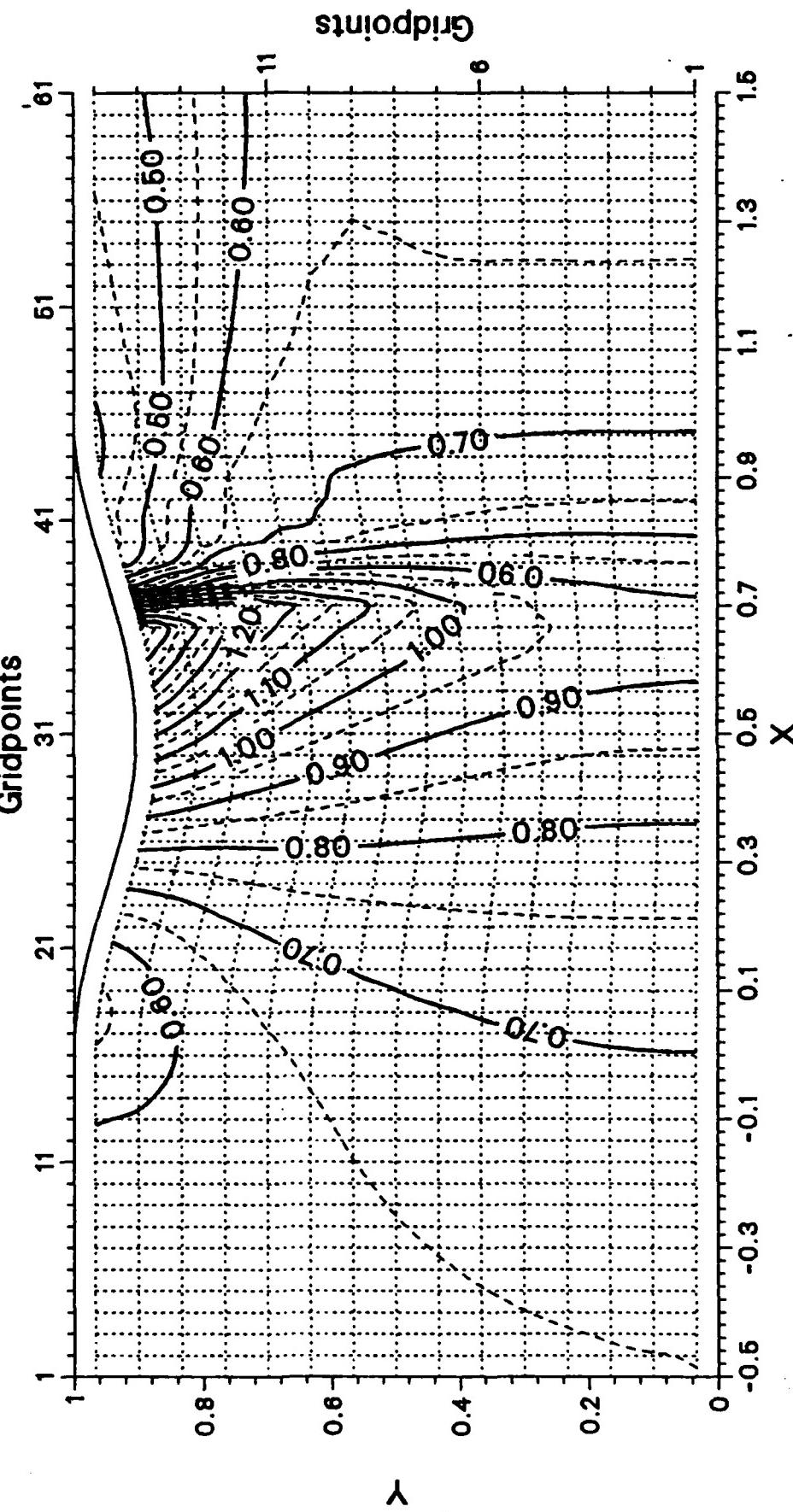


Fig. 6-41. Sinusoidal "bump"-flow. $M_{\infty}=0.675$, $\rho_0=0.7369$.

Unsteady solution for second two dimensional sample case.
 $\rho_{e,amp}=0.05$, $K=0.369$.

Mach number in physical plane

$t = \frac{21}{46} \cdot 2\pi$ RUN NUMBER = 214
 $K = 8100$

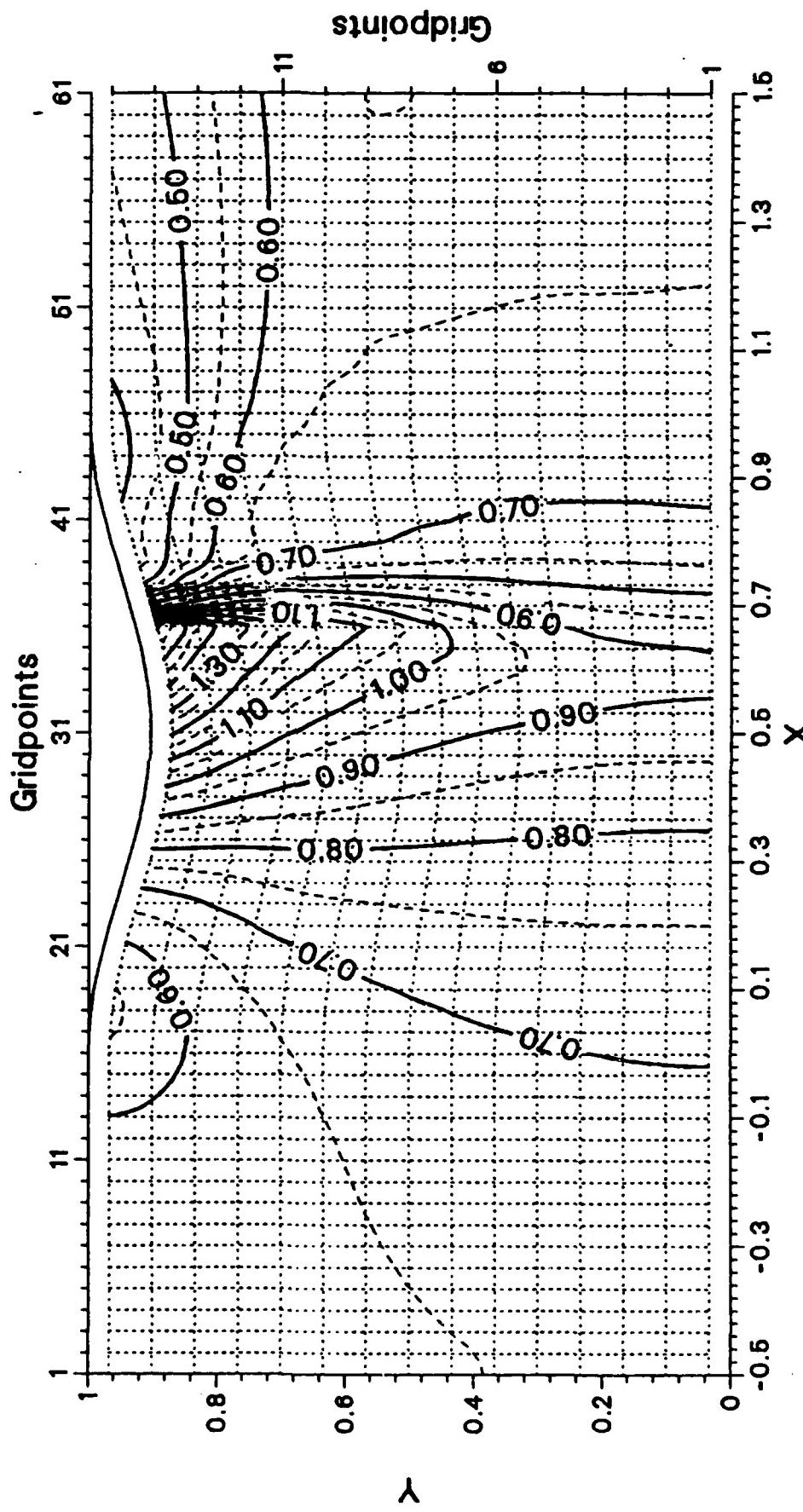


Fig. 6-42. Sinusoidal "bump"-flow. $M_{\infty}=0.675$, $\rho_0=0.7369$. Unsteady solution for second two dimensional sample case.
 $\rho_{0,amp}=0.06$, $K=0.369$.

7. Transformation From the Physical Into the Computational Plane of Reference.

The general transformation from the (x,y,t) -plane to the (ξ,η,τ) -plane will be presented in this section. The transformation in τ is straightforward, as $\tau=t$, and only (x,y) to (ξ,η) is discussed.

The transformation presented should be user friendly in as far as it should allow for simple changes of cascade geometry. It should also allow for a blade vibration, presently in circumferential direction (as seen in the rotating turbomachine, y direction in the Cartesian coordinate system in the present study), and easily be extended to accommodate any general blade vibration. In order to treat cases of propagation of disturbances through a cascade, the transformation should be able to handle several blade passages of a general profile. Furthermore, the mapping should allow for the following:

- The inlet and outlet planes are fixed in both the computational and physical planes during a generalized blade vibration.
- The leading edge position shall be constant in a predefined axial and circumferential direction in the computational plane.
- Idem for the trailing edge.
- Computational points should be clustered in the leading and trailing edge regions, and close to the blade surfaces.
- The computational points towards the inlet and outlet flow boundaries in the physical plane should be stretched away from the profile.
- The mapping should be fast as it has to be performed for every time step of the calculation, both for the calculation with vibrating blades and for the calculation with stationary blades as in both cases the slipstream from the trailing edge will move in time.

For the above objectives, it was decided to introduce the blade geometry as coordinate points, and to adopt a numerical grid of "H"-form (Fig. 7.1). This sort of grid is acceptable for capturing normal shock waves (which is the scope of the present study). Obviously, a C-grid or an O-grid would be better from the point of view of accurately resolving the flow around the leading edge. However, the creation of such grids for unsteady cascade flows is a major undertaking in itself. It is instead proposed to use an H-mesh for global resolution, and in the future overlap this global H-mesh

with a local, around and fixed with the airfoil, C-mesh. This kind of approach has been shown by Steger /55/ to be feasible for steady state flows (Euler solver) and for small unsteady perturbation potential flow by Verdon /56/.

The transformation includes clustering of points, for better resolution in regions of high flow gradients, in several locations, presently at:

- downstream of inlet boundary and/or upstream of leading edge plane.
- downstream of leading edge and/or upstream of trailing edge plane.
- downstream of trailing edge plane and/or upstream of outlet boundary.

The physical domain of interest, limited by the inlet and outlet boundaries and the upper and lower blades (Fig. 7.1), is then separated, in axial direction ($=x$), into three different regions, each extending over the number of blade passages chosen in the circumferential direction ($=y$):

Region 1: From inlet to leading edge plane ($\xi < 0$).

Region 2: Blade passages ($0 \leq \xi \leq 1$).

Region 3: From trailing edge plane to downstream boundary ($\xi > 1$).

Each of these regions are mapped into a rectangular computational plane of reference with the following transformations.

The mapping in **axial direction (x)** is given by eq. 7.1 in regions 1 and 2 /1,2/:

$$\xi(x,y,t) = \xi_{\text{start}} + (\xi_{\text{end}} - \xi_{\text{start}}) (\alpha_x + (1-\alpha_x) \ln(A_1/A_2) / \ln(A_3/A_4)) \quad (7.1)$$

where:

- $A_1 = \beta_x - 2\alpha_x + (2\alpha_x + 1)(x - x_{\text{start}}) / (x_{\text{end}} - x_{\text{start}})$
- $A_2 = \beta_x + 2\alpha_x - (2\alpha_x + 1)(x - x_{\text{start}}) / (x_{\text{end}} - x_{\text{start}})$
- $A_3 = \beta_x + 1$
- $A_4 = \beta_x - 1$
- α = variable to indicate where the mesh should be refined.
= 0.0: refinement only towards the end of the region.
= 0.5: equal refinement both towards the end and the beginning.
- β = stretching parameter ($\beta > 1$)
- Index "x": parameters in x-direction (α/β are different for each region).
- Index "start": x and ξ value at the beginning of each region.
- Index "end": x and ξ value at the end of each region.

In region 3 this mapping is given by eq. 7.2:

$$-\xi(x,y,t) = -\xi_{start} + \{\xi_{end} - \xi_{start}\}(-1 + \alpha_x + (1 - \alpha_x)\ln(A_9/A_{10})/\ln(A_3/A_4)\} \quad (7.2)$$

where:

- $A_9 = \beta_x - 2\alpha_x + (2\alpha_x + 1)(x - x_{end})/(x_{start} - x_{end})$
- $A_{10} = \beta_x + 2\alpha_x - (2\alpha_x + 1)(x - x_{end})/(x_{start} - x_{end})$

The reason for this change in the mapping between regions 2 and 3 is to have the possibility to cluster points in the beginning of zone 3, instead of towards the end as in region 1.

In the circumferential direction (y) the mapping is given by eq. 7.3:

$$\eta(x,y,t) = \eta_{start} + \{\eta_{end} - \eta_{start}\}(\alpha_y + (1 - \alpha_y)\ln(B_1/B_2)/\ln(B_3/B_4)\} \quad (7.3)$$

where:

- $B_1 = \beta_y - 2\alpha_y + (2\alpha_y + 1)(y - y_{start})/(y_{end} - y_{start})$
- $B_2 = \beta_y + 2\alpha_y - (2\alpha_y + 1)(y - y_{start})/(y_{end} - y_{start})$
- $B_3 = \beta_y + 1$
- $B_4 = \beta_y - 1$
- α = idem as for axial direction.
- β = idem as for axial direction.
- index "y": parameters in y-direction .
- index "start": y and η value at the beginning of each region (i.e. the blade surfaces).
- index "end": y and η value at the end of each region (i.e. the blade surfaces).

Here, the computational grid stretches from $\eta=0$. (for the upper surface of blade 1) till $\eta=N-1$ (for the lower surface of blade N). Thus, for blade passage "1", $\eta_{start}=0$, whereas $\eta_{end}=1$.

This transformation maps the physical plane into the computational plane (i.e. (x,y) to (ξ,η)). The inverse of the mapping $((\xi,\eta)$ to $(x,y))$ is easily computed to be:

- in axial direction, regions 1 and 2:

$$x_{i,j} = x_{start} + (x_{end} - x_{start}) [\beta_x A_8 + 2\alpha_x A_7] / [A_7(2\alpha_x + 1)] \quad (7.4)$$

where

$$\begin{aligned} i &: \text{computational point in } \xi \text{ direction} \\ j &: \text{computational point in } \eta \text{ direction} \\ A_5 &= (\xi_{i,j} - \xi_{start}) / (\xi_{end} - \xi_{start}) \\ A_6 &= (A_5 - \alpha_x) / (1 - \alpha_x) \\ A_7 &= (\beta_x + 1) A_6 + (\beta_x - 1) A_6 \\ A_8 &= (\beta_x + 1) A_6 - (\beta_x - 1) A_6 \end{aligned}$$

- in axial direction, region 3:

$$x_{i,j} = x_{end} + (x_{start} - x_{end}) [\beta_x A_8 + 2\alpha_x A_7] / [A_7(2\alpha_x + 1)] \quad (7.5)$$

where now A_5 is different from regions 1 and 2:

$$A_5 = 1 - (\xi_{i,j} - \xi_{start}) / (\xi_{end} - \xi_{start})$$

- In circumferential direction, the inverse of eq. (7.3) is:

$$y_{i,j} = y_{start} + (y_{end} - y_{start}) [\beta_y B_8 + 2\alpha_y B_7] / [B_7(2\alpha_y + 1)] \quad (7.6)$$

where

$$\begin{aligned} B_5 &= (\eta_{i,j} - \eta_{start}) / (\eta_{end} - \eta_{start}) \\ B_6 &= (B_5 - \alpha_y) / (1 - \alpha_y) \\ B_7 &= (\beta_y + 1) B_6 + (\beta_y - 1) B_6 \\ B_8 &= (\beta_y + 1) B_6 - (\beta_y - 1) B_6 \end{aligned}$$

An example of the mapping here presented is given for a symmetrical Joukowski profile at 60° stagger angle (from axial) in Fig. 7.2. Both the entire domain of consideration (Fig. 7.2a) as well as blown up versions in

different part of the flow field are shown for the physical plane, whereas a general view of the computational plane is presented (Fig. 7.3).

Fig. 7.1: Physical domain of reference with H-grid.

Fig. 7.2: Grid of Joukowski profile (15% thickness) at 60° stagger angle in the physical plane.

Fig. 7.3: Grid of Joukowski profile (15% thickness) at 60° stagger angle in the computational plane.

These figures can be seen on the computer terminal by running the program on an IBM-AT. However, no hardcopy device exists for this type of application in the "personal Computer Lab" in the "Computer Center" at the NPS. The figures can thus not be shown here.

8. Numerical Determination of Metric Terms.

The metric terms are calculated as centered differences (see Fig. 7-i). For calculation of the Jacobian determinant in the point (j,i) we need values from the surrounding points.

$$D_{j,i} = 1 / \{x_\xi y_\eta - x_\eta y_\xi\}_{j,i}$$

with

$$\begin{aligned} \{x_\xi\}_{j,i} &= (x_{j,i+1} - x_{j,i-1}) / (\xi_{j,i+1} - \xi_{j,i-1}) \\ \{y_\xi\}_{j,i} &= (y_{j,i+1} - y_{j,i-1}) / (\xi_{j,i+1} - \xi_{j,i-1}) \\ \{x_\eta\}_{j,i} &= (x_{j+1,i} - x_{j-1,i}) / (\eta_{j+1,i} - \eta_{j-1,i}) \\ \{y_\eta\}_{j,i} &= (y_{j+1,i} - y_{j-1,i}) / (\eta_{j+1,i} - \eta_{j-1,i}) \end{aligned}$$

Furthermore, for the "MUSCL"-approach, the derivatives (x_η, y_η) in the points $(j,i-1/2)$ and $(j,i+1/2)$, as well as the derivatives (x_ξ, y_ξ) in the points $(j+1/2,i)$ and $(j-1/2,i)$ are needed.

These are evaluated as:

$$\begin{aligned} \{x_\eta\}_{j,i+1/2} &= (x_{j+1,i+1/2} - x_{j-1,i+1/2}) / (2\Delta\eta) \\ &= (x_{j+1,i+1} + x_{j+1,i} - x_{j-1,i+1} - x_{j-1,i}) / (4\Delta\eta) \\ \{y_\eta\}_{j,i+1/2} &= (y_{j+1,i+1/2} - y_{j-1,i+1/2}) / (2\Delta\eta) \\ &= (y_{j+1,i+1} + y_{j+1,i} - y_{j-1,i+1} - y_{j-1,i}) / (4\Delta\eta) \\ \{x_\eta\}_{j,i-1/2} &= (x_{j+1,i-1/2} - x_{j-1,i-1/2}) / (2\Delta\eta) \\ &= (x_{j+1,i} + x_{j+1,i-1} - x_{j-1,i} - x_{j-1,i-1}) / (4\Delta\eta) \\ \{y_\eta\}_{j,i-1/2} &= (y_{j+1,i-1/2} - y_{j-1,i-1/2}) / (2\Delta\eta) \\ &= (y_{j+1,i} + y_{j+1,i-1} - y_{j-1,i} - y_{j-1,i-1}) / (4\Delta\eta) \\ \\ \{x_\xi\}_{j+1/2,i} &= (x_{j+1/2,i+1} - x_{j+1/2,i-1}) / (2\Delta\xi) \\ &= (x_{j+1,i+1} + x_{j,i+1} - x_{j+1,i-1} - x_{j,i-1}) / (4\Delta\xi) \\ \{y_\xi\}_{j+1/2,i} &= (y_{j+1/2,i+1} - y_{j+1/2,i-1}) / (2\Delta\xi) \\ &= (y_{j+1,i+1} + y_{j,i+1} - y_{j+1,i-1} - y_{j,i-1}) / (4\Delta\xi) \\ \{x_\xi\}_{j-1/2,i} &= (x_{j-1/2,i+1} - x_{j-1/2,i-1}) / (2\Delta\xi) \\ &= (x_{j,i+1} + x_{j-1,i+1} - x_{j,i-1} - x_{j-1,i-1}) / (4\Delta\xi) \\ \{y_\xi\}_{j-1/2,i} &= (y_{j-1/2,i+1} - y_{j-1/2,i-1}) / (2\Delta\xi) \\ &= (y_{j,i+1} + y_{j-1,i+1} - y_{j,i-1} - y_{j-1,i-1}) / (4\Delta\xi) \end{aligned}$$

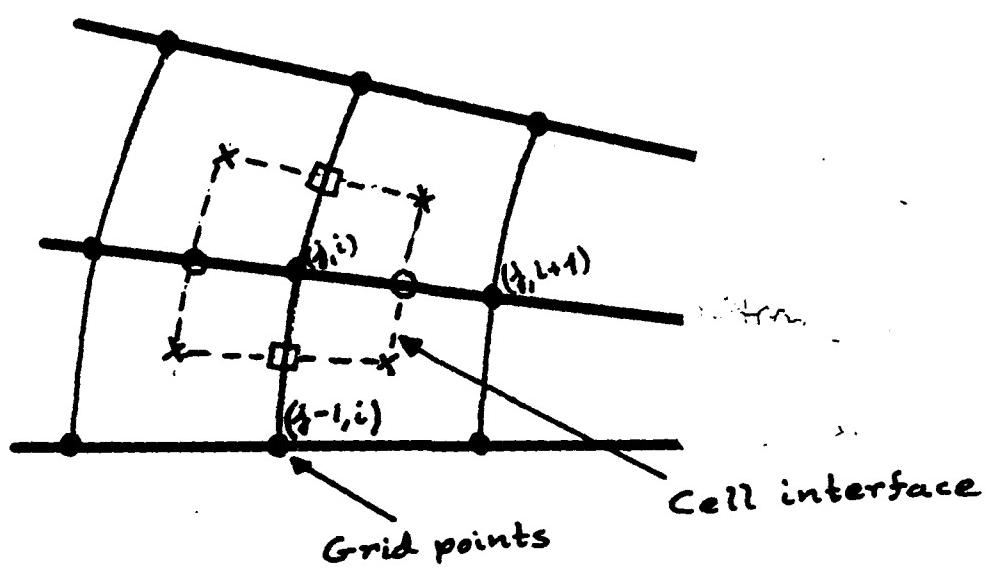


Fig. 8-1. Grid points and control volume for the evaluation of the metric terms.

9. Recommendations for Improvements.

In the following a few suggestions for improving the accuracy of the results obtained by the present method are given.

- In two dimensions the crude way of determining the departure point of the characteristic $(u-a)$ at the inlet and $(u+a)$ at the outlet certainly introduces some numerical reflection (section 3.3.2). In ref. /47/ an iterative procedure for finding this departure point has been given. This method could be tried out, still in connection with the "radiative" boundary condition at the inlet, in order to compare the numerical reflections with the present implementation.
- For an eventual improvement of the sharp capture of unsteady shocks it would be of interest to implement the flux vector splitting in van Leer's approach, and to compare this with the Steger/Warming splitting. Indications in the literature /50/ indicates that this approach may give sharper shocks than the present implementation.
- In the same direction it would be of interest to look into the possibility, as explained by Allmaras and Giles in /50/, of using the flow gradients within one cell only for obtaining a second order spatial accuracy, instead of, as present, employing two grid points for this (section 3.1).
- This method will also make it possible to keep a second order spatial accuracy at the blades, without the need for extrapolating any flow variables. Thus the accuracy of the stagnation enthalpy at the blades would improve.
- The accuracy of the stagnation enthalpy will also improve if grid points are clustered close to the walls.
- For a better accuracy of the total enthalpy at the walls, a modified splitting of the enthalpy has been proposed in /59/. The modification should be small and fairly easy to implement. According to reference /59/, the improvement of accuracy can be considerable.
- Quasi-one dimensional test cases by Adamson et al. (/39/-/45/), with shock oscillations so large that the shock moves upstream of the throat, could validate such numerical solutions. Comparisons of this kind would also serve to better understand the unsteady flow phenomena.

- In order to validate the two dimensional unsteady results, comparisons with detailed experiments could be made. Eventually could the numerous experimental results by Sajben et al serve as test cases.
- An interesting direct application of the method would be to consider the overlapping part of a transonic compressor cascade as a two dimensional curved channel and to investigate how large an unsteady back pressure fluctuation must be in order to significantly move the blade passage shock away from its steady state position.

10. Acknowledgements.

The present study was conducted during the authors stay as a National Research Council Associate at the Naval Postgraduate School, Monterey, California. This support, with Dr. R. W. Kinney as program manager and Dr. M. F. Platzer as technical adviser, is greatly appreciated.

Discussions with Dr. M. F. Platzer and Dr. J. Falcovitch regarding the physical aspects of unsteady flows and the numerical implications thereof were of large interest and very beneficial.

Finally, I would like to express my thanks to Mr. A. Krainer who introduced me to the main computer at the NPS, and who also wrote all the plot programs for presenting the one and two dimensional results in the present report.

11. References.

11/ Anderson, D. A.; Tannehill, J. C.; Pletcher, R. H.

"Computational Fluid Mechanics and Heat Transfer"

Hemisphere Publishing Corporation, New York, 1984.

12/ Roberts, G. O.

"Computational Meshes for Boundary Layer Problems"

Lecture Notes in Physics, vol. 8, pp. 171-177, Springer Verlag, New York, 1971.

13/ Zierep, J.

"Theoretische Gasdynamik"

G. Braun Verlag, Karlsruhe, 1976

14/ Vivland, H.

"Formes conservatives des équations de la dynamique des gaz"

La Recherche Aérospatiale, No. 1, 1974, pp. 65-68.

15/ Roache, P. J.

"Computational Fluid Dynamics"

Hermosa Publishers, Albuquerque, New Mexico, 1976, p.229.

16/ Moretti, G.; deNeff, T.

"Shock Fitting for Everybody"

Journal of Computers and Fluids. Vol. 8, No. 3, 1981.

17/ Fransson, T.; Pandolfi M.

"Numerical Investigation of Unsteady Subsonic Compressible Flows Through an Oscillating Cascade"

ASME Paper 86-GT-304, 1986.

18/ Verdon, J. M.

"Further Development in the Aerodynamic Analysis of Unsteady Supersonic Cascades."

ASME Paper No. 77-GT-44, 77-GT-45, 1977.

19/ Samolovtch, G.

"Resonance Phenomena in Sub- and Supersonic Flow Through an Aerodynamic Cascade"

Mekhanika Zhidkosti i Gaza, Vol. 2, No. 3, pp. 143-144, 1967.

/10/ BöIcs, A.; Fransson, T.

"Aeroelasticity in Turbomachines: Comparison of Theoretical and Experimental Cascade Results"

Communication de laboratoire de thermique appliquée et de turbomachines, No. 16, Ecole Polytechnique Fédérale, Switzerland, 1986.

/11/ Anderson, W. K.; Thomas, J. L.; van Leer, B.

"A Comparison Of Finite Volume Flux Vector Splittings for the Euler Equations."

AIAA Paper 85-0122, 1985.

/12/ Grossman, B.

"Fundamental Concepts in Computational Fluid Dynamics."

Lecture Notes presented at a short course on: "Numerical Gas Dynamics- A Designer's Tool", March 10-14, 1986, The Polytechnic University, Long Island Center, Farmingdale, New York.

/13/ Steger, J. L.; Warming, R. F.

"Flux Vector Splitting of the Inviscid Gasdynamic Equations with Application to Finite-Difference Methods"

Journal of Computational Physics, No. 40, pp. 263-293, 1981.

/14/ Steger, J. L.

"Preliminary Study of Relaxation Methods for the Inviscid Conservative Gasdynamics Equations Using Flux Splitting."

NASA CR-3415, 1981.

/15/ Holtman, H.

"Ein numerisches Verfahren zur Berechnung der instationären, zweidimensionalen Strömung durch schwingende Beschaufelungen axialer Turbomaschinen."

Ph. D. Thesis, Technische Hochschule, Aschen, West Germany, 1983.

/16/ Holtman, H.; Servaty, S.; Gallus, H. E.

"Computation of the subsonic flow field through oscillating compressor and turbine cascades."

Unsteady Aerodynamics of Turbomachines and Propellers, Cambridge, United Kingdom, September 24-27, 1984, pp. 73-92.

/17/ Joubert, H.

"Supersonic Flutter in Axial Flow Compressors."

Unsteady Aerodynamics of Turbomachines and Propellers, Cambridge, United Kingdom, September 24-27, 1984, pp. 231-254.

/18/ Roe, P. L.

"Characteristic-Based Schemes for the Euler Equations."

Annual Review of Fluid Mechanics, Vol. 18, pp. 337-365, 1986.

/19/ Chakravarthy, S.; Osher, S.

"A New Class of High Accuracy TVD Schemes for Hyperbolic Conservation Laws."

AIAA Paper 85-0363, 1985.

/20/ Moretti, G.

"The λ -Scheme."

Journal of Computational Fluids, Vol. 7, pp. 191-205, 1979.

/21/ Roe, P. L.

"Approximate Riemann Solvers, Parameter Vectors, and Difference Schemes."

Lecture Notes in Physics, Vol. 141, pp. 354-359, 1980

/22/ Pandolfi, M.

"AIAA Paper presented at the Computational Fluid Dynamics Conference in Honolulu, June 1987."

/23/ Chakravarthy, S. R.

"Development of Upwind Schemes for the Euler Equations."

NASA Contractor Report 4043, Contract NAS1-17492, January 1987.

/24/ Fransson, T.

"Numerical Investigation of Unsteady Subsonic Compressible Flows Through an Oscillating Cascade"
Communication de laboratoire de thermique appliquée et de turbomachines,
No. 12, Ecole Polytechnique Fédérale de Lausanne, Switzerland, 1985.

/25/ Fleeter S.

"Aeroelasticity Research for Turbomachine Applications"
AIAA Paper 77-437, 1977.

/26/ Platzer, M. F.

"Transonic Blade Flutter: A Survey of New Developments"
The Shock and Vibration Digest, Vol. 14, No. 7, 1982.

/27/ Arnoldi, R. A.; Mikolajczak, A.; Snyder, L.; Stargardter, H.

"Advances in Fan and Compressor Blade Flutter Analysis and Predictions."
Journal of Aircraft, Vol. 12, No. 4, 1975.

/28/ van Leer, B.

"Flux-Vector Splitting for the Euler Equations."
Eighth International Conference on Numerical Methods in Fluid Dynamics, RWTH, Aachen, Germany, June 28-July 2, 1982, pp. 507-512.

/29/ Steger, J. L.

"Implicit Finite Difference Simulation Of Inviscid and Viscous Compressible Flow."
1982.

/30/ Buning, P. G.; Steger, J. L.

"Solution of the Two-Dimensional Euler Equations with Generalized Coordinate Transformation Using Flux Vector Splitting."
AIAA Paper AIAA-82-0971, 1982.

/31/ Pulliam, T. H.

"Artificial Dissipation Models for the Euler Equations."
AIAA Journal, Vol. 24, No. 12, pp. 1931-1940, 1986.

/32/ Moretti, G.

"Experiments on Initial and Boundary Conditions."

Paper presented at "Symposium on Numerical and Physical Aspects of Aerodynamic Flow", January 1981.

/33/ Ni, R. H.

"A Multiple-Grid Scheme for Solving the Euler Equations."

AIAA Journal, Vol. 20, No. 11, pp. 1565-1571, 1982.

/34/ Eldeiman, S.; Colella, P.; Shreeve, R. P.

"Application of the Godunov Method and Higher Order Extensions of the Godunov Method for Cascade Flow Modeling."

AIAA Paper AIAA-83-1941-CP, 1983.

/35/ von Lavante, E.; Haertl, A.

"Numerical Solutions of the Euler Equations Using Simplified Flux Vector Splitting."

AIAA Paper AIAA-85-1333, 1985.

/36/ Fransson, T. H.; Kehlstadt, J. P.

"Expérience numérique et expérimentale de l'écoulement subsonique dans une canal bi-dimensionnelle."

Internal Report LTT-14-83, Swiss Federal Institut of Technology, Lausanne, Switzerland, 1983.

/37/ Barton, J. T.; Pulliam, T. H.

"Airfoil Computation at High Angles of Attack, Inviscid and Viscous Phenomena."

AIAA Journal, Vol. 24, No. 3, pp. 705-712, 1986.

/38/ Barth, T. J.; Lomax, H.

"Algorithm Development."

NASA Conference Publication 2454, pp. 191-200, 1987.

/39/ Adamson Jr., T. C; Richey, G. K.

"Analysis of Unsteady Transonic Channel Flow with Shock Waves."

AIAA Journal, Vol. 14, No. 8, pp. 1054-1061, 1976.

/40/ Adamson Jr., T. C; Chan J. S.-K.

"Unsteady Transonic Flows with Shock Waves in an Asymmetric Channel."
AIAA Journal, Vol. 16, No. 4, pp. 377-384, 1978.

141/ Adamson Jr., T. C; Messiter, A. F.; Liou, M. S.

"Large Amplitude Shock-Wave Motion in Two-Dimensional Transonic Channel Flows."

AIAA Journal, Vol. 16, No. 12, pp. 1240-1247, 1978.

142/ Adamson Jr., T. C; Messiter, A. F.

"Forced Oscillations of Transonic Channel and Inlet Flows with Shock Waves."

AIAA Journal, Vol. 22, No. 11, pp. 1590-1599, 1984.

143/ Adamson Jr., T. C; Mace, J. L.

"Shock Waves in Transonic Channel Flows at Moderate Reynolds Numbers."

AIAA Journal, Vol. 24, No. 4, pp. 591-598, 1986.

144/ Adamson Jr., T. C; Liou, M. S.

"Unsteady Motion of Shock Waves in Two Dimensional Transonic Channel Flows."

Report No. UM-014534-F, June 1977, Department of Aerospace Engineering, University of Michigan, Michigan, USA

145/ Adamson Jr., T. C; Liou, M. S.

"Unsteady Transonic Flow in Two-Dimensional Channels."

Report No. UM-015411-F, October 1978, Department of Aerospace Engineering, University of Michigan, Michigan, USA

146/ van Leer, B.; Thomas, J. L.; Roe, P. L.; Newsome, R. W.

"A Comparison of Numerical Flux Formulas for the Euler and Navier-Stokes Equations."

AIAA Paper 87-1104-CP, Honolulu, 1987.

147/ Tong, S. S.

"Time-Split Inflow Boundary Treatment"

ASME Paper 85-GT-165, 1985

148/ MacCormack, R. W.

"Numerical Solution of the Interaction of a Shock Wave with a Laminar Boundary Layer."

Lecture Notes in Physics No. 8, "Proceedings of the Second International Conference on Numerical Methodes in Fluid Dynamics", September 15-19, 1970, University of California, Berkeley, California."

/49/ Anderson, W. K.; Thomas, J. L.; Rumsey, C. L.

"Extension and Applications of Flux-Vector Splitting to Unsteady Calculations on Dynamic Meshes."

AIAA Paper 87-1152-CP, Honolulu, 1987.

/50/ Allmaras, S. R.; Giles, M. B.

"A Second Order Flux Split Scheme for the Unsteady Two-Dimensional Euler Equations on Arbitrary Meshes."

AIAA Paper 87-1119-CP, Honolulu, 1987.

/51/ Whitfield, D. L.; Janus, J. M.

"Three-Dimensional Unsteady Euler Equation Solution Using Flux Vector Splitting."

AIAA Paper 84-1552, 1984.

/52/ Warming, R. F.; Beam, R. M.

"On the Construction and Application of Implicit Factored Schemes for Conservation Laws."

Symposium in Applied Mathematics Proceedings, Vol. XI, pp. 85-129, 1976.

/53/ van Leer, B.

"Flux Vector Splitting for the Euler Equations."

Lecture Notes in Physics, Vol. 170, pp. 507-512, Springer Verlag, New York, 1982.

/54/ Hyltén-Cavallius, C.; Sandgren, L.

"Matematisk Analys II."

Berlingska Boktryckeriet, Lund, Sweden, 1968.

/55/ Steger, J. L.

"Contributions to a Short Course on Numerical Gas Dynamics."

*Short Course on "Numerical Gas Dynamics: An Engineers Tool,"
Departemnt of Mechanical and Aerospace Engineering, Polytechnic Institute
of New York, March 10-14, 1986.*

/56/ Verdon, J. M.; Usab, W. J.

"Application of a Linearized Unsteady Aerodynamic Analysis to Standard
Cascade Configurations."

NASA Contractor Report, 1985.

/57/ Peyret, R.; Taylor, T. D.

"Computational Methods for Fluid Flow."

Springer Verlag, New York, 1983, p. 319.

/58/ Mitchell, A. R.; Griffiths, D. F.

"The Finite Difference Method in Partial Differential Equations."

John Wiley & Sons, New York, 1980, pp. 182, 202.

/59/ Hänel, D.; Schwane, R.; Seider, G.

"On the Accuracy of Upwind Schemes for the Solution of the Navier-Stokes
Equations."

AIAA Paper 87-1105, 1987.

DISTRIBUTION LIST

	<u>No. of Copies</u>
1. Library Code 0142 Naval Postgraduate School Monterey, California 93943-5000	2
2. Defense Technical Information Center Cameron Station Alexandria, Virginia 22341	2
3. Chairman, Department of Aeronautics Code 67 Naval Postgraduate School Monterey, California 93943-5000	1
4. Director of Research Administration Code 012 Naval Postgraduate School Monterey, California 93943-5000	1
5. Dr. T. H. Fransson Laboratoire de Thermique Appliquee et de Turbomachines Ecole Polytechnique Federale CH-1015 Lausanne Switzerland	1
6. Chief of Naval Research 800 N. Quincy St. Arlington, VA 22217	1

ENVID

DATE

3 - 88

DTIC